UNIVERSITÉ DE STRASBOURG

Ecole Doctorale Physique

VERS LA MODELISATION DES TRAITEMENTS DE RADIOTHERAPIE :

- RADIOTHERAPIE EXTERNE PAR TOMOTHERAPIE

- APPRENTISSAGE PROFOND EN RADIOTHERAPIE

Mémoire de soutenance à l'Habilitation à Diriger des Recherches

Spécialité : Physique Médicale

Philippe MEYER

Centre Paul Strauss, Strasbourg

Date : 9 avril 2018

Composition du jury

J Thariat	PU-PH, Centre François Baclesse de Caen	Examinatrice
JM Fontbonne	IR (HDR), IN2P3-LPC de Caen, UMR 6534	Rapporteur
R Gschwind	PU, Université de Franche-Comté, UMR CNRS 6249	Rapportrice
JY Giraud	Physicien Médical (HDR), CHU Grenoble	Rapporteur
F Heitz	PU, ICube - IMAGeS Strasbourg, UMR 7357	Examinateur
D Husson	MC (HDR), IPHC - DeSIs Strasbourg, UMR 7178	Examinateur, Garant

AVANT-PROPOS

Après une formation initiale en physique appliquée et une spécialisation dans les rayonnements ionisants en médecine, j'ai effectué une thèse entre 2000 et 2003 dont le sujet était *Contribution au principe d'optimisation de la radioprotection en radiologie*. J'ai ensuite suivi la formation pratique du DQPRM au Centre Alexis Vautrin (Nancy), avant d'être embauché en 2004 en tant que physicien médical au Centre Paul Strauss (CPS).

En 2004, l'unité de physique du CPS était composée de 5 personnes dont 3 physiciens médicaux. Notre activité était intégralement consacrée à la routine clinique, et un de mes objectifs était alors de développer des activités de recherche à moyen terme. Entre 2006 et 2017, nous avons encadré 14 stagiaires de Master2 et 17 étudiants DQPRM. Au sein de l'unité de physique ou en collaboration avec l'équipe médicale, nous avons pendant ces 10 années publié une vingtaine d'articles et présenté plus de 40 posters ou présentations orales. Dans le même temps, l'unité de physique médicale du CPS est devenue un département indépendant, et est passée de 5 à 15 personnes.

Mes activités de recherche passées et actuelles concernent l'amélioration de la prise en charge des patients en radiothérapie. Nous avons pour cela travaillé avec d'autres centres de radiothérapie, et avons développé des collaborations avec des laboratoires strasbourgeois comme Aerial, des équipes de l'IPHC et d'ICube. Les thèmes que nous avons abordés sont variés : curiethérapie, détection des rayonnements, contrôle de qualité, imagerie et informatique en radiothérapie, radiothérapie clinique.

Mes recherches se sont portées principalement sur deux thèmes. Le premier concerne la radiothérapie par tomothérapie. Cette technique, installée au CPS en 2007, combine la modulation d'intensité et la radiothérapie guidée par l'image. Je me suis particulièrement investi dans l'amélioration des traitements par tomothérapie. Sur ce seul sujet, j'ai communiqué en qualité de premier auteur ou auteur associé près de 25 fois sous forme de publication écrite, poster ou orale. Mes travaux ont notamment porté sur l'imagerie de positionnement, les traitements pédiatriques et mammaires. Nous continuerons à développer ce thème de recherche à l'IRC, en nous focalisant sur les nouveaux outils de radiothérapie adaptative dédiés à cette machine. Mes travaux de recherche sur la tomothérapie font l'objet de la première partie de ce mémoire.

Le deuxième thème concerne l'intelligence artificielle appliquée à la radiothérapie, et en particulier les techniques dites d'apprentissage profond (*deep learning*). Sur ce sujet, nous collaborons depuis 2016 avec le laboratoire ICube, dont je suis aujourd'hui chercheur associé. Après avoir établi un état de l'art de l'utilisation du *deep learning* en radiothérapie, nous avons développé un algorithme de segmentation automatique des métastases cérébrales basé sur cette technologie. Cet algorithme sera évalué en conditions cliniques en 2018, et nous développerons en parallèle des outils permettant de mieux appréhender le comportement des réseaux profonds. Nos travaux de recherche sur la thématique du *deep learning* font l'objet de la deuxième partie de ce mémoire.

TABLE DES MATIERES

REMERCIEMENTS

Je tiens en premier lieu à exprimer toute ma gratitude envers Daniel Husson, qui a pris le pari de me conseiller et de m'épauler durant toute la préparation de cette HDR.

Je remercie Régine Gschwind, Jean-Marc Fontbonne et Jean-Yves Giraud, qui ont acceptés d'être les trois rapporteurs de cette HDR. Mes remerciements vont également à Juliette Thariat et Fabrice Heitz pour avoir accepté de compléter mon jury. Je leur suis particulièrement reconnaissant pour le temps important consacré à la lecture de mon mémoire, dont les thèmes sont variés.

Le contenu de ce mémoire est le fruit du travail collectif de tous les membres passés et présents de l'équipe de physique médicale du Centre Paul Strauss (CPS). Je remercie particulièrement Diran Karamanoukian, qui m'a accueilli dans son équipe et qui m'a donné l'opportunité de m'y épanouir. Je remercie aussi Christophe Mazzara, qui a pris avec brio le relais de Diran, et qui a mis en place les conditions rendant possible cette HDR. Je remercie bien sûr tous mes collègues qui sont associés autant que moi à ce mémoire, et qui auraient pu figurer sur la page de garde (s'il y avait eu assez de place) : Azziza Boutarene, Caroline Noblet, Claudine Niederst, Corinne Renaud, Cyrielle Bourrier, Delphine Jarnet, Denis Moensch, Elodie Bertheau, Frédéric Fux, Guillaume Billaud, Jennifer Couchot, Keltoum Rebiai, Matthieu Gantier, Matthieu Moreau, Nicolas Dehaynin, Pascal Pernot, Pascale Magnenet, Perrine Koell, Rui Guerra et Sébastien Perlongo. Une pensée aux stagiaires qui ont contribué à plusieurs publications : Maximilien, Hugo, Fabien et Odelin.

Le travail rapporté dans ce mémoire n'eut été impossible sans l'apport des médecins, manipulateurs et secrétaires du département de radiothérapie du CPS : qu'ils soient ici collectivement remerciés. Je n'oublie pas la direction du CPS et du département de radiothérapie, qui m'ont toujours soutenu et encouragé dans ma démarche.

Je remercie les différentes personnes des laboratoires avec lesquelles nous avons collaboré depuis 2004. Je pense notamment à Vincent Noblet, Alex Lallement et Etienne Baudrier de l'équipe MIV d'ICube ; à Nicolas Arbor, Abdel-Midj Nourredine et Ziad El Bitar des laboratoires DeSIs et Ramses de l'IPHC ; à Florent Kuntz et Alain Strasser d'Aérial ; à Mélodie Munier et Till Sohier de la société Fibermetrix ; à Alexandre Hostettler de l'IRCAD ; et à Hervé Simon de la société Eurorad.

Mes remerciements vont enfin à ma famille, et en particulier à mon épouse, mes enfants et mes parents.

I. ACTIVITES DE RECHERCHE

A. RADIOTHERAPIE EXTERNE PAR TOMOTHERAPIE

La tomothérapie (Accuray, Etats-Unis) est une technique de traitement de radiothérapie externe. Le premier patient a été traité aux Etats-Unis en 2002 (Mackie, 2006). Le succès de cette technologie a alors été immédiat, du fait de ses capacités uniques à l'époque combinant la radiothérapie conformationnelle par modulation d'intensité (RCMI) et l'imagerie de positionnement tridimensionnelle. Dans ce chapitre, je propose tout d'abord de présenter la technique de traitement de tomothérapie dans la partie I.A.1, avant de présenter nos travaux de recherche sur ce sujet dans les parties I.A.2, I.A.3 et I.A.4.

1. Introduction à la tomothérapie

Figure 1. Tomothérapie Hi-ART (à gauche) et HD (à droite) du Centre Paul Strauss.

Historique

Le concept et le terme de *tomothérapie* a été introduit pour la première fois en 1993 par Rock Mackie (Mackie et al., 1993). Ce physicien américain de l'université du Wisconsin a travaillé au préalable sur l'implémentation d'algorithmes de calcul de dose dans les systèmes de planification de traitement de radiothérapie (Mackie, 1990; Mackie et al., 1988, 1985). Avec son équipe, il a proposé le concept de tomothérapie dans le but de délivrer les faisceaux de fluence hétérogène prédits par Brahme (Brahme et al., 1982).
Il a fallu attendre une dizaine d'années entre la présentation du concept sur papier et le traitement du premier patient. Cette période de développement mouvementée a été décrite de manière détaillée par Rock Mackie lui-même (Mackie, 2006). Trois modèles de machines ont successivement été commercialisées depuis : Tomothérapie Hi-ART (2003), HD (2010) et RadiXact (2017). Tomotherapy

Inc. (Madison, Wisconsin) a développé et vendu les premiers modèles (1999-2011), avant d'être racheté par la société Accuray (Sunnyvale, Californie).

Technologie

Le principe de fonctionnement de la machine et de la délivrance de la dose n'a pas varié depuis le premier prototype, seules des évolutions technologiques différenciant les trois modèles de série. Ce principe a été largement décrit dans la littérature (Beavis, 2004; Mackie, 2003; Mahé et al., 2007; Tomsej, 2006), et nous n'en reprendrons ici que les caractéristiques principales.

L'aspect général de la tomothérapie est unique en radiothérapie, et s'apparente au premier abord à un scanner (Figure 1). Les principaux composants de la machine sont donnés sur la Figure 2. Un accélérateur linéaire monté sur un anneau tournant délivre un faisceau dont l'énergie maximale est environ égale à 5,7 et 3,5 MeV respectivement en mode traitement et imagerie (Figure 3). Ce faisceau est mis en forme par un collimateur primaire, puis collimaté par une mâchoire qui définit la taille du faisceau (*Field Width*, FW) dans le sens tête-pieds du patient (voir Figure 4). Le faisceau traverse ensuite un collimateur multilame (*Mulileaf collimator*, MLC) binaire unique en radiothérapie, dont les 64 lames ne prennent que deux positions : ouvertes ou fermées (voir Figure 5).

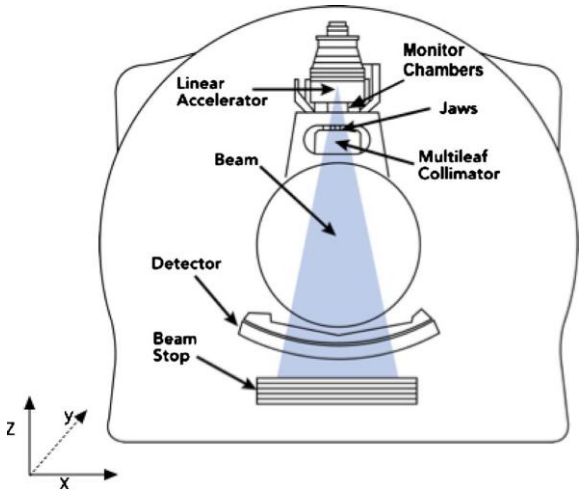

Figure 2. Principaux composants d'une machine de tomothérapie (Langen et al., 2010).

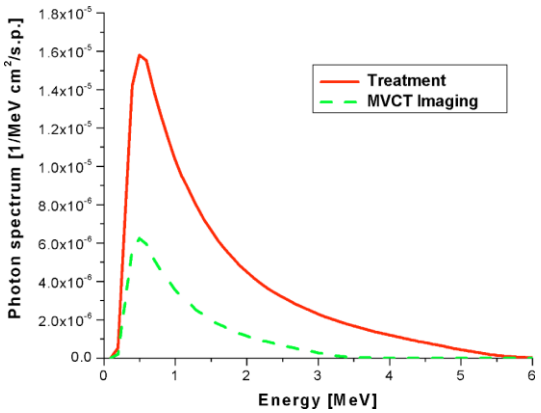

Figure 3. Spectres énergétiques du faisceau de la tomothérapie en mode traitement et imagerie. L'énergie maximale est environ égale à 5,7 et 3,5 MeV respectivement en modes traitement et imagerie, correspondant à des énergies moyennes de 1,5 et 1 MeV (Jeraj et al., 2004).

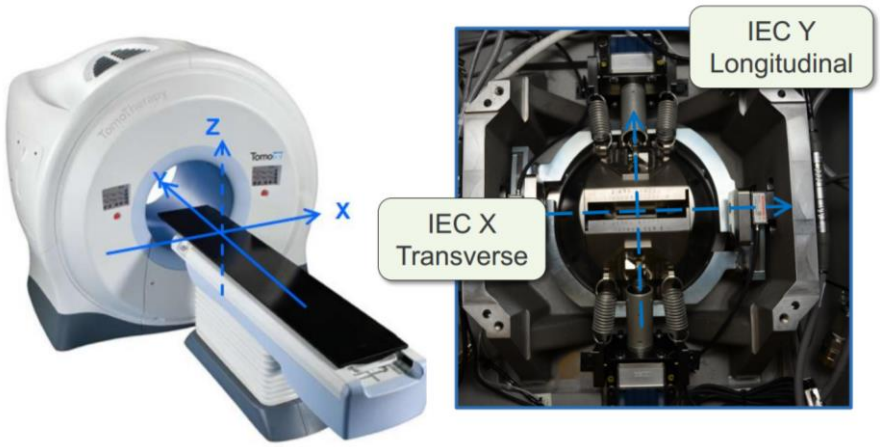

Figure 4. Détails de la mâchoire de collimation de la tomothérapie (Accuray, 2013a).

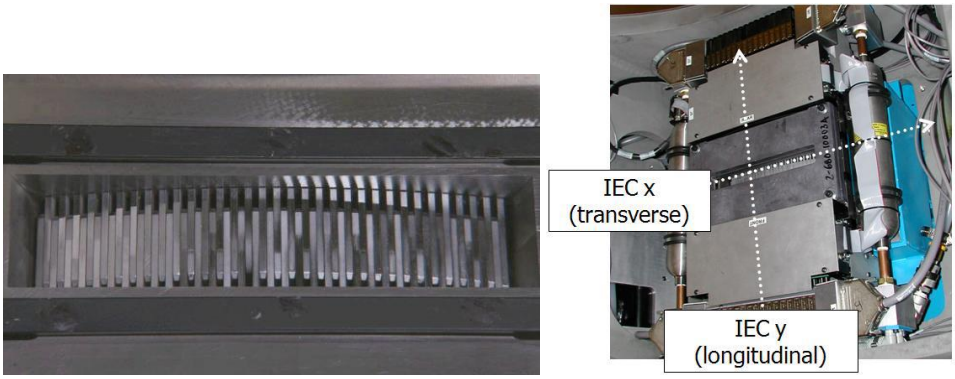

Figure 5. Détails du collimateur multilame binaire de la tomothérapie, composé de deux bancs opposés de 32 lames chacun. Les lames sont faites à 95% de tungstène et font 10 cm d'épaisseur (Accuray, 2013a).

Lorsque toutes les lames sont ouvertes, la position des mâchoires permet de définir trois tailles de champs (40 x 1 ou 40 x 2,5 ou 40 x 5 cm² à l'isocentre). L'ouverture et la fermeture des lames permettent de moduler la fluence du faisceau (Figure 6). Un système pneumatique assure le mouvement des lames : le temps de transition entre les deux positions est de l'ordre de 20 ms. Une couronne de détecteurs récupère enfin l'image radiante avec laquelle est reconstruite l'anatomie du patient en trois dimensions (voir paragraphe 3.b).

Délivrance du faisceau

Le patient est positionné sur la table de traitement, qui translate de manière continue dans l'anneau pendant l'irradiation. L'accélérateur tourne et délivre simultanément le faisceau, l'irradiation étant effectuée hélicoïdalement (Figure 7). Le débit de dose est fixe (environ 9 Gy/min à l'isocentre pour les modèles Hi-ART et HD, jusqu'à 10 Gy/min pour le modèle Radixact). La vitesse d'avancée de la table et de rotation de l'accélérateur sont déterminées par le système de planification de traitement (*Treatment Planning System*, TPS) et sont fixes pour un traitement donné. Seule la position des lames varie au cours de l'irradiation : une rotation de l'accélérateur est divisée en 51 projections, le système de planification de traitement assignant à chaque lame du collimateur multilame (MLC) un

pourcentage de temps d'ouverture par projection. Cette variation d'ouverture et de fermeture de lames permet d'obtenir la fluence prévue lors de la planification de traitement

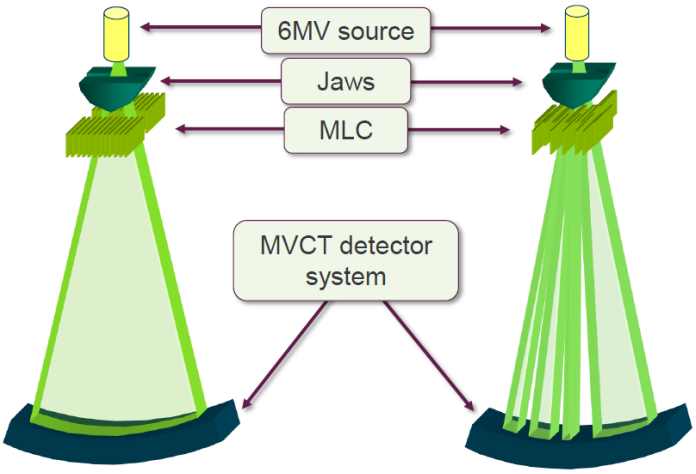

Figure 6. Représentation schématique de la modulation de la fluence du faisceau avec les lames du MLC. A gauche : toutes les lames sont ouvertes. A droite : plusieurs lames sont fermées (Accuray, 2013b).

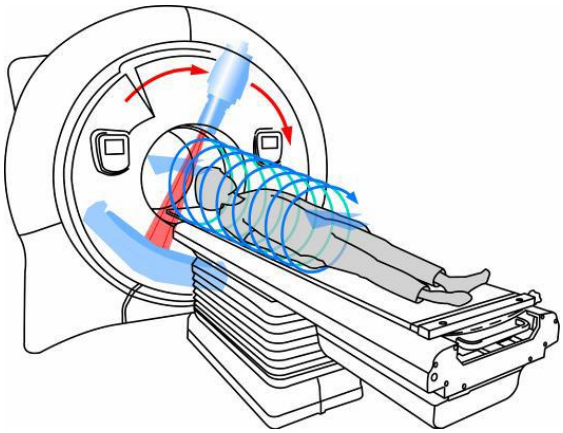

Figure 7. Irradiation hélicoïdale du patient (Accuray, 2013c).

La tomothérapie au Centre Paul Strauss (CPS)

La première machine de tomothérapie a été installée en France en 2006 à l'institut Curie. Depuis, 42 autres machines de ce type ont été installées en France, soit aujourd'hui un peu moins de 10 % du parc d'accélérateurs de radiothérapie (Institut National du Cancer, 2015). Au CPS, deux tomothérapies ont été installées en 2007 (Hi-ART) et 2013 (HD), respectivement les quatrième et seizièmes en France. A l'IRC, la tomothérapie représentera la moitié du futur parc de six accélérateurs, une troisième machine de ce type (Radixact) devant y être installée en 2018. Il s'agit d'un parc important, puisque l'IRC fera partie des trois seuls centres de radiothérapie français (sur 170) disposant de trois tomothérapies. Parmi les pionniers des utilisateurs de cette machine en France, nous nous sommes beaucoup investis dans la recherche appliquée autour des traitements par tomothérapie, et nous continuerons à travailler dans ce sens.
Le premier patient a été traité au CPS le 18 décembre 2007 sur la tomothérapie Hi-ART et le 22 octobre 2013 sur la tomothérapie HD. Depuis, 2171 et 1081 patients ont été traités respectivement

sur ces deux machines (à la date du 26/10/2017). Les localisations traitées sont diverses : cancers ORL, gynécologiques, sarcomes des tissus mous, thoraciques … (voir Figure 8).

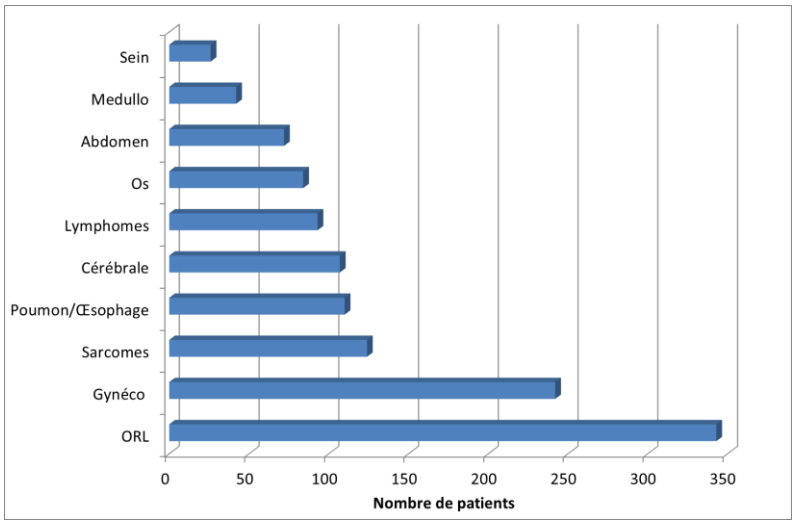

Figure 8. Répartition des patients traités au CPS par tomothérapie en fonction des localisations entre 2008 et juin 2014.

Les cancers ORL constituent la première localisation traitée par tomothérapie au CPS : leur prise en charge est en effet particulièrement adaptée sur cette machine, avec des résultats supérieurs à ceux obtenus par d'autres techniques d'irradiation (Bibault et al., 2017). Les sarcomes des tissus mous, spécialement ceux des membres supérieurs ou inférieurs, sont tous traités au CPS par tomothérapie, une machine de choix pour le traitement de ces volumes souvent longs et complexes.
Néanmoins, l'irradiation de ces cancers implique des paramètres de traitement adaptés, notamment parce que les volumes sont décentrés par rapport à l'axe du patient : ce sujet fait l'objet du chapitre I.A.2. Les cancers mammaires n'ont été que marginalement traités par tomothérapie au CPS, mais leur prise en charge par radiothérapie conformationnelle par modulation d'intensité (RCMI) est de plus en plus discutée : elle est abordée dans le chapitre I.A.3. Enfin, les traitements pédiatriques sont quasi-exclusivement effectués au CPS sur tomothérapie : environ 300 enfants et jeunes adultes ont été traités entre 2008 et 2017. Il s'agit d'une problématique particulière, qui fait l'objet du chapitre I.A.4.

2. Le traitement des sarcomes des membres en tomothérapie

Le système de planification de traitement de la tomothérapie repose sur le principe classique de planification inverse utilisé en RCMI (Ezzell et al., 2003). Des contraintes et objectifs de dose sont assignés librement par l'utilisateur aux volumes cibles et organes à risque, et un algorithme d'optimisation calcule les fluences de dose permettant de satisfaire au mieux à ces contraintes. Cette optimisation est un processus itératif, guidé par la minimisation d'une fonction objectif pouvant être exprimée comme la somme des carrés des différences entre dose souhaitée et calculée en tous points des volumes d'intérêt (Court et al., 2015).
Un nouveau logiciel de calcul de dose (*nonvoxel based broad-beam*, NVBB) sur GPU (*Graphics Processor Units*) a été implémenté par la société Accuray dans le système de planification de traitement tomothérapie en 2012 afin de réduire les temps de calcul (Lu, 2010). Il comporte deux algorithmes distincts, de *fluence-convolution broad-beam* (FCBB) pour un calcul approximatif de la dose (Lu and Chen, 2010) et de *collapsed-cone convolution-superposition* (CCCS) pour un calcul plus

précis (Q. Chen et al., 2011). L'algorithme FCBB rend le processus itératif d'optimisation faisable dans un temps réaliste, une prise en compte plus précise des hétérogénéités étant réalisée toutes les dix itérations à l'aide de l'algorithme CCCS.

Une des particularités de la planification de traitement en tomothérapie est la nécessité pour l'utilisateur de spécifier trois paramètres : la largeur de fente FW, le facteur de modulation FM et le *pitch* du traitement (De Kerf et al., 2015). Le FW a été défini précédemment. Le FM est égal au temps maximum d'ouverture des lames du MLC divisé par la moyenne des temps d'ouvertures (en excluant les lames qui restent fermées). Le *pitch* est défini comme la distance parcourue par la table pendant une rotation du bras, divisée par le FW. Le choix de ces trois paramètres est crucial, puisqu'il impacte directement la qualité dosimétrique, la qualité de la délivrance du faisceau et la durée du traitement. Le choix optimal des valeurs de ces trois paramètres est d'autre part complexe, puisqu'il dépend de nombreux facteurs comme la taille du volume cible dans le sens tête-pieds, le fractionnement ou encore la distance de la cible par rapport à l'axe de rotation de la tomotherapie.

Un mauvais choix de pitch peut générer des ondulations de dose longitudinales (dans le sens tête-pieds), aussi appelées *thread effect* (voir Figure 9). En 2005, Kissick et al. ont montré que certaines valeurs de *pitchs* (0,86/n où n est un entier) permettent d'atténuer ce phénomène (Kissick et al., 2005). Ces valeurs ont été adoptées par la communauté des utilisateurs de tomothérapie, et la majorité des traitements est effectuée avec des *pitchs* égaux à 0,43 ou 0,287 ou encore 0,215.

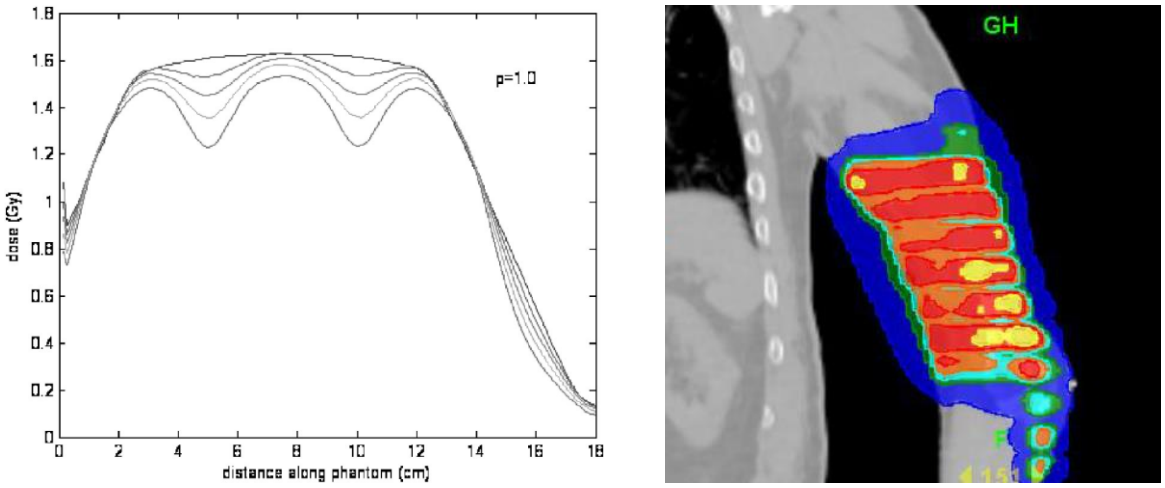

Figure 9. A gauche : profil de dose longitudinal à une distance de l'isocentre de 0, 3, 5, 7 et 9 cm avec un *pitch* = 1 et un faisceau non modulé. Les ondulations les plus importantes sont relevées à une distance de 9 cm de l'isocentre, et se réduisent jusqu'à ce qu'on ne relève aucune ondulation à l'isocentre (Kissick et al., 2005). A droite : illustration du *thread effect* lors de la planification de traitement d'un sarcome du bras gauche au CPS.

En 2011, Chen et al. ont partiellement remis en cause ces valeurs de pitch, en quantifiant de manière individuelle et combinée quatre causes du *thread effect* (Q. Chen et al., 2011): l'inverse carré de la distance (seule cause identifiée par Kissick et al.), la divergence du profil, l'atténuation et l'effet du cône (voir Figure 10). Ils ont montré que la valeur optimale du *pitch* dépend surtout de la distance de la cible à l'isocentre (voir Figure 11). Ils ont également proposé une nouvelle gamme de valeurs de *pitchs* optimaux censées être plus efficaces que ceux de Kissick, donnée en fonction du FW et de la distance entre la cible et l'isocentre de la tomothérapie.

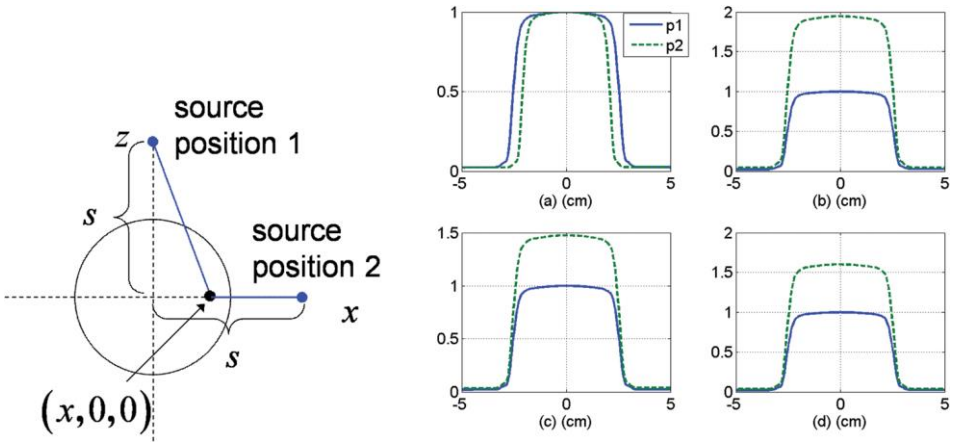

Figure 10. Illustration de la modification du profil de dose lorsque la source passe de la position 1 à la position 2. A gauche : vue transverse d'un fantôme cylindrique, avec une cible à la distance x de l'isocentre. A droite : profils de dose longitudinaux à la position de la cible pour la source en position 1 ou 2 en fonction (a) de la divergence du profil, (b) de l'atténuation, (c) de l'inverse carré de la distance et (d) de l'effet du cône (M. Chen et al., 2011).

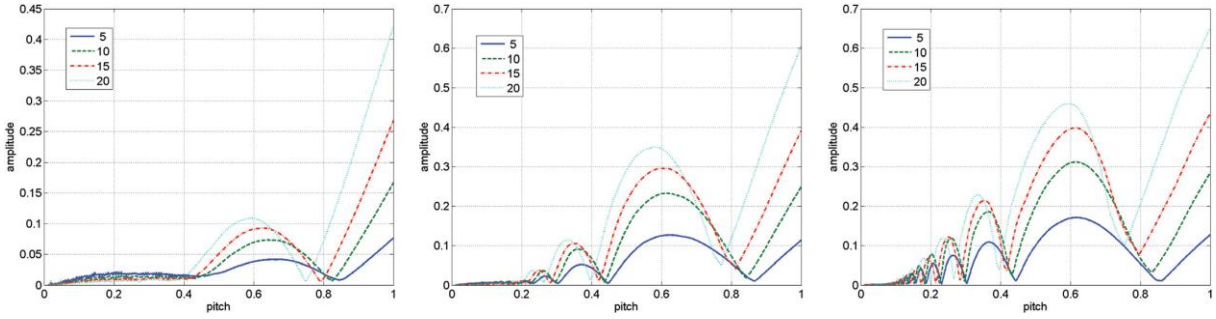

Figure 11. Amplitude du *thread effect* en fonction du pitch pour des FW de 1 (à gauche), 2,5 (au centre) et 5 cm (à droite) à 5, 10, 15 et 20 cm de distance de l'isocentre (M. Chen et al., 2011).

Au CPS, tous les sarcomes des tissus mous sont traités en tomothérapie. Parmi eux, les sarcomes des membres se distinguent par le fait qu'ils sont décentrés par rapport à l'axe du patient et à celui de l'isocentre de la tomothérapie. L'influence du pitch est donc primordiale pour ce type de traitement. Nous avons cherché à déterminer les paramètres de traitement optimaux pour le traitement des sarcomes des membres en tomothérapie, et notamment à quantifier l'intérêt d'utiliser les valeurs de *pitch* proposées par Chen et al. à la place de ceux de Kissick et al. Cette étude est présentée dans la publication suivante (Meyer et al., 2015).

Physica Medica 31 (2015) 542–552

Contents lists available at ScienceDirect

Physica Medica

journal homepage: http://www.physicamedica.com

Technical notes

The optimal tomotherapy treatment planning parameters for extremity soft tissue sarcomas

Philippe Meyer*, Hugo Bouhours, Nicolas Dehaynin, Delphine Jarnet, Matthieu Gantier, Diran Karamanoukian, Claudine Niederst

Division of Medical Physics, Department of Radiotherapy, Paul Strauss Center, Strasbourg, France

ARTICLE INFO

Article history:
Received 2 February 2015
Received in revised form
30 April 2015
Accepted 7 May 2015
Available online 29 May 2015

Keywords:
Tomotherapy planning
Sarcomas
Pitch
Modulation factor
Field width

ABSTRACT

Background and purpose: To determine the optimum combination of treatment parameters between pitch, field width (FW) and modulation factor (MF) for extremity sarcomas in tomotherapy.
Materials and methods: Six patients previously treated for extremity sarcomas (3 arms and 3 legs) with tomotherapy were included in this study. 288 treatment plans were recalculated, corresponding to all combinations between 2 FW (2.5 and 5 cm), 4 MF (1.5, 2, 2.5 and 3) and 6 pitches (0.215, 0.287, 0.43 and 3 off-axis pitches). The treatment parameters (MF, FW or pitch) are modified between each plan, and the calculation is relaunched for 400 iterations, without modifying the optimisation constraints of the plan under which the patient has been treated.
Results: We suggest eliminating the 0.43 pitch and never combining a 0.215 pitch with an MF $\leq$ 2. We also do not recommend using an MF = 1.5 unless treatment time is an absolute priority over plan quality. We did not see any advantage in using Chen off-axis pitches, except for targets far from the axis (>15 cm) treated with a high pitch. A combination of MF = 2/FW = 5 cm/pitch = 0.287 gives plans of acceptable quality, combined with reduced treatment times. These conclusions are true only for extremity sarcomas treated in 2 Gy/fraction.
Conclusions: We have shown that the choice of pitch/MF/FW combination is crucial for the treatment of extremity sarcomas in tomotherapy: some produce good dosimetric quality with a reduced irradiation time, while others may increase the time without improving the quality.

Introduction

Irradiation of extremity tissue sarcomas is not technically straightforward, given the considerable mobility of limbs, which makes accurate and reproducible positioning difficult. In addition, these lesions, usually voluminous and irregular in shape, can be sufficiently long to be located in different zones of the extremity in terms of depth. Helical tomotherapy is the system of choice for this type of localisation: intensity modulation helps to overcome the difficulties of PTV coverage and OARS saving [1–5], and daily MVCT 3D imaging guarantees control of the position of the extremity.

When planning tomotherapy treatment, the user can vary 3 parameters: pitch, field width (FW) and modulation factor (MF). The choice of values applied to these 3 parameters is crucial, as quality of treatment plans and treatment time depend on them. In 2005, Kissick et al. proposed pitch values equal to 0.86/n, where n is an integer, in order to minimise head-foot dose fluctuations, known as "thread effect" [6]. In 2011, Chen et al. partly called these pitch values into question for targets far from the axis, such as extremity sarcomas [7]. Other authors have attempted to propose optimum parameter combinations for different locations: whole brain with hippocampus avoidance [8], head and neck [9], TMI [10,11], prostate [12,13] or extremity sarcomas [14]. The results of these studies are sometimes contradictory: for the prostate, Skorska et al. estimate for example that reducing the MF from 2.5 to 1.5 does not change treatment time [12], but compromises dose distribution, while Cao et al. conclude the opposite [13]. Woch et al. show that increasing the pitch helps reduce treatment time without compromising dose distribution [15]; this is not consistent with the results of another study [9]. The diversity of these results shows the difficulty of identifying an optimum combination of treatment parameters in tomotherapy.

* Corresponding author. 3 rue de la porte de l'hôpital, 67000 Strasbourg, France. Tel.: +33 388258544.
E-mail address: pmeyer@strasbourg.unicancer.fr (P. Meyer).

http://dx.doi.org/10.1016/j.ejmp.2015.05.005
1120-1797/

The aim of this study is to determine the optimum treatment parameters for extremity sarcomas in tomotherapy.

Materials and methods

6 patients already treated in our department were included in this study: 3 for arm sarcomas and 3 others for leg sarcomas (see Table1 and Fig. 1). For each patient, the prescribed dose was 50 Gy in 25 fractions of 2 Gy. A directional block was used with the aim of protecting the patient's opposite leg or torso. The skin corridor was delineated by the radiotherapist, without particular rules other than to guarantee that a maximum volume of healthy tissue receives the smallest possible dose.

48 treatment plans were recalculated for each patient, corresponding to all possible combinations between 2 FW (2.5 and 5 cm), 4 MF (1.5, 2, 2.5 and 3) and 6 pitches (0.215, LPO, 0.287, MPO, 0.43, HPO). 3 of these pitch values are those recommended by Kissick et al. (0.215. 0.287 and 0.43), and the 3 others are the corresponding values formulated by Chen et al. [7]. As these latter depend on the off-axis distance of the target (distance from target to axis of tomotherapy) and on the FW, they are different for each patient. For this reason we will call them Low Pitch Off-axis (LPO), Medium Pitch Off-axis (MPO) and High Pitch Off-axis (HPO). As the PTV is not a single point, we have chosen the maximum off-axis distance of a patient's PTV to choose the pitch value to apply, with a maximum value of 20 cm. The detail of the pitch off-axis values for each patient is given in Table 2.

We studied the FW of 5 and 2.5 cm only, because of the significant CTV-PTV margins in the head-foot direction for the sarcomas [16], which makes irradiation time prohibitive with an FW of 1 cm. Finally, we considered 4 MF, between 1.5 and 3, as these correspond to the limit values currently found in the literature and used by us in our hospital.

For each patient, we took the optimisation constraints of the plan with which the patient was treated. The treatment parameters (MF, FW or pitch) were modified between each plan, and the calculation was relaunched for 400 iterations, without altering the optimisation constraints, to allow comparison of the plans with each other. This number (400) seems sufficient to minimize the impact of iterating on dosimetric results [7]. Planning constrains/weights, that may be different depending on the patient, were chosen to obtain the best compromise PTV coverage/organ sparing. The calculations were made on HD Tomotherapy planning station version 5.0.1.7 (Accuray Inc, Madison, WI), without tomoedge. The calculation grid size was set on normal.

The comparison between the various treatment plans was made using Artiview v 2.8.1 (Aquilab, France). Treatment plan quality was quantified through the D98 and D2 of the PTV, the bone V40 [17] and the skin corridor V20 [3]. We calculated the PTV conformation number (CN), defined as $CN = \frac{V_{T,Ref}}{V_{Ref}} \times \frac{V_{T,Ref}}{V_T}$, where $V_{T,Ref}$ is the volume of the PTV covered by the reference isodose, V_{Ref} is the volume of the reference isodose and V_T is the volume of the PTV [18]. The reference isodose corresponds to 95% of the prescribed dose. This CN definition was chosen because it simultaneously takes into account irradiation of the target volume and irradiation of healthy tissue [19]. Finally, the homogeneity index (HI) of the PTV was calculated as $HI = \frac{D_2 - D_{98}}{D_{50}}$ [20]. The treatment time was stated for each plan.

Depending on the number of eligible data, two-sided Wilcoxon Signed Rank or t-Student tests were performed to compare the various treatment plans. Significance for these tests was set at a level of $p < 0.05$.

Results

The detailed results of the 288 treatment plans obtained for the 6 patients are described in Appendix A.

Influence of the FW

For each patient, the relative variation of the dose distribution indexes was calculated at constant pitch and MF when passing from an FW of 5 to an FW of 2.5 cm. The average variation in these indexes for each patient is given in Appendix B.

Influence of MF

The variation in dose distribution indexes was calculated when the MF was increased, with constant FW and pitch; Appendix B shows this variation according to the FW when the MF passes from 1.5 to 2, from 2 to 2.5 and from 2.5 to 3, averaged for all patients and pitches.

The actual MF was not included into the statistical analysis, even if it is an interesting value that may help to adapt the plan MF when planning a patient.

Influence of pitch

We initially studied the interest in choosing the off-axis pitches proposed in the publication by Chen et al., rather than those of Kissick et al. With the MF and FW both constant, we analysed the influence of transition from a pitch of 0.212 to an LPO pitch, from 0.287 to MPO and from 0.43 to HPO. The results appear in Appendix B, which shows for these transitions the average variation in HI, V20 skin corridor and V40 bone. We decided to split them into 2 groups: those concerning the 2 patients with a PTV off-axis distance of >15 cm, and those of the 4 other patients with a PTV off-axis distance of <15 cm.

We also analysed the impact of the order of magnitude of pitch. In this case, we studied the average variation of dose distribution indexes with constant MF and FW for transition from a pitch of 0.215–0.287, and from 0.287 to 0.43. Appendix B shows these results, all patients and MFs combined, according to FW.

Table 1
Details of the 6 patients included in this study.

Patient	Age	Sex	Localisation	PTV head-feet length (cm)	PTV off-axis distance (cm)
1	72	F	Right leg mixofibrosarcoma	28.1	−3.4 to 7.8
2	65	F	Left leg liposarcoma	38.8	−5.0 to 8.9
3	55	F	Right arm leiomyosarcoma	19.2	3.1 to 13.4
4	54	F	Left arm fusocellular sarcoma	22.5	8.4 to 21.7
5	50	F	Left leg liposarcoma	34.5	−2.7 to 11.9
6	71	M	Left arm pleomorphic sarcoma	23.5	8 to 22

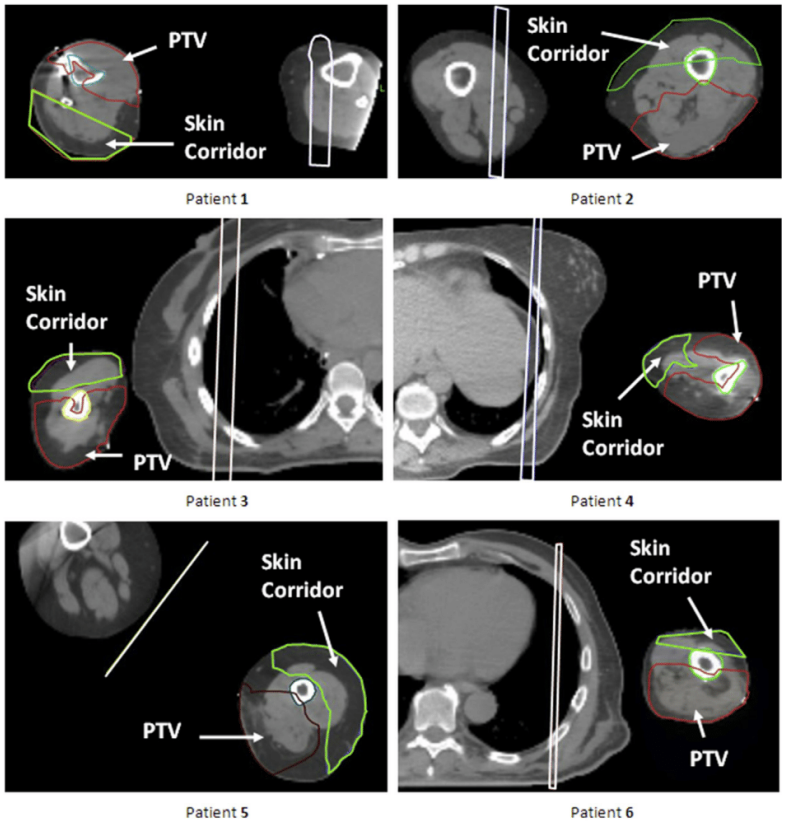

Figure 1. Axial view of the 6 patients included in this study. A directional block protects the torso or the opposite leg.

Variation in treatment time according to pitch and MF

Figure 2 shows, for each FW, the variation in treatment time averaged for the 6 patients according to MF and pitch, normalised at 1 for the combination MF = 3/HPO pitch.

The detail of the values with the associated standard deviations appears in Appendix C.

Discussion

Before discussing the results, everyone should be aware that our results are true only for extremity sarcomas treated at 2 Gy/fraction. For any other localization or fractionation, our findings may not be applicable.

Table 2
Off-axis pitch values used for the 6 patient of this study.

		FW 2.5 cm			FW 5 cm		
Patient	PTV off-axis distance	LPO	MPO	HPO	LPO	MPO	HPO
1	7	0.231	0.300	0.443	0.229	0.301	0.440
2	8	0.229	0.299	0.440	0.228	0.300	0.438
3	13	0.218	0.288	0.427	0.220	0.291	0.425
4	20	0.197	0.264	0.397	0.200	0.267	0.397
5	11	0.223	0.293	0.433	0.223	0.295	0.430
6	20	0.197	0.264	0.397	0.200	0.267	0.397

Abbreviations: LPO = Low Pitch Off-axis; MPO = Medium Pitch Off-axis; HPO = High Pitch Off-axis.

Effect of FW on treatment plan quality and irradiation time

We observed in Appendix B that the reduction in FW from 5 to 2.5 cm significantly helps improve the PTV D98 (1.7 ± 1.1%), D2 (−0.8 ± 0.5%), HI (−25.1 ± 11.7%) and CN (3.2 ± 2.6%), and also better spares the skin corridor (V20: -15.3 ± 9.4%) and the bone (V40: -3.3 ± 3.3%). However, this plan quality improvement has a relatively significant associated standard deviation, thus emphasising that its magnitude depends on the patient and on the pitch/MF combination.

The FW is the sole optimisation parameter, which independently of others has a clear impact on treatment time: moving from 5 to 2.5 cm implies a systematic increase in treatment time (84 ± 6.8%), whatever the patient or the pitch/MF coupling.

The improvement in treatment plan quality and increase in irradiation time when the FW reduces are confirmed by the results published for other localizations [8,9,11,13], although Moldovan et al. note that the differences in dose distribution are perhaps not significant in radiobiological terms (9).

Effect of MF on treatment plan quality

With constant pitch and FW, the increase in MF from 1.5 to 3 is accompanied by an improvement in the skin corridor V20 and in the PTV HI. More subtly, we have noted in Appendix B that the improvement in skin corridor sparing is significant when moving from an MF of 1.5 to an MF of 2, and much less pronounced when

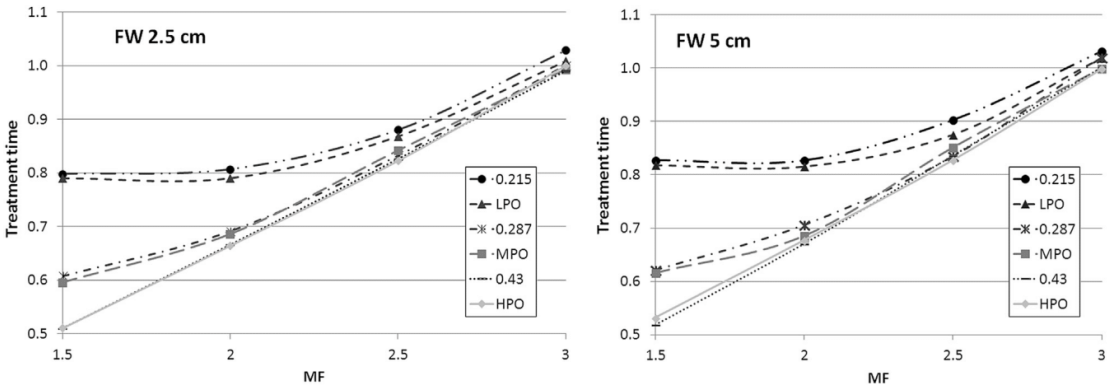

Figure 2. Mean treatment time variation for the 6 patients, according to Modulation Factor and pitch, for the Field Width 2.5 cm and 5 cm. Treatment time values are normalised at 1 for Modulation Factor = 3/pitch HPO.

the MF moves from 2 to 3. For example, for an FW of 2.5 cm, the skin corridor V20 reduces by an average of 33.6 ± 18.1% when the MF moves from 1.5 to 2, then by 10.2 ± 3.4% when the MF moves from 2 to 2.5, and finally by 4.8 ± 2.0% when the MF moves from 2.5 to 3.

We have not been able to find any significant effect of the MF on the bone V40.

We observed a significant reduction in the CN with the increase of the MF. This deterioration can be explained by the better saving of the skin corridor, combined with an increase in the volume of the prescription isodose in the healthy zones.

These results are consistent with those of Skorska et al., even though this latter does not nuance the effect of the MF between 1.5 and 3.5 [12]. By cons, Cao et al. does not observe any effect of the MF between 1.8 and 3.5 on the dosimetric indexes of the PTV and OARs [13].

Effect of pitch on treatment plan quality

Initially, we are looking to assess the effect of moving from one magnitude of pitch to another: 0.43 to 0.287 and 0.287 to 0.215. We note in Appendix B that when the pitch moves from 0.43 to 0.287, the dosimetric indexes concerning the PTV significantly improves: 18.3 ± 6.7% for example for HI, with a 5 cm FW. The HI also improves when the pitch moves from 0.285 to 0.215, although with a smaller amplitude: 9.7 ± 4.9% for example for the HI, with a 5 cm FW. When the pitch reduces, a significant improvement is also observed for the skin corridor, but the effect on the bone V40 is much less pronounced.

These results partly confirm those of the literature [12,13] but are very different from those of Woch et al. [15], which suggest that using a pitch of 0.43 does not compromise the treatment plan.

We have also studied the interest of using off-axis pitches rather than the 0.86/n pitches. We observed in Appendix B that the only notable dosimetric improvement concerns the HI when an HPO pitch is used instead of a pitch of 0.43, and only for the group of patients with an off-axis PTV of >15 cm. For all other patients and indexes, we did not observe any clear difference between the treatment plans calculated with a pitch of 0.86/n and those calculated with an off-axis pitch.

O'Doherty et al. observed that using an off-axis pitch instead of a pitch of 0.86/n significantly reduces the thread effect for an HPO pitch vs. 0.43 and a target 19 cm from the axis [14], which remains consistent with our results. Takahashi et al. showed that the magnitude of the oscillations increases significantly for >20 cm off-axis distances, and that the 0.43 pitch is one of the most sensitive [10], which also concurs with our results. Finally, Chen et al., explain that for real cases, patient heterogeneity and optimisation process can reduce the sensitivity of the plan to pitch choice [7]. This may explain why we do not observe any effect of type of pitch on treatment plans, except for the 0.43 pitch and patients with an off-axis PTV of >15 cm.

Influence of pitch and MF on irradiation time

We observe first of all that the variation in treatment time with pitch or MF is independent of the FW and the type of pitch (0.86/n or the corresponding off-axis value).

The variation of treatment time with the MF depends on the pitch; for a pitch of 0.43, 0.287 and 0.215, Fig. 2 shows that treatment time increases linearly and respectively for an MF moving from 1.5 to 3, from 2 to 3 and from 2.5 to 3. In extreme cases, the treatment time does not vary when the MF varies from 1.5 to 2 for a pitch of 0.215.

Similarly, it is observed that the variation in treatment time with pitch depends on the MF: for an MF of 1.5, the treatment time highly depends on the pitch, while it is independent therefrom, or almost so, for an MF $\geq$ 2.5.

These observations are linked to the gantry rotation period [21]: when the gantry rotation speed has reached its maximum (T = 11.9 s), pitch reduction is accompanied by an increase in the treatment time, the gantry speed not being able to compensate the increase in the number of rotations to perform (MLC leaves will be closed most of the time). Similarly, and always for plans where the gantry speed is maximum, reducing the MF will not modify treatment time. This highlights the importance of not generating a plan that is saturated in terms of gantry speed, otherwise the treatment time could be increased without dosimetric benefit, or the dosimetric quality could be deteriorated without benefit in treatment time.

We have therefore chosen to show in Table 3 the number of patients with limited gantry rotation speed, of the 6 included in this study, according to pitch and MF. This table displays in dark colours the pitch/MF combinations that may produce inefficient treatment plans: for example, for an MF 1.5 combined with an LPO or 0.215 pitch, all patients plans have limited gantry rotation speed.

Table 3
Number of patients (of the 6 in the study) with limited gantry rotation speed according to pitch and Modulation Factor. The results are identical for the 2.5 and 5 cm Field Width.

	1.5	2	2.5	3
HPO	0	0	0	0
0.43	0	0	0	0
MPO	3	1	0	0
0.287	3	1	0	0
LPO	6	4	1	0
0.215	6	4	1	0

Key: HPO = High Pitch Off-axis; MPO = Medium Pitch Off-axis; LPO = Low Pitch Off-axis.

We have thus shown that in order to discuss the effect of the pitch or MF on treatment time, the associated MF or pitch had to be placed in perspective. In our opinion, it is because this is not always done that we note inconsistencies between our results and those in the literature: some works do not show any change in treatment time when the pitch varies [9,13], but there is no specification of the associated MF value. Skorska et al. conclude that transition from an MF of 2.5 to one of 1.5 does not affect the treatment time, but does not specify to which pitch this applies [12].

Optimum treatment parameters for extremity sarcomas treated at 2 Gy/fraction

First of all, we suggest to carefully use a 0.43 pitch when planning extremity sarcomas: its use may compromise the dose distribution without any notable saving on treatment time. Table 3 shows us that a pitch of 0.215 should not be combined with an MF $\leq$ 2, as there is a risk of altering dose distribution without saving time. Given the low dosimetric quality combined with it, an MF = 1.5 should only be applied to treatments for which treatment time is an absolute priority: Table 3 reminds us that it is then essential to combine it with a high pitch in order to be certain of making the anticipated time saving. We did not see any interest in using Chen's off-axis pitches, except for targets far from the axis (>15 cm) treated with an HPO pitch.

In general, the use of FW = 5 cm should be avoided; however, treating with an FW = 5 cm for the particular type of treatment volume and OARs in extremity sarcoma is a good chance to reduce the treatment time, without compromising notably the dose distribution. One must not forget that the effect of the head-foot penumbra is certainly less pronounced for this localization than for others, as OARS are less likely to be located directly above or below the PTV. However, an FW of 2.5 cm may be preferred for a particular patient; then it must be accepted that the expected dose distribution improvement comes at the cost of an 80% irradiation time increase.

We finally asked two experienced physicians to determine the optimum treatment plans for each patient. According to their subjective criterion, a combination MF = 2/FW = 5 cm/pitch = 0.287 produces plans of acceptable quality, combined with reduced treatment times.

If the proposed combination does not give satisfactory dose distributions, the MF can still be raised and the pitch reduced, taking care to remain within the light-coloured zones of Table 3. In this case, we have shown that the gain is significant for an MF moving from 1.5 to 2 and for a pitch moving from 0.43 to 0.287, and noticeably lower for an MF moving from 2 to 3 and for a pitch moving from 0.287 to 0.125.

Conclusions

We have identified the optimum combinations of MF, FW and pitch for extremity sarcomas treated in tomotherapy at 2 Gy/fraction. We have also shown the effect of the individual variation of these parameters on treatment plan quality and on irradiation time. Our results underline the importance of having a proper knowledge of tomotherapy behaviour, in order to avoid the use of unsuitable combinations that lead either to an increase in treatment time without improvement in dose distribution, or to a loss of treatment plan quality with no change in irradiation time.

Acknowledgements

We thank Bernard A for the statistical analysis.

Appendix A

Appendix A1
Detailed results for the patient 1.

							PTV				OARs	
Plan number	MF	FW	Pitch	Actual MF	Gantry period (s)	Treatment time (s)	D2 (%)	D98 (%)	HI	CN	V20 – Skin Corridor (%)	V40 – Bone (%)
1	1.5	2.5	0.215	1.084	12	696.7	103.5	92.8	0.107	0.78	5.06	42.5
2	1.5	2.5	0.287	1.103	12	523.3	103.5	92.9	0.106	0.79	5.06	42.7
3	1.5	2.5	0.43	1.143	12	350.4	104.6	92.7	0.119	0.78	5.31	42.7
4	1.5	2.5	LPO	1.089	12	648.9	103.4	92.9	0.106	0.78	5.07	42.7
5	1.5	2.5	MPO	1.105	12	499.3	103.4	93.0	0.105	0.79	5.11	42.7
6	1.5	2.5	HPO	1.142	12	344.2	104.7	92.7	0.120	0.78	5.37	43.0
7	1.5	5	0.215	1.058	12	379.8	104.4	91.3	0.131	0.75	6.06	44.4
8	1.5	5	0.287	1.079	12	287.5	105.2	91.4	0.138	0.75	6.15	44.6
9	1.5	5	0.43	1.143	12	193.4	107.3	91.1	0.162	0.73	6.54	44.0
10	1.5	5	LPO	1.064	12	356.5	104.5	91.4	0.133	0.75	6.12	44.5
11	1.5	5	MPO	1.085	12	276	105.5	91.4	0.141	0.75	6.21	44.8
12	1.5	5	HPO	1.144	12	190.8	107.0	90.9	0.160	0.72	6.71	45.1
13	2	2.5	0.215	1.354	12	696.5	101.9	95.4	0.066	0.77	2.93	42.4
14	2	2.5	0.287	1.414	12	523.3	102.3	95.9	0.064	0.76	2.95	42.8
15	2	2.5	0.43	1.488	15	435.6	103.1	95.9	0.072	0.76	3.05	43.1
16	2	2.5	LPO	1.369	12	648.9	102.0	95.6	0.064	0.77	2.93	42.6
17	2	2.5	MPO	1.416	12	499.3	102.3	96.0	0.063	0.76	2.99	42.8

Les pages 547 à 551 comportent des annexes et ne sont pas représentées ici.

Table B4
Average variation (% ± 1 SD) in dose distribution indexes when pitch varies from 0.215 to 0.287, and from 0.287 to 0.43, depending on FW.

		Average variation (% ± 1 SD)				
		V20 -Skin Corridor	V40 Bone	D2	D98	HI
FW 2.5 cm	Pitch 0.215 → 0.287	0.9 ± 0.7 *(P<0.001)*	0.8 ± 1.1 *(P =0.001)*	0.4 ± 0.3 *(P<0.001)*	0.2 ± 0.3 *(P =0.02)*	2.5 ± 3.2 *(P<0.001)*
	Pitch 0.287 → 0.43	1.3 ± 1.7 *(P<0.001)*	0.3 ± 0.8 *(P =0.03)*	1.0 ± 0.4 *(P<0.001)*	-0.3 ± 0.5 *(P<0.001)*	14.7± 6.5 *(P=0.002)*
FW 5 cm	Pitch 0.215 → 0.287	1.5 ± 2.1 *(P<0.001)*	1.0 ± 1.1 *(NS)*	0.9 ± 0.4 *(P<0.001)*	-0.2 ± 0.5 *(P =0.002)*	9.7 ± 4.9 *(P<0.001))*
	Pitch 0.287 → 0.43	3.3 ± 3.3 *(P<0.001)*	0.9 ± 1.9 *(NS)*	1.1 ± 0.5 *(P<0.001)*	-1.2 ± 1.0 *(P<0.001)*	18.3 ± 6.7 *(P<0.001)*

Key: HI = Homogeneity Index; FW = Field Width.

Appendix C

Mean treatment time for the 6 patients, as a function of FW, MF and pitch, normalized to MF 3 and pitch HPO.

FW	MF	Pitch	Mean treatment time, normalised to FW 2.5, MF 3, pitch HPO	1 SD
2.5	1.5	0.215	0.798	0.165
2.5	1.5	0.287	0.607	0.117
2.5	1.5	0.43	0.510	0.029
2.5	1.5	LPO	0.790	0.117
2.5	1.5	MPO	0.596	0.100
2.5	1.5	HPO	0.511	0.025
2.5	2	0.215	0.807	0.157
2.5	2	0.287	0.691	0.060
2.5	2	0.43	0.666	0.013
2.5	2	LPO	0.790	0.117
2.5	2	MPO	0.686	0.046
2.5	2	HPO	0.664	0.023
2.5	2.5	0.215	0.880	0.102
2.5	2.5	0.287	0.832	0.015
2.5	2.5	0.43	0.826	0.018
2.5	2.5	LPO	0.868	0.071
2.5	2.5	MPO	0.842	0.015
2.5	2.5	HPO	0.823	0.013
2.5	3	0.215	1.029	0.027
2.5	3	0.287	1.000	0.008
2.5	3	0.43	0.990	0.016
2.5	3	LPO	1.009	0.030
2.5	3	MPO	0.993	0.022
2.5	3	HPO	1.000	0.000
5	1.5	0.215	0.828	0.166
5	1.5	0.287	0.621	0.130
5	1.5	0.43	0.519	0.029
5	1.5	LPO	0.818	0.122
5	1.5	MPO	0.616	0.106
5	1.5	HPO	0.532	0.028
5	2	0.215	0.828	0.166
5	2	0.287	0.706	0.068
5	2	0.43	0.671	0.020
5	2	LPO	0.816	0.121
5	2	MPO	0.686	0.061
5	2	HPO	0.678	0.013
5	2.5	0.215	0.903	0.106
5	2.5	0.287	0.835	0.017
5	2.5	0.43	0.837	0.006
5	2.5	LPO	0.876	0.083
5	2.5	MPO	0.851	0.019
5	2.5	HPO	0.828	0.009
5	3	0.215	1.033	0.042
5	3	0.287	1.020	0.027
5	3	0.43	1.002	0.009
5	3	LPO	1.020	0.017
5	3	MPO	1.000	0.023
5	3	HPO	1.000	0.000

Conflict of interest statement

The authors have no conflict of interest.

References

[1] Alektiar KM, Brennan MF, Healey JH, Singer S. Impact of intensity-modulated radiation therapy on local control in primary soft-tissue sarcoma of the extremity. J Clin Oncol 2008;26:3440–4.
[2] Folkert MR, Singer S, Brennan MF, Folkert WK, Crago AM, Alektiar KM. Local control comparison of conventional and intensity modulated radiation therapy (IMRT) for primary soft-tissue sarcomas of the extremity. Int J Radiat Oncol Biol Phys 2013;87–2(Suppl.):S63.
[3] Steward AJ, Lee YK, Saran FH. Comparison of conventional radiotherapy and intensity-modulated radiotherapy for post-operative radiotherapy for primary extremity soft tissue sarcoma. Radiother Oncol 2009;93:125–30.
[4] Sladowska A, Hetnal M, Dymek P, Kabat D, Kisielewicz K, Wawrzak M, et al. Application of IMRT in adjuvant treatment of soft tissue sarcomas of the thigh-Preliminary results. Rep Pract Oncol Radiother 2011;16:110–4.
[5] Donnay L, Dejean C, Amsellem E, Bourezgui H, de Figueiredo BH, Duparc A, et al. Radiotherapy for soft tissue sarcomas of extremities. Preliminary comparative dosimetric study of 3D conformal radiotherapy versus helical tomotherapy. Cancer Radiother 2008;12:809–16.
[6] Kissick MW, Fenwick J, James JA, Jeraj R, Kapatoes JM, Keller H, et al. The helical tomotherapy thread effect. Med Phys 2005;38:1414–23.
[7] Chen M, Chen Y, Chen Q, Lu W. Theoretical analysis of the thread effect in helical tomotherapy. Med Phys 2011;38:5945–60.
[8] Gutiérrez AN, Westerly DC, Tomé WA, Jaradat HA, Mackie TR, Bentzen SM, et al. Whole brain radiotherapy with Hippocampal avoidance and simultaneously integrated brain metastases boost : a planning study. Int J Radiat Oncol Biol Phys 2007;69:589–97.
[9] Moldovan M, Fontenot JD, Gibbons JP, Lee TK, Rose II, Fields RS, et al. Investigation of pitch and jaw width to decrease delivery time of helical tomotherapy treatments of head and neck cancer. Med Dosim 2011;36:397–403.
[10] Takahashi Y, Verneris MR, Dusenbery KE, Wilke CT, Storme G, Weisdorf DJ, et al. Peripheral dose heterogeneity due to the thread effect in total marrow irradiation with helical tomotherapy. Int J Radiat Oncol Biol Phys 2013;87:832–9.
[11] Hui SK, Kapatoes J, Fowler J, Henderson D, Olivera G, Manon RR, et al. Feasibility study of helical tomotherapy for total body or total marrow irradiation. Med Phys 2005;32:3214–24.
[12] Skorska M, Piotrowski T. Optimization of treatment planning parameters used in tomotherapy for prostate cancer patients. Med Phys 2013;29:273–85.
[13] Cao Y, Lee S, Chang K, Shim J, Lee J, Yang D, et al. Optimization of treatment planning parameters used in tomotherapy for prostate cancer: using dosimetric physical index and plan evaluation scoring index. Int J Radiat Oncol Biol Phys 2013;87–2(Suppl.):S698.
[14] O'Doherty D, Lenane M, Geater A, Tudor S. Pitch choice for off-axis blocked targets treated with tomotherapy. Radiother Oncol 2012;103(Suppl.1):S138–9.
[15] Woch K, Soisson E, Kapatoes J, Olivera G. Acceleration of tomotherapy treatment delivery by increasing pitch and decreasing modulation. Med Phys 2008;35:2636.
[16] Faivre JC, Le Péchoux C. Target volumes in soft tissue sarcoma of the extremities. Cancer Radiother 2013;17:444–52.
[17] Haas RLM, DeLaney TF, O'Sullivan B, Keus RB, Le Pechoux C, Olmi P, et al. Radiotherapy for management of extremity soft tissue sarcomas: why, when, and where? Int J Radiat Oncol Biol Phys 2012;84:572–80.
[18] Riet A, Mak ACA, Moerland MA, Elders LH, Zee W. A conformation number to quantify the degree of conformality in brachytherapy an external beam irradiation: application to the prostate. Int J Radiat Oncol Biol Phys 1997;37:731–6.
[19] Feuvret L, Noel G, Mazeron JJ, Bey P. Conformity index : a review. Int J Radiat Oncol Biol Phys 2006;64:333–42.
[20] International Commission on Radiation Units and Measurements. Prescribing, recording, and reporting photon-beam intensity-modulated radiation therapy (IMRT). ICRU Report 83. Bethesda: ICRU; 2010.
[21] Westerly DC, Soisson E, Chen Q, Woch K, Schubert L, Olivera G, et al. Treatment planning to improve delivery accuracy and patient throughput in helical tomotherapy. Int J Radiat Oncol Biol Phys 2009;74:1290–7.

3. Le traitement du sein seul par TomoDirect

Le cancer du sein est la première localisation traitée par radiothérapie au CPS (543 patients sur les 2182 patients traités par radiothérapie en 2016). Le nombre de patients traités par tomothérapie au CPS pour des cancers mammaires a longtemps été marginal, mais est en forte augmentation ces dernières années (voir Figure 12). La tomothérapie permet en effet de couvrir les volumes cibles ganglionnaires de manière optimale, tout en réduisant les fortes doses aux organes à risque (Aoulad et al., 2017; Vandendorpe et al., 2017). L'impact de l'augmentation des faibles doses sur les tissus sains étant mal connu, il est important de noter qu'il n'existe néanmoins à ce jour aucune recommandation de la Haute Autorité de Santé (HAS) concernant l'utilisation de RCMI dans le cadre du traitement du cancer du sein (Bourgier et al., 2016). Les patients traités au CPS en tomothérapie pour des cancers mammaires ont généralement des anatomies particulières (pectus excavatum), nécessitant des irradiations bilatérales ou pour lesquelles l'irradiation ganglionnaire est insatisfaisante en radiothérapie conformationnelle 3D (RC3D). Ces patients sont traités en tomothérapie hélicoïdale, comme décrit précédemment. Il existe cependant un autre mode d'irradiation mammaire par tomothérapie, dit TomoDirect, que nous décrivons maintenant.

TomoDirect

TomoDirect est un mode de traitement optionnel de la tomothérapie, disponible en série depuis la commercialisation du modèle HD. Durant l'irradiation, la table avance et la modulation est effectuée par le MLC mais, à la différence du mode hélicoïdal, la position du bras reste fixe durant l'irradiation. Il est possible d'effectuer de deux à douze champs d'irradiation successifs. Concernant les paramètres d'irradiation, la seule différence avec le mode hélicoïdal est la définition du *pitch*, qui s'exprime ici en cm/projection. Le pourcentage d'ouverture d'une lame du MLC étant donné par projection, le pitch exprime donc directement la résolution de la matrice de fluence dans le sens-pieds. Nous avons mené une étude visant à déterminer les paramètres optimaux de traitement du sein par TomoDirect, dont les résultats ont été communiqué sous forme de poster au congrès de l'ESTRO en 2016 (Scius et al., 2016).

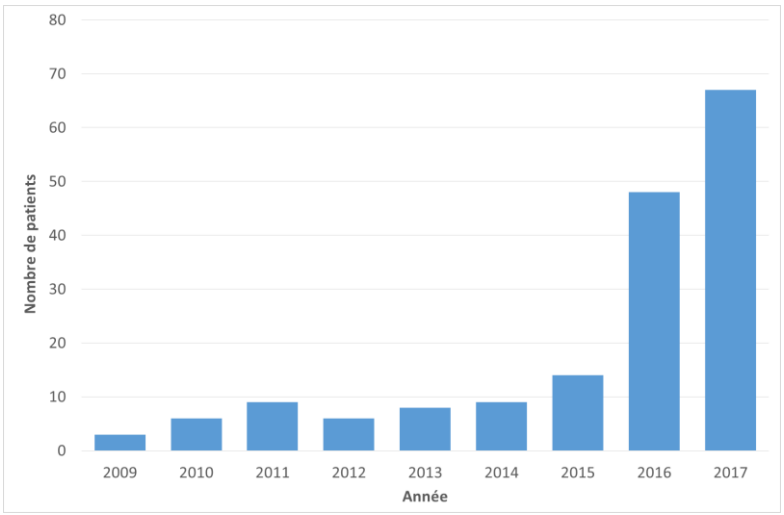

Figure 12. Nombre de patientes traitées par an en tomothérapie pour des cancers mammaires au CPS (statistiques au 26/10/2017).

TomoDirect a été conçu pour traiter des cibles ne nécessitant pas de nombreuses incidences de traitement. Les premières simulations ont été effectuées sur fantôme (Gonzalez et al., 2006; Olivera et al., 2005; Reynders et al., 2009), avant que TomoDirect ne soit disponible sur la tomotherapie HD. Depuis, ce mode d'irradiation a été évalué pour diverses localisations (Franco et al., 2011; Murai et al., 2013; Tsang et al., 2017; Zhang et al., 2017), mais l'indication principale reste le sein seul (sans atteinte ganglionnaire). Une étude prospective a montré que le mode TomoDirect permet de réduire la toxicité aigüe cutanée pour des traitements hypo-fractionnés mammaires avec boost intégré sur lit opératoire (Franco et al., 2014). Une autre étude prospective sur des patients traités pour des cancers mammaires par TomoDirect en normo-fractionné et boost intégré sur lit opératoire a montré une toxicité acceptable associée à des résultats dosimétriques optimums (Lee et al., 2014).
Entre janvier 2016 et novembre 2017, nous avons traité 17 patientes par TomoDirect au CPS pour des irradiations mammaires seules (25 séances de 2 Gy) et boost sur lit opératoire (8 séances de 2 Gy). Pour ce type de traitement, nous avons en parallèle abordé la problématique de l'asservissement respiratoire et de l'imagerie de positionnement.

a) Problématique de l'asservissement respiratoire

La technique de l'inspiration profonde bloquée (*Deep Inspiration Breath-Hold*, DIBH) permet de réduire la dose au cœur et au poumon lors des irradiations mammaires (Latty et al., 2015). Lors d'une séance de radiothérapie avec DIBH, le patient inspire profondément et retient sa respiration pendant une vingtaine de secondes. Au CPS, nous utilisons un système sous contrôle spirométrique (Garcia et al., 2002) lorsque la dose cardiaque est trop importante pour les irradiations mammaires gauches. Ce système, utilisé en RC3D sur des accélérateurs classiques, n'est cependant pas transposable sur tomothérapie, en raison du manque de contrôle sur l'instant précis de démarrage du faisceau avec cette machine. Nous avons cherché à déterminer dans quelle mesure les capacités de modulation du mode TomoDirect permettent de s'affranchir du DIBH pour les irradiations du sein gauche seul. Ce travail est présenté dans la publication suivante (Meyer et al., 2016).

Physica Medica 32 (2016) 644–650

Contents lists available at ScienceDirect

Physica Medica

journal homepage: http://www.physicamedica.com

Original paper

Is the lack of respiratory gating prejudicial for left breast TomoDirect treatments?

Philippe Meyer [a,*], Claudine Niederst [a], Maximilien Scius [a], Delphine Jarnet [a], Nicolas Dehaynin [a], Matthieu Gantier [a], Waisse Waissi [a], Nicolas Poulin [b], Diran Karamanoukian [a]

[a] Division of Medical Physics, Department of Radiotherapy, Paul Strauss Center, Strasbourg, France
[b] CeStatS, Advanced Mathematics Research Institute, UMR 7501, Strasbourg University and CNRS, Strasbourg, France

ARTICLE INFO

Article history:
Received 5 February 2016
Received in Revised form 1 April 2016
Accepted 4 April 2016
Available online 29 April 2016

Keywords:
Breast cancer
TomoDirect
Heart sparing
Deep inspiration breath-hold
Radiotherapy

ABSTRACT

Background and purpose: TomoDirect (TD) can only operate in free-breathing. The purpose of this study is to compare TD with breath-hold 3D conformal radiotherapy (3DCRT) and intensity modulated radiotherapy (IMRT) techniques for left breast treatments, and to determine if the lack of respiratory gating is a handicap for cardiac sparing.
Materials and methods: 15 patients treated for left breast had two computed tomography simulation, in free breathing (FB) and in deep-inspiration breath-hold (DIBH). Four treatments were planned: TD-FB, 3DCRT-FB, 3DCRT-DIBH and IMRT-DIBH. Dose to PTV, heart, lungs, right breast and patient were compared.
Results: A slightly lower cardiac mean dose is found for 3DCRT-DIBH than for TD-FB group (1.99 Gy Vs 2.89 Gy, $p = 0.0462$), while no statistical difference is found for heart V_{20}. TD-FB plans show the best PTV dose homogeneity (0.053, $p < 0.001$) and the lowest left lung mean dose (5.16 Gy, $p < 0.001$). No major differences are found for the other organs.
Conclusions: TomoDirect and breath-hold 3DCRT are complementary techniques for left breast treatments: for a minority of patients, respiratory gating is mandatory to lower cardiac dose; for the remaining majority of patients, TomoDirect achieves better PTV homogeneity and reduced left lung dose, with cardiac dose equivalent to 3DCRT-DIBH.

Introduction

Breast cancer is the most common women cancer, with an incidence rate of over one million cases per year worldwide [1]. Radiation therapy has a major role in the management of this disease, to reduce local recurrence and improve overall survival probability [2]. This treatment modality has long been suspected of causing cardiac toxicities, especially for left breast cases. These toxicities were confirmed notably by a large follow-up work conducted by Darby et al. over 2158 patients [3], which showed that the risk of coronary events would increase by 7.4% per gray delivered to the heart, even if the possibility of a threshold could not be excluded. The beneficial role of radiotherapy is indisputable in breast cancer treatments, and new radiation techniques have been introduced to reduce the irradiated heart volume.

One possibility to reduce this volume is to use breath-hold methods. Several devices, widely described in the literature [4,5], have the objective of delivering treatment when the heart is the most distant from the chest wall [6]: in a recent literature review including studies published by 18 teams, Drew Latty et al. showed that deep-inspiration breath-hold (DIBH) provides a relative reduction in mean heart dose ranging from 26.2% to 75% [7].

Another way to reduce the cardiac dose is intensity modulated radiotherapy (IMRT) by conventional linac or TomoDirect. Whatever the IMRT technique used on a conventional linac (forward-planned, reverse planned, hybrid-IMRT . . .), dosimetric comparison to a 3D conformal radiotherapy (3DCRT) generally shows a better homogeneity in the target volume and a decrease in the mean dose to the heart [8]. The TomoDirect technique (Accuray, USA), which is a treatment modality of Tomotherapy by fixed angle [9], was also investigated in various comparisons with 3DCRT and static IMRT [8–10]. Dosimetric results for PTV coverage are in favor of TomoDirect [10]. For heart and lung ipsilateral, the average doses obtained by TomoDirect are reduced compared to those obtained by 3DCRT [8,9,11].

* Corresponding author at: 3 rue de la porte de l'hôpital, 67000 Strasbourg, France.
E-mail address: pmeyer@strasbourg.unicancer.fr (P. Meyer).

http://dx.doi.org/10.1016/j.ejmp.2016.04.001
1120-1797/

Other studies have shown that combining the respiratory gating with static IMRT would further reduce the average dose to the heart: by comparing IMRT and 3DCRT delivered both with respiratory gating, Mast has shown that IMRT can reduce the average cardiac dose by 17% [12].

TomoDirect is not compatible with respiratory gating techniques, mainly because an unpredictable time delay (from several second to >10 s) occurs between the launch of the tomotherapy treatment beam by the operator and the effective beam delivery. This lack of respiratory gating can potentially be a handicap for reducing dose to the heart. To check if the modulation level of the TomoTherapy allows overcoming this handicap, we have compared the dosimetric performance of left breast TomoDirect treatments, which can be only performed in free breathing, with those by static IMRT and 3DCRT associated with DIBH.

Materials and methods

Patient selection and image acquisition

15 patients previously treated at Paul Strauss Cancer Center by 3DCRT with DIBH for left breast alone without nodes were enrolled in this study. The average age is 55 years, and the average volume of the PTV = 726 cm^3. Detailed characteristics for the 15 patients are given in Appendix 1.

All patients treated for left breast in our hospital have two computed tomography (CT) simulation: one in free breathing (FB) and another one in DIBH, the same day and in the same position. The radiotherapist checks visually (no quantitative criteria) on CT slices if DIBH may potentially help to increase the ribs to heart distance, and then chooses to plan treatment with or without DIBH. It is important to note that the 15 patients recruited for this study are therefore a priori patients for whom the DIBH reduces cardiac doses.

The CT simulation is performed with the patient in supine position and arms above the head using a Posiboard (CIVCO, USA). 2.5 mm CT axial images are obtained at 120 kV using a GE Optima 580 RT CT (General Electric, USA).

Note that using fast helical CT for planning of patients with significant breast motion due to breathing may not properly account for motion effect when treating in FB, resulting in differences between planned and delivered doses. Untagged average 4DCT data are therefore recommended for planning in FB cases [13].

DIBH method

The breath-hold system used is SDX (SDX, Dyn'R, France), a spirometer dedicated to the practice of breath-hold [4]. Respiratory gating is performed in inspiration by voluntary breath-hold, during both image acquisition and irradiation. The patient is able to monitor its breathing curve with video glasses (Fig. 1).

The reference level is defined as 75 to 85% of the maximal inspiratory capacity, depending on the patient compliance: if possible, a 85% level is preferred, to maximize the potential cardiac sparing. Three consecutive acquisitions of 20–25 s are then performed, to ensure the patient could comfortably maintain the breathing level.

Delineation and dose constraints

The left and right lung, right breast and heart are delineated with Focal v.4.80.01 (Elekta, Sweden) on both FB and DIBH scans. The PTV is created with an isotropic extension of 5 mm around the left breast, and a 5 mm skin retraction. To control the dose in healthy areas excluding organs at risk (OARs) for IMRT planning,

Fig. 1. Patient positioning during computed tomography simulation, with the SDX spirometer (SDX, Dyn'R, France). An acquisition is also made in free breathing without the SDX system, with identical equipment and positioning.

two optimization structures are created: PTV + 1 mm and PTV + 5 cm. PTV + 1 mm is only used for overlapping, to avoid any pixel overlap between PTV and OARs. PTV + 5 mm is used to fasten dose gradient around the PTV and to avoid hot spots in healthy region not covered by OARs. An example of delineation is given in Fig. 2.

The prescription dose is 50 Gy in 25 fractions of 2 Gy. As part of this dosimetric study, the additional boost to the tumor bed is not planned. PTV constraints are $D_{98\%} > 95\%$ (47.5 Gy) and $D_{2\%} < 107\%$ of the prescribed dose (53.5 Gy). Regarding the OARs, the objective is to minimize the delivered doses while trying to respect PTV constraints.

Treatment planning

3DCRT treatments are planned using XiO Version 4.80 (Elekta, Sweden) for both the FB (3D-FB) and the DIBH CT scans (3D-DIBH). Plans consist of opposed tangential fields (2 or more) that use 6 MV and 15 MV photon beams. Dynamic wedge filters, MLC, different beam weighting and point prescription may be use to optimize dose distribution.

TomoDirect planning is performed using Tomotherapy HD planning station version 5.0.1.7 (Accuray, USA), only on the FB CT

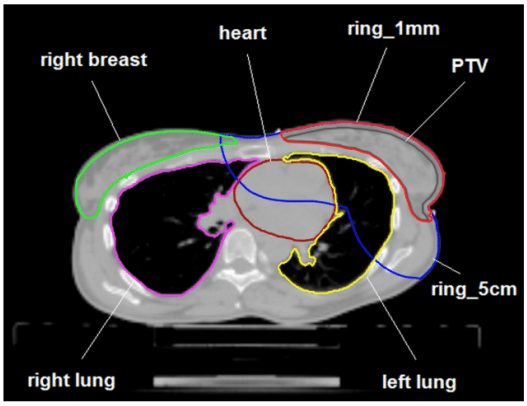

Fig. 2. Example of delineation on a deep inspiration breath-hold Computed Tomography simulation scan; ring_1 mm and ring_5 cm are helping structures for IMRT optimization.

scan (TD-FB). The prescribed dose is 50% of the PTV. Two tangential beams are created with the same angulations than for 3DCRT, with two additional beams at ±5°, making sure to not irradiate directly the right breast. A field width of 5 cm, a pitch of 0.5 cm and a modulation factor set to 2 are used. Treatment is performed in IMRT mode with three "flash" leaves left open. The dose calculation grid "normal" is used for optimization ($4.10 \times 4.10\ mm^2$) and "fine" when calculating the final dose ($2.05 \times 2.05\ mm^2$). Dynamic Jaw option is not enabled.

Static IMRT planning is performed using Eclipse Version 11.0.47 using the DVO.11.0.31 optimization algorithm (Varian Medical Systems, USA) in sliding window mode, only on the DIBH CT scan (IMRT-DIBH). Two tangential beams are created with the same angulations than for 3DCRT, also with two or more additional beams at ±5°.

Plan review

The 60 treatment plans corresponding to the 15 patients calculated in TD-FB, 3D-FB, 3D-DIBH and IMRT-DIBH are exported to ARTIVIEW (Aquilab, France), where 10 dosimetric parameters are evaluated for each plan. Fig. 3 shows a representative isodose distribution for the 4 plans. $D_{2\%}$ (near-max), $D_{98\%}$ (near-min) and homogeneity index (HI) are used to quantify the quality of PTV coverage: $HI = (D_{2\%} - D_{98\%})/D_{50\%}$ [14]. For OARs, we record the average dose to the heart, to the left and right lungs, the volume of the heart and left lung receiving at least 20 Gy (V_{20}), and the maximum dose to the right breast. We also calculate the patient integral dose (ID), with ID = average dose to patient $*$ patient volume [15].

Statistical analysis

For each variable, data are composed of repeated measurements among 15 patients. To deal with pseudo-replication among these repeated measurements, linear mixed effects models were fitted with identity of the patient as random effect and technique, breast volume and its interaction as fixed effects. A backward model selection was performed on the base of the lowest Akaike information criterion (AIC). Data were log-transformed when needed to assess normality of the residuals. Pairwise comparisons tests were performed with a Tukey correction.

Significance level of statistical tests was set to 5%. Statistical analysis was performed with R [16] and its packages nlme and multcomp.

Results

The detailed dosimetric results of the 60 treatment plans are given in Appendix 2. The AIC and best model statistical analysis results are given in Appendix 3. A statistical effect was found between treatment modality and all dosimetric parameters, except for the right breast ($p = 0.738$).

The mean dosimetric group values and p-values for pairwise comparison between modalities are summarized in Table 1: for example, PTV HI is significantly lower for TD-FB (HI = 0.053) compared to other techniques (HI = 0.113 to 0.117, with $p < 0.001$ for TD-FB Vs all modalities).

For each model except the one explaining the integral dose, model selection led to an optimal model with only the technique as fixed effect. However, the effect of breast volume remains very low even for integral dose. So, as observed by Michalski [10], we found that neither interaction between breast volume and technique nor breast volume have an effect on dosimetric parameters, including PTV homogeneity.

Discussion

Heart

The most irradiating technique for the heart is by far 3DCRT in free breathing: the mean cardiac dose is equal to 4.94 Gy in 3D-FB, while it is less than 3 Gy for the 3 other techniques.

TomoDirect gives higher dose to the heart than 3D-DIBH, with a 31% increase for the mean cardiac dose, however at significance level limit ($p = 0.0462$). The average gain for the mean dose to

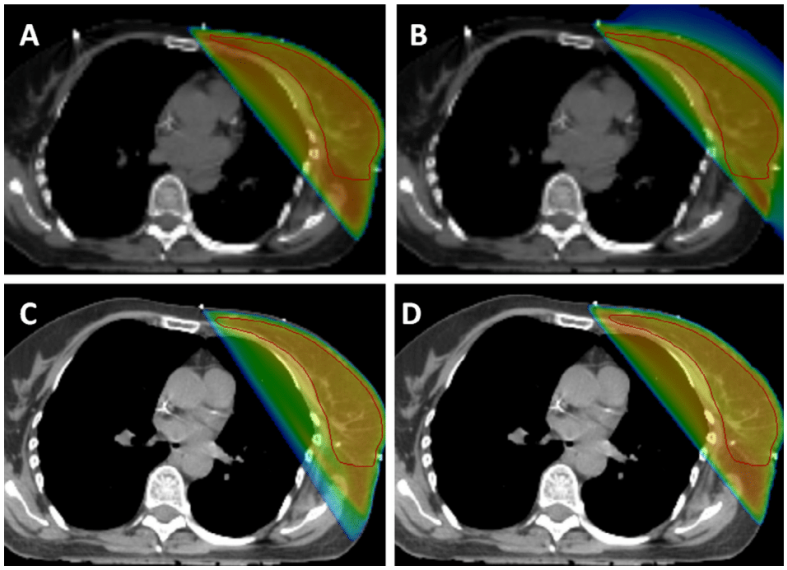

Fig. 3. An example of isodose distribution for (A) 3D-FB, (B) TD-FB, (C) IMRT-DIBH and (D) 3D-DIBH plans (patient 7). The isodose represents a dose >20 Gy.

Table 1
Average results for the 15 patients to the PTV and OARs for TD-FB, 3D-FB, 3D-DIBH and IMRT DIBH planning techniques, including the *p*-values for pairwise comparisons (grayed cell when significant effect is observed).

	mean ± SD				*p*-Value					
	TD-FB	3D-FB	3D-DIBH	IMRT-DIBH	TD-FB *vs* 3D-FB	TD-FB *vs* 3D-DIBH	TD-FB *vs* IMRT-DIBH	3D-FB *vs* 3D-DIBH	3D-FB *vs* IMRT-DIBH	3D-DIBH *vs* IMRT-DIBH
PTV										
$D_{2\%}$ (Gy)	51.05 ± 0.31	52.91 ± 0.66	52.97 ± 0.41	52.58 ± 0.78	<0.001	<0.001	<0.001	0.985	0.221	0.105
$D_{98\%}$ (Gy)	48.42 ± 0.52	47.25 ± 0.66	47.13 ± 0.75	46.86 ± 1.62	<0.001	<0.001	<0.001	0.975	0.567	0.817
HI	0.053 ± 0.013	0.113 ± 0.018	0.117 ± 0.020	0.114 ± 0.038	<0.001	<0.001	<0.001	0.946	0.998	0.982
Heart										
D_{mean} (Gy)	2.89 ± 1.38	4.94 ± 2.44	1.99 ± 1.38	2.36 ± 1.48	<0.001	0.0462	0.415	<0.001	<0.001	0.713
V_{20Gy} (%)	3.72 ± 2.98	8.16 ± 4.99	2.2 ± 2.38	2.35 ± 2.83	<0.001	0.156	0.237	<0.001	<0.001	0.997
Left Lung										
D_{mean}(Gy)	5.16 ± 2.20	7.89 ± 3.15	6.81 ± 2.31	7.60 ± 2.25	<0.001	<0.001	<0.001	0.007	0.822	0.090
V_{20Gy} (%)	9.13 ± 5.03	14.98 ± 6.55	12.73 ± 4.81	14.36 ± 5.32	<0.001	<0.001	<0.001	0.015	0.848	0.134
Right Lung										
D_{mean} (Gy)	0.25 ± 0.06	0.18 ± 0.06	0.16 ± 0.05	0.12 ± 0.07	<0.001	<0.001	<0.001	0.114	<0.001	<0.001
Right Breast										
D_{max} (Gy)	1.80 ± 0.40	2.79 ± 3.62	1.74 ± 0.9	2.09 ± 0.92	0.979	0.891	0.999	0.683	0.953	0.937
Patient										
ID (Gy.cm^3)	106.4 ± 39.1	105.0 ± 34.1	98.85 ± 34.72	100.8 ± 34.20	0.876	<0.001	0.013	0.005	0.100	0.730

Abbreviations: SD: standard deviation. ID: integral dose. HI: homogeneity index. $D_{2\%}$, $D_{98\%}$: dose encompassing 2% and 98% of the volume respectively. V_{20Gy} (%): volume receiving 20 Gy. TD-FB: TomoDirect in free-breathing. 3D-FB: 3D conformal radiotherapy in free-breathing. 3D-DIBH: 3D conformal radiotherapy in deep inspiration breath-hold. IMRT-DIBH: intensity modulated radiotherapy in deep inspiration breath-hold.

the heart associated with the respiratory gating relative to TomoDirect is 0.9 Gy, which remains relatively small in terms of absolute dose. There is no significant difference for the heart V_{20} between these two techniques ($p = 0.156$). Note that these results may be different with a higher DIBH level, potentially resulting in better cardiac sparing with the 3D-DIBH technique.

If we look at TomoDirect and 3D-DIBH plans per patient (see Fig. 4) and we choose 3 Gy as a limit not to exceed, only 3 of 15 patients benefit from respiratory gating. Remind that we have included only patients who should benefit from respiratory gating (cf. Section 2). With a randomized selection, the number of patients for whom TomoDirect and 3D-DIBH would be equivalent for cardiac sparing should theoretically be even more important.

Without respiratory gating, the heart is better saved with TomoDirect: mean dose to the heart is reduced by 41% relative to the 3D-FB ($p < 0.001$), which is consistent with the results obtained by Chi (52%) [17] and Michalski (28%) [10].

When comparing 3DCRT with and without respiratory gating, we find that DIBH helps reducing the average dose and V_{20} to the heart respectively by 60% and 73% ($p < 0.001$). These results are comparable to those of the review of Latty who showed that respiratory gating achieves an average reduction of 51% in cardiac mean dose [7].

We did not observe any significant difference for heart sparing between 3DCRT and IMRT both with breath-hold (D_{mean} $p = 0.713$; V_{20} $p = 0.997$). These results are contrary to those of Mast, which shows a slight gain of 17% on cardiac mean dose when IMRT is combined with DIBH [12]. The differences between algorithms and planning techniques used may explain the conflict between our results and those of literature.

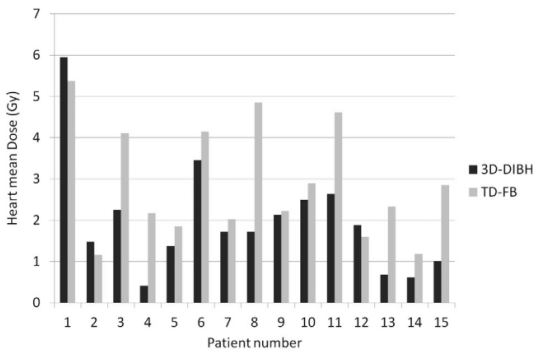

Fig. 4. Mean dose to the heart for deep inspiration breath-hold 3D conformal radiotherapy (3D-DIBH) and free-breathing TomoDirect (FB-TD) per patient.

PTV coverage

PTV $D_{2\%}$ and $D_{98\%}$ are statistically better for TD-FB than for the other techniques studied. PTV near-min dose is significantly better for TomoDirect ($D_{98\%} = 48.4$ Gy) than for 3DCRT or IMRT

Appendix 1
Characteristics of the 15 patients enrolled in this study.

Patient #	Age	PTV volume (cm^3)
1	51	795
2	66	518
3	40	317
4	64	378
5	66	411
6	38	1729
7	45	430
8	42	331
9	53	778
10	58	826
11	55	289
12	54	1117
13	60	713
14	72	1177
15	68	1082
Mean	55	726
SD	11	412

Abbreviations: SD: standard deviation.

Appendix 2
Detailed results for each patient.

Patient #	Breast Vol. (cm^3)	Technique	PTV			Heart		Left lung		Right lung	Right breast	Patient
			D_2 (Gy)	D_{98} (Gy)	IH	D_{mean} (Gy)	V_{20} (%)	D_{mean} (Gy)	V_{20} (%)	D_{mean} (Gy)	D_{max} (Gy)	ID (Gy cm^3)
1	795	3D-DIBH	52.7	46.5	0.124	5.95	8.92	10.66	20.4	0.27	2.08	117.1
		3D-FB	52.6	46.5	0.122	9.06	15.72	11.44	22.0	0.35	2.69	124.0
		IMRT-DIBH	51.7	46.8	0.098	6.09	9.37	10.94	22.5	0.30	2.09	117.5
		TD-FB	50.8	48.4	0.048	5.37	8.18	6.47	11.6	0.39	1.85	121.0
2	518	3D-DIBH	53.2	47.4	0.116	1.48	0.63	9.37	17.5	0.16	2.76	88.3
		3D-FB	53.9	47.4	0.131	3.00	3.25	12.25	23.4	0.21	2.79	92.1
		IMRT-DIBH	52.2	48.3	0.077	1.28	0.39	9.76	19.3	0.10	2.03	85.6
		TD-FB	51.1	48.7	0.048	1.16	0.44	8.04	15.5	0.23	1.22	83.1
3	317	3D-DIBH	53.2	47.7	0.111	2.25	1.99	6.03	10.7	0.15	2.69	69.5
		3D-FB	53.2	46.8	0.128	6.47	10.60	5.50	9.7	0.17	3.29	72.2
		IMRT-DIBH	53.6	48.6	0.099	2.02	1.30	7.99	15.7	0.14	2.10	71.8
		TD-FB	50.9	48.2	0.055	4.11	6.72	3.08	4.7	0.22	1.37	66.9
4	378	3D-DIBH	53.1	47.0	0.122	0.41	0.00	3.98	7.3	0.08	1.31	66.6
		3D-FB	52.9	46.9	0.120	2.45	3.86	5.07	9.6	0.07	2.03	66.9
		IMRT-DIBH	52.4	47.8	0.092	0.79	0.00	4.62	7.6	0.07	2.32	72.0
		TD-FB	51.6	48.4	0.062	2.17	2.08	4.00	6.5	0.16	2.21	79.7
5	411	3D-DIBH	52.8	46.9	0.119	1.37	1.33	5.18	9.6	0.15	1.42	53.1
		3D-FB	53.0	47.6	0.109	5.56	9.71	5.67	10.5	0.16	0.69	78.7
		IMRT-DIBH	52.7	47.7	0.099	1.50	0.56	5.48	9.4	0.05	1.84	70.7
		TD-FB	50.8	48.8	0.039	1.85	1.33	1.84	1.5	0.20	1.36	69.3
6	1729	3D-DIBH	53.2	45.7	0.152	3.46	5.03	8.57	16.3	0.19	1.74	170.7
		3D-FB	52.9	46.4	0.130	7.61	13.41	9.69	18.5	0.21	1.80	181.0
		IMRT-DIBH	53.0	45.4	0.151	4.77	7.36	10.32	21.5	0.19	2.14	178.9
		TD-FB	51.3	47.8	0.070	4.15	5.48	6.43	11.4	0.35	2.28	191.4
7	430	3D-DIBH	51.9	47.5	0.087	1.72	1.24	7.06	13.1	0.10	3.03	83.3
		3D-FB	51.0	47.0	0.080	4.33	6.41	9.75	18.7	0.16	3.54	92.6
		IMRT-DIBH	52.0	47.6	0.090	0.91	0.00	7.29	14.2	0.07	1.94	79.3
		TD-FB	51.0	47.9	0.063	2.02	2.28	6.64	12.7	0.21	1.45	85.4
8	331	3D-DIBH	53.2	47.7	0.110	1.72	2.11	7.52	14.6	0.16	1.00	66.3
		3D-FB	53.0	47.8	0.104	6.52	12.00	9.74	19.3	0.19	1.27	67.9
		IMRT-DIBH	51.7	47.6	0.082	1.92	1.40	7.45	13.6	0.11	1.95	63.9
		TD-FB	50.7	48.8	0.038	4.85	8.87	6.86	12.6	0.22	2.17	69.1
9	778	3D-DIBH	53.0	48.0	0.101	2.13	2.54	8.04	15.9	0.20	1.39	114.7
		3D-FB	52.9	47.8	0.102	2.44	3.35	7.74	15.2	0.18	1.26	111.1
		IMRT-DIBH	52.4	47.5	0.098	2.26	1.13	8.18	15.4	0.16	3.85	109.9
		TD-FB	50.9	48.5	0.048	2.22	2.19	7.17	14.5	0.32	1.89	124.7
10	826	3D-DIBH	52.3	48.3	0.080	2.49	2.48	3.21	4.8	0.13	3.38	104.8
		3D-FB	52.2	48.6	0.071	4.58	6.52	2.25	2.9	0.12	3.31	110.0
		IMRT-DIBH	51.3	46.2	0.102	2.87	3.42	4.33	7.0	0.08	2.74	103.9
		TD-FB	51.2	49.1	0.041	2.90	3.66	1.72	1.4	0.21	1.96	114.4
11	289	3D-DIBH	53.3	47.2	0.122	2.63	4.25	7.41	14.2	0.12	0.79	56.1
		3D-FB	53.4	47.3	0.122	8.94	17.28	9.83	19.3	0.16	0.92	64.9
		IMRT-DIBH	52.1	47.6	0.090	2.95	4.38	8.75	16.3	0.05	3.07	59.5
		TD-FB	50.9	48.0	0.059	4.61	7.98	5.76	10.8	0.16	1.56	56.7
12	1117	3D-DIBH	53.2	46.8	0.129	1.88	1.97	8.44	16.2	0.23	2.12	125.8
		3D-FB	53.4	46.9	0.129	2.75	3.67	7.99	15.3	0.24	15.35	128.8
		IMRT-DIBH	53.7	46.6	0.142	2.47	2.34	8.98	18.0	0.17	2.67	125.5
		TD-FB	50.9	48.1	0.055	1.59	0.98	5.96	11.1	0.26	2.22	126.8
13	713	3D-DIBH	52.9	47.8	0.102	0.68	0.00	6.05	11.2	0.14	0.65	91.5
		3D-FB	53.3	48.2	0.101	3.91	6.39	7.61	14.5	0.15	1.00	99.0
		IMRT-DIBH	53.5	47.9	0.113	1.09	0.00	6.80	11.8	0.11	2.16	94.8
		TD-FB	50.8	49.3	0.030	2.33	2.07	4.43	7.5	0.26	2.27	101.9
14	1177	3D-DIBH	53.3	46.8	0.131	0.61	0.00	2.47	3.5	0.12	0.97	143.5
		3D-FB	53.3	47.3	0.121	1.05	0.41	2.39	3.3	0.11	0.94	147.8
		IMRT-DIBH	52.8	42.2	0.212	1.21	0.28	3.63	5.0	0.06	0.27	140.6
		TD-FB	51.7	48.9	0.056	1.18	0.00	1.62	0.8	0.24	1.18	166.3
15	1082	3D-DIBH	53.3	45.9	0.149	1.01	0.46	8.10	15.7	0.15	0.73	131.7
		3D-FB	52.7	46.3	0.128	5.48	9.79	11.46	22.7	0.18	0.95	137.9
		IMRT-DIBH	53.7	45.2	0.170	3.20	3.33	9.45	18.3	0.15	0.20	137.4
		TD-FB	51.2	47.5	0.075	2.85	3.49	7.32	14.3	0.26	1.99	138.9

Abbreviations: ID: integral dose. HI: homogeneity index. $D_{2\%}$, $D_{98\%}$: dose encompassing 2% and 98% of the volume respectively. V_{20Gy} (%): volume receiving 20 Gy. TD-FB: TomoDirect in free-breathing. 3D-FB: 3D conformal radiotherapy in free-breathing. 3D-DIBH: 3D conformal radiotherapy in deep inspiration breath-hold. IMRT-DIBH: intensity modulated radiotherapy in deep inspiration breath-hold.

($D_{98\%}$ = 46.9 to 47.2 Gy, $p < 0.001$). In addition, near-maximum dose is lower for TomoDirect ($D_{2\%}$ = 51 Gy) than for 3DCRT and IMRT ($D_{2\%}$ = 52.6 to 53 Gy, $p < 0.001$), with no impact from DIBH.

PTV homogeneity is significantly better for TomoDirect than for IMRT. This ability of TomoDirect to produce a more homogeneous target dose has already been observed for breast treatments relative to static IMRT [10] and 3DCRT [11,18]. This significant improvement in the homogeneity of the dose may result with potential improvements in cosmetic outcome [19], even if a beneficial effect on quality of life remains to be demonstrated [20].

Static IMRT is deemed able to improve PTV homogeneity compared to 3DCRT [8,21]. Yet, like many other authors [10,22,23], we did not observe significant difference between 3DCRT and IMRT techniques. The main hypotheses is in our opinion that our 3DCRT technique can compensate very effectively over and underdosages, by the use of wedge filters, MLC field in field or beam weights.

Right breast, right lung and patient

The averaged maximum dose to the right breast is less than 2.8 Gy for all techniques. We took care not to irradiate the contralateral breast with a direct beam when planning, so it is not surprising that we found no significant difference between the 4 modalities studied. Equivalent results were published for various dosimetric comparisons [8,10,24].

The mean right lung dose varies from 0.12 to 0.25 Gy, depending on the technique. It is statistically higher with TomoDirect and lower with IMRT-DIBH ($p < 0.001$). However, given the very low dose values, it is very unlikely to have any clinical impact.

The risk of radiation-induced cancer may increase with the integral dose to the patient [25]. In our study, the lowest ID is obtained with breath-hold, with a significant gain of about 5% compared to free-breathing techniques. Remember that TomoDirect plans have been calculated without the Dynamic Jaw option, which can potentially reduce ID by 9% [26]. We observe no link between IMRT and ID: our results are in line with those of Olch [27] and Abo-Madyan [28], who concluded that IMRT do not necessarily increase the ID, and that the risk of second cancers for breast irradiation are equivalent for tangential fields, regardless of the technology (3DCRT or IMRT).

Left lung

TomoDirect is the best technique to spare the left lung, despite the lack of respiratory gating: TD-FB reduces the average dose to the left lung respectively by 35%, 24% and 32% compared to 3D-FB, 3D-DIBH and IMRT-DIBH. Similar values are obtained for the V_{20} and comparable results can be found in the literature [10,11,18].

We found no benefit to use IMRT-DIBH rather than 3D-DIBH to reduce ipsilateral lung dose, as also observed by Ashraf [22]. However, other authors showed that IMRT can reduce the average dose to the left lung from 7 to 19% compared to 3DCRT [10,12,23]. These discrepancies may be explained by the modest values found in the literature, often at limit of significance level, and by planning techniques that can vary according to the authors.

When comparing 3DCRT with and without breath-hold, we found that DIBH can reduce the average dose to the left lung by 14% (p = 0.007), which is comparable to some results 7 to 28% in the literature [5,17,29]. However, several publications show no significant effect of the DIBH technique on pulmonary sparing [30]. These discrepancies may again find their origin in the various planning techniques, and in the modest values of lung dose reductions obtained with respiratory gating.

What is the best technique?

TomoDirect can only operate in free breathing: is it an insurmountable handicap for the treatment of the left breast, or is the TomoTherapy modulation capable to compensate for the lack of respiratory gating? To our knowledge, no study had yet compared TomoDirect with breath-hold techniques.

The lack of gating in TomoDirect is detrimental to some patients for whom DIBH remains essential for cardiac sparing. Nevertheless, the average gain to the heart obtained with DIBH remains relatively small, and significant dose differences are achieved only for a limited number of patients. For PTV dose homogeneity and left pulmonary dose, TomoDirect can achieve better plans than 3DCRT and IMRT, with or without DIBH.

Thus, it seems to us that the TomoDirect technique is complementary to a 3DCRT technique with DIBH. For a minority of patients, breath-hold should be used if the cardiac dose reduction is a priority over PTV homogeneity or left pulmonary dose. For the majority of the remaining patients, TomoDirect achieves similar cardiac dose than the one obtained with 3DCRT or IMRT with respiratory gating, with a significant reduction in the left pulmonary dose and an improvement of PTV homogeneity. Use of Dynamic Jaw option remains then mandatory to reduce the integral dose to the patient.

Incidentally, our results show as many other studies that DIBH reduces the dose to the heart compared with a 3DCRT technique without DIBH. We are much more reserved about the contribution of static IMRT with DIBH, whether for the heart, the left lung or the

Appendix 3
Detailed AIC statistical analysis results.

	Log-transformed?	Best-model	$F_{3,42}$	p-Value for best-model effect
PTV				
$D_{2\%}$ (Gy)	No	Technique only	55.18	<0.001
$D_{98\%}$ (Gy)	No	Technique only	10.43	<0.001
HI	Yes	Technique only	42.45	<0.001
Heart				
D_{mean} (Gy)	No	Technique only	28.75	<0.001
V_{20Gy} (%)	No	Technique only	29.40	<0.001
Left lung				
D_{mean}(Gy)	No	Technique only	26.20	<0.001
V_{20Gy} (%)	No	Technique only	24.18	<0.001
Right lung				
D_{mean} (Gy)	No	Technique only	65.05	<0.001
Right breast				
D_{max} (Gy)	Yes	Technique only	0.422	0.738
Patient				
ID (Gy cm^3)	No	Technique and breast volume	7.294	<0.001

Abbreviations: ID: integral dose. HI: homogeneity index. $D_{2\%}$, $D_{98\%}$: dose encompassing 2% and 98% of the volume respectively. V_{20Gy} (%): volume receiving 20 Gy.

PTV dose homogeneity: an efficient 3DCRT technique with respiratory gating may be sufficient.

Conclusion

For a small number of patients treated for left breast radiotherapy, lack of respiratory gating in TomoDirect is a handicap for the cardiac dose. However, the sparing of the left lung and the PTV dose homogeneity are routinely better for TomoDirect than for 3DCRT with deep-inspiration breath-hold. Free breathing TomoDirect and breath-hold 3DCRT treatments are therefore complementary: for a minority of patients, respiratory gating remains mandatory if cardiac dose is a priority; for the remaining majority of patients, TomoDirect helps to achieve better PTV homogeneity and reduced left lung dose, with cardiac dose equivalent to that obtained for 3DCRT with breath-holding.

Appendix A

See Appendices 1–3.

References

[1] Ferlay J, Soerjomataram I, Ervik M, et al. GLOBOCAN 2012 v1.0. Cancer incidence and mortality Worldwide: IARC CancerBase No. 11. Lyon, France: International Agency for Research on Cancer; 2013. Available from: http://globocan.iarc.fr.

[2] Clarke M, Collins R, Darby S, et al. Effects of radiotherapy and of differences in the extent of surgery for early breast cancer on local recurrence and 15-year survival: an overview of the randomised trials. Lancet 2005;366:2087–106.

[3] Darby SC, Ewertz M, McGale P, et al. Risk of ischemic heart disease in women after radiotherapy for breast cancer. N Engl J Med 2013;368:987–98.

[4] Garcia R, Oozeer R, Thanh HL, et al. Radiotherapy of lung cancer: the inspiration breath hold with spirometric monitoring. Cancer/Radiotherapie 2002;6:30–8.

[5] Hepp R, Ammerpohl M, Morgenstern C, et al. Deep inspiration breath-hold (DIBH) radiotherapy in left-sided breast cancer. Strahlenther Onkol 2015;191:710–6.

[6] Remouchamps VM, Letts N, Vicini FA, et al. Initial clinical experience with moderate deep-inspiration breath hold using an active breathing control device in the treatment of patients with left-sided breast cancer using external beam radiation therapy. Int J Radiat Oncol Biol Phys 2003;56:704–15.

[7] Latty D, Stuart KE, Wang W, Ahern V. Review of deep inspiration breath-hold techniques for the treatment of breast cancer. J Med Radiat Sci 2015;62:74–81.

[8] Schubert LK, Gondi V, Sengbusch E, et al. Dosimetric comparison of left-sided whole breast irradiation with 3DCRT, forward-planned IMRT, inverse-planned IMRT, helical tomotherapy, and topotherapy. Radiother Oncol 2011;100:241–6.

[9] Reynders T, Tournel K, De Coninck P, et al. Dosimetric assessment of static and helical TomoTherapy in the clinical implementation of breast cancer treatments. Radiother Oncol 2009;93:71–9.

[10] Michalski A, Atyeo J, Cox J, Rinks M, Morgia M, Lamoury G. A dosimetric comparison of 3D-CRT, IMRT, and static tomotherapy with an SIB for large and small breast volumes. Med Dosim 2014;39:163–8.

[11] Qi XS, Liu TX, Liu AK, et al. Left-sided breast cancer irradiation using rotational and fixed-field radiotherapy. Med Dosim 2014;39:227–34.

[12] Mast ME, Kempen-Harteveld L, Heijenbrok MW, et al. Left-sided breast cancer radiotherapy with and without breath-hold: does IMRT reduce the cardiac dose even further? Radiother Oncol 2013;108:248–53.

[13] El-Sherif O, Yu E, Xhaferllari I, Gaede S. An assessment of intrafraction breathing motion on left anterior descending artery dose during left-sided breast radiation therapy. Int J Radiat Oncol 2016 (in press; published online: February 12 2016).

[14] . J ICRU 2010;10(1). Report 83.

[15] D'Arienzo M, Masciullo SG, Sanctis V, Osti MF, Chiacchiararelli L, Enrici RM. Integral dose and radiation-induced secondary malignancies: comparison between stereotactic body radiation therapy and three-dimensional conformal radiotherapy. Int J Environ Res Public Health 2012;9:4223–40.

[16] R Core Team. R: a language and environment for statistical computing. Vienna, Austria: R Foundation for Statistical Computing; 2015. URL http://www.R-project.org/.

[17] Chi F, Wu S, Zhou J, et al. Dosimetric comparison of moderate deep inspiration breath-hold and free-breathing intensity-modulated radiotherapy for left-sided breast cancer. Cancer/Radiothérapie 2015;19:180–6.

[18] Borca VC, Franco P, Catuzzo P, et al. Does TomoDirect 3DCRT represent a suitable option for post-operative whole breast irradiation? A hypothesis-generating pilot study. Radiat Oncol 2012;7:211.

[19] Vicini FA, Sharpe M, Kestin L, et al. Optimizing breast cancer treatment efficacy with intensity-modulated radiotherapy. Int J Radiat Oncol 2002;54:1336–44.

[20] Donovan E, Bleakley N, Denholm E, et al. Randomised trial of standard 2D radiotherapy (RT) versus intensity modulated radiotherapy (IMRT) in patients prescribed breast radiotherapy. Radiother Oncol 2007;82:254–64.

[21] Kestin LL, Sharpe MB, Frazier RC, et al. Intensity modulation to improve dose uniformity with tangential breast radiotherapy: initial clinical experience. Int J Radiat Oncol Biol Phys 2000;48(5):1559–68.

[22] Ashraf M, Janardhan N, Bhavani P, et al. Dosimetric comparison of 3DCRT versus IMRT in whole breast irradiation of early stage breast cancer. Int J Cancer Ther Oncol 2014;2(3):020318.

[23] Al-Rahbi ZS, Ravichandran R, Binukumar JP, Davis CA, Satyapal N, Al-Mandhari Z. A dosimetric comparison of radiotherapy techniques in the treatment of carcinoma of breast. J Cancer Ther 2013;4:10–7.

[24] Qiu JJ, Chang Z, Horton JK, Wu QRJ, Yoo S, Yin FF. Dosimetric comparison of 3D conformal, IMRT, and V-MAT techniques for accelerated partial-breast irradiation (APBI). Med Dosim 2014;39:152–8.

[25] Tukenova M, Guibout C, Hawkins M, et al. Radiation therapy and late mortality from second sarcoma, carcinoma, and hematological malignancies after a solid cancer in childhood. Int J Radiat Oncol Biol Phys 2011;80(2):339–46.

[26] Han EY, Kim DW, Zhang X, et al. Dosimetric effect on pediatric conformal treatment plans using dynamic jaw with Tomotherapy HAD. Med Dosim 2015;40(3):244–7.

[27] Olch AJ. Is intensity-modulated radiation therapy too risky ? In: Olch AJ, editor. Pediatric radiotherapy. Planning and treatment. CRC Press; 2013. p. 19–23.

[28] Abo-Madyan Y, Aziz MH, Aly MMOM, et al. Second cancer risk after 3D-CRT, IMRT and VMAT for breast cancer. Radiother Oncol 2014;110:471–6.

[29] Tanguturi S, Lyatskaya Y, Chen YH, et al. Prospective assessment of deep inspiration breath hold using 3-dimensional surface tracking for irradiation of left-sided breast cancer. Pract Radiat Oncol 2015;5(6):358–65.

[30] Lee HY, Chang JS, Lee IJ, et al. The deep inspiration breath hold technique using Abches reduces cardiac dose in patients undergoing left-sided breast irradiation. Radiat Oncol J 2013;31:239–46.

b) *Problématique de l'imagerie de positionnement*

Le système d'imagerie de la tomotherapie a été largement décrit dans la littérature (Keller et al., 2002; Meeks et al., 2005; Ruchala et al., 2000, 1999). Le détecteur est composé de 738 cavités remplies de Xenon, séparées par des septums de 0,32 mm de large (Figure 13). La distance source-détecteur est de 145 cm. Sur ces 738 détecteurs, 540 sont utilisés pour créer une image tomodensitométrique (*MegaVoltage Computed Tomography*, MVCT). L'image MVCT reconstruite, dont le *Field-Of-View* (FOV) est de 40 cm, permet de visualiser l'anatomie du patient en vue axiale, sagittale et coronale (Figure 13). Notons que nous avons évalué la précision du repositionnement des patients par MVCT sur 259 patients traités entre 2008 et 2011, et communiqué les résultats sous forme de présentation orale au congrès de l'ASTRO à Miami en 2011 (Meyer et al., 2011).

Trois modes d'acquisition sont disponibles (*fine, normal, coarse*), dont dépendent la résolution spatiale longitudinale de l'image, la dose délivrée et le temps d'acquisition. Pour une longueur scannée de 20 cm, le temps d'acquisition est de 186, 271 et 526 secondes respectivement en mode *coarse*, *normal* et *fine* (Jung et al., 2012). La dose délivrée au patient varie de 1 à 4 cGy par MVCT, en fonction du mode d'acquisition et de la localisation (Mege et al., 2016).

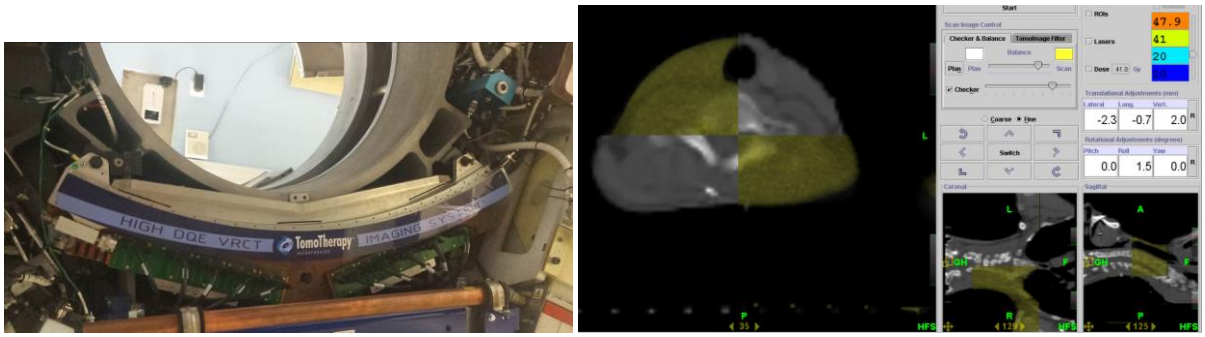

Figure 13. A gauche : couronne de détecteurs de la tomothérapie Hi-ART du CPS. A droite : interface opérateur permettant de recaler l'image MVCT quotidienne (en jaune) avec l'image de référence (en gris).

Ces ordres de grandeur de temps d'acquisition et de doses déposées par MVCT sont acceptables pour la majorité des indications traitées sur tomothérapie, en excluant peut-être le traitement du sein seul par TomoDirect. En effet, une image 2D du champ d'irradiation tangentiel est habituellement réalisée lors d'un traitement du sein seul en RC3D, qui permet de s'assurer très rapidement (en quelques secondes) que le sein est correctement positionné. Ce mode d'imagerie 2D ne délivre en outre pas de dose sur les organes sains. L'imagerie 3D inhérente à la tomothérapie est donc un frein potentiel à l'utilisation du mode TomoDirect pour le traitement du sein seul. **Nous avons cherché à montrer l'intérêt potentiel d'une imagerie topographique 2D acquise avec le détecteur de la tomothérapie, qui n'est pas disponible en mode clinique sur cette machine**. Ce travail, réalisé en collaboration avec l'équipe MIV d'ICUBE, est présenté dans la publication suivante (Meyer et al., 2017).

Physica Medica 39 (2017) 33–38

Contents lists available at ScienceDirect

Physica Medica

journal homepage: http://www.physicamedica.com

Original paper

Megavoltage 2D topographic imaging: An attractive alternative to megavoltage CT for the localization of breast cancer patients treated with TomoDirect

Philippe Meyer [a,*], Fabien Le Pennec [a], Susanta K. Hui [b], Nicolas Dehaynin [a], Delphine Jarnet [a], Matthieu Gantier [a], Claudine Niederst [a], Christophe Mazzara [a], Etienne Baudrier [c], Vincent Noblet [c]

[a] Department of Medical Physics, Paul Strauss Center, Strasbourg, France
[b] Department of Radiation Oncology, City of Hope, LA, USA
[c] ICube-UMR 7357, Strasbourg, France

ARTICLE INFO

Article history:
Received 6 April 2017
Received in Revised form 12 June 2017
Accepted 14 June 2017

Keywords:
Topographic megavoltage 2D imaging
TomoTherapy treatments
Breast cancer

ABSTRACT

Purpose: To show the usefulness of topographic 2D megavoltage images (MV2D) for the localization of breast cancer patients treated with TomoDirect (TD), a radiotherapy treatment technique with fixed-angle beams performed on a TomoTherapy system.
Methods: A method was developed to quickly localize breast cancer patients treated with TD by registering the MV2D images produced before a TD treatment with reference images reconstructed from a kilovoltage CT simulation scanner and by using the projection of the beam-eye-view TD treatment field. Dose and image quality measurements were performed to determine the optimal parameters for acquiring MV2D images. A TD treatment was simulated on a chest phantom equipped with a breast attachment. MVCT and MV2D images were performed for 7 different shifted positions of the phantom and registered by 10 different operators with the simulation kilovoltage CT images.
Results: Compared to MVCT, MV2D imaging reduces the dose by a factor of up to 45 and the acquisition time by a factor of up to 49. Comparing the registration shift values obtained for the phantom images obtained with MVCT in the coarse mode to those obtained with MV2D, the mean difference is 1.0 ± 1.1 mm, −1.1 mm ± 1.1, and −0.1 ± 2.2 mm, respectively, in the lateral, longitudinal, and vertical directions.
Conclusions: With dual advantages (very fast imaging and a potentially reduced dose to the heart and contralateral organs), MV2D topographic images may be an attractive alternative to MVCT for the localization of breast cancer patients treated with TomoDirect.

1. Introduction

The TomoTherapy unit (Accuray, Madison, WI, USA) is a radiation therapy treatment system consisting of a 6 MeV linear accelerator that continually rotates around a patient who translates through the beam, resulting in helical fan beam delivery. TomoDirect is a radiotherapy treatment technique with fixed-angle beams performed on the TomoTherapy system [1]. Up to 12 beams can be set up at different fixed gantry angles. Each beam is delivered as the patient advances through the ring and the beam fluence is modulated by the binary multileaf collimator of the TomoTherapy system. This intensity-modulated radiation therapy (IMRT) modality has shown to be a promising treatment of the single breast, allowing better PTV dose coverage and helping to spare organs at risk compared to 3D techniques and linac-based IMRT [2,3].

The localization of patients receiving radiation therapy for breast cancer is challenging because of the mobility of the treated area. Even with thoracic thermoplastic immobilization systems, inter-fraction positioning errors remain significant [4]. To prevent a degradation of the PTV coverage during a breast treatment with TomoTherapy, a daily pre-treatment imaging control is mandatory [5].

The TomoTherapy imaging system has been widely described in the literature [6]. It uses megavoltage-computed tomography (MVCT) and allows a 3D reconstruction of the patient's anatomy from a helical acquisition. The dose delivered to the patient during

* Corresponding author at: 3 rue de la porte de l'hôpital, 67000 Strasbourg.
E-mail address: pmeyer@strasbourg.unicancer.fr (P. Meyer).

http://dx.doi.org/10.1016/j.ejmp.2017.06.015
1120-1797/

image acquisition depends on several parameters [7] and is less than 1 cGy per image if considering the coarse irradiating acquisition mode [8]. Although the doses to the organs at risk (OAR) are low in absolute value, they generate an additional risk to the patient: daily MVCT imaging would increase the risk of developing a second cancer by 33% and 63%, respectively, in the contralateral breast and lungs [9].

The theory of the TomoTherapy topographic images was presented for the first time in 2010 by Moore et al., who showed the results of using 2D topographic megavoltage images (MV2D) generated from topographic data of the TomoTherapy imager [10]. The term topographic commonly refers to scout images in conventional CT imaging: the TomoTherapy MV radiation source is placed at a fixed angulation, the patient translates with the movement of the table, and the acquisition is carried out using the TomoTherapy imager. A 2D image can then be reconstructed from the data retrieved by the imager. Kiely et al. designed a post-image process to improve the quality of MV topographic images by reducing noise and enhancing the bony anatomy [11]. Besides these theoretical studies, Takahashi studied the clinical relevance of MV2D imaging applied to a specific indication with a very long target size, total marrow irradiation (TMI) [12]. The image acquisition is much faster for MV2D than for MVCT, so MV2D can be very interesting for TMI, for which MVCT acquisition time takes $\geq$600 s [12]. The usefulness of MV2D imaging has never been studied in the clinical context of breast treatments: however, even though imaging acquisition time is not as decisive since the breast target volume is not so large, the dose delivered by MVCT imaging may have a significant impact, as shown previously.

The purpose of this work is to present pre-clinical characterization of MV2D imaging using phantom simulating localization of breast cancer patients treated with TomoDirect.

2. Materials and methods

2.1. Determination of the optimal MV2D acquisition parameters

To acquire the data needed to create MV2D images, the maintenance mode of the TomoTherapy is used by the technicians (referred as the calibration mode). It is possible to vary 3 parameters: the couch speed (CS), the jaw size (JS), and the compression factor (CF) of the data generated by the detector. The CS is the speed of the couch during the acquisition of the image, and the JS describes the jaw width used to collimate the beam in the head-feet direction. We performed several dose and image quality measurements to determine the best combination of parameters.

The MV2D imaging dose was measured using an Exradin A1SL ionization chamber with a volume of 0.056 cm^3 (Standard Imaging, Middleton, WI, USA). The chamber was placed into 1 of the holes of the TomoPhant (Gammex, Middleton, WI, USA), a water-equivalent PMMA cylindrical phantom 18 cm wide with a 30 cm diameter. The ionization chamber signal was read by an electrometer (Standard Imaging, Middleton, WI, USA). The measuring chain was calibrated in a ^{60}Co beam by the Accredited Dosimetry Calibration Laboratory (University of Wisconsin, Madison, WI, USA) in terms of the absorbed dose of water. The dedicated TomoTherapy formalism [13] was used to calculate the imaging dose (see Supplementary 1 for details).

The ionization chambers were placed at 2 cm and 15 cm depth from the top surface of the TomoPhant to reflect respectively peripheral and central dose (Fig. 1). The phantom was centered on the TomoTherapy isocenter and the dose was measured for a scan length of the whole TomoPhant in the head-foot direction. Each measurement was performed 10 times. The dose was also measured for comparison of the same conditions for an MVCT acquisition in the coarse and normal modes, which had a couch speed of 12 mm and 8 mm per gantry rotation, respectively.

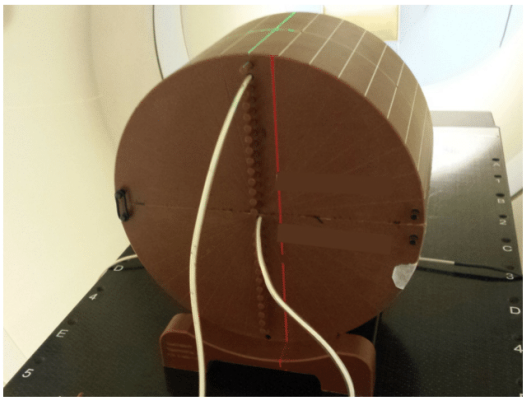

Fig. 1. Experimental setup for dose measurements. The A1SL ion chambers are inserted in dedicated drilled holes at 2 and 15 cm from the top surface of the TomoPhant phantom, which is centered on the TomoTherapy isocenter.

These dose measurements were made by varying 2 acquisition parameters, the CS and the JS. We chose to study the 0.3 and 1 cm JS: we discarded the 2.5 and 5 cm JS due to the high delivered dose [12], which makes MV2D imaging unfavorable. The TomoTherapy CS may vary from 0.00125 cm/s to 4 cm/s. We chose to retain 4 CS: 1, 2, 3, and 4 cm/s and to exclude couch speeds of less than 1 cm/s, which involve acquisition times that we consider too large.

The image quality was evaluated using a Las Vegas phantom, an aluminum slab with a matrix of 10 $\times$ 10 holes of different diameters and depths. A contrast-detail curve was determined by the same observer for images acquired with CS and JS values identical to those used for the measuring dose. Furthermore, we varied the CF (1 or 5) in order to check if sampling the data collected from the TomoTherapy imager would have an impact on the image quality. For comparison, an image of the same phantom was acquired in 6 MV with 2 electronic portal imaging devices (EPID) on conventional linacs: AS1000 (Varian Medical Systems, Palo Alto, CA, USA) and TheraView (Cablon Medical, Leusden, the Netherlands).

2.2. MV2D images and beam eye view (BEV)

To create MV2D images, we followed the method described by Moore [10]. The topographic data generated by the TomoTherapy imaging system were acquired in the maintenance mode and retrieved in a .csv file using TQA software version 1.6.2.4 (Accuray, Madison, WI, USA). The creation of the MV2D image was performed using MATLAB (MathWorks, Natick, MA, USA). The correction of the detector response and image width deformation followed the method described by Takahashi [12].

We created BEV images consisting of the projection of the planned TD treatment fields on MV2D images acquired at the beam angles. Each BEV was created from the multileaf collimator (MLC) data for each treatment projection (MLC sinogram) and corresponded to the maximal MLC opening for each projection.

To handle these MV2D and BEV images, we developed in-house software with MATLAB that allowed us to manually register a MV2D image with a reference image (kVtopo) created from the kilovoltage CT (kVCT) simulation scanner. To match the geometry of the TomoTherapy imaging system, the kVTopo image was generated in fan-beam geometry. This in-house software requires 4 MV2D images: anterior (0°) and lateral (90°) MV2D images to localize a patient in the lateral (x), longitudinal (y), and vertical

(z) directions, and an MV2D image acquired at each treatment beam angle (there are at least 2 beams for a TD treatment) to generate the BEV used to check if the breast is included in the beam. A screenshot of the interface of the in-house software is shown in Supplementary 2.

2.3. MV2D/kVTopo vs MVCT/kVCT registration

To quantify the localization accuracy of MV2D imaging, we used the in-house software after simulating a TD breast treatment on a chest phantom (IMRT thorax phantom, CIRS, Norfolk, VA, USA) equipped with a single left breast attachment.

The CT simulation of the phantom was performed using a GE Optima 580 RT CT (General Electric, Boston, MA, USA) with 2.5 mm CT axial images obtained at 120 kV. After delineating the breast target volume and the left lung, TomoDirect treatment was planned on this phantom using TomoTherapy HD planning station version 5.1.0.24 (Accuray, Madison, WI, USA). Two tangential beams (115° and 308°) were created with 3 leaves left open around the PTV in the air beyond the skin (referred as "flash" leaves). The treatment was optimized in the dynamic jaw IMRT mode (jaws are opening and closing at the beginning and at the end of treatment, reducing the craniocaudal dose spread) with a field width of 5 cm. The pitch was set to 0.5 and the modulation factor to 2, defining respectively the ratio of the couch travel per gantry rotation divided by the treatment slice width, and the longest leaf opening time in a plan divided by the average opening time of all nonzero leaf opening times. The dose calculation grid "normal" was used for optimization ($4.10 \times 4.10\ mm^2$) and "fine" when calculating the final dose ($2.05 \times 2.05\ mm^2$), the longitudinal grid size being given by the slice thickness (2.5 mm).

The phantom was placed on a TomoTherapy HD couch (see Fig. 2), and we applied 7 different shifts with respect to its nominal position (see Table 1 for the offset values) to simulate setup errors. For each of the 7 positions of the phantom, MVCT in the 3 mm coarse mode (MVCTc), in the 2 mm normal mode (MVCTn), and MV2D images were acquired. MV2D images were acquired with a JS = 0.3 cm, a CS = 4 cm/s, and a CF = 5 at 0° and 90° angles to allow for registration and at 115° and 308° for the BEV projection.

To reduce inter-observer variations, 10 different operators (physicists and therapists) registered the MVCT with the kVCT images using the TomoTherapy registration software and the 0° and 90° angles MV2D with the kVTopo images using our in-house software. The registration was carried out without rotating the images; only the translations were used. We compared the MV2D/kVTopo shift values to those of the MVCT/kVCT in the lateral, longitudinal, and vertical directions.

3. Results

3.1. Determination of the optimal MV2D acquisition parameters

The dose measured in the TomoPhant and the acquisition time according to the CS and JS are shown in Table 2. The same measurements are given for MVCT in the normal and coarse modes.

We observed that the dose and acquisition time of the MV2D images were inversely proportional to the CS: for example, the dose went from 8.84 mGy to 2.21 mGy (at a 2 cm depth) and the acquisition time from 20 s to 5 s when the CS changed from 1 cm/s to 4 cm/s. We also observed that the dose was multiplied by a factor of about 4 when the JS size went from 0.3 cm to 1 cm.

The most advantageous MV2D acquisition parameters in terms of acquisition time and dose were therefore a CS of 4 cm/s and a JS of 0.3 cm: in this case, MV2D reduced the acquisition time by a factor of 34 compared to MVCTc and the dose by a factor of 18 and 31 at depths of 2 cm and 15 cm, respectively. Relative to MVCTn, MV2D reduced the acquisition time by a factor of 49 and the dose by a factor 28 and 45 at depths of 2 cm and 15 cm, respectively.

Concerning image quality, examples of the Las Vegas phantom images obtained with MV2D, AS1000, and TheraView are shown in Fig. 3. We observed that at a JS of 1 cm, the details were not discernible, regardless of the diameter and depth of the object.

The contrast-detail curves are therefore shown only for JS = 0.3 cm (Fig. 3). We first observed that the choice of the CS and CF did not seem to have a major impact on the quality of MV2D images. We also noticed that the quality of the images produced by the AS1000 and TheraView systems was significantly better than that of the MV2D images (Fig 3.A and .B): in the best case, MV2D images allowed us to detect the 13 mm diameter holes only to a depth of 0.5 mm, vs 0.1 mm and 0.3 mm, respectively, for the AS1000 and TheraView EPIDs. Furthermore, MV2D images never allowed us to distinguish the holes with the smallest diameter of 1 mm, while they could be detected from depths of 2 mm and 4.5 mm, respectively, for the AS1000 and TheraView EPIDs.

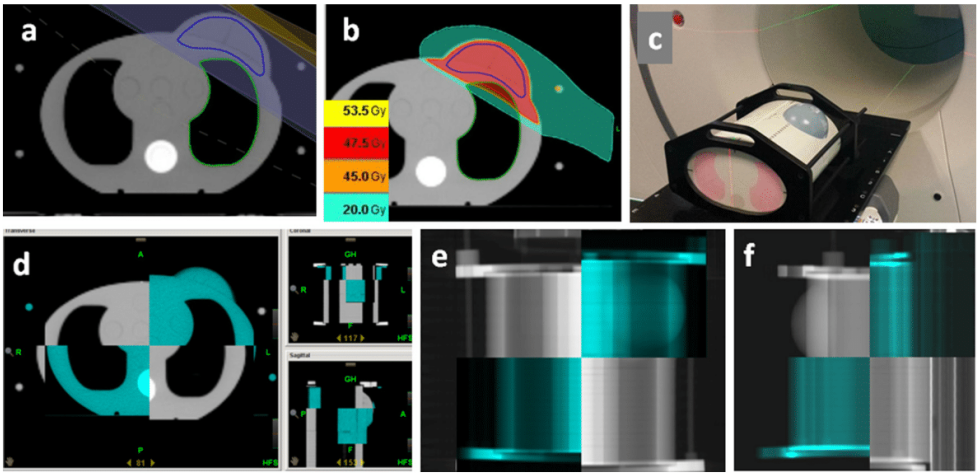

Fig. 2. (a and b) a TomoDirect treatment is planned on a thorax phantom equipped with a breast attachment. This phantom is positioned with intentional shifts on a Tomotherapy unit (c), in order to compare the registration accuracy of the MVCT (d) with 2 orthogonal MV2D images (e and f).

Table 1
Registration values averaged per image over all operators (mm ± standard deviation). The voluntarily phantom shift values are given in the 1st line (in mm).

Shift direction	Imaging modality	Image1 (x = 15; y = 0;z = 0)	Image2 (x = 0; y = 20;z = 0)	Image3 (x = 0; y = 0;z = 30)	Image4 (x = 15; y = 20;z = 30)	Image5 (x = 15; y = 20;z = 0)	Image6 (x = 15; y = 0;z = 30)	Image7 (x = 0; y = 20;z = 30)
x	$MVCT_n$	14.9 ± 0.6	0.2 ± 0.4	−0.0 ± 0.0	15.0 ± 0.5	14.9 ± 0.6	15.0 ± 0.0	−0.2 ± 0.3
	$MVCT_c$	14.8 ± 0.6	−0.2 ± 0.4	−0.5 ± 0.7	14.6 ± 0.5	14.8 ± 0.4	14.9 ± 0.3	−0.5 ± 0.5
	MV2D	16.1 ± 1.2	0.5 ± 0.8	0.7 ± 0.8	16.3 ± 1.2	15.8 ± 0.8	15.4 ± 1.1	0.3 ± 0.7
y	$MVCT_n$	0.5 ± 1.2	20.5 ± 1.5	1.4 ± 1.0	20.8 ± 1.5	20.8 ± 1.8	0.6 ± 0.8	20.5 ± 1.0
	$MVCT_c$	0.5 ± 1.1	20.3 ± 1.3	1.1 ± 0.9	21.2 ± 1.8	21.1 ± 0.3	1.1 ± 1.0	20.8 ± 0.9
	MV2D	−0.5 ± 0.7	19.3 ± 0.7	0.2 ± 0.6	19.4 ± 1.6	19.9 ± 0.6	0.0 ± 0.5	19.8 ± 0.8
z	$MVCT_n$	−0.9 ± 0.3	−0.8 ± 0.4	29.3 ± 0.5	29.4 ± 0.5	−0.4 ± 0.7	30.1 ± 0.3	29.9 ± 0.6
	$MVCT_c$	−1.0 ± 0.2	−1.1 ± 0.3	29.5 ± 0.5	29.3 ± 0.5	−0.1 ± 0.6	30.1 ± 0.3	30.1 ± 0.6
	MV2D	0.8 ± 1.4	−0.5 ± 2.3	29.4 ± 2.7	29.9 ± 3.1	−0.6 ± 2.1	29.4 ± 2.7	29.9 ± 2.7

Key: x = lateral; y = longitudinal; z = vertical; MVCTn = MVCT in normal mode: MVCTc = MVCT in coarse mode.

Table 2
Acquisition time and dose measured at depth of 2 and 15 cm in the cheese phantom for MV2D images, according to the couch speed and jaw size. The same values are given for MVCT images.

Couch Speed (cm/s)	Jaw Size (cm)	Mean dose ± SD (mGy)		Acquisition time (s)
		2 cm depth	15 cm depth	
1	0.3	2,35 ± 0,11	1,14 ± 0,17	20
	1	8,84 ± 0,12	4,68 ± 0,15	20
2	0.3	1,17 ± 0,09	0,63 ± 0,13	10
	1	4,38 ± 0,08	2,34 ± 0,07	10
3	0.3	0,76 ± 0,11	0,41 ± 0,04	7
	1	2,96 ± 0,12	1,57 ± 0,06	7
4	0.3	0,57 ± 0,12	0,31 ± 0,03	5
	1	2,21 ± 0,05	1,18 ± 0,04	5
MVCT normal		16,1 ± 1,8	13,9 ± 0,9	245
MVCT coarse		10,1 ± 0,5	9,6 ± 0,6	170

Key: SD = Standard Deviation.

The optimum parameters for acquiring a MV2D image were JS = 0.3 cm, CS = 4 cm/s, and CF = 5 since these settings allowed us to minimize the dose and acquisition time with equivalent image quality.

3.2. Registration accuracy: MV2D vs MVCT

The registration shift values averaged per image over all of the operators are given in Table 1. The detailed registration values obtained by the 10 operators for the 7 different positions of the phantom are given in Supplementary 3.

The mean differences were computed between the registration shift values obtained using MVCT and MV2D images. The mean and standard deviations of these differences are shown in Table 3.

We first observed that registration shift values were similar between the normal and coarse MVCT modes: the average difference between these 2 imaging modalities was less than 0.3 mm whatever the direction. When comparing MVCT to MV2D, there was a mean deviation of less than 1.1 mm between the registration shift values: the difference was about 1 mm in the x and y directions, whereas it was 0.2 mm in the z direction. The standard deviations calculated in the x and y directions show that the dispersion of the values was comparable between the different imaging modes, indicating that inter-operator and inter-image variability was similar between MVCT and MV2D imaging modes. A notable exception concerns the z direction, indicating that some operators had trouble performing the registration of the lateral MV2D image, perhaps disturbed by the phantom geometry.

4. Discussion

We first note that the doses we measured for MVCT imaging correlated with those reported in the literature, either in the center or periphery of the phantom [12,7]: the maximum deviation was about 30%, which can be explained by the variability of the measurement conditions and the impact of various parameters (vertical offset couch, scanned length, and sinusoidal shape of the dose profile) on the dose measurement [7]. The measured doses in MV2D imaging were identical to those reported in the literature for JS = 1 cm but were about 2 times greater for JS = 0.3 cm [12].

In accordance with observations in previous publications [12,10], doses and acquisition times were greatly reduced when using MV2D rather than MVCT. The reduction magnitude of the acquisition time for MV2D was a factor of about 30 compared to MVCT in the coarse mode with the acquisition parameters that we used. As highlighted by Blanco [11], the integration of the MV2D imaging into the TomoTherapy system would allow us to check quickly if the patient moved during treatment. Our study focused on the opportunity to replace MVCT with MV2D for the initial localization of a breast cancer patient treated with TomoDirect: the acquisition time should then be multiplied by 4, because 4 images are needed (anterior, lateral, and the 2 BEV incidences). The MV2D remains clearly advantageous, since the acquisition time would increase to 20 s for 4 images of 20 cm length in the longitudinal direction vs 170 s for MVCTc of equivalent length.

Shah et al. estimated that the average dose to the heart delivered by MVCTn is 1.12 cGy [14], which for a treatment of 33 sessions corresponds to 0.37 Gy. When considering the worst case scenario (2 cm depth), MV2D was about 28 times less irradiating than MVCT of an equivalent longitudinal length. When extrapolating these phantom dose measurement results to the potential impact on a patient, the gain on the cardiac dose could be still in the order of a factor of 7 (with 4 MV2D images) compared to MVCT: the mean heart dose delivered by MV2D imaging could then be equal to 0.05 Gy for the entire treatment. Although this dose reduction is moderate in absolute terms, it potentially reduces the risk of coronary events, which would increase by

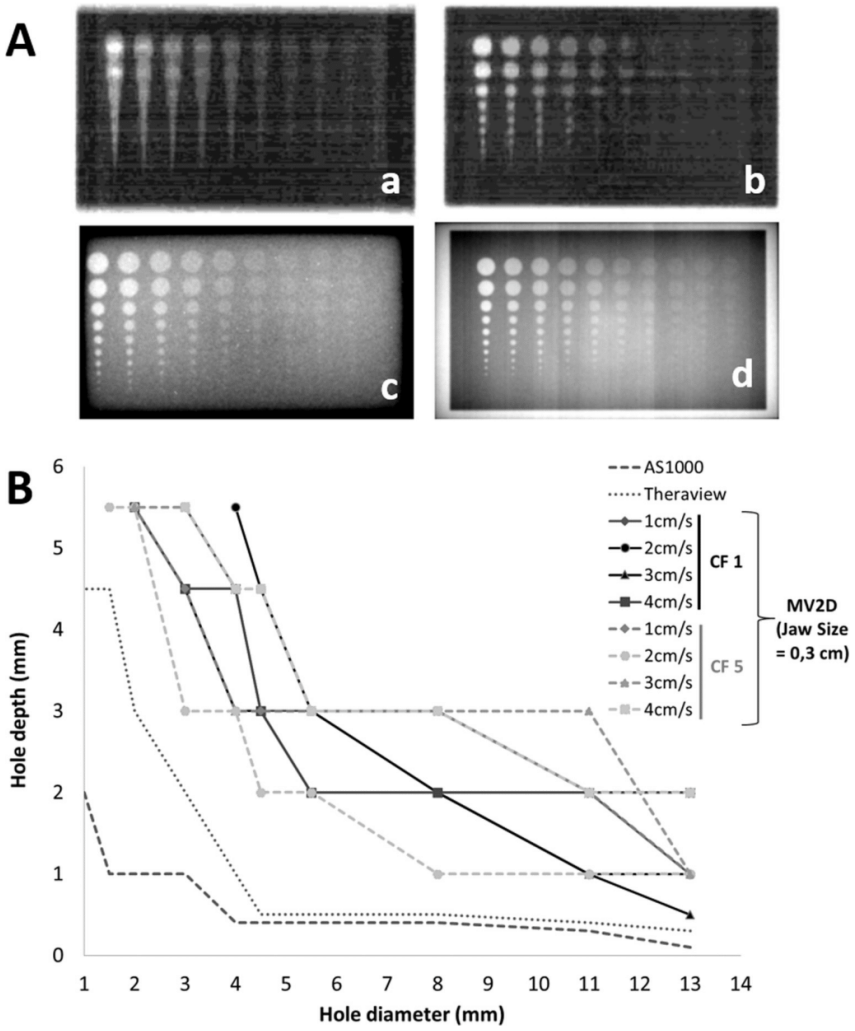

Fig. 3. (A). Examples of the Las Vegas phantom images obtained with (a) MV2D (JS = 1 cm, CS = 4 cm/s), (b) MV2D (JS = 0.3 cm, CS = 4 cm/s), (c) Theraview et (d) AS1000. (B). Contrast-detail curves determined with Las Vegas phantom images obtained with an AS1000 imager, a Theraview imager and with MV2D images for a JS = 0.3 cm, CF (Compression Factor) of 1 and 5, and different couch speed.

Table 3
Differences between the registration values obtained with the MVCTn, MVCTc and the MV2D images, averaged over all operators and phantom positions (mm ± standard deviation).

		Shift direction		
		x	y	z
Mean differences between	$MVCT_n$ - $MVCT_c$	−0.3 ± 0.6	0.2 ± 1.2	0.0 ± 0.6
	$MVCT_n$ - MV2D	0.8 ± 1.1	−1 ± 1.3	−0.0 ± 2.2
	$MVCT_c$ - MV2D	1.0 ± 1.1	−1.1 ± 1.1	−0.1 ± 2.2

Key: x = lateral; y = longitudinal; z = vertical; MVCTn = MVCT in normal mode: MVCTc = MVCT in coarse mode.

7.4% per Gy as suggested by Darby et al. [15]. A similar rationale may be conducted for the contralateral organs (breast and lungs): by reducing the delivered dose, MV2D would help to reduce the potential increase of developing secondary cancers in contralateral breast and lungs.

Concerning image quality, we have shown that MV2D performances are below those of conventional portal imaging equipping accelerators. With the smallest field size (JS = 0.3 cm), the quality of MV2D images is however comparable to clinically useful images. The average differences between registration results obtained with MV2D and MVCT images of a chest phantom with a single attachment breast are relatively small, regardless of the direction, magnitude of the shift applied, or operator. Note that applying Laplacian and Gaussian filters to image processing significantly improves the

quality of MV2D images [11]. Furthermore, the ability to check the projection of TD BEV during registration allows us to match what has traditionally been performed on conventional accelerators to verify the positioning of patients treated for breast cancer in conformal radiotherapy. MV2D appears to be a potentially attractive alternative to MVCT for the positioning of breast cancer patients treated with TD.

This research raises the question of the use of a phantom, which is a limitation of this study: to what extent would the accuracy of the MV2D imaging be equivalent to MVCT in the case of a real patient, when the operator must often face inelastic anatomical deformations? Although the phantom results we have obtained are encouraging, a large-scale study should be conducted on real patients to address this issue.

5. Conclusions

We have shown the benefit of using topographic MV2D imaging to verify the setup of breast cancer patients treated with TomoDirect. The potential for reducing doses to the heart and contralateral organs, the short acquisition time, and the ability to check the TD BEV during registration make it an alternative to MVCT. The integration of MV2D imaging for TomoDirect treatment is desirable for improving the positioning of breast cancer patients.

Conflict of interest statement

The authors have no COI to report.

Acknowledgements

We thank Isabelle Buchheit and Vincent Marchesi from ICL Nancy for the phantom lending, and Pascale, Corinne, Cyrielle, Keltoum, Matthieu, Anis and Maximilien for the MV2D and MVCT registration. We also thank Yutaka Takahashi from Osaka University for his help.

Appendix A. Supplementary data

Supplementary data associated with this article can be found, in the online version, at http://dx.doi.org/10.1016/j.ejmp.2017.06.015.

References

[1] Reynders T, Tournel K, De Coninck P, et al. Dosimetric assessment of static and helical TomoTherapy in the clinical implementation of breast cancer treatments. Radiother Oncol 2009;93:71–9.
[2] Michalski A, Atyeo J, Cox J, et al. A dosimetric comparison of 3D-CRT, IMRT, and static tomotherapy with an SIB for large and small breast volumes. Med Dosim 2014;39:163–8.
[3] Meyer P, Niederst C, Scius M, et al. Is the lack of respiratory gating prejudicial for left breast TomoDirect treatments? Phys Medica 2016;32:644–50.
[4] Agostinelli S, Garelli S, Bellini A, et al. Helical Tomotherapy of the breast: can thermoplastic immobilization improve the reproducibility of the treatment setup and the accuracy of the delivered dose ? Phys Medica 2015;31:49–53.
[5] Goddu SM, Yaddanapudi S, Pechenaya OL, et al. Dosimetric consequences of uncorrected setup errors in helical Tomotherapy treatments of breast-cancer patients. Radiother Oncol 2009;93:64–70.
[6] Ruchala KJ, Olivera GH, Schloesser E, et al. Megavoltage CT on a tomotherapy system. Phys Med Biol 1999;44:2597–621.
[7] Mege JP, Wenzhao S, Veres A, et al. Evaluation of MVCT imaging dose levels during helical IGRT: Comparison between ion chamber, TLD, and EBT3 films. J Appl Clin Med Phys 2016;17:143–57.
[8] Jung JH, Cho KH, Kim YH, et al. Effect of jaw size in megavoltage CT on image quality and dose. Med Phys 2012;39:4976–83.
[9] Quinn A, Holloway L, Hardcastle N, et al. Normal tissue dose and second cancer risk due to megavoltage fan-beam CT, static tomotherapy and helical tomotherapy in breast radiotherapy. Radiother Oncol 2013;108:266–8.
[10] Moore KL, Palaniswaamy G, White BM, et al. Fast, low-dose patient localization on TomoTherapy via topogram registration. Med Phys 2010;37:4068–77.
[11] Blanco Kiely JP, White BM, Low DA, et al. Geometric validation of MV topograms for patient localization on TomoTherapy. Phys Med Biol 2016;61:728–39.
[12] Takahashi Y, Vagge S, Agostinelli S, et al. Multi-institutional feasibility study of a fast patient localization method in total marrow irradiation with helical tomotherapy: A global health initiative by the international consortium of total marrow irradiation. Int J Radiat Oncol Biol Phys 2015;91:30–8.
[13] Langenet KM, Papanikolaou N, Balog J, et al. QA for helical tomotherapy: report of the AAPM task group 148. Med Phys 2010;37(9):4817–53.
[14] Shah AP, Langen KM, Ruchala KJ, et al. Patient dose from megavoltage computed tomography imaging. Int J Radiat Oncol Biol Phys 2008;70:1579–87.
[15] Darby SC, Ewertz M, McGale P, et al. Risk of ischemic heart disease in women after radiotherapy for breast cancer. N Engl J Med 2013;368:987–98.

Supplementary 2. Screenshot of the software developed in this study. The right part allows the user to load the image files and to manually apply the lateral, longitudinal and vertical shifts. The main window in the left upper part shows the MV2D (in blue) and kVtopo (in grey) anterior image of a thorax phantom equipped with a single breast attachment. It's also possible to select a lateral view. While registering the MV2D to the kVtopo image, the user can check how the Beam Eye View of two TomoDirect fields are projected on the MV2D images acquired at the beam angle.

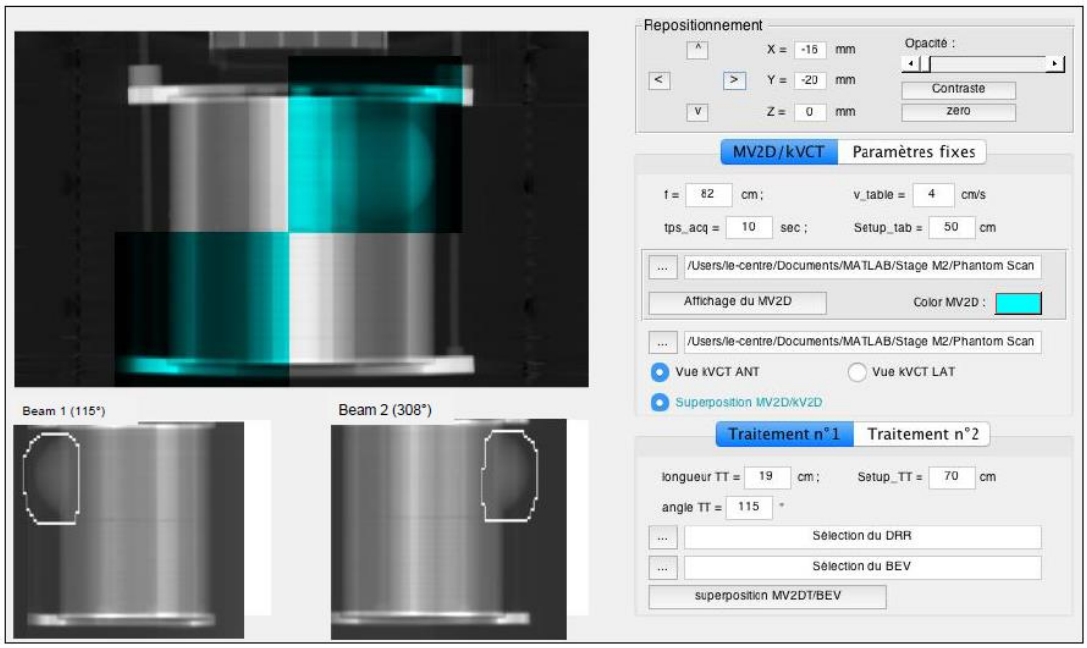

4. Pédiatrie et Tomotherapie

1367 patients de moins de 24 ans ont été traités par radiothérapie en France en 2013. Parmi ces patients, 618 enfants (0-15 ans) et 688 adolescents ou jeunes adultes (16-24 ans) ont été traités par photonthérapie, et 61 enfants et jeunes adultes par protonthérapie. Les tumeurs du système nerveux central, osseuses, les lymphomes Hodgkiniens et les neuroblastomes font partie des indications les plus fréquentes (INCA, 2016).
Au CPS, les enfants et jeunes adultes sont quasi-exclusivement traités par tomothérapie depuis 2008. Entre 2007 et 2017, environ 300 enfants et jeunes adultes ont été traités en tomothérapie au CPS. Les indications traitées reflètent la fréquence nationale évoquée précédemment (voir Figure 14). Au CPS, les traitements pédiatriques sur tomothérapie ont été parmi les premiers en France. De ce fait, nous avons été amenés à réaliser plusieurs études visant à évaluer la prise en charge pédiatrique par tomothérapie, dont les plus significatives sont présentées ci-après.

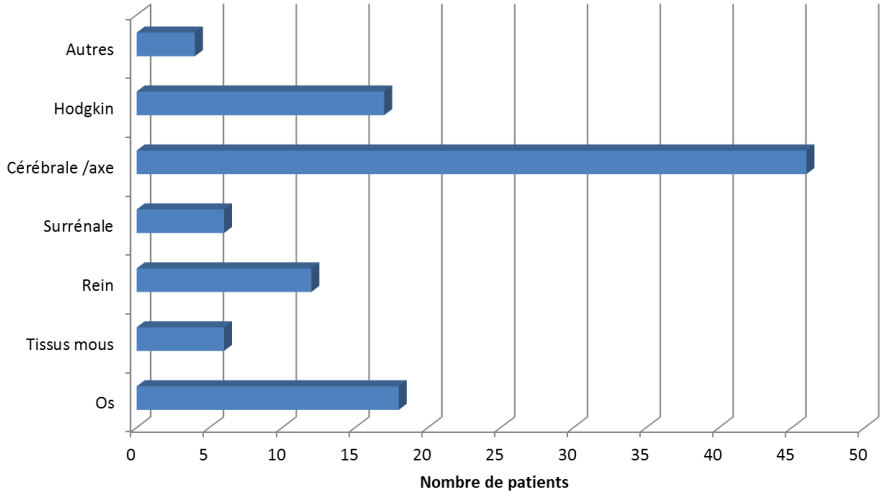

Figure 14. Répartition du nombre d'enfants traités au CPS par tomothérapie en fonction des localisations entre 2008 et juin 2014.

a) Neuroblastomes

Nous avons publié une étude sur l'intérêt de la tomothérapie dans le cadre de la prise en charge des neuroblastomes de haut risque (Beneyton et al., 2012, 2009a). La prise en charge standard de ce type de cancer inclut la chimiothérapie, la chirurgie et la radiothérapie à dose relativement faible (21 Gy). Nous avons recalculé une dosimétrie tomothérapie pour sept enfants âgés de 21 mois à cinq ans (médiane de trois ans) traités en RC3D pour un neuroblastome rétropéritonéal de haut risque selon le protocole HRNBL-1 (deux exemples sont donnés Figure 15). Avec des contraintes au rein identiques pour les deux techniques (V12Gy ≤12 % en cas de rein unique et V15Gy ≤15 % dans le cas des deux reins fonctionnels), nous avons observé que la tomothérapie permet d'obtenir une couverture du PTV satisfaisante (V95%>95%) pour 6/7 patients, contre 3/7 seulement en RC3D. La tomothérapie apporterait donc une meilleure couverture du volume cible par rapport au RC3D, tout en respectant la protection des reins. Pour une dose prescrite modérée de 21 Gy, les conséquences des faibles doses délivrées restent cependant à évaluer à long terme.

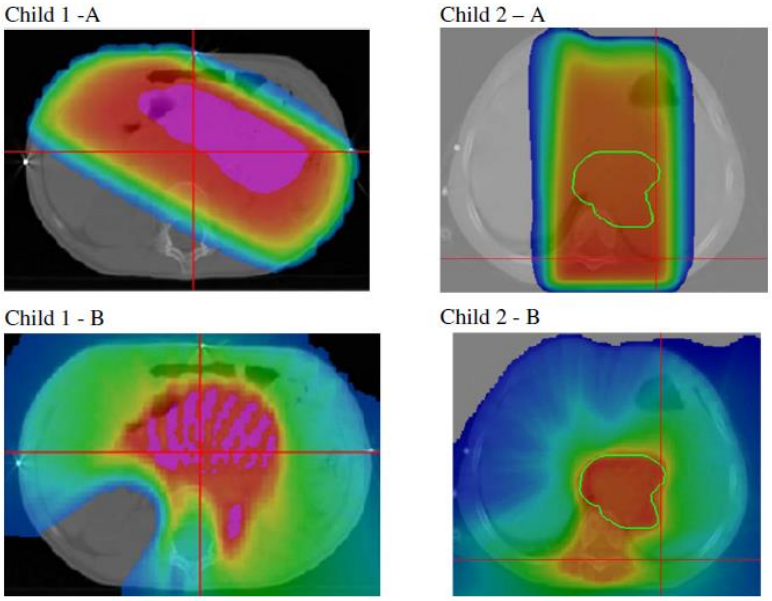

Figure 15. Exemple de coupes transverses dosimétriques pour deux enfants traités pour neuroblastomes en RC3D (A) et tomothérapie (B) (Beneyton et al., 2012).

b) *Tumeurs du tronc cérébral*

Les tumeurs cérébrales sont les tumeurs solides les plus fréquentes de l'enfant. Nous avons évalué l'intérêt de la tomothérapie devant le pronostic défavorable des tumeurs du tronc et la présence d'organes à risque proches de ces lésions limitant la dose délivrée. Les résultats ont été communiqués sous forme de poster (Beneyton et al., 2009b). Quatre enfants âgés de 3,5 à 6 ans ont été irradiés par tomothérapie pour une tumeur du tronc (gliome, astrocytome ou épendymome), pour une dose prescrite de 50,4 à 64,68 Gy. Nous avons réalisé une étude comparative dosimétrique entre tomothérapie et RC3D. Nous avons observé que la tomothérapie permet de couvrir le PTV avec des V95%>95 % pour trois patients sur quatre en tomothérapie, contre deux sur quatre en RC3D, tout en réduisant les doses maximales et moyennes dans l'hypophyse, le chiasma, les cochlées et les lobes temporaux.

c) *Maladie de Hodgkin*

La maladie de Hodgkin est une tumeur maligne du système lymphatique, principalement observée chez les adolescents et les jeunes adultes. Les principes de traitement sont basés sur une chimiothérapie suivie par une radiothérapie. Le pronostic du lymphome de Hodgkin est généralement très bon, avec un taux de survie à 5 ans de plus de 90%. Les principales complications tardives après traitement sont les toxicités cardiaques et pulmonaires, ainsi que les seconds cancers. Nous avons publié une étude concernant treize patientes d'âge médian 29,7 ans (17-53 ans) traitées par tomothérapie pour des maladies de Hodgkin supra-diaphragmatiques de grande taille (douze stade IIA, un stade IIB) (Antoni et al., 2013). Toutes les patientes avaient une atteinte ganglionnaire cervicale et médiastinale (deux exemples de patientes sont illustrées Figure 16). La dose prescrite était de 30 Gy

aux sites initialement envahis et un boost de 6 Gy dans les zones résiduelles suspectes. Avec un suivi médian de 23 mois, nous avons observé une survie sans progression sur deux ans de 91,6% et une survie globale à deux et trois ans de 100%. Nous n'avons observé aucun effet secondaire aigu du cœur ou du poumon. Les plans de traitement tomothérapie ont été d'autre part comparés à la RC3D, montrant que la tomothérapie a permis d'améliorer la couverture du PTV et de considérablement diminuer les fortes doses dans les organes à risque : par exemple pour le cœur, la V20Gy et la V30Gy étaient respectivement 1,4 et 2 fois plus bas en tomothérapie qu'en 3D-CRT. Il est également à noter que la dose intégrale était identique en RC3D et en tomothérapie. En conclusion, le traitement a été bien toléré, mais un suivi plus long est nécessaire pour confirmer la traduction de ces améliorations dosimétriques sur un plan clinique et évaluer l'impact des très faibles doses.

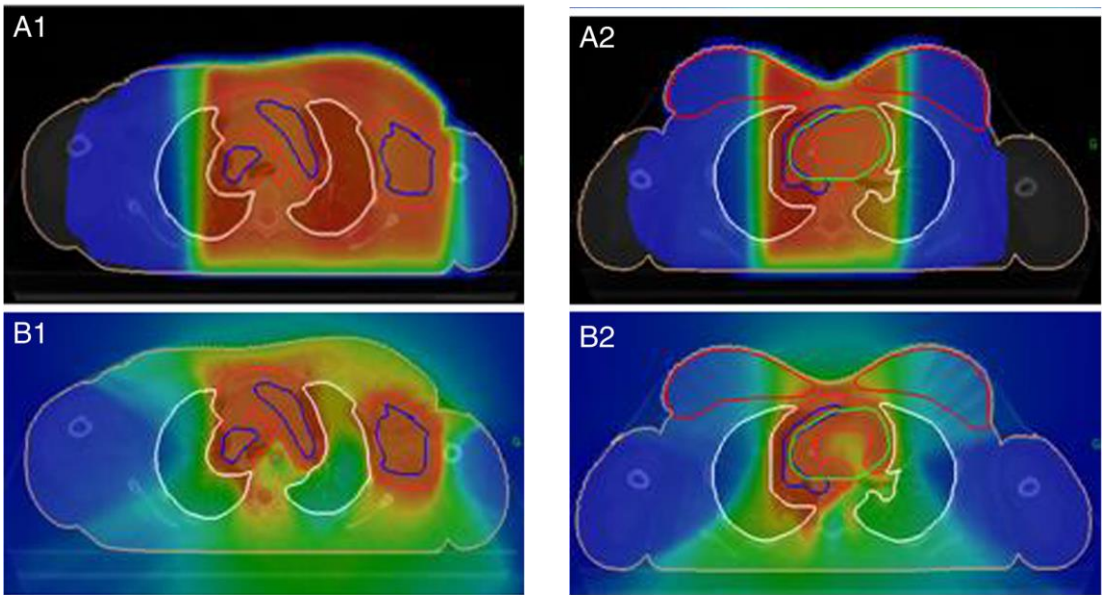

Figure 16. Exemple de coupes transverses dosimétriques pour deux patientes traitées pour maladie de Hodgkin en RC3D (A1 et A2) et tomothérapie (B1 et B2) (Antoni et al., 2013).

d) <u>Médulloblastome</u>

Le médulloblastome est une tumeur cérébrale maligne primitive principalement pédiatrique, puisqu'elle se développe dans 80 % des cas chez des enfants avec un âge médian de six à sept ans. Elle représente la principale tumeur cérébrale maligne primitive de l'enfant. La stratégie thérapeutique classique comportait jusque dans les années 1990 une exérèse chirurgicale, puis une irradiation craniospinale de 36 Gy, suivie d'un complément d'irradiation dans la fosse postérieure pour atteindre une dose totale de 54 Gy. Les taux de survie globale à cinq ans obtenus via cette approche variaient de 53 à 65 %.

Depuis 2008, tous les médulloblastomes ont été traités au CPS sur tomothérapie. Par rapport au RC3D, cette technologie permet en effet d'éviter les jonctions entre champs, inévitables sur accélérateurs classiques, de réduire la dose aux organes à risque et d'obtenir une dose plus homogène au PTV (Schiopu et al., 2017). Nous avons publié l'expérience du CPS dans la prise en charge des médulloblastomes (pas seulement celle liée à la tomothérapie) et confronté nos résultats à ceux décrits dans la littérature (Vigneron et al., 2016). Cinquante-deux enfants d'âge moyen 6,5 ans (11

mois-17,5 ans) irradiés entre 1974 et 2012 pour un médulloblastome au CPS ont été inclus dans l'étude. La radiothérapie a été réalisée en 2D, RC3D et tomothérapie respectivement chez trente-neuf, neuf et quatre patients. Les irradiations 2D et RC3D ont été réalisées par cobalthérapie (dix-neuf patients), combinaison cobalthérapie et électrons (trois patients), combinaison de photons X de 6 à 25 MV et électrons (quatorze patients), combinaison de photons X de 6 à 25 MV (six patients) et exclusivement photons X de 6 MV (six patients). Les taux de survie globale de 62 % à cinq ans et de 57 % à dix ans sont proches de ceux rapportés dans la littérature. L'insuffisance de réalisation de suivi neuropsychologique (qui est aujourd'hui régulière et organisée) n'a pas permis de caractériser le taux de toxicité cognitive. Ce retour d'expérience a notamment permis de souligner l'importance pour les médulloblastomes d'une prise en charge multidisciplinaire en milieu spécialisé, afin d'homogénéiser les stratégies thérapeutiques.

e) Anesthésie générale

Lors d'une séance de radiothérapie, il est impératif que le patient soit installé dans la même position que lors de l'étape de simulation, et qu'il ne bouge pas durant la séance. Pour les très jeunes enfants, le plus souvent avant quatre à cinq ans, une anesthésie générale (AG) est nécessaire, dont le but est de garantir l'immobilité (voir Figure 17). Le CPS est le seul centre du Grand Est à proposer l'AG en radiothérapie pédiatrique. Nous avons publié notre expérience sur quinze enfants d'un âge moyen de 29 mois (13-56 mois) traités sur tomothérapie sous AG entre 2009 et 2013 (Vigneron et al., 2013). Cela représente 386 AG. La durée moyenne d'induction était de 1,6 minute, celle de l'anesthésie générale de 15,5 minutes et celle du réveil de 2,6 minutes. Les complications relevées ont été rares et ont représenté deux séances sur 386 (0,5 %). Ce faible taux de complications est retrouvé dans la littérature, sous la réserve capitale de l'expérience de l'équipe d'anesthésie en termes de surveillance et de gestion rapide des événements indésirables en pédiatrie. L'anesthésie générale est dans notre pratique de radiothérapie un traitement bien toléré, compatible avec une qualité de vie acceptable, présentant un faible taux de complications, même chez les enfants les plus jeunes.

Figure 17. Masque de contention avec masque laryngé pour anesthésie (Vigneron et al., 2013).

f) Mesure des neutrons secondaires en protonthérapie

Sous l'impulsion d'un groupe de recherche de l'IPHC (Institut Pluridisciplinaire Hubert Curien), nous avons récemment publié un article sur la mesure des neutrons secondaires en radiothérapie (Arbor et al., 2017). Il s'agit d'une problématique importante en radiothérapie pédiatrique, en raison de la survenue potentielle de seconds cancers. Pour les jeunes patients, le risque de cancer radio-induit doit en effet être pris en compte: les patients ayant eu de la radiothérapie dans l'enfance présentent un risque trois à six fois plus élevé de développer un second cancer (Chargari and Cosset, 2013). Même si ces seconds cancers surviendraient principalement dans les zones à forte dose (5-50 Gy), l'impact des faibles doses hors champ ne doit pas être négligé, même pour des organes à risques éloignés de la tumeur. Certaines études ont montré que ce risque augmente après une exposition de 50 à 100 mSv, et jusqu'à quarante ans après le traitement (Gottschalk, 2006; Hall, 2006). Une estimation précise de la distribution des doses hors champ est donc une quantité dosimétrique clé pour l'étude de l'induction des cancers secondaires en radiothérapie pédiatrique.

En collaboration avec le laboratoire IPHC, nous avons publié pour la première fois une étude du capteur CMOS AlphaRad (14 µm d'épaisseur, 2,5*2,5 mm²) utilisé pour la mesure temps réel des neutrons secondaires en radiothérapie. Combiné à des simulations Monte-Carlo et à l'utilisation de détecteurs passifs de type CR-39, le capteur CMOS a permis de mesurer simultanément des neutrons rapides et thermiques pour évaluer avec précision les dépendances de la taille du champ et de la position de l'accélérateur dans les calculs de dose. Avec une incertitude statistique d'environ 6 % sur le comptage des neutrons pour un traitement de radiothérapie classique, nous avons montré que la sensibilité d'une puce unique est suffisamment élevée pour observer la variation de la production de neutrons par rapport à la taille du champ. De manière plus détaillée, toutes nos mesures (CMOS, CR-39, simulations MC) ont montré que la production de neutrons thermiques ne dépend pas de la taille du champ, en accord avec la littérature (voir Figure 18). La corrélation entre taille de champ et production de neutrons rapides est cependant plus complexe. Si certaines de nos mesures ont montré que cette production diminuait avec la taille de champ (voir Figure 18), d'autres mesures effectuées à l'isocentre ont montré l'inverse. La relation entre production de neutrons rapides et taille de champ est donc fonction de la localisation autour de l'accélérateur, ce qui a été montré dans d'autres études. Ces résultats expérimentaux sont prometteurs pour l'utilisation future de capteurs CMOS dans le cadre d'un système de surveillance neutronique, combinant des mesures en temps réel et une simulation de Monte Carlo, pour l'évaluation de la dose hors champ en radiothérapie.

Pour conclure, notons l'intérêt potentiel de ce type de détecteur en protonthérapie. Nous avons vu précédemment que la protonthérapie reste encore marginale en France pour les traitements pédiatriques. Néanmoins, cette situation pourrait évoluer dans les années à venir, puisque sept projets d'implantation de protonthérapie à court et moyen terme sont en cours en France (INCA, 2016). Les experts estiment à 410 le nombre d'enfants et de jeunes adultes par an qui pourraient être traités par protonthérapie pour les tumeurs intra-crâniennes et de 100 à 150 pour les sites extra-crâniens. Le comportement des protons dans les tissus, dont le dépôt d'énergie est maximum lorsque le proton s'arrête à une profondeur précise (pic de Bragg), fait en effet de la protonthérapie une technique de choix particulièrement chez les enfants (Chargari et al., 2016). En protonthérapie, les doses hors champs sont principalement produites par les particules secondaires que sont les neutrons (Farah et al., 2014), dangereux même à faible dose, en raison de leur facteur de pondération radiologique élevé. Or les connaissances sur les doses hors champ en protonthérapie sont aujourd'hui

limitées : elles concernent les anciennes installations de protonthérapie, remplacées aujourd'hui par de nouvelles technologies, notamment de spot scanning. L'intérêt du détecteur CMOS AlphaRad y est potentiellement important. L'IPHC prévoit d'insérer ces détecteurs, de faible dimension, à l'intérieur de fantômes, en vue de valider les modélisations Monte-Carlo.

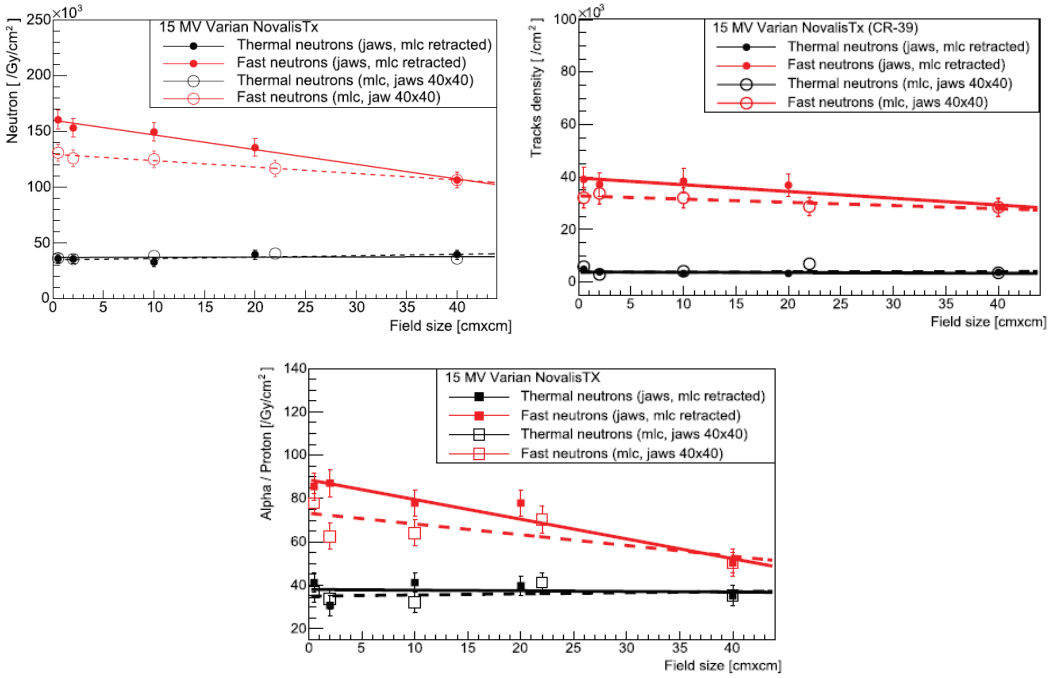

Figure 18. Simulations Monte-Carlo (en haut à gauche), mesures CR-39 (en haut à droite) et mesures CMOS (en bas) de la production de neutrons secondaires en fonction de la taille du champ du faisceau de 15 MV du Novalis TX du CPS. Les symboles rouges et noir correspondent respectivement au champ formé par le MLC ou les mâchoires (Arbor et al., 2017).

CONCLUSIONS DU CHAPITRE I.A

Depuis l'installation de la première tomothérapie au Centre Paul Strauss en 2007, nous avons mené plusieurs travaux de recherche visant à améliorer la prise en charge des patients avec cette technique. Nos principales études ont été décrites dans ce chapitre.

A l'IRC, nous continuerons à nous investir fortement sur les traitements par tomothérapie, notamment sur les nouveaux outils de radiothérapie adaptative dédiés à cette machine. Nous continuerons également à travailler sur le système d'imagerie de la tomothérapie, en y intégrant des outils d'intelligence artificielle tels que ceux offerts par le *deep learning*.

L'utilisation du *deep learning* en radiothérapie est en effet un axe de recherche sur lequel nous avons commencé à travailler en 2016, et que nous souhaitons continuer à développer dans le futur. Le prochain chapitre est consacré à ce volet de nos activités.

B. APPRENTISSAGE PROFOND EN RADIOTHERAPIE

Le deuxième volet de mes activités de recherche actuelles et futures concerne l'intelligence artificielle, dont l'apprentissage profond (*deep learning*, DL) est une des techniques les plus en vues. Le *deep learning* a été popularisé par des applications en imagerie, et les premiers travaux portant sur leur utilisation en radiothérapie ont été publiés en 2017. Dans la première partie I.B.1 de ce chapitre, je propose tout d'abord d'expliquer ce qu'est l'apprentissage profond, en m'arrêtant plus longuement sur les réseaux convolutionnels. Nos travaux sur ce sujet entrepris en collaboration avec l'équipe MIV du laboratoire ICube sont en cours de publication et sont présentés par la suite : une revue des méthodes du deep learning en radiothérapie dans la deuxième partie I.B.2, et une méthode de segmentation des métastases cérébrales sur IRM dans la troisième partie I.B.3.

1. Introduction à l'apprentissage profond

Cette courte introduction au *deep learning* a pour objet de rendre ses aspects de base accessibles aux néophytes dont je me revendique. Une compréhension approfondie nécessite en effet des connaissances solides en mathématiques et en informatique. Les éléments présentés ci-après proviennent principalement d'une revue synthétique (LeCun et al., 2015) et d'un livre en ligne (Goodfellow et al., 2016).

Le DL décrit un ensemble de modèles de calcul composés de multiples couches de traitement de données, qui permettent d'apprendre en représentant ces données par de plusieurs niveaux d'abstraction. A partir d'un grand nombre de données d'entrainement, ces modèles découvrent des structures récurrentes en affinant automatiquement leurs paramètres internes via un algorithme de rétropropagation.

Chaque couche du réseau transforme le signal de façon non-linéaire dans le but d'augmenter la sélectivité et l'invariance de la représentation. Avec un nombre de couches suffisant, le réseau peut générer une hiérarchie de représentations qui rendront le modèle à la fois sensible à de très petits détails et insensible à de grosses variations.

Les approches de DL font partie de la famille des techniques informatiques dites d'apprentissage automatique (*machine learning,* ML), qui est un domaine de l'intelligence artificielle (Figure 19). Le réseau de neurones convolutionnels est une approche particulière du DL, dédiée au traitement d'image.

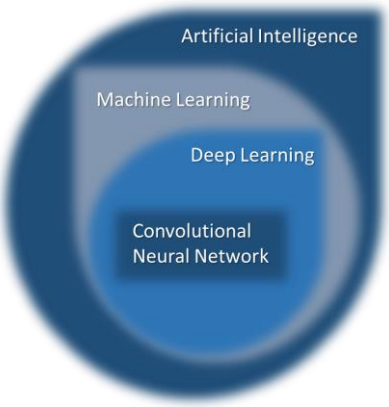

Figure 19. Illustration d'une classification possible des méthodes d'intelligence artificielle. Ces différents concepts sont décrits dans les paragraphes suivants.

a) Intelligence artificielle et apprentissage automatique

Historique

Le terme *intelligence artificielle* (IA) a été introduit en 1956 par un des pionniers du domaine, John Mc Carthy (Crevier, 1993; McCarthy and Hayes, 1969). Il existe de nombreuses définitions : le Larousse définit aujourd'hui l'IA comme « un ensemble de théories et de techniques mises en œuvre en vue de réaliser des machines capables de simuler l'intelligence humaine ». On peut aussi citer Boden, qui définit l'IA comme une science dont l'objectif est de faire faire aux machines des tâches qui requerraient de l'intelligence si elles étaient effectuées par un humain (Boden, 1977).
Le concept d'IA est cependant plus ancien. Les contours de son avènement sont difficiles à fixer, les premiers concepts historiques relevant de la philosophie, de la fiction et de l'imagination (Buchanan, 2005). Certains auteurs citent les philosophes du 17ème et 18ème siècles comme les précurseurs du concept d'IA (Chrisley and Begeer, 2000). Descartes, en affirmant que l'animal n'est rien d'autre qu'une machine ou un automate perfectionné, aborde la réflexion d'une vision mécaniste du réel (Vizier, 1996). Disciple de Descartes, La Mettrie va plus loin que lui en faisant de l'homme (et non plus seulement de son corps) une machine (Diagne, 2006). Selon cet auteur, le langage n'est pas un caractère inné de l'homme, comme le soutenait Descartes, mais un instrument acquis (Pignataro, 2005), ouvrant ainsi la voie au concept d'apprentissage. Pascal et Leibniz ont, entre temps, inventé de nouvelles machines à calculer qui ont mécanisé l'arithmétique. Cet environnement philosophique et scientifique est propice à la création d'œuvres fantastiques et de science-fiction, qui « inspireront de nombreux chercheurs en IA » (Buchanan, 2005). Issu du mythe grec de Prométhée qui crée la race humaine à partir d'une motte d'argile, le thème des créatures artificielles devient courant (Baudou, 2011) : on le retrouve chez Mary Shelley, qui écrit *Frankenstein* en 1818, chez Gustav Meyrink auteur du *Golem* en 1915 ou encore chez Baum qui décrit l'invention d'un homme mécanique en 1914 (voir Figure 20).

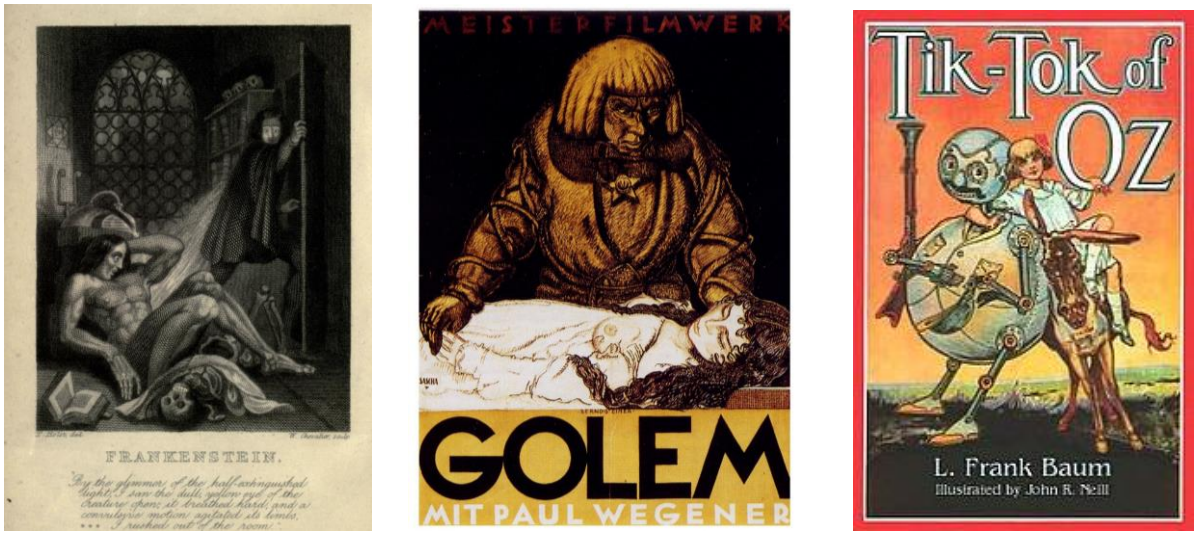

Figure 20. A gauche : couverture de l'édition de 1831 de *Frankenstein* de Mary Shelley. Au centre : affiche du film *Golem*, adapté du roman de Meyrink de 1915. A droite : couverture du roman *Tik-Tok of Oz* de Baum de 1914.

Si l'on considère l'IA dite contemporaine, plusieurs auteurs placent l'article *Computing machinery and intelligence* publié en 1950 comme l'un des travaux fondateurs (Turing, 1950). Plutôt qu'une démonstration formelle, Turing ouvre cet article sur la question *Can machines think ?* Il propose d'y répondre avec un jeu, connu sous le nom de *test de Turing,* qui consiste à confronter verbalement un homme soit à un autre homme soit à une machine, sans qu'il ne sache avec lequel il échange. Six ans plus tard, Newell et Simon proposent l'algorithme *Logic Theorist,* souvent considéré comme le premier programme informatique relevant du domaine de l'IA (Newell and Simon, 1956). Cet algorithme avait comme objectif d'imiter les capacités humaines de résolution des problèmes, et a ouvert la voie aux nombreuses méthodes d'IA que nous connaissons aujourd'hui. Parmi ces méthodes, le *machine learning* fut proposé pour une des premières fois en 1959 par Samuel, qui a développé un programme d'IA pouvant jouer aux dames, basé sur un paramétrage partiel par l'expérience acquise (Samuel, 1959). Le jeu de dames est devenu par la suite l'équivalent pour l'IA de ce que représente la mouche drosophile pour la génétique : croissance rapide et facile à élever pour l'une, modèle idéal pour comparer les performances d'un algorithme et d'un homme pour l'autre (McCarthy and Feigenbaum, 1990).

Apprentissage automatique

Le *machine learning* (ML), apprentissage automatique en français, est un sous-domaine de l'IA. Il peut être défini comme un ensemble de méthodes qui apprennent automatiquement à reconnaitre un modèle complexe et qui prend une décision basée sur des données sans intervention humaine (Natarajan et al., 2017). Exprimé plus simplement, le ML est un algorithme capable d'apprendre à partir de données (Goodfellow et al., 2016). Il permet de s'attaquer à des tâches qu'il serait trop difficile à résoudre avec des programmes écrits exclusivement par l'homme.

Nous renvoyons à notre article *Deep learning for radiotherapy*, présenté dans le chapitre B.2, pour la présentation des principes généraux du ML et des grandes familles d'apprentissage. Pour résumer, il existe deux méthodes d'apprentissage : supervisées et non supervisées. Dans les méthodes supervisées, les données sont labellisées et le réseau cherche à ajuster ses paramètres pour faire correspondre le label de sortie à la donnée d'entrée. Dans l'apprentissage non supervisé, les données ne sont pas labellisées, et le réseau cherche à reconnaitre des structures récurrentes dans les données d'entrée. Les méthodes d'apprentissage non supervisées ont fait l'objet de nombreux développements, mais sont aujourd'hui éclipsées par les méthodes supervisées qui sont largement majoritaires dans tous les domaines.

On ajoute ici quelques éléments, qui visent à définir plus précisément ce que veut dire « apprendre » pour un algorithme, avec des exemples concrets en radiothérapie. Ces éléments sont tirés des définitions de Mitchell (Mitchell, 1997) : pour définir concrètement un apprentissage, il faut spécifier trois paramètres : la tâche T à effectuer, la mesure de la performance P à améliorer et la source de l'expérience E. On peut dire qu'un algorithme apprend à effectuer une tâche T à partir d'une expérience E, si ses performances mesurées P dans la tâche T s'améliorent avec l'expérience E. Pour illustrer sa proposition, Mitchell reprend la problématique de l'apprentissage du jeu de dames : la tâche T est « jouer aux échecs », la performance P est « le pourcentage de parties gagnées contre des opposants, et l'expérience E « les parties jouées par le système contre lui-même ». Cet exemple peut être généralisé à de nombreuses autres applications, de la conduite autonome à la reconnaissance de caractères, et bien sûr à la radiothérapie dont nous avons illustré quelques applications dans le Tableau 1 .

Problématique d'apprentissage	Tâche T	Mesure de la performance P	Expérience d'apprentissage E
Apprendre à jouer aux dames	Jouer aux dames	Ratio (%) de parties gagnées contre un adversaire	Parties jouées par le programme contre lui-même
Reconnaissance d'écriture	Reconnaitre et classifier des mots manuscrits	Ratio (%) de mots correctement classifiés	Base de données de mots manuscrits classifiés
Voiture autonome	Rouler de Hochfelden à St Claude sur des routes publiques	Distance moyenne parcourue sans erreur (jugée par un observateur humain)	Séquences de vidéos, d'images, et de commandes de direction enregistrées en observant un conducteur humain
Segmentation automatique d'images médicales	Délinéer la prostate sur une IRM	Ratio (%) de pixels communs avec une segmentation d'expert humain	Base de données d'organes segmentés et classifiés par des experts humains
Détection automatique sur images médicales	Détecter les métastases cérébrales sur IRM	Ratio (%) de métastases non détectées ou détectées en trop par rapport à une détection d'expert humain	Base de données d'images IRM avec métastases segmentées par des experts humains
Planification du traitement de radiothérapie sur IRM	Générer une image pseudo-CT à partir d'une IRM	Ecart moyen entre les nombres Hounsfield des pixels de l'image pseudo-CT et d'une image CT de référence	Base de données d'images IRM et d'images CT correctement recalées
Réduire la dose délivrée en IGRT (Image Guided RadioTherapy)	Réduire le bruit dans les images fluoroscopiques kV	Ecart entre le rapport signal sur bruit moyen mesuré sur une image kV corrigée et sur une moyenne de 10 images kV	Base de données d'images KV fluoroscopiques de patients en cours de traitement de radiothérapie
Aide à la planification automatique du traitement de radiothérapie	Prédire la dose délivrable à partir d'un fichier structure	Ratio (%) de pixels communs entre les isodoses prédites et réelles	Base de données de plans de traitement de radiothérapie avec fichiers structures et doses
Eviter les collisions entre le patient et l'accélérateur	Reconnaitre et classifier le matériel et le patient dans un bunker de traitement	Ratio (%) d'objets correctement classifiés	Base de données d'objets classifiés
Aide au choix thérapeutique en radiothérapie	Prédire la toxicité rectale d'un traitement de radiothérapie d'un cancer de l'utérus	Ecart entre toxicités prédites et toxicités réelles	Base de données de plans de traitement de radiothérapie avec fichiers structures et doses + Base de données médicales avec gradation de la toxicité rectale

Tableau 1. Quelques exemples liés à des problématiques d'apprentissage automatique. Les 3 premières lignes sont reprises de Mitchell et al (Mitchell, 1997). Les autres exemples (en grisé) sont tirés d'applications réelles de *Machine Learning* en radiothérapie, qui peuvent être trouvées dans le chapitre II.2.

b) *Les réseaux de neurones*

De nombreuses méthodes de *machine learning* ont été développées pour modéliser une expérience E (Murphy, 2012). Les réseaux de neurones sont une de ces méthodes. L'idée d'un programme informatique qui pourrait trouver lui-même la représentation d'un modèle à partir d'un ensemble de données est ancienne. Le Perceptron est une des premières approches ayant pour but de conceptualiser des données provenant directement de l'environnement (Rosenblatt, 1957). Elle s'inspire de la biologie du cerveau, à travers la formalisation mathématique du fonctionnement d'un neurone (Figure 21). Le principe est de simuler le transfert d'information à travers un neurone : la somme pondérée de signaux d'entrée est calculée, le résultat est multiplié par une fonction d'activation non linéaire, et un signal de sortie est activé si un seuil est dépassé (Figure 22 - gauche). On parle aussi d'unité élémentaire de calcul. Le signal de sortie d'une unité alimentera d'autres unités, organisées en couches, et ainsi de suite, formant un réseau de neurones artificiels (*artificial neural network*, ANN, voir Figure 22 - droite). Lorsqu'il est composé de plusieurs couches cachées intermédiaires, on parle alors de réseaux neuronaux multicouches ou de réseaux de neurones profonds (*Deep neural network*, DNN), décrits dans la partie I.A.1.c).

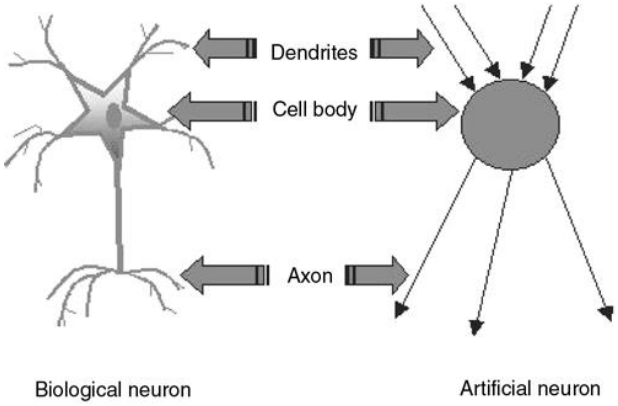

Figure 21. Analogie entre un neurone artificiel et un neurone biologique (Sánchez Mesa et al., 2005).

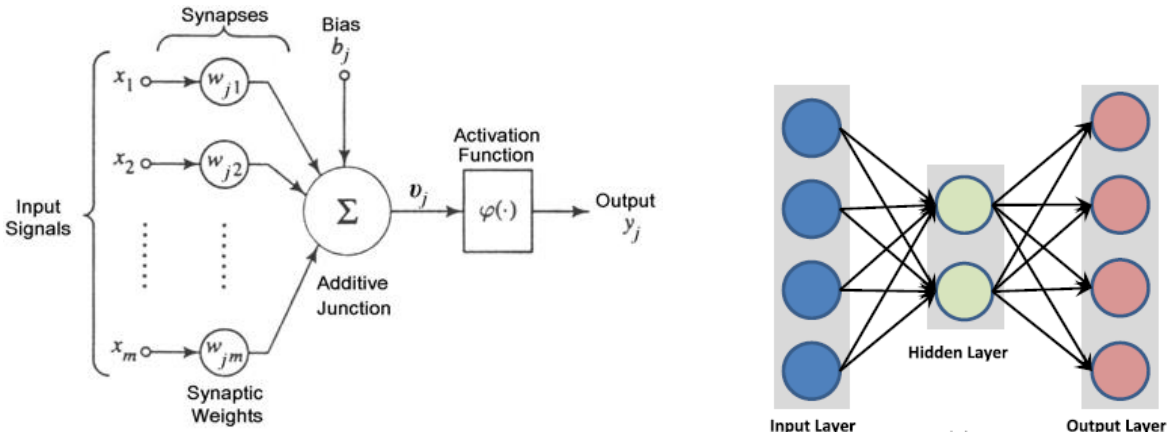

Figure 22. A gauche : un neurone artificiel (Guarnieri et al., 2006). Les signaux d'entrée sont représentés par *x*. Le biais *b* et la fonction d'activation φ sont paramétrables par l'utilisateur. Les poids *w* sont ajustés automatiquement par le réseau. A droite : illustration schématique d'un réseau de neurones à couche unique (Ravì et al., 2017). Les neurones non contenus dans la couche d'entrée ou de sortie sont contenus dans des couches cachées. Lorsqu'il y a plusieurs couches cachées, on parle de réseau de neurones profond.

Le processus d'entrainement/d'apprentissage

La fonction d'activation et le biais sont fixes et paramétrables par l'utilisateur. La fonction d'activation la plus populaire est aujourd'hui appelée *rectified linear unit* (ReLU), qui permet un apprentissage rapide des DNN (Figure 23). Il s'agit d'un simple filtre qui élimine les signaux négatifs.

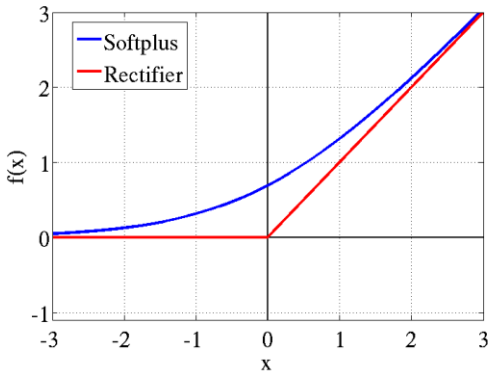

Figure 23. En rouge : fonction d'activation rectified linear unit (ReLU), utilisée couramment dans les réseaux de neurones profonds (Glorot et al., 2011).

Les pondérations des signaux d'entrée (*w* dans la Figure 22) sont par contre ajustées automatiquement par le réseau lors d'un processus itératif d'apprentissage. Un réseau de neurones doit en effet passer par une première phase dite d'apprentissage avant d'être utilisable. Dans un processus supervisé, cet apprentissage consiste à minimiser une fonction objectif qui exprime l'écart entre la donnée calculée par le réseau et celle souhaitée. L'ajustement des poids est effectué à l'aide d'un algorithme de rétropropagation de gradients (Lecun, 1985; Rumelhart et al., 1986), dont le plus utilisé aujourd'hui est appelée *stochastic gradient descent* (SDG). L'équation d'ajustement des poids est propagée successivement de couches en couches, depuis la sortie du réseau jusqu'à son entrée.

c) *L'apprentissage profond*

Historique

Qualifié récemment de *Deep learning*, nous avons vu que la recherche sur les réseaux de neurones profonds date des années 1950 et a en réalité une longue et riche histoire (Goodfellow et al., 2016). D'après Lecun, les réseaux multicouches ne convainquent et n'intéressent qu'une poignée de chercheurs dans le monde pendant de nombreuses années (LeCun et al., 2015). Il faut attendre 2006 pour que le renouveau de l'intérêt du DL ne soit catalysé par le regroupement d'une poignée de chercheurs par un institut canadien. De nombreuses applications suivent rapidement, de la reconnaissance vocale aux véhicules autonomes. Depuis, le DL permet de répondre à des applications de plus en plus complexes, avec une précision de plus en plus importante.
Pour comprendre les causes de ce succès soudain, on prendra comme exemple la compétition ImageNet de 2012, considérée comme le tournant qui popularisera définitivement le DL dans le grand public. ImageNet est une compétition de classification d'images ayant lieu tous les ans depuis 2010, qui met à disposition une base de données d'environ 1,2 million d'images labélisées dans 1000 classes différentes et qui confronte des équipes de recherche du monde entier. Lors de l'édition de 2012, une

équipe réussit à la surprise générale à réduire de moitié le taux d'erreurs de classification des images (Figure 24). Cette équipe, la seule à utiliser une architecture de DL, développe un réseau (*AlexNet*) à neuf couches composé de 650 000 neurones et de 60 millions de paramètres (Krizhevsky et al., 2012a). Dans les deux éditions suivantes de ce challenge, toutes les équipes utilisent des approches par DL, et le taux d'erreur des algorithmes est aujourd'hui inférieur à 5 %, équivalent à celui d'un observateur humain (Dodge and Karam, 2017).

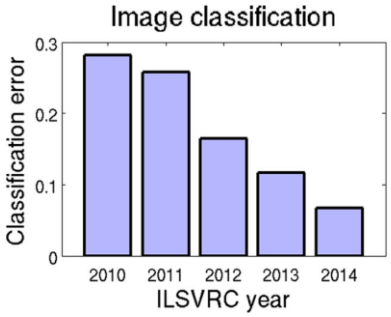

Figure 24. Performances par années du vainqueur de la compétition ImageNet (Russakovsky et al., 2015).

Le succès du réseau développé par Krizhevsky et al. repose sur son architecture, sur la puissance des calculs sur carte graphique GPU et sur la mise à disposition d'un grand nombre de données d'entrainement. C'est la conjonction de ces trois facteurs qui leur a permis d'obtenir des résultats spectaculaires, et qui place aujourd'hui le DL en tête des approches en IA. Le calcul sur GPU permet en effet de gérer dans un temps acceptable (quelques heures) la mémoire nécessaire aux processus d'apprentissage et d'ajustement des milliards de pondérations des réseaux contemporains. Pour que les capacités de généralisation d'un réseau DL soient performantes, il est impératif que le nombre de données d'entrainement soit suffisamment important pour qu'elles soient représentatives de la réalité. C'est ce qui est le cas aujourd'hui pour la reconnaissance d'image avec les banques d'images labellisées disponibles grâce à internet. Notons que ces bases de données correctement labellisées sont potentiellement plus difficiles à obtenir dans le domaine médical, ce qui peut y représenter un frein au déploiement des méthodes de DL. Le dernier facteur ayant permis l'émergence du DL est l'amélioration de l'architecture des réseaux, qui ont bénéficié récemment de nombreux développements, tant dans leur structure que dans les outils mathématiques et statistiques utilisés pour l'apprentissage et le traitement des données.

Les différentes architectures de réseaux

Il existe de nombreuses architectures de réseau profond, utilisées en fonction d'applications ou de données d'apprentissage spécifiques. Plusieurs classifications sont possibles, qui sont détaillées dans les références suivantes : Litjens et al., 2017; Ravì et al., 2017; Shickel et al., 2017; Zhou et al., 2017. Ravi et al donnent notamment une classification des différentes architectures en fonction d'applications particulières dans le domaine de la santé. Nous décrivons brièvement ici les architectures les plus fréquemment utilisées (Figure 25).

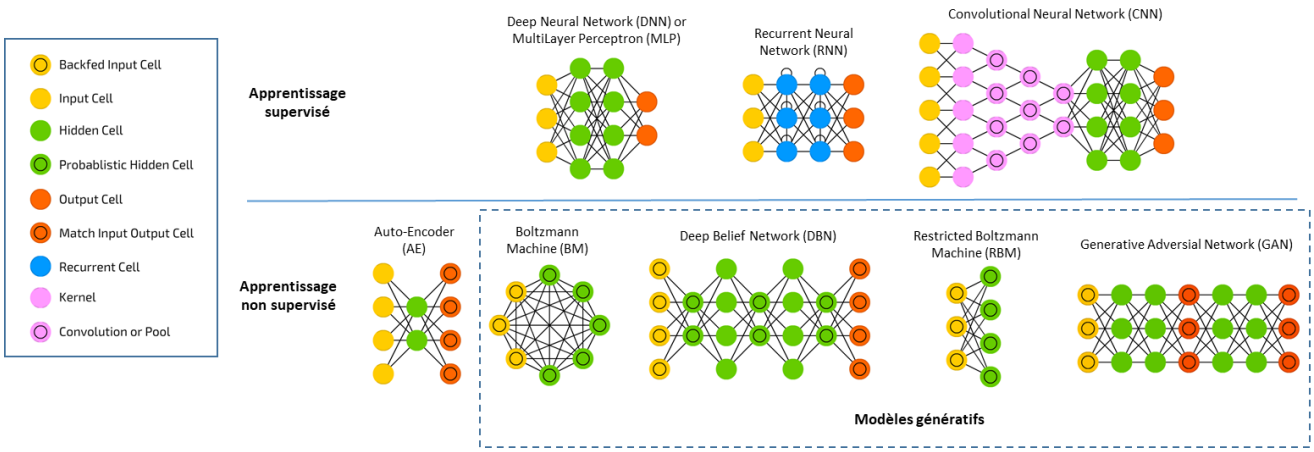

Figure 25. Représentation schématique des architectures de réseau les plus courantes en *deep learning*. Illustrations tirées de (Veen, 2016) et classification inspirée de (Shickel et al., 2017).

- Un DNN, parfois aussi appelé perceptron multicouche (*Multilayer Perceptron* – MLP), est composé de plusieurs couches cachées dans lequel tous les neurones d'une couche *i* sont connectés à tous les neurones de la couche *i+1*. Cette architecture simple a l'inconvénient de présenter un processus d'apprentissage potentiellement lent.
- Un réseau de neurones récurent (*Recurrent Neural Network* - RNN) est adapté au traitement d'informations ayant une dépendance temporelle. C'est le type de réseau utilisé pour le traitement de la parole ou encore de la vidéo. Contrairement à d'autres types de réseaux profonds, l'idée est ici de garder en mémoire les informations traitées précédemment, pour aider le réseau à prédire les données suivantes. La sortie y_t du réseau est donc fonction non seulement de l'entrée x_t à un temps t mais aussi des entrées x_{t-i} aux temps t-i. On compte parmi les RNN les modèles dits de *Long Short-Term Memory* (LSTM) et de G*ated Recurrent Unit* (GRU).
- Un auto-encodeur (*Auto-Encoder* - AE) est un réseau à une couche cachée de dimension inférieure à celle d'entrée. Cette couche cachée sert de couche d'encodage, dans le but d'identifier une structure dominante latente de dimension réduite par rapport au signal d'entrée. Les neurones de la couche d'entrée sont tous connectés à ceux de la couche cachée, qui sont tous connectés à la couche de sortie. Lorsque la couche d'encodage sert d'entrée à une autre AE, on parle d'empilement d'AE (*Stacked Auto-Encoder*, SAE), ce qui permet de générer plusieurs niveaux d'abstraction. Plusieurs variantes ont été proposées : *Stacked Denoising* (SDAE), *Sparse* (SAE) et *Variational* (VAE). Un des avantages de cette méthode est d'être utilisable dans le cadre d'apprentissages non supervisés, ne nécessitant pas de donnés labellisées.
- La machine de Boltzmann (*Boltzmann Machine* - BM) est une autre architecture d'apprentissage non supervisé. L'objectif est le même que dans un AE (extraire des représentations), mais basé sur un modèle statistique différent. Les connections entre les neurones sont bidirectionnelles, une BM étant donc assimilable à un modèle dit génératif, c'est-à-dire qui peut générer de nouvelles données d'entrée pendant l'apprentissage. Dans une BM standard, tous les neurones sont connectés entre eux, tandis que seuls les neurones de couches distinctes le sont dans une machine de Boltzmann restreinte (*Restricted Boltzmann Machine* - RBM).
- Les *Deep Belief Network* (DBN) sont essentiellement des SAEs dans lesquelles les couches d'encodage sont remplacées par des RBMs. Seules les deux couches les plus profondes possèdent des

connections bidirectionnelles. L'entrainement est réalisé de façon non supervisé, sauf pour l'ajustement final des paramètres du réseau réalisé de manière supervisée via l'ajout d'une couche de classification en sortie de réseau. La machine de Boltzmann profonde (*Deep Boltzmann Machine* - DBM) est l'équivalent du DBN, mais avec des connections bidirectionnelles entre les neurones de chaque couche.

- L'architecture d'un *Generative Adversial Networks* (GAN) repose sur deux modèles : un modèle génératif G qui produit des données synthétiques et un modèle discriminant D qui estime la probabilité que ces données fassent partie des données d'entrainement. L'objectif du processus est de rendre capable le modèle G de tromper D.
- Le réseau de neurones convolutionnels (*Convolutional Neural Network* - CNN) est l'architecture de DL utilisée par Krizhevsky et al. en 2012 (cf précédemment). C'est l'architecture utilisée majoritairement aujourd'hui dans le traitement d'image. C'est aussi celle que nous avons utilisée dans notre travail portant sur la détection automatique des métastases cérébrales sur Imagerie par Résonnance Magnétique (IRM) présenté dans le paragraphe I.B.3.

d) <u>Les réseaux de neurones convolutionnels</u>

Description

Le réseau de neurone convolutionnel (CNN) est l'approche par DL la plus utilisée aujourd'hui en traitement d'image. Un CNN est composé de plusieurs couches successives de traitement de données, qui ont pour but de trouver à chaque étape des motifs caractéristiques de l'image d'entrée, d'abord simples, puis de plus élaborés au fur et à mesure que les couches se succèdent (voir Figure 26).

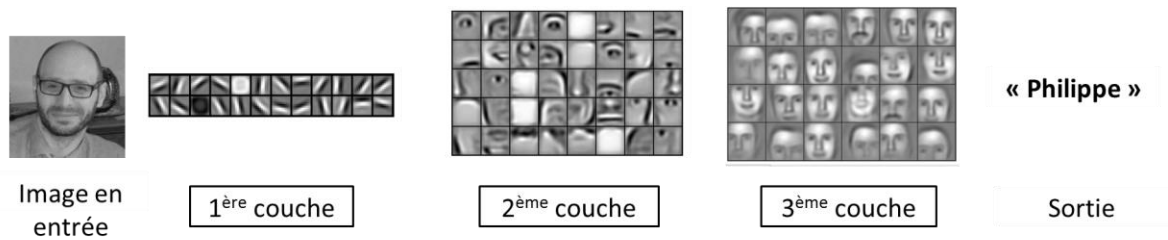

Figure 26. Illustration schématique du rôle de chaque couche d'un CNN utilisé pour la reconnaissance de visage (Lee et al., 2009). Les couches supérieures représentent des géométries simples (bords, lignes). Lorsque les couches sont plus profondes, ces formes simples s'assemblent pour constituer des formes plus complexes.

Pour comprendre le fonctionnement de cette architecture, prenons l'exemple de la Figure 27 dans lequel l'image à analyser est composée de 6*6 pixels pouvant prendre individuellement des valeurs de niveaux de gris différentes (pour simplifier, des valeurs -1, 0 et 1). Les coordonnées des pixels de l'image peuvent s'écrire sous la forme (x,y), avec x le numéro de la ligne et y le numéro de la colonne. Prenons ensuite un *filtre*, constitué ici de 3*3 pixels dont les valeurs sont fixées de manière arbitraire (pour le moment). Plaquons ce filtre dans le coin supérieur gauche de l'image à analyser, en le centrant sur le pixel (2,2). Multiplions la valeur de chaque pixel (x,y) de l'image par chaque pixel (x,y) correspondant du filtre et sommons les valeurs obtenues. On obtient une valeur que l'on divise par le nombre de pixels de l'opération (dans notre cas 9), et que l'on attribue au pixel (2,2) d'une nouvelle

image. Glissons ensuite ce filtre d'une colonne vers la droite, de manière à le centrer sur le pixel (2,3) de l'image à analyser, et effectuons la même opération, qui permet d'attribuer une valeur au pixel (2,3) de la nouvelle image. Notons que l'opération de glissement de la fenêtre d'une colonne vers la droite est souvent désignée par *stride = 1*. En balayant ainsi toute l'image, il est possible de recréer intégralement une nouvelle image (sauf les bords): cette opération est qualifiée de *convolution*, d'où les CNN tirent leur nom. Le rôle de cette transformation est de détecter des caractéristiques locales dans différentes parties d'une image, en préservant l'information spatiale de l'entrée. On appelle *feature map* FM (carte de caractéristique) l'image créée après l'opération de convolution.

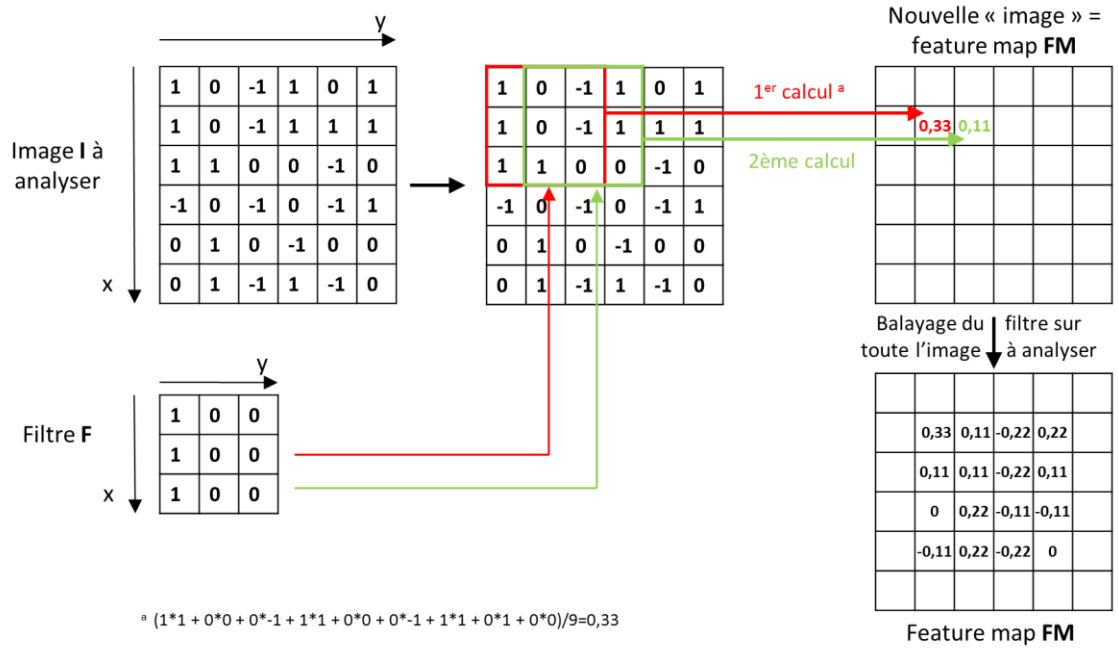

Figure 27. Opération de convolution appliquée à une image.

Si l'on transpose cette opération dans la représentation schématique des réseaux de neurones, les valeurs des pixels peuvent être vues comme les signaux d'entrée, et les valeurs du filtre comme les poids synaptiques (voir Figure 28). Notons que le filtre F est souvent désigné par le terme *kernel*. Dans l'exemple précédent, les valeurs des filtres (donc des pondérations) sont fixées de manière arbitraire. En réalité, le réseau ajuste de manière itérative ces valeurs pendant la phase d'entrainement, de manière à ce que les différentes couches puissent extraire efficacement des représentations caractéristiques de l'image d'entrée.

L'opération de convolution de l'image par le *kernel* F qui produit la *feature map* FM constitue une couche du réseau de neurone. Les multiples couches cachées d'un CNN représentent donc des opérations successives de convolution : les données d'entrée sont les pixels de l'image à analyser pour la première couche, et ceux des FM pour les couches suivantes. Chaque couche inclut en réalité plusieurs filtres : dans l'exemple donné sur la Figure 29, la première couche est constituée de trois filtres différents de taille 3*3, la FM résultante étant composée de 3 images. La couche suivante est constituée de quatre filtres de taille 3*3 et de profondeur 3 qui, convolués avec la FM de la couche 1, produit une FM de profondeur 4.

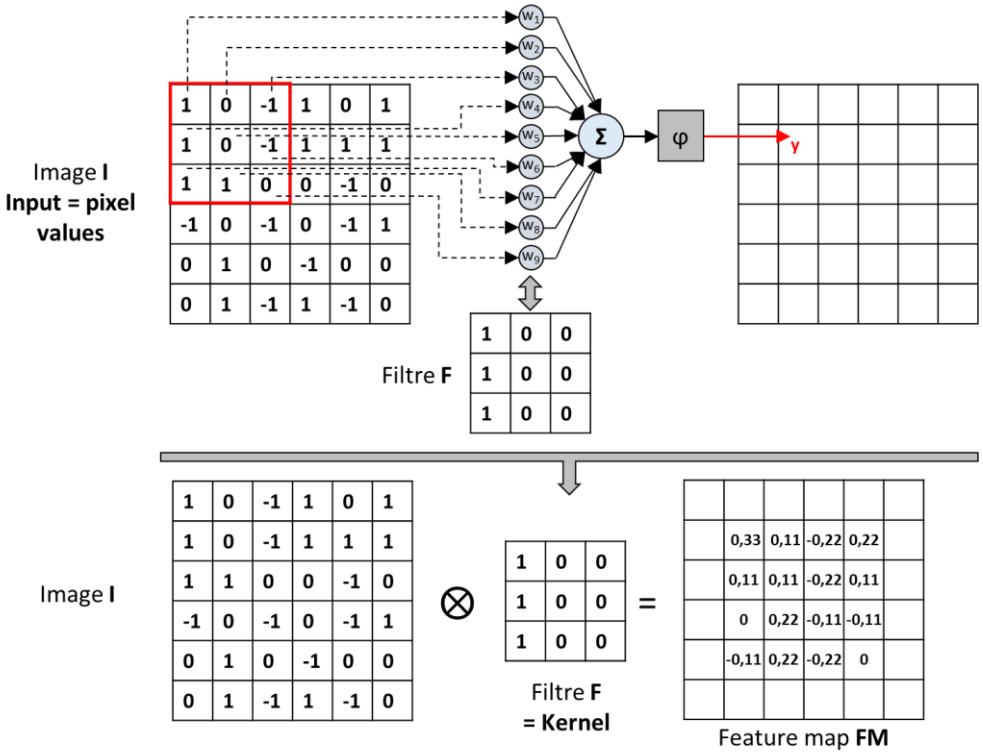

Figure 28. Représentation schématique d'une opération de convolution par un réseau de neurones.

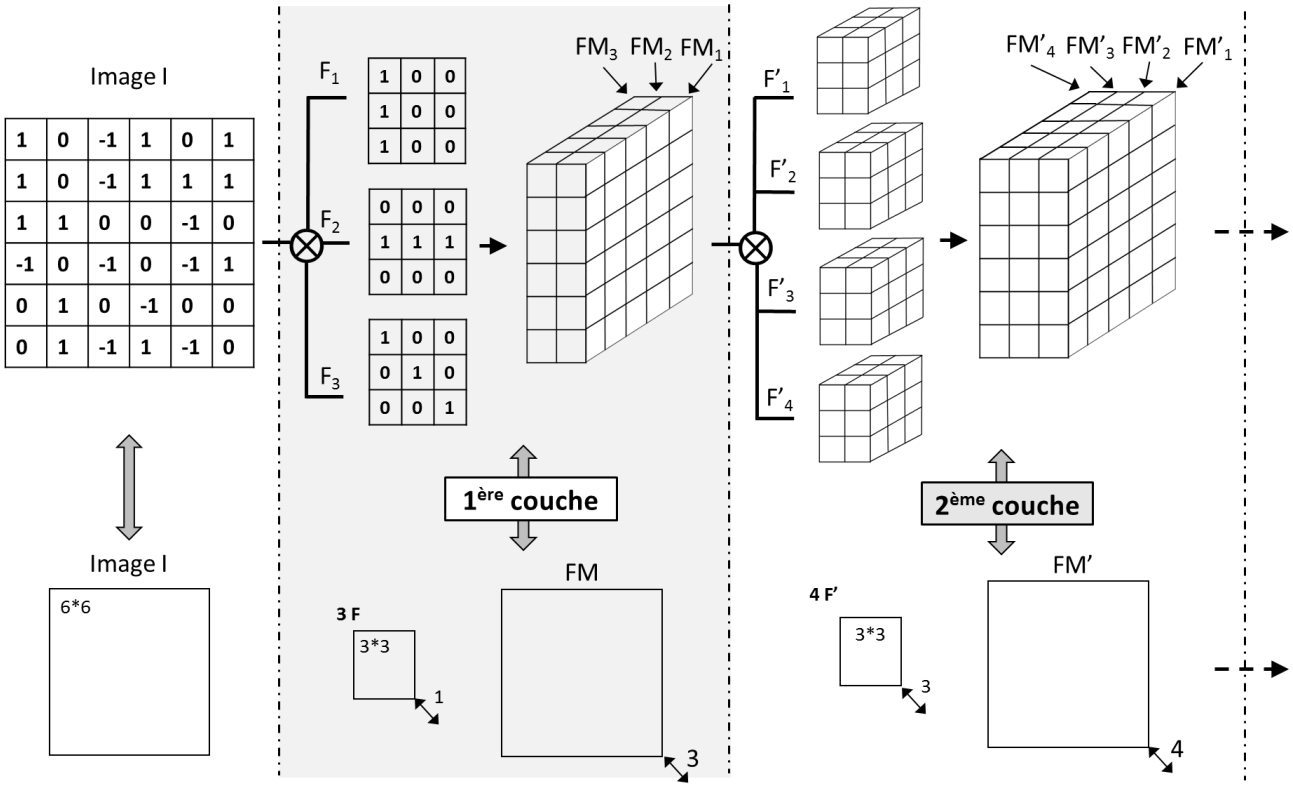

Figure 29. Illustration des opérations de convolution des deux premières couches cachées d'un CNN. La partie inférieure de l'image est une vue synthétique de la partie supérieure.

Pooling

Dans les réseaux CNN contemporains, chaque couche est composée de plusieurs dizaines de filtres, le nombre et la dimension des filtres pouvant varier entre les couches. Une image étant composée de plusieurs dizaines de milliers de pixels, le nombre d'opérations requises pour un réseau à plusieurs couches cachées devient rapidement important. Pour diminuer ce nombre et la charge de calcul, il est commun d'intercaler une couche dite de *pooling* entre deux couches de convolution. Le rôle de cette couche est de réduire la dimension des FM produites par la couche de convolution précédente. La technique classique dite de max pooling consiste à ne garder que la valeur du pixel la plus importante dans une certaine zone, de manière à conserver la caractéristique de l'image. La Figure 30 illustre une opération de max pooling effectué sur la FM de notre exemple précédent. Avec un filtre de dimension 2*2 (à ne pas confondre avec les filtres des opérations de convolution), cette opération consiste ici à ne garder que le pixel dont la valeur est maximale dans une zone définie par une matrice de dimension 2x2. Cette matrice est déplacée ici de deux pixels (*stride* = 2), et balaye toute la zone de l'image. La FM passe donc dans cet exemple de seize à quatre pixels.

Figure 30. Exemple d'un filtre de max *pooling* de dimension = 2*2 et de stride = 2.

Nous nous sommes jusqu'ici attachés à décrire le fonctionnement de CNN appliqués à des images 2D. Les images médicales étant souvent volumiques, des CNN 3D ont été développés, qui calculent des FM 3D à partir de *kernels* 3D. Pour réduire le degré de complexité et le temps de calcul de ces modèles, des CNN 2,5D (ou *tri-planar*) ont été développés, dans lesquels le volume 3D est décomposé en vues axiales, sagittales et coronales.

Exemple de CNN : AlexNET

Nous avons vu que la structure de base d'un réseau CNN est constituée d'une alternance de couches de convolution et de *pooling*. Nous ne l'avons pas mentionné jusqu'ici, mais une opération de non-linéarité de type ReLU est implicite après chaque couche (voir chapitre B.1.b).
Autour de ce schéma de base, de nombreuses variantes ont été proposées en fonction du type d'application souhaité. Le réseau AlexNet dont il a été question précédemment est représenté sur la Figure 31 (Krizhevsky et al., 2012b). Sa fonction est la classification d'image : à partir d'une image 2D en entrée, il attribue en sortie une probabilité à chacune des mille classes proposées dans la compétition. Il est composé de cinq couches de convolution, de trois couches de *pooling* et de trois couches entièrement connectées en sortie (*fully connected*). La première couche est composée de 96 filtres de dimension 11*11*1, appliqués à l'image d'entrée avec un *stride* = 4. La première FM résultante, de dimension de 55*55*96, est prise comme entrée de la deuxième couche et convoluée avec 256 filtres de taille 5*5*96. Après une opération de *max-pooling* (3*3, *stride* =2), les dimensions de la deuxième FM sont de 27*27*256. Ces opérations se répètent jusqu'à la dernière couche de

convolution, qui génère une FM de dimension 13*13*256. Après une dernière opération de *pooling* qui réduit les dimensions de la FM à 6*6*256 (non représentée sur la figure), trois couches entièrement connectées se succèdent. Contrairement aux couches de convolution qui visent à détecter des motifs en scrutant successivement différentes parties de l'image, les couches entièrement connectées prennent simultanément comme donnée d'entrée tous les pixels de la FM. La première couche entièrement connectée est composée de 9216 neurones, et génère un vecteur de dimension 4096*1*1. En sortie, une fonction mathématique appelée *softmax* transforme ce vecteur de 4096 valeurs en un vecteur de probabilité de dimension 1000*1*1 qui attribue une probabilité à chacune des 1000 classes utilisées.

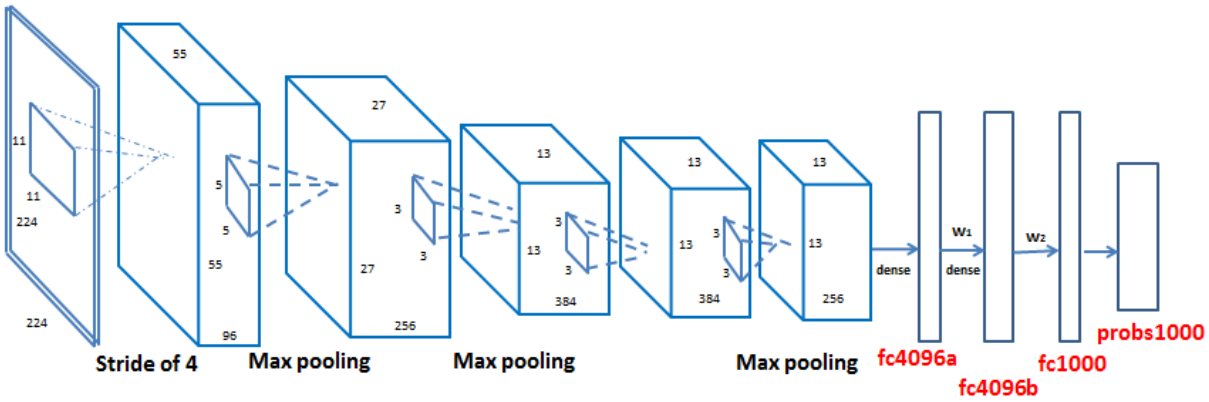

Figure 31. Représentation du réseau AlexNet (tiré de Wang et al., 2015).

Différentes variantes de CNN

Outre AlexNET, les CNNs ont fait l'objet de différentes variantes, en fonction d'applications spécifiques. Entre autre réseaux sortant du lot, VGG (Visual Geometry Group) est caractérisé par une structure très simple (uniquement des filtres de convolution de taille 3*3 et de pooling de taille 2*2) et par une profondeur importante (au moins 16 couches) (Simonyan and Zisserman, 2014). Il a été développé pour la classification d'images, et joue sur la notion qu'un DNN est plus performant lorsqu'il est plus profond. Si l'on supprime les dernières couches entièrement connectées d'un CNN, on obtient un *Fully Convolutional Network* (FCN), habituellement dédié à des tâches de segmentation. L'idée est de garder l'information spatiale, en l'augmentant dans une dernière couche de dimension suffisamment importante. Cependant, après les nombreuses couches de *pooling*, la résolution finale est potentiellement faible. Pour contourner ce problème, le réseau U-net, qui a également été développé pour des tâches de segmentation, propose une architecture consistant à joindre à la première partie classique de convolution une deuxième partie symétrique dans laquelle les couches de pooling sont remplacées par des couches d'interpolation (Ronneberger et al., 2015). La résolution de l'image de sortie est ainsi améliorée. Autre application, les réseaux *deconvnet* tels que ZF-NET ont pour objet la visualisation des FM. Cela permet de mieux appréhender le fonctionnement du réseau à chaque couche (Zeiler and Fergus, 2014). Dernier exemple, DeepMedic a été développé pour la segmentation de structures cérébrales (Kamnitsas et al., 2017). Il s'agit d'un réseau 3D multi-échelle, qui permet d'utiliser des images IRM 3D et qui comporte deux chemins convolutifs, l'un qui utilise des informations très localisées, et l'autre le contexte. Il est utilisable librement, et est généralisable à

d'autres applications que celles pour laquelle il a été conçu. C'est pour ces deux raisons que nous avons adapté ce réseau à la détection de métastases cérébrales sur IRM, travail présenté dans la partie I.B.0.

2. Les applications de l'apprentissage profond en radiothérapie

Les technologies employées en radiothérapie sont de plus en plus complexes, et l'aide de l'intelligence artificielle y devient incontournable. Les méthodes basées sur le *deep learning* commencent à faire leur apparition dans toutes les étapes de la chaine du processus de radiothérapie, de la consultation initiale au suivi post-traitement du patient. Nous avons fait une revue de ces méthodes publiée dans l'article suivant (Meyer et al., 2018).

Computers in Biology and Medicine 98 (2018) 126–146

Contents lists available at ScienceDirect

Computers in Biology and Medicine

journal homepage: www.elsevier.com/locate/compbiomed

Survey on deep learning for radiotherapy

Philippe Meyer [a,*], Vincent Noblet [b], Christophe Mazzara [a], Alex Lallement [b]

[a] Department of Medical Physics, Paul Strauss Center, Strasbourg, France
[b] ICube-UMR 7357, Strasbourg, France

ARTICLE INFO

Keywords:
Radiotherapy
Deep-learning
Convolutional networks

ABSTRACT

More than 50% of cancer patients are treated with radiotherapy, either exclusively or in combination with other methods. The planning and delivery of radiotherapy treatment is a complex process, but can now be greatly facilitated by artificial intelligence technology. Deep learning is the fastest-growing field in artificial intelligence and has been successfully used in recent years in many domains, including medicine.

In this article, we first explain the concept of deep learning, addressing it in the broader context of machine learning. The most common network architectures are presented, with a more specific focus on convolutional neural networks. We then present a review of the published works on deep learning methods that can be applied to radiotherapy, which are classified into seven categories related to the patient workflow, and can provide some insights of potential future applications. We have attempted to make this paper accessible to both radiotherapy and deep learning communities, and hope that it will inspire new collaborations between these two communities to develop dedicated radiotherapy applications.

1. Introduction

Patient workflow in radiotherapy is one of the most complex workflows. There are many steps involved: choice of the radiotherapy treatment scheme; image acquisition of the patient in treatment position; segmentation of the target volumes and organs-at-risk (OAR) using multimodal imaging; treatment planning; delivery of treatment including monitoring of patient positioning, movements, and delivered dose; and finally, post-treatment follow-up.

To facilitate and improve the efficiency of this workflow, artificial intelligence (AI) systems have been proposed for automatic organ segmentation, error prevention, or treatment planning [1,2]. However, these systems are still seldom used in clinical routines. For instance, manual delineation of target volumes and OAR is still the standard routine for most clinical centers, even though it is time consuming and prone to intra- and inter-observer variations [3]. One issue is the limited performance of current commercial software. In radiotherapy, toxic and fatal doses are sometimes delivered at 1 or 2 mm from risk organs; therefore, it is vital that segmentation is extremely accurate (see Fig. 1). However, current automatic segmentation software cannot achieve the necessary level of accuracy. Consequently, radiation oncologists may lose more time correcting automatically segmented structures than by manually segmenting the structures themselves.

Deep learning (DL) is a branch of AI and machine learning, which has enjoyed considerable success in recent years in diverse fields including science, business, and government. DL has dramatically supplanted other machine learning methods for applications such as recognition and image processing in computer vision, by achieving human-equivalent performance on some tasks [4–6]. DL techniques also open promising perspectives in AI applied to radiotherapy and may significantly improve the radiotherapy patient workflow in the coming years [7,8]. To illustrate the rapidly evolving interest aroused by these new techniques in radiotherapy, Fig. 2 shows the number of DL papers published in this field since 2012.

Several reviews about DL in medical imaging have already been published [5,9–11], but none were specifically dedicated to radiotherapy. In this paper, we first explain the basic concepts of machine learning, in Section 2, adapted to radiation oncologists and medical physicists. We then present a simple introduction to DL and to the different network architectures, with a focus on convolutional neural networks (CNNs). In Section 3, we present a brief review of research works in which DL methods are or could potentially be applied to a step of the radiotherapy workflow, trying to make it accessible to non-radiotherapy specialists. We have chosen to classify the reviewed papers into seven categories relevant to the different radiotherapy steps. These categories are as follows: *images used for radiotherapy planning and*

* Corresponding author. 3 rue de la porte de l'hôpital, 67000 Strasbourg, France.
E-mail address: pmeyer@strasbourg.unicancer.fr (P. Meyer).

https://doi.org/10.1016/j.compbiomed.2018.05.018
Received 3 March 2018; Received in revised form 15 May 2018; Accepted 15 May 2018

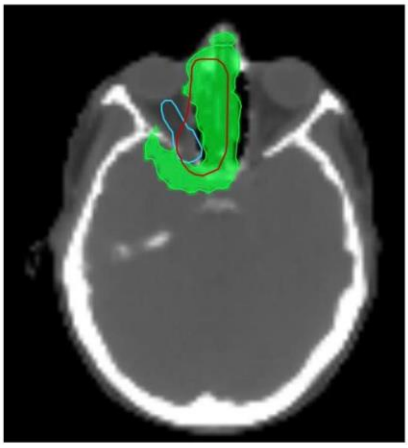

Fig. 1. Planned dose distribution for nasopharyngeal cancer treatment. The 54-Gy isodose (in green) should cover the target volume (in red) and must not cover the optic nerve (in blue), because the risk of blindness becomes too high when doses exceeding 54 Gy are used. This case illustrates the extreme accuracy required for the segmentation of organs in radiotherapy. (For interpretation of the references to colour in this figure legend, the reader is referred to the Web version of this article.)

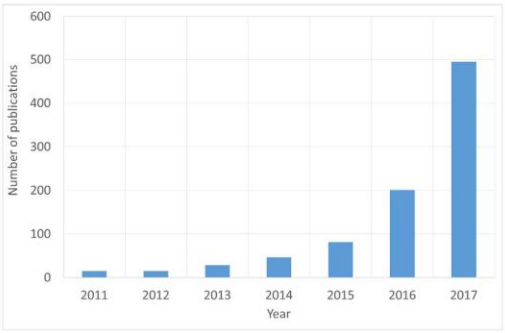

Fig. 2. Number of publications for the search phrases with at least the terms *radiotherapy* or *radiation therapy* or *radiation oncology* and at least the terms *deep learning* or *deep network* or *convolutional network*. Publication statistics are obtained from Google Scholar.

treatment setup, *image segmentation, computer-aided detection and diagnosis, image registration, treatment planning, motion management/patient setup during treatment*, and *medical data extraction and outcome prediction in radiotherapy*. Note that a survey mainly dedicated to DL-based medical image segmentation and computer-aided detection tasks has recently been proposed by Litjens et al. who reviewed 306 papers [5]. Other reviews also exist for medical data extraction by DL [12–14]. Therefore, we have not conducted exhaustive reviews for these specific categories but we have selected articles of particular importance in radiotherapy.

2. What is deep learning?

DL describes a set of computational models composed of multiple layers of data processing, which make it possible to learn by representing these data through several levels of abstraction [4,15–17]. From a large amount of training data, these models discover recurrent structures by automatically refining their internal parameters via a backpropagation algorithm. Each layer of the network transforms the signal nonlinearly in order to increase the selectivity and invariance of the representation. With a sufficient number of layers, the network can generate a hierarchy of representations that will make the model both sensitive to very small details and insensitive to large variations. In recent years, DL has been successfully used to solve real problems in a wide range of applications. However, because the underlying tuned model is composed of millions of parameters, there is still no clear understanding of the inner working mechanisms. Thus, many time-consuming trial-and-errors procedures are required to correctly train the model.

DL approaches are part of the so-called *machine learning*, which is a field of AI. CNN is a special approach to DL, dedicated to image processing (Fig. 3). Machine learning, DL, and CNN are explained respectively in Sections 2.1, 2.2, and 2.3.

2.1. Machine learning

The term AI was introduced in 1956 by one of the pioneers of the field, John McCarthy [18,19]. Boden defined AI as a science, whose purpose is to make machines perform tasks that would require human intelligence [20]. If we consider contemporary AI, several authors cited the article *Computing machinery and intelligence* published in 1950 as one of the founding works [21]. Six years later, Newell and Simon proposed the *logic theorist algorithm*, often considered as the first computer program in the field of AI, which opened the way to the many AI methods we currently know [22]. Among these methods, machine learning was proposed for the first time in 1959 by Samuel, who developed an AI program that can play checkers based on partial setting using the experience gained [23].

Considering that designing and programming explicit models for complex tasks with satisfactory performance is sometimes difficult or infeasible, machine learning attempts to make data-driven decisions by automatically building a model from large-scale training data [24,25]. The key concept of machine learning is thus to produce accurate predictions on new unseen data after being trained on a finite learning dataset, in other words, to generalize from limited experience.

To concretely define what *learning* means, Mitchell et al. proposed to specify three parameters, namely T, P, and E [26]: "a computer program is said to learn from experience E with respect to some class of tasks T and performance measure P if its performance on tasks in T, as measured by P, improves with experience E." Table 1 provides radiotherapy application examples to illustrate this proposal.

Examples of machine learning scenarios include supervised, unsupervised, reinforcement, and transfer learning [27]. In supervised

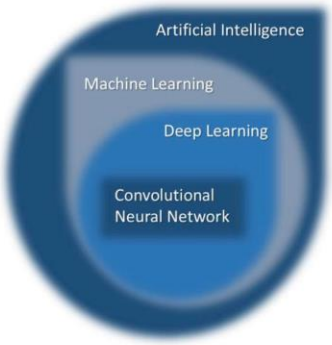

Fig. 3. A possible classification of some artificial intelligence methods.

Table 1
Some examples related to machine learning problems. The first 3 lines are taken from Refs. [26] and [25]. The other examples (in gray) are taken from published applications of machine learning in radiotherapy, which can be found in Section 3.

Example learning problem	Task T	Performance measure P	Training experience E
Learning checkers	Playing checkers	Percentage of games won against opponents	Learner playing practice games against itself
Handwriting recognition	Recognizing handwritten words	Percentage of words correctly recognized	Handwritten words with given classification
Self-driving car	Driving from Hochfelden to Saint-Claude	Distance traveled before an error (as judged by a human overseer)	Videos, images, and steering commands recorded while observing a human driver
Automatic segmentation of medical images	Segment the prostate on MRI	Percentage of common pixels between automatic and human expert segmentation	MRI database with prostate segmented by human experts
Computer-aided detection on medical images	To detect brain metastases (BM) on MRI	Percentage of false negative or false positive (FP)	MRI database with BM segmented by human experts
Dose calculation on MRI	To generate a pseudo-computed tomography (CT) image from an MRI	Average mean difference of Hounsfield units between the pseudo-CT and a reference CT image	Database with registered MRI and CT images
Image-guided radiotherapy dose reduction	To reduce noise in fluoroscopic kV images	Signal to noise ratio difference between a corrected kV image and the mean of 10 kV images	Database of fluoroscopic kV patient images during radiotherapy treatment
Automatic treatment planning help	To predict planned dose from organ segmentation	Percentage of common pixels between predicted and calculated dose	Database of RT structures and RT dose files
Avoidance of patient collision during radiotherapy treatment	To recognize and classify objects and patient inside the treatment room	Percentage of correctly classified objects	Database of classified objects
Decision-making tool for radiation oncologists	To predict rectal toxicity after cervical cancer radiotherapy	Difference between real and predicted toxicities	Database of radiotherapy treatment plans including RT structures and dose files + medical database with rectal toxicity evaluation

learning, the algorithm is presented with training inputs and their corresponding desired outputs (i.e., labels); the goal is to learn a rule that maps inputs to outputs. For example, a set of quantitative features extracted from a mammography image can be considered as input and the corresponding expert diagnosis (cancerous versus healthy) as the desired output. The goal is then to automatically categorize new mammograms that have not been evaluated by an expert (i.e., classification) [28]. In unsupervised learning, no referenced outputs are given to the algorithm and the goal is to find a structure in the inputs. As examples, one can imagine distinguishing patients at risk from other patients based on clinical notes extracted from electronic health record (EHR) systems (i.e., clustering) [29], or to learn high-level features from images (i.e., dimensionality reduction) [30]. In reinforcement learning, the algorithm must perform a certain goal through interaction with its dynamic environment. A feedback is used to adjust the learning process in a way to maximize long-term rather than immediate reward trade-offs. Reinforcement learning is thus based on communication and exploration rather than on explicit education. This type of approach can be used, for example, to study different scenarios of tumor growth and radiotherapy [31]. For many medical applications, only a small amount of training data is often available, mostly due to confidentiality reasons or incomplete information. Because the available input data are insufficient to train a network from scratch, transfer learning aims to use a pre-trained network to perform another task that it was not originally intended for. An additional training step is then performed using a small amount of labeled data to fine-tune the network weights [32].

2.2. Deep neural networks

Deep neural networks (DNNs) are forms of machine learning methods. In machine learning, it is often necessary to reduce the complexity of the input data and make relevant patterns more visible for the learning algorithms to function. Indeed, their performance greatly depends on how accurately these features have been identified and extracted. Given that this feature engineering process is based on domain knowledge and is specific to the data type, it is difficult and expensive in terms of time and expertise to apply. In contrast, DNNs independently learn a hierarchical representation of the input data adapted to the task at hand; this eliminates the task of developing new features extractors for every problem. The main drawback is that DNNs require a large amount of input data to be effective. The idea of a computer program that could find itself representing a model from a dataset is not new. Perceptron is one of the first approaches to conceptualize data directly from the environment [33]. It is inspired by the biology of the brain: an artificial neuron is a mathematical function conceived as a coarse model of a biological neuron (Fig. 4). The principle is to simulate the transfer of information through a neuron: weighted nodes receive the inputs (representing the synapses), sum them to produce an activation (representing the axon), and pass this activation to a nonlinear function called activation or transfer function, in order to generate the output signal. Each neuron acts as an elementary processing unit. The output signal of one

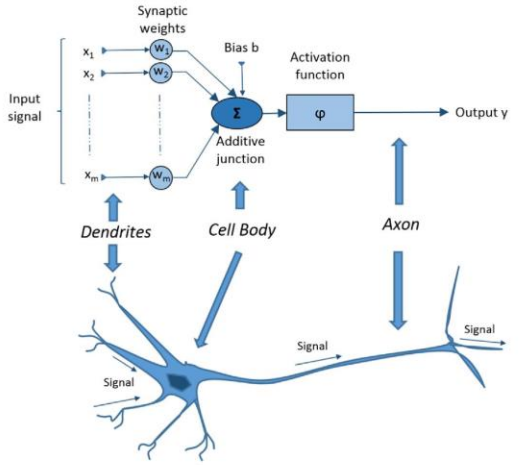

Fig. 4. Analogy between an artificial neuron and a biological neuron. The input signals are represented by x. The bias b and the activation function φ can be parameterized by the user. Weights w are adjusted automatically by the network.

unit will feed the other units, organized in layers, and so on, forming an artificial neural network (ANN). When it is composed of several intermediate hidden layers, it is called *multilayer neural networks* or DNNs (Fig. 5). Note that the multilayer perceptron (MLPs) is an intermediate link in the transition from the simple perceptron to the DNN. DNNs are a recent advance in the field that conceptually expands the MLP by adding a significant number of layers (instead of 1–3 that the typical MLP has).

Actually, DL uses a cascade of multiple layers of nonlinear processing units for feature extraction and transformation, with each successive layer using the output from the previous layer as input. The first layer is the input layer that receives the dataset. The last layer is the output layer that delivers the result. In between, layers transforming the signal are called hidden layers. The underlying assumption is that these successive hidden layers correspond to levels of abstraction. Varying the number, size, and composition of each layer can thus provide different amounts of abstraction, and allows high-level features to be derived from low-level features in order to form a hierarchical representation. The challenge is to find the appropriate level of granularity, given the size and dimension of the available training dataset and the complexity of the task. Note that high-level feature extraction (abstraction), which indeed takes place, creates features that are very difficult for humans to interpret meaningfully and match to metrics of observable procedures.

2.2.1. The training process

It is important to keep in mind that a neural network must be trained in a dedicated phase. Training a neural network consists of learning each neuron's weights (***w*** in Fig. 4). In supervised learning, it can be formulated as an error function minimization between the network's output (the prediction) and the desired output (the labels). As this error function is highly nonlinear and non-convex, there is no analytical solution that can minimize it. The usual solution is to update the weights iteratively by means of a backpropagation gradient algorithm [34,35], the most commonly used being the *stochastic gradient descent*. At first, all the weights are randomly initialized. Then the output of the network is computed with respect to the training input. The gradient can be efficiently computed by propagating errors from the output layer back to the input layer by a chain rule. Once the gradient vector is computed for all layers, the weights can be updated. This update process repeats until convergence is reached or a predefined number of iterations have been performed.

The transfer function and the bias are fixed and user-definable. The transfer function is usually defined as monotonically increasing, continuous, differentiable, and bounded. The most popular transfer function is called rectified linear unit (ReLU), which allows fast learning of DNNs (Fig. 6).

2.2.2. Why deep learning now?

Recently qualified as DL, we saw that research on DNNs dates back to the 1950s and actually has a long and rich history [15]. Multilayered networks are not convincing and attracted only a few researchers

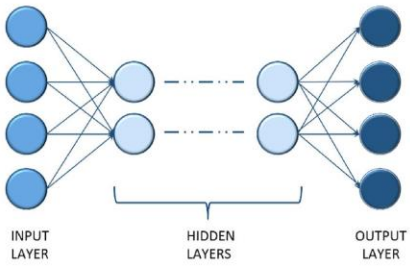

Fig. 5. Schematic illustration of a deep neural network. Neurons not contained in the input or output layer are contained in the hidden layers.

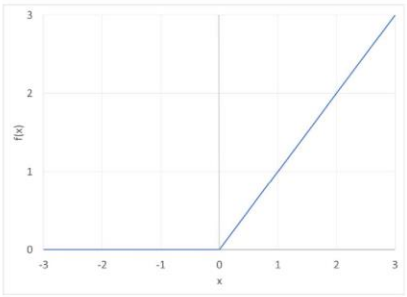

Fig. 6. Rectified linear unit transfer function (ReLU) commonly used in deep neural networks.

worldwide for many years [4]. The renewal of interest on DL was catalyzed in 2006 by the grouping of a few researchers by a Canadian institute. Since then, DL has been able to respond to increasingly complex applications, with ever-greater accuracy.

The reasons for this sudden success can be traced in the 2012 ImageNet competition, when a team (the only one to use a DL architecture) was able to halve the rate of misclassification [36]. The success of the network developed by Krizhevsky et al. is due to its architecture, the power of calculations on graphics processing unit (GPU), and the large amount of training data. The combination of these three factors currently places DL at the forefront of AI approaches. The GPU calculation makes it possible to manage the memory required for the learning and adjustment processes of billions of weights of contemporary networks in an acceptable time. To generalize correctly, it is imperative that the number of training data should be large enough to represent reality. Note that these properly labeled databases are potentially difficult to obtain in the medical field, which can be a hindrance to the deployment of DL methods. The last factor that led to the emergence of DL is the improvement in network architectures, which has recently benefited from numerous developments.

2.2.3. Network architectures commonly used in deep learning

Many DL network architectures have been developed depending on specific applications or learning data. Several classifications are possible, which are detailed in the following references dedicated to medical applications [5,13,14,37]. Ravi et al. specifically provided a classification of the different architectures according to particular applications in the medical field. Here, we briefly describe the architectures most frequently used in radiotherapy applications (Fig. 7).

- A DNN is composed of several hidden layers in which all neurons of a layer i are connected to all the neurons of the i+1 layer. This simple architecture has the disadvantage of presenting a potentially slow learning process.
- A recurrent neural network (RNN) is suitable for the processing of temporally dependent information [39]. This is the type of network used for speech processing or video. Different from other types of deep networks, the idea here is to keep in mind the information previously processed, to help the network predict the succeeding data. The output y_t of the network is therefore a function not only of the input x_t at a time t but also of the inputs x_{t-i} at times t-i. The RNNs include long short-term memory (LSTM) and gated recurrent unit models.
- An auto-encoder (AE) is composed of a hidden layer of smaller size than the input one [40]. This hidden layer serves as an encoding layer for identifying a latent dominant structure of reduced size with respect to the input signal. The neurons in the input layer are all connected to those in the hidden layer, all of which are connected to

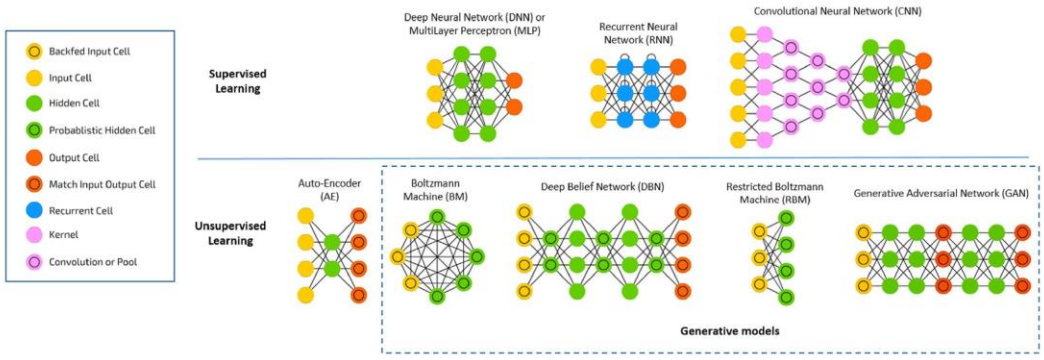

Fig. 7. Schematic representation of the most common network architectures in deep learning for radiotherapy applications (illustrations used with permission from Ref. [38] and classification inspired by Ref. [13]).

the output layer. When the encoding layer serves as input to another AE, it is called a stacked auto-encoder (SAE), which allows generating several levels of abstraction. Several variants have been proposed: stacked denoising (SDAE), sparse (SSAE), and variational (VAE). One of the advantages of this method is that it can be used in the context of unsupervised learning, which does not require labeled data.

- The Boltzmann machine (BM) is another unsupervised learning architecture. The objective is the same as in an AE (extract representations), but is based on a different statistical model. The connections between the neurons are bidirectional; therefore, a BM is comparable to a so-called generative model, which can generate new input data during learning. In a standard BM, all the neurons are connected to each other, whereas only the neurons of distinct layers are connected in a restricted Boltzmann machine (RBM) [41].
- Deep belief network (DBNs) are essentially SAEs in which the encoding layers are replaced by RBMs [42]. Only the two deepest layers have bidirectional connections. The training is performed in an unsupervised manner, except for the final adjustment of the network parameters performed in a supervised manner by adding a classification layer at the output of the network. The deep Boltzmann machine (DBM) is the equivalent of DBN, but with bidirectional connections between the neurons of each layer.
- The architecture of generative adversarial networks (GANs) is based on two models: a generative model G that produces synthetic data, and a discriminant model D that estimates the probability that these data are part of the training data [43]. The goal of the process is to enable the G model to fool D.
- CNN is the DL architecture used by Krizhevsky et al., in 2012 (see discussion above). This architecture is widely used currently in image processing, for example, in automatic segmentation or computer-aided diagnostic in medical images. This is why we detail it more precisely in the next section.

2.3. Convolutional neural networks

2.3.1. Description

In a fully connected neural network, each neuron's output of a given layer is connected to an input node of every neuron in the succeeding layer, and neurons of the same layer are completely independent of each other. This is a very general-purpose connection pattern, as it makes no assumptions about the features in the data. However, information contained in medical images is generally spatially structured. One can notice that neighboring pixels corresponding to the same anatomical structure share similar intensity characteristics, which means that a specifically parameterized patch of neurons might be able to detect each pixel corresponding to the same structure. Furthermore, because the location of the structure searched is variable from one patient to another (lesions such as metastases for example) and from one image to another (due to differences in acquisition conditions), their location in the corresponding images will differ. Hence, the previously mentioned patch of neuron should have some type of invariance in spatial location in order to behave in the same way on the entire image. CNNs are specifically designed to take advantage of this spatially structured information.

CNN procedures have several advantages over most standard medical computer vision systems comprising manually engineered static programs [44]. Standard image features representations include scale-invariant feature transform (SIFT), histogram of oriented gradients (HoG), textons, spin images, and so forth. Identifying the right set of attributes most relevant to the problem addressed is often difficult and time-consuming and requires expert knowledge. Furthermore, the interaction between the characteristics of the environment might not be completely understood at the design stage, or the amount of knowledge might be too large and complex for explicit encoding. Thus, CNNs now outperform these algorithms.

CNNs are the most common DL-based networks applied to image analysis. They were popularized after their stunning results in the ImageNet competition [36]. A CNN consists of several successive layers of data processing, whose aim is to find representative features of the input image, first simple, then more elaborate as the layers succeed each other (see Fig. 8). CNNs belong to the unsupervised or supervised learning category or both, depending on their architecture.

To better understand how this architecture works, let us take the example in Fig. 9, where the image to be analyzed is composed of 6×6 pixels that can take individually different gray level values (for simplicity, values -1, 0, and 1). The coordinates of the pixels of the image can be written in the form (x, y), with x the line and y the column number. Square a filter, here consisting of 3×3 pixels, whose values are fixed arbitrarily (for the moment), in the upper left corner of the image to be analyzed, centering it on pixel (2, 2). Multiply the value of each pixel (x, y) of the image with each corresponding pixel (x, y) of the filter, sum the values obtained, divide it by the number of pixels of the operation (in our case 9), and apply the result to pixel (2, 2) of a new image, called a *feature map* (FM). Then, drag this filter one column to the right, in order to center it on pixel (2, 3) of the image to be analyzed, and carry out the same operation, which makes it possible to assign a value to pixel (2, 3) of the FM. The dragging operation of the window of one column to the right is often referred to as *stride* $= 1$. By thus sweeping the entire image, it is possible to recreate an entire new image (except the border): this operation is qualified as a *convolution*, from which the CNNs derive their name. The role of this transformation is to detect local features in

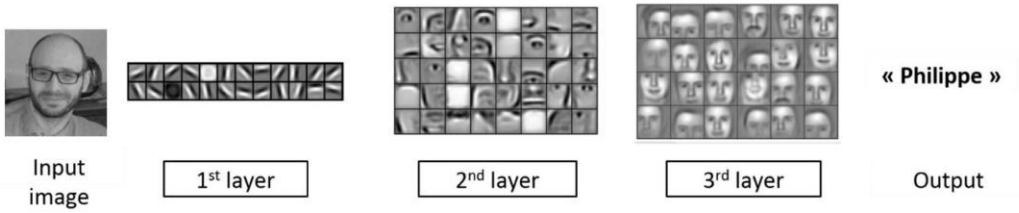

Fig. 8. Schematic illustration of the role of each layer of a CNN used for face recognition [42] (used with permission). The upper layers represent simple geometries (edges, lines). When the layers are deeper, simple features assemble to form shapes that are more complex.

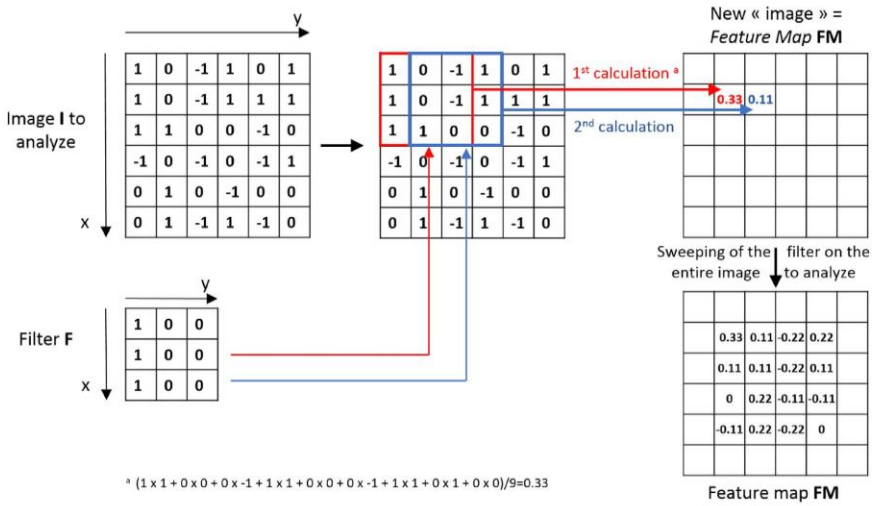

Fig. 9. Convolution operation applied to an image.

different parts of an image, preserving the spatial information of the input.

If this operation is transposed into a schematic representation of the neural networks, the pixel values can be seen as the input signals, and the filter values as the synaptic weights (see Fig. 10). Note that the filter F is often referred to as a *kernel*. In the previous example, the values of the filters (and thus weights) are set arbitrarily. In reality, we have already seen that the network iteratively adjusts these values during the training phase, so that the different layers can effectively extract characteristic representations of the input image. The convolution of the image by the kernel F, which produces the FM, constitutes a layer of the neural network. The multiple hidden layers of a CNN therefore represent successive convolution operations: the input data are the pixels of the image to be analyzed for the first layer, and those of the FM for the subsequent layers. Each layer actually includes several filters: in the example given in Fig. 11, the first layer consists of three different filters of size 3×3, the resulting FM being composed of three images (depth = 3). The next layer consists of four filters of size 3×3 and depth 3, which, convoluted with the FM of layer 1, produces an FM of depth 4.

2.3.2. Pooling

Practically in contemporary CNN, each convolutional layer is composed of dozens of grids of different weighted filters. Because an image is composed of tens of thousands of pixels, the number of operations required for CNN becomes important. To reduce this number and the computing load, it is common to insert a so-called pooling layer between two convolution layers. The role of this layer is to reduce the size of the FM produced by the previous convolution layer. The classic technique of max pooling is to keep only the value of the largest pixel in a certain area, to maintain the characteristic of the image. Fig. 12 illustrates a max pooling operation performed on the FM of our previous example. With a filter of dimension 2×2 (not to be confused with the filters of the convolution operations), this operation consists here of keeping only the pixel whose value is maximum in an area defined by a matrix of dimension 2×2. This matrix is moved here by two pixels (stride = 2), and sweeps the whole area of the image. FM thus passes in this example from 16 to 4 pixels.

We have so far focused on 2D images. To exploit the actual 3D nature of many medical images, 3D CNNs have been developed, which calculate 3D FMs from 3D kernels. To reduce the degree of complexity and computation time of these models, 2.5D (or tri-planar) CNNs have been developed, in which the 3D volume is decomposed into axial, sagittal, and coronal views [45]. However, with the rapid improvement of computing power on GPUs, 3D CNNs could prevail in the future.

2.3.3. Better understanding through an example of CNN: AlexNET

We have seen that the basic structure of a CNN consists of alternating convolution and pooling layers. We have not mentioned it so far, but a nonlinearity operation such as ReLU is implicit after each layer. Around this basic scheme, many variants have been proposed depending on the

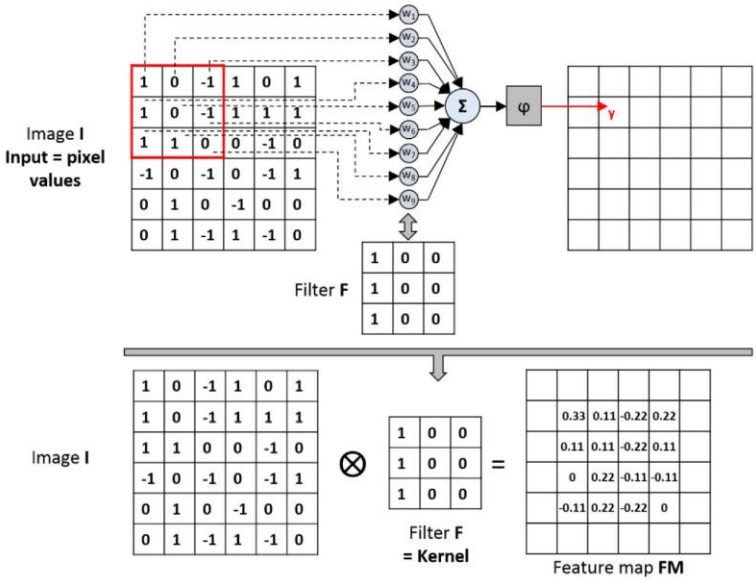

Fig. 10. Schematic representation of a convolution operation by a neural network.

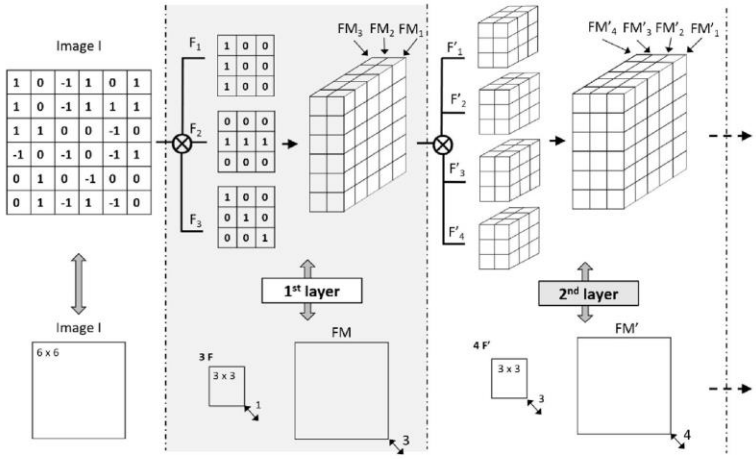

Fig. 11. Illustration of convolution operations performed in the first two hidden layers of a CNN. The lower part of the image is a synthetic view of the upper part.

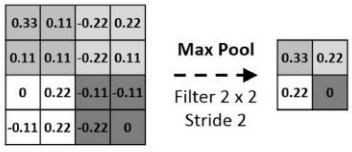

Fig. 12. Example of a max pooling filter of dimension 2×2 and stride $= 2$.

type of application. The AlexNet network discussed earlier is shown in Fig. 13. Its function is image classification: from a 2D input image, it assigns a probability output to each of the thousand classes proposed in the competition. It consists of five layers of convolution, three layers of pooling, and three fully connected layers as output. The first layer is composed of 96 filters of dimension $11 \times 11 \times 1$, applied to the input image with a stride $= 4$. The first resulting FM, of dimension $55 \times 55 \times 96$, is taken as input of the second layer and convolved with 256 filters of size $5 \times 5 \times 96$. After a max-pooling operation (3×3, stride $= 2$), the dimension of the second FM is $27 \times 27 \times 256$. These

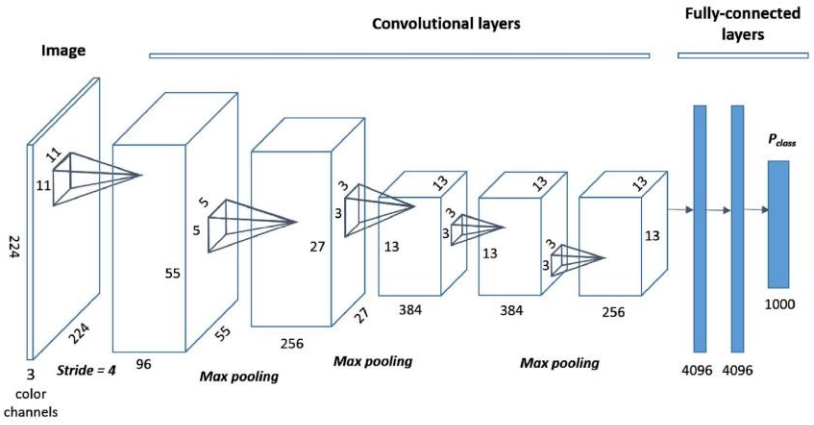

Fig. 13. Schematic representation of the AlexNet network (from Ref. [46]).

operations are repeated until the last convolution layer generates an FM of size $13 \times 13 \times 256$. After a last pooling operation that reduces the size of the FM to $6 \times 6 \times 256$ (not shown in the figure), three fully connected layers follow each other. In contrast to convolutional layers that aim to detect patterns by successively scanning different parts of the image, the fully connected layers simultaneously take as input all the pixels of the FM. The first fully connected layer is composed of 9216 neurons and generates a $4096 \times 1 \times 1$ size vector. At the output, a mathematical function called softmax transforms this vector of 4096 values into a probability vector of dimension $1000 \times 1 \times 1$, which assigns a probability to each of the 1000 classes used.

2.3.4. Other examples of CNN

In addition to AlexNET, other CNNs have been the subject of different variants, depending on specific applications. Among other outstanding networks, Visual Geometry Group (VGG) is characterized by a very simple structure (only convolution filter size 3×3 and pooling size 2×2) and by a significant depth of at least 16 layers [47]. It was developed for image classification, and performs on the concept that a DNN is more powerful when it is deeper. If the last fully connected layers of a CNN are deleted, you obtain a fully convolutional network (FCN), usually dedicated to segmentation tasks. The idea is to keep spatial information, increasing it in a last layer of sufficiently large size. However, after many layers of pooling, the final resolution is potentially low. To work around this problem, the U-net network, which was also developed for segmentation tasks, is proposed to add to the first convolutional part a second symmetrical part in which the pooling layers are replaced by interpolation layers [48]. The resolution of the output image is thus improved. Another application, deconvnet networks such as ZF-NET allowed a better understanding of how the network operates at each layer [49].

3. Deep learning methods applied to the radiotherapy workflow

Many teams are now developing DL methods that could straightforwardly be applied to one of the steps of the radiotherapy workflow (see Fig. 14). We made a review of the literature, and chose to classify the papers into seven categories relevant to these different radiotherapy

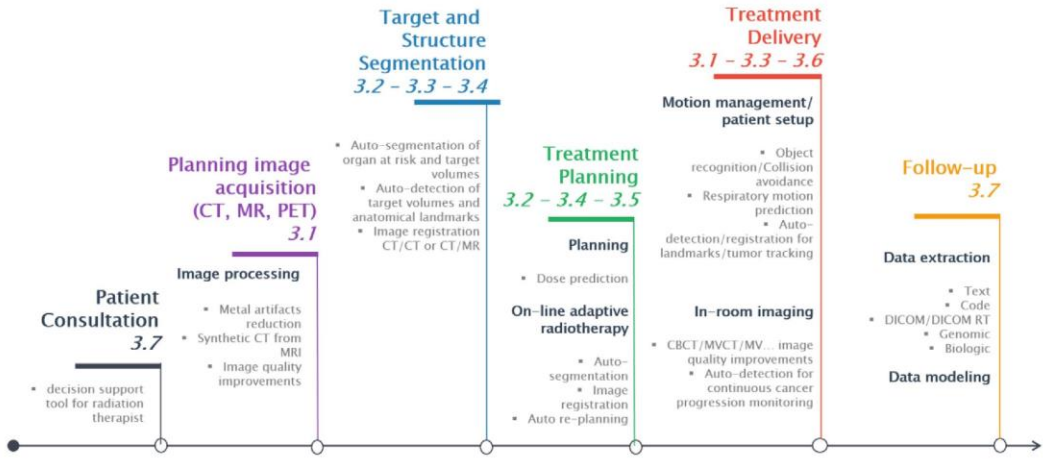

Fig. 14. Potential applications of deep learning approaches in the radiotherapy workflow. Numbers 3.1 to 3.7 refer to the sections in this article.

steps: images used for radiotherapy planning and treatment set-up, image segmentation, computer-aided detection and diagnosis, image registration, treatment planning, motion management/patient setup during treatment, and data extraction and outcome prediction in radiotherapy. A synthesis of these DL applications in radiotherapy is proposed as presented in Table 2.

3.1. Images used for radiotherapy planning and treatment setup

Radiotherapy planning images are used to segment OAR and the target volume, and to plan the treatment. In order to calculate the dose delivered to the patient, it is necessary to provide the electronic tissue density to the algorithms used by the treatment planning systems (TPS). Through a simple calibration between electronic density and Hounsfield number, this density can be directly estimated from the CT planning imagery, which is the reference imaging for dosimetric calculation in radiotherapy [50]. Because MRI has some advantages in soft tissue contrast for several cancers (brain, prostate, etc.), it would be desirable to substitute this CT planning scan by an MRI planning scan [51]. However, due to the need of estimating the electron density, a standard CT planning scan is still acquired in addition to the MRI scan [52]. To overcome this limitation, a solution is to generate synthetic CT (sCT) images from MRI [53].

Different methods have been developed in recent years [165] and a commercial solution has been recently evaluated on 170 prostate cancer patients [166]. CNNs appear to be one of the most promising methods for sCT generation. Han et al. proposed a novel U-net-based algorithm, the encoding part being based on the VGG 16-layer model [55]. Owing to transfer learning, they achieved a very satisfactory performance with limited training data (only 15 training subjects). They obtained a mean absolute error of 85 HU as compared to 95 HU for a standard atlas-based method. Another advantage is the processing time, which is approximately a few seconds for DL as compared to several minutes for the standard methods. However, the method generates each slice independently, resulting in potential discontinuity in the sCT [58]. Nie et al. proposed a 3D FCN for estimating CT images from MRI, while exploring different activation functions [56]. When tested on a pelvic phantom, they showed a better performance than three widely used approaches, with a 42.4 HU mean absolute error versus 48.1 to 66.1 for the other approaches. Wolterink et al. showed that a GAN can be trained to synthesize sCT with unpaired CT and MR images, avoiding the issue of misalignment between paired images [57]. They found that the model trained using unpaired data outperformed the model trained using paired data. Xiang et al. developed an original "deep embedding" CNN to synthesize sCT [58]. The embedded blocks help fill the large gap between MRI and CT appearance and speed up the mapping. They demonstrated that their network performance is superior to three conventional and one CNN approaches on brain and prostate cases with reduced processing time. Stimpel et al. compared the use of three DL-based architecture (U-net, residual net, and cascade refinement network) to generate X-ray from MR projections, but so far, only on phantom images [54]. Note that the generation of synthetic images is not always done from MRI to CT. Actually, Zhao et al. proposed a whole brain segmentation method for CT images that first uses a DL network to synthesize an MRI from a CT image and then uses the synthetic MRI for segmentation [59].

Magnetic resonance spectroscopic image (MRSI) is a promising tool to detect metabolites within tissues, notably for glioblastoma and prostate cancer management in radiotherapy [167]. However, the presence of spectral artifacts is a problem in the routine clinical workflow. Gurbani et al. developed a CNN to identify poor-quality spectra and filter out artifacts with a high degree of sensitivity and specificity [61].

Artifacts on CT images related to the presence of metals in patients (dental fillings, spinal implants, hip prostheses, etc.) are problematic in radiotherapy. Actually, they can interfere with radiation diagnoses during the segmentation step and bias the calculation of the dose. To overcome these issues, many metal artifact reduction (MAR) algorithms have been proposed [168,169]. Recently, Gjesteby combined a CNN with an MAR into the image reconstruction process to achieve additional correction in critical image region, such as those with multiple metal objects [62,63]. Their results indicated that deep networks are valuable tools for improving or even replacing state-of-the-art MAR algorithms.

These DL image processing methods for both the generation of sCT from MRI and the correction of metallic implant artifacts involve learning a mapping from an image to another. This general concept could naturally be extended to other applications such as improving image quality, removing artifacts related to patient movements, synthesizing other image contrasts, or implementing rapid image acquisition strategies [170]. For example, Dong et al. used what they called a super resolution CNN method, which learns a mapping between low-/high-resolution images to restore image quality [64]. While these methods could be applied to radiotherapy planning images, they have also a great potential for image guided radiation therapy (IGRT) techniques to set up the patient during treatment. IGRT techniques are commonly based on X-ray (kilovoltage, megavoltage, cone beam CT (CBCT), megavoltage CT), MR, or ultrasound (US) imaging [171–173]. To reduce noise artifacts in CBCT images produced by a Leksell Gamma Knife Icon (Elekta, Sweden), Afshaq investigated the use of CNNs [65]. He showed that the proposed method outperforms conventional algorithms at the cost of a much higher computational time. These findings were only proved on synthetic CBCT images. To the best of our knowledge, the only one who used clinical IGRT images is Mori. He tested several types of deep CNN and AE models to process 430 X-ray images acquired on prostate cancer patients with oblique fluoroscopic units during patient setup procedure [66]. With a standard desktop computer, he achieved real-time image processing at 30 frames per second, including contrast enhancement and image denoising. Other DL methods originally developed for conventional diagnostic images could also have potential applications to IGRT images. For example, Bahrami et al. trained a CNN to reconstruct 7 T-like images from 3 T MRI, providing improved resolution and contrast [60]. This could be particularly useful for improving MR images produced by recent low-field MR systems (from 0.35 to 1.5 T) integrated into radiotherapy devices [174]. Concerning CT imaging, Zhang et al. developed a CNN to reduce artifacts produced by filtered back projection methods conducted on limited CT angle acquisition ranging from 130° to 170° [69]. This may be applicable on CBCT image acquisition, where limited angle acquisition is used to reduce the acquisition time and delivered dose. Reducing imaging dose delivered during IGRT is indeed a critical point, evidenced by an accident in France, where 409 prostate patients received 8–10% overexposure due to excessive portal imaging controls, leading to the death of two of them after grade 4 rectal fistula [175]. In this context, deep CNN methods such as those developed by Chen et al. may be useful [67]. Their CNN, trained to match low-dose CT images toward normal-dose CT images, showed a better performance for noise reduction than iterative reconstruction and post-reconstruction processing. Yang et al. proposed a GAN to denoise low-dose CT images [68]. Compared to a CNN-based method, their method helped avoid the over-smoothing effect, but at the cost of losing critical features. All these methods have the potential to reduce the dose delivered during X-ray imaging used to localize patient during radiotherapy treatments.

3.2. Image segmentation

For each patient treated with radiotherapy, the radiation oncologist delineates slice by slice the target volume and the OAR on the planning images (CT or MR scans). Even if this task remains mainly manual in clinical routine, automated medical image segmentation plays an increasing role to help doctors in delineating anatomical structures or tumor regions. Many automatic segmentation methods have been explored, with varying degrees of success depending on the type of application or imagery studied [176,177]. There are now more than a dozen commercial segmentation software dedicated to radiotherapy, integrated or not into TPS [3].

Table 2
Summary of the different deep learning based applications by radiotherapy treatment step.

Radiotherapy treatment step	Application	Input data	DL-based method	Reference
Images used for radiotherapy planning and treatment setup	Pseudo X-ray image synthesis	MRI	U-net, Residual net, Cascaded refinement net	[54]
	Pseudo CT image synthesis	MRI	U-net, VGG	[55]
			FCN	[56]
			GAN	[57]
			Deep embedding CNN	[58]
	Pseudo MRI synthesis	CT	FCN	[59]
	Pseudo 7 T MRI synthesis	3 T MRI	CNN	[60]
	MR spectroscopic images (MRSI) artifact correction	MRSI	CNN	[61]
	Image artifact reduction	CT	CNN	[62,63]
	Spatial resolution improvement	Images	Super resolution CNN	[64]
	Image denoising	Synthetic CBCT	2D CNN	[65]
		On-board radiotherapy fluoroscopic X-rays	CNN, SAE	[66]
		CT	CNN	[67]
		CT	GAN	[68]
	Image prediction for limited-angle tomography	CT	CNN	[69]
Image segmentation	Portal vein	CT	2.5D CNN	[70,71]
	Brain glioma	MRI	CNN, U-net, FCN	[72]
			CNN	[73]
			3D CNN	[74,75]
			Holistically nested network	[76]
	Brain metastases	MRI	3D CNN	[77,78]
	Brain structures	MRI	DNN	[79]
		MRI	2.5D CNN	[37]
	Multi-age brain structures	MRI	CNN	[80]
	Brainstem	MRI	SDAE	[81]
	Hippocampus	MRI	DNN	[82]
		MRI	U-net	[83]
	Optic structures	MRI	SDAE	[84]
		CT	3D CNN	[85]
	Subcortical structures	MRI	3D CNN	[86]
		MRI	2.5D CNN	[87]
	Neuroanatomy structures	MRI	3D CNN	[88]
		MRI, US	2D, 2.5D, 3D CNNs	[89]
	Breast tissue	MRI	U-net	[90]
	Prostate	MRI	SAE, SSAE	[91]
		MRI	FCN	[92]
		CT	CNN	[93]
	Thoracic organs	CT	FCN	[94]
		CT	FCN	[95,96]
		CT	CNN	[97]
	Head and neck (H&N) organs	CT	2.5D CNN	[98]
	Esophagus	CT	3D CNN	[99]
	Abdominal organs	CT	3D CNN	[100]
	Spine	CT	CNN, FCN	[101]
	Liver and/or hepatic metastases	CT	Deep deconvolutional NN (DDNN)	[102]
		CT	FCN	[103]
		CT	3D CNN	[104]
		CT	CNN	[105]
		MRI, CT	FCN	[106]
	Rectal cancer and organs	CT	Deep dilated CNN	[107]
	Skin cancer	Dermoscopic images	CNN	[108]
	Rectal Cancer	MRI	CNN	[109]
	Bladder Cancer	CT	CNN	[110]
	Liver tumor	CT	CNN	[111]
	Nasopharyngeal tumor	CT	DDNN	[112]
	Nasopharyngeal tumor	MRI	CNN	[113]
	Oropharyngeal tumor	CT	CNN	[114]
	Tumor	Positron emission tomography (PET) -CT	CNN	[115]
Computer-aided detection	Pulmonary nodules	CT	3D CNN	[116]
		CT	CNN	[117]
		CT	CNN	[118]
		CT	CNN	[119]
		CT	CNN	[120]
	Prostate cancer	MRI	SAE	[121]
	Brain Metastases	MRI	CNN	[78,122]
	Brachytherapy catheters	MRI	(planned)	[123]
	L3 vertebra	CT	CNN	[124]
	Specific CT slice	CT	CNN	[125]
	Bone metastases	CT	CNN	[126]
	Specific vertebra	MRI	CNN	[127]

(*continued on next page*)

Table 2 (*continued*)

Radiotherapy treatment step	Application	Input data	DL-based method	Reference
	Specific vertebra	US	CNN, SAE	[128, 129]
	Carotid artery bifurcation	CT	DNN	[130]
	Anatomic landmarks	MRI, US, CT	CNN	[131]
	Brain, prostate landmarks	MRI, CT	CNN	[132]
Computer-aided diagnostic	Skin cancer	Images	CNN	[133]
	Pulmonary nodules	CT	DBN, CNN	[134]
		CT	AE	[135]
		CT	CNN, DNN, SAE	[136]
		CT	CNN, DBN, SDAE	[137]
		CT	CNN	[138]
	Breast cancer	Mammography	CNN	[139]
		Mammography	CNN	[140]
	Prostate cancer	MRI	DNN, VGG	[141]
	Rhabdomyosarcomas subtype	MRI	CNN	[142]
Image registration	Deformation prediction	MRI	VGG	[143]
	X-ray 2D/3D registration	Fluoroscopic X-rays	CNN	[144]
	2D/3D registration initialization	Fetal MRI	CNN	[145]
	MRI/MRI registration	MRI	SAE	[146]
	CT/MRI registration	CT,MRI	DNN	[147]
	X-ray 2D/3D registration	CBCT, 2D X-rays	FCN	[148]
Treatment planning	Predict dose from organ structures	RT Struct, RT Dose	U-net, CNN	[149]
		RT Struct, RT Dose	AE	[150, 151]
Motion management/patient setup during treatment	Motion correction alignment setup with a soft robot activator	Motion capture camera images	MLP, RNN, LSTM	[152]
	Real-time, markerless, tumor-contouring to prevent mistracking on X-ray fluoroscopy	Fluoroscopic X-rays	CNN	[153]
	Intra- and inter-fractional variation prediction of lung tumors	Cyberknife breathing signal	NN	[154]
	Collision avoidance	3D camera images	Not described	[155]
Data extraction and outcome prediction in radiotherapy	Local failure after lung stereotactic body radiotherapy (SBRT)	CT, clinical risk factors (CRF)	DNN	[156]
	Survival risk after rectal cancer chemo-radiotherapy	PET-CT, survival rate	CNN	[157]
	Quality of life after prostate SBRT	Dose Volume Histogram, quality of life scores	DNN	[158]
	Rectum toxicity after cervical cancer brachy/radiotherapy	RT dose, Toxicity scores	VGG	[159]
	Survival rate for lung and H&N patients	CT	DNN	[160]
	Automated radiation adaptation in lung cancer	Clinical, genetic, dosimetric, PET data	GAN, CNN	[161]
	Medical image classification	24 organs on MRI, CT, PET	CNN	[162]
	Named entity recognition in clinical text	Electronic health records	DNN	[163]
	Clinical relation extraction	CRF	SAE	[164]

Automatic segmentation is a frequent application of DL. The literature on this subject is already very broad, and our objective is not to be exhaustive, but rather to show that various published works can be applied to all radiotherapy indications. Nearly all the regions of human anatomy are concerned: cerebral, H&N, thoracic, abdominal, or pelvic. Different types of medical data are used for the segmentation of anatomical structures by DL, including MRI and CT images that are the reference imaging modalities for radiotherapy.

MRI is mostly used to investigate soft tissues and is the gold standard for the segmentation of the cerebral structures. Akkus et al. recently reviewed the numerous brain MRI segmentation methods involving DL [178]. The authors listed the most popular quantitative measures of brain segmentation quality, and the main brain segmentation challenges, including the multimodal brain tumor segmentation challenge (BraTS) [179]. This annual challenge dedicated to the automatic segmentation of gliomas since 2012 makes available a large database of multimodal MRI, composed in 2017 of 262 MRI for glioblastomas and 199 MRI for low-grade gliomas [180]. The availability of such large database partly explains why glioma is one of the most studied tumors for automatic segmentation by DL [73,75]. As highlighted by Isis et al. in their review on MRI-based brain tumor segmentation, DL methods can actually be considered as the current state-of-the-art method for glioma segmentation [181]. Tested on the 2013 BraTS dataset, Havaei et al. demonstrated that their CNN architecture outperforms the currently published state-of-the-art one, while being over 30 times faster [73]. With their CNN network called DeepMedic, Kamnitsas et al. obtained top ranking performance on BraTS 2015 [74]. Furthermore, the authors demonstrated the generalization capabilities of systems such as DeepMedic, which can be applied without significant modifications to other segmentation tasks such as for brain injuries and ischemic stroke, while still outperforming the state-of-the-art methods. In 2017, Kamnitsas et al. merged three DNN architectures to segment brain tumors on MRI: their CNN DeepMedic, two versions of U-net, and three fully connected networks. With this robust model, they won the first position in the BraTS final testing stage among more than 50 competing teams [72]. Zhuge et al. have proposed a new holistically nested neural network, and stated that it outperforms the classical CNN method for MRI-based glioma segmentation [76]. Compared to this many works concerning gliomas, BM have only very rarely been the subject of segmentation methods by DL. Liu et al. obtained competitive results with a CNN-based segmentation method for BM on MRI, although the partial use of the BraTS database in their validation and test sets led to nuances in their conclusions [77].

The segmentation of brain OAR on MRI by DL methods has also been the subject of several studies. Brebisson et al. were the first to segment the whole brain into 134 anatomical regions using DNN [79]. Pai et al. worked on the same dataset of Brebisson and obtained equivalent results, but they also observed that the performance of their tri-planar CNN was inferior to standard methods, notably because of the lack of training cases [37]. Moeskoeps et al. designed a unique CNN network to precisely

segment brain outlines regardless of age (prenatal, 23, and 70 years old) [80]. They also showed that this network could straightforwardly be applied to segment other anatomical regions while improving the results of Brebrisson. Other studies used SDAE, U-net or CNN to focus on a given structure, such as the brainstem [81] or the hippocampus [82,83], or on a group of structures such as those located in the optic region (optic nerve, chiasm, and pituitary) [84] or in the subcortical regions [86,87], and simultaneously up to 25 to 26 regions of the neuroanatomy [88,89]. While Milletari et al. compared different types of CNN architectures [89], Wachinger et al. used a 3D CNN to segment 25 brain structures with statistically significant improvements over several state-of-the-art methods, although the results were not as clear for subcortical structures [88]. Note that auto-segmentation of small volumes, such as optical structures (chiasm, optic nerves, etc.), is often difficult. To overcome this problem, 3D CNN with multi-scale patches (large patch to locate the tissue and small patch to label each voxel) has been developed with significantly better performance than the best scores reported in the literature [85].

MRI is also the reference modality for prostate segmentation, due in particular to the difficulty of differentiating on CT scans its contours with neighboring soft tissues in the base and apex regions [182]. Because prostate cancer is the most common cancer for men in developed countries [183], the automatic segmentation of this organ by DL has already been the subject of several studies. Guo et al. showed the superiority of their SAE model over state-of-the-art ones using handcrafted features, particularly on both anterior and posterior parts of the prostate [91]. Mehrtash et al. proposed an open-source toolkit called "DeepInfer" for developing DL models for different segmentation or detection tasks in medical imaging [184]. They tested their toolkit on prostate segmentation for targeted MRI-guided biopsy.

Many other organs can also be automatically segmented in MRI by DL. Google's DeepMind Health has started a partnership with a hospital on H&N cancer to automatically segment tumor volumes and organs at risk on MRI scans [185]. Automated segmentation of breast and fibroglandular tissues may also be useful in radiotherapy, particularly because breast intensity modulated radiotherapy indications increased in recent years. Dalmis et al. showed that the U-net-based method they applied on MRI significantly outperformed existing algorithms in breast segmentation [90]. Christ et al. used an open-source DL framework to build a cascaded FCN model, which combined the segmentation of the liver and of hepatic lesions on MRI, and obtained results that compete with state-of-the-art methods [106]. They also showed that their method could be generalized to segment the liver and lesions on CT images.

While MR imaging has become the gold standard for organ segmentation of certain indications in radiotherapy, CT remains as the reference imaging modality (explained in Section 3.1). Several teams developed DL segmentation methods on CT images for various anatomical regions. Zhou et al. segmented 19 organs from different regions of the human anatomy on CT images, obtaining equivalent results to those of state-of-the-art methods with the advantage of using a single FCN architecture for all organs [94]. With a CNN dedicated to H&N cancers, Ibragimovic et al. segmented 9 organs, including 4 structures in the optic region [98]. They compared their findings not only with methods from academic research, as is generally the case with the studies cited in this paragraph, but also with three commercial software used in radiotherapy departments (VelocityAI 2.6.2, MIM 5.1.1, and ABAS 2.0 systems). They observed that DL methods demonstrate a superior or comparable performance to the commercial software for all organs at risk, except for chiasm and submandibular glands. The esophagus, which is a structure with heterogeneous appearance and complex shape, was automatically and successfully segmented on public CT images from the "Multi-Atlas Labeling Beyond the Cranial Vault Challenge" with a 3D CNN developed by Fechter et al. They evaluated their method on the Synapse dataset, and showed that it outperformed all existing approaches [99]. Trullo et al. proposed an FCN framework for the joint segmentation of thoracic OAR, namely the heart, esophagus, trachea, and aorta. They obtained competitive results, particularly by accounting for relationship between these organs [95,96]. Hu et al. achieved an accuracy comparable to state-of-the-art methods with much higher efficiency for segmentation of the liver, spleen, and both kidneys [100]. By evaluating their automatic liver segmentation method on two public datasets of CT images (MICCAI-Sliver07 and 3Dircabd), Lu et al. showed that it demonstrates a superior segmentation accuracy than most of state-of-the-art methods [104]. Ben Cohen et al. and Yuan et al. developed several CNN and FCN approaches to automatically segment the liver on CT images and detect the lesions in the liver segmentation [102,103]. Still, for liver segmentation, Qin et al. proposed an original approach based on a CNN pipeline working with superpixels and an additional boundary class [105]. It achieved superior performance in comparison with U-net, CNN, and classical approaches. To better assess toxicity after SBRT, Ibragimovic et al. proposed a tri-planar CNN to segment and annotate portal vein on CT images [70,71]. Vania et al. combined a CNN and an FCN to automatically segment the spine on CT images [101]. Their results were better compared to those of conventional results, but slightly worse than those of U-net. The prostate can also be automatically segmented from CT using a CNN and multi-atlas fusion with satisfactory results [93].

DL methods were not only used to segment OAR, but also recently target volumes. Men et al. developed a CNN-like network to simultaneously segment abdomino-pelvic risk organs and the clinical target volume (CTV) of rectal cancers [107]. CNN were developed to segment oropharyngeal and nasopharyngeal CTV respectively on CT and MRI images, with close agreement when compared to inter-observer variability [113,114]. Other applications for segmentation of target volumes are presented in Section 3.5.

Medical Image Computing and Computer Assisted Intervention (MICCAI) has organized one of the first tumor delineation segmentation challenge in PET images [115]. Thirteen methods where implemented by challengers, and a CNN was ranked first. Automatic DL segmentation methods have also been developed for imaging modalities that are usually not used in the radiotherapy segmentation step. Automatic skin lesion segmentation in dermoscopic images, for example, is an important research field in dermatology, but may also help to define the target volume when treating skin lesions in radiotherapy. Experimental results show that CNN-based methods outperform other state-of-the-art dermoscopic segmentation algorithms [186,187]. US was also the subject of automatic segmentation attempts by CNN, for example for brain structures [89]. Automatic US image segmentation by DL could be useful in radiotherapy. Actually, patient or organ monitoring can be performed in some cases by US during treatment delivery [188–190]. This is also the case in prostate brachytherapy, where US endo-rectal imaging is used to monitor the procedure [191].

Despite these numerous DL automatic segmentation methods, there are few evaluations of their actual clinical contribution. The work of Lustberg et al. is one of the first to have evaluated the clinical interest of a commercial DL segmentation software prototype (Mirada DLC Expert prototype, Mirada Medical Ltd. United Kingdom). In a clinical radiotherapy context, they quantified the segmentation time using this software prototype for the segmentation of 6 thoracic OAR on CT, and compared those of manual contouring and atlas-based commercial automatic contouring [97]. The median time was 20 min for manual, 12.2 min for atlas-based, and 10 min for DL-based contouring.

3.3. Computer-aided detection (CADe) and diagnosis (CADx)

Although the concept of computer-aided medical image analysis appeared in the 1960s, the first developments on this subject began in the early 1980s [192]. Computer-aided medical image analysis can be divided into two categories: computer-aided detection (CADe) and diagnosis (CADx) [193]. The goal of a CADe system is to identify the location of organs, tumors, anatomical regions, or medical equipment in the images, and to help the medical staff for specific tasks. The objective of a CADx system is to provide medical information for the classification

of a disease. Currently, automatic detection and diagnosis based on medical images have become a major research subject in the medical field. Esteva et al. for example, have recently developed a CNN that is capable of classifying skin cancer with a performance similar to that of dermatologists, and stated that it could be implemented on standard smartphones [133]. Even if a robust prospective validation in a blinded clinical trial must be undertaken in this particular example to ensure that this smartphone application is not harmful [194], DL technology opens promising perspectives for medical image analysis.

3.4. Computer-aided diagnosis

Classifying pulmonary nodules on CT images according to their benign or malignant nature is a difficult task, and many teams have developed tools whose performances are regularly compared in challenges, such as the recent LungX Challenge [195]. One of the first studies that applied DL techniques to the problem of pulmonary nodule classification on CT images was performed by Hua et al. who showed that a combined DBN-CNN framework outperformed CADx systems relying on conventional handcrafted feature [134]. Since then, several authors developed other DL algorithms for this purpose. Ali et al. developed a reinforcement learning-based model for a CNN [120]. Kumar et al. proposed to use deep features extracted from an AE network combined with a binary decision tree as a classifier [135]. Song et al. compared the performances of three deep networks (CNN, DN and SAE) for lung cancer classification [136]: the CNN achieved the best performances. Sun et al. developed and compared the performances of three multichannel deep structured algorithms (CNN, DBN, and SDAE) and a classical handcrafted algorithm [137]. The best performance was obtained with the CNN. Instead of using CT images, Wang et al. recently tried to classify lung nodules from PET images, and compared a DL method with four classical machine learning methods. They showed that the performance of their CNN was not significantly different from the best classical methods, but that this performance could be improved by incorporating diagnostic features [138].

Breast cancer is the most common cancer in women worldwide [183], and one of the most treated with radiotherapy. Breast cancer CADx is therefore a crucial task, and CNN approaches were recently implemented for analyzing mammography images [139,140]. MRI has also been the subject of various works related to DL-based CADx algorithms. By finishing 4th place on the ProstateX challenge (classification of clinically significant prostate lesions on MRI), Chen et al. demonstrated that public state-of-the-art DL models such as VGG-16 could quickly and efficiently be retrained with limited data [141]. By analyzing multiparametric MRI, Banerjee et al. presented a CNN-based CADx for the classification of rhabdomyosarcoma subtypes [142].

3.5. Computer-aided detection

In their systematic review of articles published in December 2014 dealing with CADe of pulmonary nodules on CT images, Valente et al. stated that the latest techniques have not yet overcome all the challenges of this task, mainly because of high FP per patient rates [193]. Nevertheless, none of the articles cited by Valente et al. relies on DL methods. Anirudh et al. were one of the first to explore lung nodule detection on CT images using 3D CNN, achieving a sensitivity of 60% for 3 FP per scan [116]. Roth et al. proposed a CNN method that improved the state-of-the-art CADe systems, with a mediastinal lung node sensitivity of 70% for 3 FP per patient [117]. Recently, all currently reported results on mediastinal lung nodule detection were surpassed with a CNN architecture adapted from the complex GoogLeNet model, achieving an 86% sensitivity and 3 FP per patient [118]. Teramoto et al. also concluded that CNN can be employed for FP detection rate reduction, showing that their method eliminates approximately half of the FPs as compared to a previous study concerning lung nodule detection on PET/CT [119].

Despite the high incidence of BM that affect up to one third of cancer patients, few detection DL-based methods have been published to date. Losch et al. were the first, to our knowledge, to use a CNN to detect BM on MRI [122]. They explored several kernel sizes and network depths, and observed that their network performances are comparable to the conventional state-of-the-art ones. Odelin et al. that it was possible to adapt an existing CNN (DeepMedic) to detect BM on multimodal MRI [78]. They used real and virtual patients, and obtained 98% sensitivity with only 7.2 false positive per patient. Sunwoo et al. developed a handcrafted feature-oriented CAD of BM on MRI, and used a simple one hidden layer ANN as the final FP discrimination method [196]. What is interesting is that they evaluated their CAD system in a clinical context, and showed that their CAD helps radiologists improve their diagnostic performance in the detection of BM on MRI, particularly for less-experienced reviewers.

Zhu et al. proposed an SAE method for detection of prostate cancer regions using multi-parametric MRI. They achieved a better performance than the conventional handcrafted features, with the advantage of directly identifying cancer regions from the entire prostate, compared to conventional prostate cancer detection methods that identify cancer only in specific regions of interest [121]. An original use of DL algorithms on MRI is the detection of catheters for brachytherapy, which are difficult to distinguish from neighboring tissues. In their work, Mastmeyer et al. used classical handcrafted features to detect and segment these brachytherapy catheters from MRI, but stated that they have begun investigating the training of DL networks [123].

An interesting application of CADe for radiotherapy is the automatic detection of anatomical landmarks. As stated before, this could be a valuable aid in preventing, for example, the delineation or treatment of wrong target, or in tracking a particular part of the anatomy. A good example is the level labeling of vertebra, which is an error-prone task because of the high-appearance similarity between consecutive vertebrae. CNN-based systems have been developed for detecting a particular slice on CT images, which achieved an average localization error of 4.8 mm for the third lumbar vertebra (L3) [125,197]. Again on CT images, a deep CNN was used to detect sclerotic metastases (bone lesions), while reducing the FP detection rate [126]. MRI can also be used to detect vertebrae. The CNN proposed by Forsberg et al. showed a detection accuracy on T1 and T2 images of less than 2.6 mm for lumbar and cervical vertebrae, with a labeling accuracy of 97.0% [127]. CNN and SAE were also proposed for the identification of the vertebra level on US images. Compared to matches of manually selected labels, DL matches of predicted vertebral level were correct in 94% of cases [128,129]. Originally developed for percutaneous needle insertion procedures, this type of application could also be applied to non-ionizing patient position monitoring during radiotherapy treatments. Other landmark detection methods performed by CNN could be used to assess the correct localization of the patient on various imaging modalities, such as carotid artery bifurcation on CT images [130], mitral annulus on US images [131], or apical/basal cardiac slices on MRI [132].

CADe and CADx algorithms are mainly useful in the medical diagnosis phase and do not at first glance directly concern radiotherapy. Nevertheless, these methods could find their place in the radiotherapy workflow in many cases. For example, automatic detection tools could help to control the positioning or to track in real time tumors/organs while the treatment is delivered. It could also support the radiation oncologist during the delineation stage by identifying anatomical landmarks such as the vertebral level. It might also open up new opportunities for exploiting the daily positioning images, for instance, by automatically screening for new metastases or identifying tumor progression/regression.

3.6. Image registration

Image registration is defined as the mathematical transformations applied to an image to make it correspond to a reference image. Registration methods are available in almost all radiotherapy software used to manage images. The American Association of Physicists in Medicine recently reviewed current approaches in radiotherapy [198]. In their

survey about medical image registration techniques, Viergever et al. reviewed the developments that took place between 1998 and 2016 [199]. They observed major trends, notably that intensity-based techniques and rigid methods are now forming the basis of the vast majority of registration in clinical practice, and that registration use has progressed particularly in radiotherapy. They also concluded that it is unlikely that mutual information will be able to maintain its popularity, and that DL approaches applied to image registration could be the new challenger that could definitively make image registration fully integrated into routine clinical imaging.

DL algorithms have been proposed just to make the images comparable before using intensity-based methods for registration and to directly estimate the transformation parameters. Yang et al. proposed a DL network to predict image deformation, tested on 2D and 3D MRI datasets [143]. They achieved an equivalent prediction accuracy compared to state-of-the-art methods, with a significant speed-up of 1500x/66x respectively for 2D and 3D image registration. Miao et al. developed a CNN-based method for real-time 2D/3D registration, trained on synthetic data only [144,148]. They tested their method on three clinical applications (total knee arthroplasty, virtual implant planning system, and X-ray echo fusion), by registering X-ray images from fluoroscopic videos with 3D models. Results showed that their CNN method is very fast as it is capable of real-time registration at 10 fps, and significantly outperforms intensity-based methods. They also recently proposed a new FCN-based training strategy, and succeeded to reduce training time and improve registration robustness against artifacts [148]. A CNN approach was proposed by Hou et al. to solve the 2D/3D initialization problem in imaging applications, where the patient is moving during acquisition, such as fetal MRI [145]. Integrated into a full motion compensation framework, their method allowed to efficiently correct highly motion-corrupted scans. An unsupervised-based SAE network developed by Wu et al. for MRI registration consistently demonstrated a better performance compared to state-of-the-art methods [146]. The authors also showed that their proposed framework was quickly and efficiently adaptable to 7.0 T MRI, for which existing deformable methods developed for 3.0 T MRI did not work well. Ma et al. proposed a multimodal DNN-based registration algorithm to register real-time patient depth images with pre-operative CT or MRI [147]. Even if these applications are not directly related to radiotherapy, this type of DL method could be used during the treatment delivery, for example, by matching the kV or MV real-time images with the 3D model.

3.7. Treatment planning

Radiotherapy treatment planning aims to determine the optimal irradiation parameters (number of beams/arcs, multileaf collimator conformation/modulation, etc.). This planning is carried out using dedicated software (TPS) and is still currently mainly driven by the human user. However, many semi- or fully automated planning methods have been developed for several years, with the aim of reducing planning time while improving the quality of treatment plans. Some of them have been recently integrated and successfully tested in commercial solutions [200–203]. They mainly use machine learning methods that are trained on existing treatment plans [204–207]. DL methods are therefore applicable to the problem of automated treatment planning. To date, there are few published works in which a DL scheme is proposed to facilitate the radiotherapy planning task. Mardani et al. proposed a deep AE-based relation map between dose and structure that is learned from a dataset of 115 previously treated intensity-modulated radiotherapy (IMRT) prostate patients, allowing to predict achievable dose from the structures segmented on the planning images [150,151]. As compared to the state-of-art knowledge-based planning schemes, this novel predictive model has the advantage of being independent from patient and tumor site variability. Nguyen et al. proposed the same type of model, and used a U-net architecture with additional CNN layers to predict dose from structures [149]. The PTV, bladder, body, left and right femoral heads, and rectum structures of 80 IMRT prostate patients were used to train the model, as well as the 2D dose map of the central PTV slice. They obtained an average mean and maximum dose differences of all structures within 2.3% of the prescription dose.

If we deviate a bit from the heart of the planning process itself, the DL approaches for automatic segmentation and image registration, which we have described in the previous sections, are particularly adapted to the specific workflow of adaptive radiotherapy (ART). ART is defined as a radiotherapy treatment process, where the treatment plan can be modified using a systematic feedback of measurements performed during treatment [208]. The ART process can be applied in real-time conditions, while the patient is on the bed inside the treatment room [209–211]. In this case, the DL approaches for automatic segmentation and image registration, which are potentially faster than standard approaches, could allow reduction of the patient treatment time. The DL accuracy performance in terms of automatic segmentation can also prove to be useful in the ART process. Trebeschi et al. showed that a CNN can improve the speed and accuracy of diffusion weighted MRI-based rectal cancer segmentation [109]. Another example of potential application is bladder cancer. Segmentation of bladder cancer is crucial, because monitoring its volume variation during neoadjuvant chemotherapy is used to predict treatment outcome. One can envision that it may also be useful for ART to monitor changes during the course of treatment. Cha et al. developed a CNN model to automatically segment the bladder cancer region on CT images, which showed a better performance than another method they have developed beforehand [110]. Vivanti et al. described a CNN-based method to quantify liver tumor burden on longitudinal CT scans [111]. Men et al. developed the DDNN method to segment nasopharyngeal gross tumor volume and CTV on planning CT, outperforming a VGG-based model [112]. These four examples of DL-based segmentation illustrate applications that could take place in the ART process. Nevertheless, they were tested on high-quality images compared to those used for patient positioning in radiotherapy with IGRT. To our knowledge, no DL segmentation approach has yet been applied to these types of images, thus opening up interesting research perspectives.

3.8. Motion management/patient setup during treatment

Managing intra- and inter-fraction patient and organ motion has become a central topic in contemporary medical physics research, stimulated by the technical realization and subsequent clinical implementation of hybrid beam delivery [212–214]. Machine learning techniques have been used for many years [215], and DL approaches have now also been investigated in this area. Ogunmolu et al. developed a soft-robot actuator to position patients in maskless H&N radiotherapy. Combined with two Kinect cameras and a single inflatable air bladder, it allowed to track the patient's face and to control the soft robot, achieving 2.5 mm accuracy in head positioning [216,217]. Originally based on a linear quadratic Gaussian feedback model, the authors developed several deep architectures (MLP, RNN, and LSTM) that they planned to use with their soft-robot motion alignment system [152]. Respiratory tumor motion management is also a challenging task, particularly because stereotactic lung radiotherapy techniques have become popular [218]. To predict intra- and inter-fractional variation in lung tumor location, Park et al. developed a neural network with embedded fuzzy logic systems trained on breathing data of 130 patients collected on a Cyberknife facility [154]. Their framework allowed estimating the next breathing signal before the next incoming signal arrives. Compared to existing methods, it improved the prediction accuracy, while reducing the computational time by a factor of more than 100. With an average processing time of 1.5 ms, it could achieve real-time prediction and can therefore help in improving tracking techniques. Terunuma et al. developed a CNN-based contouring method to track tumors in real-time on X-ray fluoroscopy [153]. They validated their method on simulated fluoroscopic images, achieving a 30 frames per second processing time.

Wrong patient positioning is a potential pitfall in radiotherapy

treatment, which could lead to mis-irradiation or patient collision with the gantry. Using a set of 3D cameras placed inside the treatment room, Santhanam et al. developed a DL-based system to automatically detect potential patient safety hazards during the radiotherapy setup [155]. Three-dimensional objects such as the gantry and bed were first recognized and classified, and a DL framework was used to analyze these objects, allowing the system to recognize wrong patient or accessory setup.

Finally, as already mentioned in previous sections, DL segmentation, detection, or registration algorithms have an interesting potential for motion management in radiotherapy including the tracking of structures on imaging systems used to control patient positioning.

3.9. Medical data extraction and outcome prediction in radiotherapy

Currently, many medical records are numerically collected from patients treated with radiotherapy, such as administrative (codes), genomics, clinical (text), biological (blood tests, cardiac tests, etc.), diagnostic/simulation imaging (DICOM), and treatment plan data (DICOM RT plan, structures and dose, DICOM positioning control images) [219]. This information is often referred to as EHR or big data in the literature, which are concepts that evolved continuously in recent years [220,221].

These data represent a considerable source of new medical knowledge, if they could be analyzed on a large scale. The goal is to link the patient's disease, its treatment, and its clinical effects, in order to design decision-making tools that will help the physician to better orient and personalize the patient therapy. In order to achieve this, algorithms should be first designed to extract intelligible data to provide inputs to other algorithms that model the clinical effects in a second step.

Several DL methods have already been applied to extract medical information, reviewed recently by Shickel et al. [13]. As examples at different levels of data extraction, Qayyum et al. proposed a CNN framework to retrieve and classify multimodal medical images (MR, CT, PET) for 24 body organs, obtaining a 99.77% accuracy [162]. Wu et al. developed a DNN model to recognize clinical texts in medical documents, which outperformed state-of-the-art methods [163]. Other DL methods have been developed for identifying and extracting the relation existing between patient medical problems, treatments, and tests ("clinical relation extraction"). Tested on the i2b2 relation challenge dataset [222], Lv et al. proposed an SAE-based relation classification model [164]. They showed that their model performed better than one based on the original word features. Therefore, even if these studies have not been carried out directly in relation to radiotherapy, they are applicable to the extraction of the majority of data useful for radiotherapy predictive modeling (text, codes, DICOM).

Multiple radiation oncology research groups have shown the value of machine learning methods for predicting radiotherapy outcomes, although clinical adoption is going slow due to the huge barrier of understanding these complex models by clinicians [223–225]. The prediction of radiation toxicities has, for example, been studied with machine learning techniques for several diseases such as lung [226], prostate [227], or H&N cancer [228]. Meanwhile, many DL methods have been applied to the analysis of medical data (including outcome prediction), and have already been the subject of recent reviews [13,14]. DL methods appear indeed to be promising for outcome prediction in radiotherapy. In prostate radiotherapy big data analytics, Coates et al. stated that DL strategies may prove to be useful in the case of radiation-induced biological effects, given the complexity of the physical and biological processes involved [229]. Concerning neuroblastoma, a pediatric cancer disease that is in some cases irradiated, Salazar et al. emphasized the fact that a genetic approach alone is unlikely to yield fruitful drug discovery, as there are very rare recurrent somatic mutations detected in this disease [230]. That is why DL approaches, which can integrate more sophisticated data generated from patients and animal models, may be best suited to model the complexity of neuroblastoma etiology. Muthalaly et al. demonstrated that DL networks can be trained to predict mortality in acute lymphoblastic leukemia, a childhood disease for which radiotherapy may be used as part of treatment [231]. Nevertheless, no consistent work combining DL methods and modeling of radiotherapy clinical effects has been published until early 2017 [219]. Since then, several authors have tried to model, using very different DL-based approaches, the risks associated with radiotherapy treatments. Zhen et al. demonstrated that a pre-trained CNN is able to model rectum dose distribution and predict rectum toxicity after cervical cancer radiotherapy [159]. They showed that transfer learning might overcome the difficulty to train a CNN from scratch, as patient sample size is often small. Jochem et al. learned a three-layer DNN model on radiomic features for survival prediction in lung and H&N cancers [160]. Although they did not observe a superior performance compared to that of conventional modeling strategies, they demonstrated that DL methods represent a major advantage because feature selection is no longer a required component. To predict local failure following SBRT, Aneja et al. merged a CNN and a DNN to analyze respectively patient CT simulation and CRF. They showed that DNN could improve the predictive ability compared to logistic regression [156]. Li et al. also used imaging data to predict survival risks for rectal cancer patients. They used the biological target volume from PET-CT as training data for a CNN, and stated that their model could predict the tumor recurrence risk better than current models [157]. To predict quality of life (QOL) in urinary and bowel domains after prostate SBRT, Qi et al. proposed a DNN model trained with DVH data [158]. They showed that their model was able to predict the QOL scores with ±5 points. A combination of three learning components (GAN, DNN, and deep Q-network) was proposed by Tseng et al. to build an autonomous clinical decision support system for a response-based ART [161]. Using clinical, genetic, and radiomic features, their framework allowed to adapt patient dose per fraction in a response-adapted treatment setting.

3.10. Summary

We reviewed publications in which DL approaches were applied in radiotherapy. We observed that all steps of patient workflow in radiotherapy were related, to a greater or lesser degree, to potential applications of DL. Automatic segmentation of medical structures is, for example, already widely discussed in the literature, for all locations and for many imaging modalities. However, there have been few studies on tumor delineation, for which there is still considerable room for improvement. It should be noted that the automatic delineation of tumors has applications during the treatment planning stage as well as during adaptive radiotherapy, for example, to automatically monitor the evolution of tumor lesions through patient positioning images.

We believe that these images, made during radiotherapy treatments to control patient positioning, are indeed an important source of inspiration for DL applications. They are available in large numbers because several images can be made during each treatment fraction, and patient treatments usually comprise about thirty fractions. One disadvantage of these images is that they are generally of poorer quality than diagnostic images; we have noted that the first publications regarding improvement of their quality by DL methods have been published recently. Regarding this application of positioning images, DL could make a major contribution through some CADx and CADe techniques that are currently used for diagnosis. For example, DL could assist in the detection of new metastases during treatment or the development of new tracking techniques. Patient motion management is indeed a problem in which there is still much room for improvement in the context of radiotherapy, in which the very first applications of DL methods were published. There have been very few studies on DL applications for treatment planning published to date, while the dosimetric databases are widespread and quite easily exploitable. Finally, concerning the use of DL for outcome prediction in radiotherapy, the first studies have been published recently, and the field of research on this subject remains vast and complex.

4. Deep learning criticisms

Despite their many advantages, DNNs have not been imposed much in clinical routine. One of the main criticisms is the lack of theory concerning DL and the fact that standard general principles are mostly empirically obtained. The choice of the general architecture of the network (the layout of the layers, their number, the size of filters, etc.) best suited to the problem to be solved is mostly guided by intuition and carried out experimentally. There are also some recognized tricks and tips for improving learning but without theory to justify them.

The true generalization capability of DNNs in image vision can also be questioned because they can be fooled [232]. Changing an image in a way imperceptible to humans can thus lead a DNN to label it as something entirely different. It is also possible to produce images that are completely unrecognizable to the human eyes but labeled with certainty by the neural network. It is therefore important to keep in mind that even if some DNNs can perform at near-human ability, the way they perceive and interpret the world is far different from the human way. Among other things, they lack explicit ways of representing causal relationships and of integrating abstract knowledge, which make them prone to error due to unavoidable finite and incomplete training set.

The need to build coherent and sufficiently large databases in the field of medicine is another challenge. Indeed, DNNs require a large diversity of training examples in order to be effective in real-world operation. This implies that neural networks need to be trained with a sufficient variety of representative examples to be able to capture the data underlying structure that allows them to generalize new cases. Another consequence is that a neural network trained on datasets collected with biases (due to intra- or inter-expert variation for example) will certainly exhibit the same biases. Furthermore, when the algorithm is based on supervised learning, the classes of the patterns must be known as well, which requires extra effort from clinical experts. Rigorous collection of data is thus a critical and often underestimated and time-consuming part of DL (and machine learning in general). For example, in one of our previous works focused on brain metastases segmentation in multimodal MRI, the constitution of a database composed of information of 182 patients required nearly three months of work [78]. With current radiotherapy treatment planning systems each patient's data often still needs to be manually selected, restored, opened on the manufacturer's software, and then exported individually to obtain exploitable DICOM files.

This difficulty in building large databases has been noted in many of the publications cited above, in almost all categories in Section 3. Although the use of picture archiving and communication systems (PACS) in most western hospitals allows access to millions of medical images [5], many authors indicate for example that there is a lack of properly labeled imagery databases for the development of automatic segmentation methods based on DL [88,104,233]. Limited availability of datasets is also an issue for the further advancement of CAD, and building well annotated datasets seems at least as crucial as developing new algorithms [118]. This is particularly true if these methods have to be applied to low-quality images, such as those used to localize patient during IGRT procedures. As pointed out by Viergever et al. the development of registration-based DL methods may be hampered by one of the main obstacles to the implantation of registration techniques in medical imaging, namely, the lack of reference datasets for validation, and thus for learning [199]. Concerning outcome prediction, the road toward predictive radiotherapy by DL methods could still be long. It is first crucial that radiation oncologists should be able to understand the prediction of DL algorithms. However, these algorithms are still considered "black boxes", and their interpretation is often difficult [13]. About training, major challenges, such as heterogeneous data, non-standardized terminologies, and computer or workflow incompatibility will make the dream of big data research difficult in radiotherapy [234].

5. Conclusion

Several DL methods that can be applied to a step of the radiotherapy workflow have been recently published. Despite their promising results, we are probably, at this time, only at the prehistory of the use of these methods in radiotherapy. The number of applications and their performance will likely evolve rapidly in the coming years. The main obstacle to this development could be related to the lack of training data, as pointed out by many authors cited in this survey. We have tried to provide a number of ideas and perspectives to explore, but obviously, there are still many approaches to be developed and many applications to imagine in this exciting field of DL for radiotherapy.

Conflicts of interest

None declared.

Funding

This research did not receive any specific grant from funding agencies in the public, commercial, or not-for-profit sectors.

References

[1] I.E. Naqa, M.J. Murphy, What is machine learning? in: I.E. Naqa, R. Li, M.J. Murphy (Eds.), Mach. Learn. Radiat. Oncol Springer International Publishing, 2015, pp. 3–11, https://doi.org/10.1007/978-3-319-18305-3_1.
[2] M. Feng, G. Valdes, N. Dixit, T.D. Solberg, Machine learning in radiation oncology: opportunities, requirements, and needs, Front. Oncol. 8 (2018), https://doi.org/10.3389/fonc.2018.00110.
[3] G. Sharp, K.D. Fritscher, V. Pekar, M. Peroni, N. Shusharina, H. Veeraraghavan, J. Yang, Vision 20/20: perspectives on automated image segmentation for radiotherapy, Med. Phys. 41 (2014), https://doi.org/10.1118/1.4871620.
[4] Y. LeCun, Y. Bengio, G. Hinton, Deep learning, Nature 521 (2015) 436–444, https://doi.org/10.1038/nature14539.
[5] G. Litjens, T. Kooi, B.E. Bejnordi, A.A.A. Setio, F. Ciompi, M. Ghafoorian, J.A.W.M. van der Laak, B. van Ginneken, C.I. Sánchez, A survey on deep learning in medical image analysis, Med. Image Anal. 42 (2017) 60–88, https://doi.org/10.1016/j.media.2017.07.005.
[6] D. Wu, N. Sharma, M. Blumenstein, Recent advances in video-based human action recognition using deep learning: a review, in: 2017 Int. Jt. Conf. Neural Netw. IJCNN, 2017, pp. 2865–2872, https://doi.org/10.1109/IJCNN.2017.7966210.
[7] I. El Naqa, K. Brock, Y. Yu, K. Langen, E.E. Klein, On the Fuzziness of machine learning, neural networks, and artificial intelligence in radiation oncology, Int. J. Radiat. Oncol 100 (2018) 1–4, https://doi.org/10.1016/j.ijrobp.2017.06.011.
[8] L. Xing, E.A. Krupinski, J. Cai, Artificial intelligence will soon change the landscape of medical physics research and practice, Med. Phys. (2018), https://doi.org/10.1002/mp.12831.
[9] J.-G. Lee, S. Jun, Y.-W. Cho, H. Lee, G.B. Kim, J.B. Seo, N. Kim, Deep learning in medical imaging: general overview, Korean J. Radiol. 18 (2017) 570, https://doi.org/10.3348/kjr.2017.18.4.570.
[10] K. Suzuki, Overview of deep learning in medical imaging, Radiol. Phys. Technol (2017) 1–17, https://doi.org/10.1007/s12194-017-0406-5.
[11] D. Shen, G. Wu, H.-I. Suk, Deep learning in medical image analysis, Annu. Rev. Biomed. Eng. 19 (2017) 221–248, https://doi.org/10.1146/annurev-bioeng-071516-044442.
[12] R. Miotto, F. Wang, S. Wang, X. Jiang, J.T. Dudley, Deep learning for healthcare: review, opportunities and challenges, Briefings Bioinf. (2017), https://doi.org/10.1093/bib/bbx044.
[13] B. Shickel, P.J. Tighe, A. Bihorac, P. Rashidi, Deep EHR: a survey of recent advances in deep learning techniques for electronic health record (EHR) analysis, IEEE J. Biomed. Health Inform. PP (2017), https://doi.org/10.1109/JBHI.2017.2767063, 1–1.
[14] D. Ravì, C. Wong, F. Deligianni, M. Berthelot, J. Andreu-Perez, B. Lo, G.Z. Yang, Deep learning for health informatics, IEEE J. Biomed. Health Inform 21 (2017) 4–21, https://doi.org/10.1109/JBHI.2016.2636665.
[15] I. Goodfellow, Y. Bengio, A. Courville, Deep Learning, MIT Press, 2016. http://www.deeplearningbook.org/.
[16] T. Zhou, G. Han, B.N. Li, Z. Lin, E.J. Ciaccio, P.H. Green, J. Qin, Quantitative analysis of patients with celiac disease by video capsule endoscopy: a deep learning method, Comput. Biol. Med. 85 (2017) 1–6, https://doi.org/10.1016/j.compbiomed.2017.03.031.
[17] Y. Bengio, Learning deep architectures for AI, found. Trends® mach, Learning 2 (2009) 1–127, https://doi.org/10.1561/2200000006.
[18] D. Crevier, Ai: the Tumultuous History of the Search for Artificial Intelligence, first ed., Basic Books, New York, NY, 1993.
[19] J. McCarthy, P. Hayes, Some philosophical problems from the standpoint of artificial intelligence, Read. Plan 393 (1969) 1–51.
[20] M.A. Boden, Artificial Intelligence and Natural Man, Basic Books, 1977.

[21] A.M. Turing, Computing machinery and intelligence, Mind 59 (1950) 433–460.
[22] A. Newell, H. Simon, The logic theory machine–A complex information processing system, IEEE Trans. Inf. Theor. 2 (1956) 61–79, https://doi.org/10.1109/TIT.1956.1056797.
[23] A.L. Samuel, Some studies in machine learning using the game of checkers, IBM J. Res. Dev. 3 (1959) 210–229, https://doi.org/10.1147/rd.33.0210.
[24] R.S. Michalski, J.G. Carbonell, T.M. Mitchell, Machine Learning: an Artificial Intelligence Approach, Springer Science & Business Media, 2013.
[25] P. Natarajan, J.C. Frenzel, D.H. Smaltz, Demystifying Big Data and Machine Learning for Healthcare, CRC Press, 2017.
[26] T.M. Mitchell, Machine Learning, McGraw-Hill, New York, 1997.
[27] M. Mohri, A. Rostamizadeh, A. Talwalkar, Foundations of Machine Learning, The MIT Press, 2012.
[28] K.M.V. Perumal, Performance evaluation and comparative analysis of various machine learning techniques for diagnosis of breast cancer, Biomed. Res. 27 (2016). http://www.alliedacademies.org/abstract/performance-evaluation-and-comparative-analysis-of-various-machine-learning-techniques-for-diagnosis-of-breast-cancer-4545.html. (Accessed 19 April 2018).
[29] R. Miotto, L. Li, B.A. Kidd, J.T. Dudley, Deep patient: an unsupervised representation to predict the future of patients from the electronic health records, Sci. Rep. 6 (2016) 26094, https://doi.org/10.1038/srep26094.
[30] B. Mwangi, T.S. Tian, J.C. Soares, A review of feature reduction techniques in neuroimaging, Neuroinformatics 12 (2014) 229–244, https://doi.org/10.1007/s12021-013-9204-3.
[31] A. Jalalimanesh, H. Shahabi Haghighi, A. Ahmadi, M. Soltani, Simulation-based optimization of radiotherapy: agent-based modeling and reinforcement learning, Math. Comput. Simulat. 133 (2017) 235–248, https://doi.org/10.1016/j.matcom.2016.05.008.
[32] N. Tajbakhsh, J.Y. Shin, S.R. Gurudu, R.T. Hurst, C.B. Kendall, M.B. Gotway, J. Liang, Convolutional neural networks for medical image analysis: full training or fine tuning? IEEE Trans. Med. Imag. 35 (2016) 1299–1312, https://doi.org/10.1109/TMI.2016.2535302.
[33] F. Rosenblatt, The perceptron, a perceiving and recognizing automaton, Cornell Aeronaut. Lab. - Repp. 85–460-1, http://blogs.umass.edu/brain-wars/files/2016/03/rosenblatt-1957.pdf, 1957. (Accessed 9 November 2017).
[34] Y. Lecun, Une procedure d'apprentissage pour reseau a seuil asymmetrique (A learning scheme for asymmetric threshold networks), Cognitiva 85 (1985) 599–604.
[35] D.E. Rumelhart, G.E. Hinton, R.J. Williams, Learning representations by back-propagating errors, Nature 323 (1986), https://doi.org/10.1038/323533a0, 323533a0.
[36] A. Krizhevsky, I. Sutskever, G.E. Hinton, Imagenet classification with deep convolutional neural networks, in: Adv. Neural Inf. Process. Syst, 2012, pp. 1097–1105.
[37] S.K. Zhou, H. Greenspan, D. Shen, Deep Learning for Medical Image Analysis, Academic Press, 2017.
[38] F. van Veen, The neural network Zoo, Asimov Inst, http://www.asimovinstitute.org/neural-network-zoo/, 2016. (Accessed 10 November 2017), http://www.asimovinstitute.org/neural-network-zoo/.
[39] T. Mikolov, M. Karafiát, L. Burget, J. Černocký, S. Khudanpur, Recurrent neural network based language model, in: Elev. Annu. Conf. Int. Speech Commun. Assoc, 2010.
[40] P. Baldi, Autoencoders, unsupervised learning, and deep architectures, in: Proc. ICML Workshop Unsupervised Transf. Learn, 2012, pp. 37–49.
[41] I. Sutskever, G.E. Hinton, G.W. Taylor, The recurrent temporal restricted Boltzmann machine, in: D. Koller, D. Schuurmans, Y. Bengio, L. Bottou (Eds.), Adv. Neural Inf. Process. Syst, vol. 21, Curran Associates, Inc., 2009, pp. 1601–1608. http://papers.nips.cc/paper/3567-the-recurrent-temporal-restricted-boltzmann-machine.pdf.
[42] H. Lee, R. Grosse, R. Ranganath, A.Y. Ng, Convolutional deep belief networks for scalable unsupervised learning of hierarchical representations, in: Proc. 26th Annu. Int. Conf. Mach. Learn., ACM, 2009, pp. 609–616.
[43] I. Goodfellow, J. Pouget-Abadie, M. Mirza, B. Xu, D. Warde-Farley, S. Ozair, A. Courville, Y. Bengio, Generative adversarial nets, in: Adv. Neural Inf. Process. Syst, 2014, pp. 2672–2680.
[44] G. Antipov, S.-A. Berrani, N. Ruchaud, J.-L. Dugelay, Learned vs. Hand-Crafted features for pedestrian gender recognition, in: Proc. 23rd ACM Int. Conf. Multimed, ACM, New York, NY, USA, 2015, pp. 1263–1266, https://doi.org/10.1145/2733373.2806332.
[45] J. Bernal, K. Kushibar, D.S. Asfaw, S. Valverde, A. Oliver, R. Martí, X. Lladó, Deep Convolutional Neural Networks for Brain Image Analysis on Magnetic Resonance Imaging: A Review, ArXiv171203747 Cs, 2017, http://arxiv.org/abs/1712.03747.
[46] H. Wang, Y. Cai, Y. Zhang, H. Pan, W. Lv, H. Han, Deep learning for image retrieval: what works and what Doesn't, in: IEEE, 2015, pp. 1576–1583, https://doi.org/10.1109/ICDMW.2015.121.
[47] K. Simonyan, A. Zisserman, Very Deep Convolutional Networks for Large-Scale Image Recognition, ArXiv14091556 Cs, 2014, http://arxiv.org/abs/1409.1556.
[48] O. Ronneberger, P. Fischer, T. Brox, U-net: convolutional networks for biomedical image segmentation, in: Int. Conf. Med. Image Comput. Comput.-Assist. Interv, Springer, 2015, pp. 234–241.
[49] M.D. Zeiler, R. Fergus, Visualizing and understanding convolutional networks, in: Eur. Conf. Comput. Vis, Springer, 2014, pp. 818–833.
[50] G.C. Pereira, M. Traughber, R.F. Muzic, The role of imaging in radiation therapy planning: past, present, and future, BioMed Res. Int. 2014 (2014) 1–9, https://doi.org/10.1155/2014/231090.
[51] A.M. Owrangi, P.B. Greer, C.K. Glide-Hurst, MRI-only treatment planning: benefits and challenges, Phys. Med. Biol. 63 (2018), https://doi.org/10.1088/1361-6560/aaaca4, 05TR01.
[52] M.A. Schmidt, G.S. Payne, Radiotherapy planning using MRI, Phys. Med. Biol. 60 (2015) R323–R361, https://doi.org/10.1088/0031-9155/60/22/R323.
[53] S.-H. Hsu, Y. Cao, K. Huang, M. Feng, J.M. Balter, Investigation of a method for generating synthetic CT models from MRI scans of the head and neck for radiation therapy, Phys. Med. Biol. 58 (2013) 8419, https://doi.org/10.1088/0031-9155/58/23/8419.
[54] B. Stimpel, C. Syben, T. Würfl, K. Mentl, A. Dörfler, A. Maier, MR to X-Ray Projection Image Synthesis, ArXiv171007498 Cs, 2017, http://arxiv.org/abs/1710.07498.
[55] X. Han, MR-based synthetic CT generation using a deep convolutional neural network method, Med. Phys. 44 (2017) 1408–1419, https://doi.org/10.1002/mp.12155.
[56] D. Nie, X. Cao, Y. Gao, L. Wang, D. Shen, Estimating CT image from MRI data using 3D fully convolutional networks, in: G. Carneiro, D. Mateus, L. Peter, A. Bradley, J.M.R.S. Tavares, V. Belagiannis, J.P. Papa, J.C. Nascimento, M. Loog, Z. Lu, J.S. Cardoso, J. Cornebise (Eds.), Deep Learn. Data Labeling Med. Appl, Springer International Publishing, 2016, pp. 170–178, https://doi.org/10.1007/978-3-319-46976-8_18.
[57] J.M. Wolterink, A.M. Dinkla, M.H.F. Savenije, P.R. Seevinck, C.A.T. van den Berg, I. Išgum, Deep MR to CT synthesis using unpaired data, in: Simul. Synth. Med. Imaging, Springer, Cham, 2017, pp. 14–23, https://doi.org/10.1007/978-3-319-68127-6_2.
[58] L. Xiang, Q. Wang, D. Nie, L. Zhang, X. Jin, Y. Qiao, D. Shen, Deep embedding convolutional neural network for synthesizing CT image from T1-Weighted MR image, Med. Image Anal. 47 (2018) 31–44, https://doi.org/10.1016/j.media.2018.03.011.
[59] C. Zhao, A. Carass, J. Lee, Y. He, J.L. Prince, Whole brain segmentation and labeling from CT using synthetic MR images, in: Mach. Learn. Med. Imaging, Springer, Cham, 2017, pp. 291–298, https://doi.org/10.1007/978-3-319-67389-9_34.
[60] K. Bahrami, F. Shi, I. Rekik, D. Shen, Convolutional neural network for reconstruction of 7T-like images from 3T MRI using appearance and anatomical features, in: Deep Learn. Data Labeling Med. Appl, Springer, Cham, 2016, pp. 39–47, https://doi.org/10.1007/978-3-319-46976-8_5.
[61] S.S. Gurbani, E. Schreibmann, A.A. Maudsley, J.S. Cordova, B.J. Soher, H. Poptani, G. Verma, P.B. Barker, H. Shim, L.A.D. Cooper, A convolutional neural network to filter artifacts in spectroscopic MRI, Magn. Reson. Med. (2018), https://doi.org/10.1002/mrm.27166.
[62] L. Gjesteby, Q. Yang, Y. Xi, Y. Zhou, J. Zhang, G. Wang, Deep learning methods to guide CT image reconstruction and reduce metal artifacts, in: Med. Imaging 2017 Phys. Med. Imaging, International Society for Optics and Photonics, 2017, p. 101322W, https://doi.org/10.1117/12.2254091.
[63] L. Gjesteby, Q. Yang, Y. Xi, B. Claus, Y. Jin, B. De Man, G. Wang, Reducing metal streak artifacts in CT images via deep learning: pilot results, in: 14th Int. Meet. Fully Three-dimens. Image Reconstr. Radiol. Nucl. Med, 2017, pp. 611–614.
[64] C. Dong, C.C. Loy, K. He, X. Tang, Image super-resolution using deep convolutional networks, IEEE Trans. Pattern Anal. Mach. Intell. 38 (2016) 295–307, https://doi.org/10.1109/TPAMI.2015.2439281.
[65] A. Ashfaq, Segmentation of Cone Beam CT in Stereotactic Radiosurgery, TRITA-sth, 2016:104, KTH, School of Technology and Health (STH)., 2016. http://kth.diva-portal.org/smash/record.jsf?pid=diva2:975179. (Accessed 28 September 2017).
[66] S. Mori, Deep architecture neural network-based real-time image processing for image-guided radiotherapy, Phys. Med. 40 (2017) 79–87, https://doi.org/10.1016/j.ejmp.2017.07.013.
[67] H. Chen, Y. Zhang, W. Zhang, P. Liao, K. Li, J. Zhou, G. Wang, Low-dose CT via convolutional neural network, Biomed. Optic Express 8 (2017) 679–694, https://doi.org/10.1364/BOE.8.000679.
[68] Q. Yang, P. Yan, Y. Zhang, H. Yu, Y. Shi, X. Mou, M.K. Kalra, G. Wang, Low Dose Ct Image Denoising Using a Generative Adversarial Network with Wasserstein Distance and Perceptual Loss, ArXiv170800961 Cs, 2017, http://arxiv.org/abs/1708.00961.
[69] H. Zhang, L. Li, K. Qiao, L. Wang, B. Yan, L. Li, G. Hu, Image Prediction For Limited-Angle Tomography Via Deep Learning With Convolutional Neural Network, ArXiv Prepr. ArXiv160708707, 2016, https://arxiv.org/abs/1607.08707. (Accessed 26 July 2017).
[70] B. Ibragimov, D. Toesca, D. Chang, A. Koong, L. Xing, Combining deep learning with anatomical analysis for segmentation of the portal vein for liver SBRT planning, Phys. Med. Biol. 62 (2017) 8943–8958, https://doi.org/10.1088/1361-6560/aa9262.
[71] B. Ibragimov, D.A.S. Toesca, D.T. Chang, A.C. Koong, L. Xing, Deep learning-based autosegmentation of portal vein for prediction of central liver toxicity after SBRT, Int. J. Radiat. Oncol. Biol. Phys. 99 (2017). E672.
[72] K. Kamnitsas, W. Bai, E. Ferrante, S. McDonagh, M. Sinclair, N. Pawlowski, M. Rajchl, M. Lee, B. Kainz, D. Rueckert, B. Glocker, Ensembles of multiple models and architectures for robust brain tumour segmentation, in: Brainlesion Glioma Mult. Scler. Stroke Trauma. Brain Inj, Springer, Cham, 2017, pp. 450–462, https://doi.org/10.1007/978-3-319-75238-9_38.
[73] M. Havaei, A. Davy, D. Warde-Farley, A. Biard, A. Courville, Y. Bengio, C. Pal, P.-M. Jodoin, H. Larochelle, Brain tumor segmentation with deep neural networks, Med. Image Anal. 35 (2017) 18–31, https://doi.org/10.1016/j.media.2016.05.004.

[74] K. Kamnitsas, E. Ferrante, S. Parisot, C. Ledig, A.V. Nori, A. Criminisi, D. Rueckert, B. Glocker, Deepmedic for brain tumor segmentation, in: Brainlesion: Glioma, Multiple Sclerosis, Stroke and Traumatic Brain Injuries, Springer, Cham, 2016, pp. 138–149, https://doi.org/10.1007/978-3-319-55524-9_14.

[75] K. Kamnitsas, C. Ledig, V.F.J. Newcombe, J.P. Simpson, A.D. Kane, D.K. Menon, D. Rueckert, B. Glocker, Efficient multi-scale 3D CNN with fully connected CRF for accurate brain lesion segmentation, Med. Image Anal. 36 (2017) 61–78, https://doi.org/10.1016/j.media.2016.10.004.

[76] Y. Zhuge, A.V. Krauze, H. Ning, J.Y. Cheng, B.C. Arora, K. Camphausen, R.W. Miller, Brain tumor segmentation using holistically nested neural networks in MRI images, Med. Phys. 44 (2017) 5234–5243, https://doi.org/10.1002/mp.12481.

[77] Y. Liu, S. Stojadinovic, B. Hrycushko, Z. Wardak, S. Lau, W. Lu, Y. Yan, S.B. Jiang, X. Zhen, R. Timmerman, L. Nedzi, X. Gu, A deep convolutional neural network-based automatic delineation strategy for multiple brain metastases stereotactic radiosurgery, PLoS One 12 (2017), e0185844, https://doi.org/10.1371/journal.pone.0185844.

[78] O. Charron, A. Lallement, D. Jarnet, V. Noblet, J.-B. Clavier, P. Meyer, Automatic detection and segmentation of brain metastases on multimodal MR images with a deep convolutional neural network, Comput. Biol. Med. 95 (2018) 43–54, https://doi.org/10.1016/j.compbiomed.2018.02.004.

[79] A. de Brebisson, G. Montana, Deep neural networks for anatomical brain segmentation, in: proc. IEEE Conf. Comput. Vis. Pattern Recognit, Works (2015) 20–28.

[80] P. Moeskops, M.A. Viergever, A.M. Mendrik, L.S. de Vries, M.J.N.L. Benders, I. Isgum, Automatic segmentation of MR brain images with a convolutional neural network, IEEE Trans. Med. Imag. 35 (2016) 1252–1261, https://doi.org/10.1109/TMI.2016.2548501.

[81] J. Dolz, N. Betrouni, M. Quidet, D. Kharroubi, H.A. Leroy, N. Reyns, L. Massoptier, M. Vermandel, Stacking denoising auto-encoders in a deep network to segment the brainstem on {MRI} in brain cancer patients: a clinical study, Comput. Med. Imag. Graph. 52 (2016) 8–18, https://doi.org/10.1016/j.compmedimag.2016.03.003.

[82] M. Kim, G. Wu, D. Shen, Unsupervised deep learning for Hippocampus segmentation in 7.0 tesla MR images, in: Proc. 4th Int. Workshop Mach. Learn. Med. Imaging vol. 8184, Springer-Verlag New York, Inc., New York, NY, USA, 2013, pp. 1–8, https://doi.org/10.1007/978-3-319-02267-3_1.

[83] L. Cao, L. Li, J. Zheng, X. Fan, F. Yin, H. Shen, J. Zhang, Multi-task neural networks for joint hippocampus segmentation and clinical score regression, Multimed. Tool. Appl. (2018) 1–18, https://doi.org/10.1007/s11042-017-5581-1.

[84] J. Dolz, N. Reyns, N. Betrouni, D. Kharroubi, M. Quidet, L. Massoptier, M. Vermandel, A deep learning classification scheme based on augmented-enhanced features to segment organs at risk on the optic region in brain cancer patients, ArXiv170310480 Cs (2017). http://arxiv.org/abs/1703.10480. (Accessed 10 April 2017).

[85] X. Ren, L. Xiang, D. Nie, Y. Shao, H. Zhang, D. Shen, Q. Wang, Interleaved 3D-CNNs for joint segmentation of small-volume structures in head and neck CT images, Med. Phys. 45 (2018) 2063–2075, https://doi.org/10.1002/mp.12837.

[86] J. Dolz, C. Desrosiers, I.B. Ayed, 3D fully convolutional networks for subcortical segmentation in MRI: a large-scale study, Neuroimage (2017), https://doi.org/10.1016/j.neuroimage.2017.04.039.

[87] K. Kushibar, S. Valverde, S. Gonzalez-Villa, J. Bernal, M. Cabezas, A. Oliver, X. Llado, Automated Sub-Cortical Brain Structure Segmentation Combining Spatial and Deep Convolutional Features, ArXiv170909075 Cs, 2017, http://arxiv.org/abs/1709.09075.

[88] C. Wachinger, M. Reuter, T. Klein, DeepNAT: deep convolutional neural network for segmenting neuroanatomy, Neuroimage (2017), https://doi.org/10.1016/j.neuroimage.2017.02.035.

[89] F. Milletari, S.-A. Ahmadi, C. Kroll, A. Plate, V. Rozanski, J. Maiostre, J. Levin, O. Dietrich, B. Ertl-Wagner, K. Bötzel, N. Navab, Hough-CNN: deep learning for segmentation of deep brain regions in MRI and ultrasound, Comput. Vis. Image Understand. 164 (2017) 92–102, https://doi.org/10.1016/j.cviu.2017.04.002.

[90] M.U. Dalmış, G. Litjens, K. Holland, A. Setio, R. Mann, N. Karssemeijer, A. Gubern-Mérida, Using deep learning to segment breast and fibroglandular tissue in MRI volumes, Med. Phys. 44 (2017) 533–546, https://doi.org/10.1002/mp.12079.

[91] Y. Guo, Y. Gao, D. Shen, Deformable MR prostate segmentation via deep feature learning and sparse patch matching, IEEE Trans. Med. Imag. 35 (2016) 1077–1089, https://doi.org/10.1109/TMI.2015.2508280.

[92] F. Milletari, N. Navab, S.A. Ahmadi, V-net: fully convolutional neural networks for volumetric medical image segmentation, in: 2016 Fourth Int. Conf. 3D Vis. 3DV, 2016, pp. 565–571, https://doi.org/10.1109/3DV.2016.79.

[93] L. Ma, R. Guo, G. Zhang, F. Tade, D.M. Schuster, P. Nieh, V. Master, B. Fei, Automatic segmentation of the prostate on CT images using deep learning and multi-atlas fusion, in: International Society for Optics and Photonics, 2017, p. 101332O, https://doi.org/10.1117/12.2255755.

[94] X. Zhou, T. Ito, R. Takayama, S. Wang, T. Hara, H. Fujita, Three-dimensional CT image segmentation by combining 2D fully convolutional network with 3D majority voting, in: Deep Learn. Data Labeling Med. Appl, Springer, Cham, 2016, pp. 111–120, https://doi.org/10.1007/978-3-319-46976-8_12.

[95] R. Trullo, C. Petitjean, S. Ruan, B. Dubray, D. Nie, D. Shen, Segmentation of organs at risk in thoracic CT images using a SharpMask architecture and conditional random fields, in: 2017 IEEE 14th Int. Symp. Biomed. Imaging ISBI 2017, 2017, pp. 1003–1006, https://doi.org/10.1109/ISBI.2017.7950685.

[96] R. Trullo, C. Petitjean, D. Nie, D. Shen, S. Ruan, Joint segmentation of multiple thoracic organs in CT images with two collaborative deep architectures, in: Deep Learn. Med. Image Anal. Multimodal Learn. Clin. Decis. Support, Springer, Cham, 2017, pp. 21–29, https://doi.org/10.1007/978-3-319-67558-9_3.

[97] T. Lustberg, J. van Soest, M. Gooding, D. Peressutti, P. Aljabar, J. van der Stoep, W. van Elmpt, A. Dekker, Clinical evaluation of atlas and deep learning based automatic contouring for lung cancer, Radiother. Oncol. J. Eur. Soc. Ther. Radiol. Oncol (2017), https://doi.org/10.1016/j.radonc.2017.11.012.

[98] B. Ibragimov, L. Xing, Segmentation of organs-at-risks in head and neck CT images using convolutional neural networks, Med. Phys. 44 (2017) 547–557, https://doi.org/10.1002/mp.12045.

[99] T. Fechter, S. Adebahr, D. Baltas, I. Ben Ayed, C. Desrosiers, J. Dolz, Esophagus segmentation in CT via 3D fully convolutional neural network and random walk, Med. Phys. 44 (2017) 6341–6352, https://doi.org/10.1002/mp.12593.

[100] P. Hu, F. Wu, J. Peng, Y. Bao, F. Chen, D. Kong, Automatic abdominal multi-organ segmentation using deep convolutional neural network and time-implicit level sets, Int. J. Comput. Assist. Radiol. Surg (2016) 1–13, https://doi.org/10.1007/s11548-016-1501-5.

[101] M. Vania, D. Mureja, D. Lee, Automatic Spine Segmentation Using Convolutional Neural Network Via Redundant Generation of Class Labels for 3D Spine Modeling, ArXiv171201640 Cs, 2017, http://arxiv.org/abs/1712.01640.

[102] Y. Yuan, Hierarchical Convolutional-Deconvolutional Neural Networks for Automatic Liver and Tumor Segmentati, ArXiv171004540 Cs, 2017, http://arxiv.org/abs/1710.04540.

[103] A. Ben-Cohen, I. Diamant, E. Klang, M. Amitai, H. Greenspan, Fully convolutional network for liver segmentation and lesions detection, in: Deep Learn. Data Labeling Med. Appl, Springer, Cham, 2016, pp. 77–85, https://doi.org/10.1007/978-3-319-46976-8_9.

[104] F. Lu, F. Wu, P. Hu, Z. Peng, D. Kong, Automatic 3D liver location and segmentation via convolutional neural network and graph cut, Int. J. Comput. Assist. Radiol. Surg 12 (2017) 171–182, https://doi.org/10.1007/s11548-016-1467-3.

[105] W. Qin, J. Wu, F. Han, Y. Yuan, W. Zhao, B. Ibragimov, J. Gu, L. Xing, Superpixel-based and boundary-sensitive convolutional neural network for automated liver segmentation, Phys. Med. Biol. (2018), https://doi.org/10.1088/1361-6560/aabd19.

[106] P.F. Christ, F. Ettlinger, F. Grün, M.E.A. Elshaera, J. Lipkova, S. Schlecht, F. Ahmaddy, S. Tatavarty, M. Bickel, P. Bilic, Others, Automatic Liver and Tumor Segmentation of CT and MRI Volumes Using Cascaded Fully Convolutional Neural Networks, ArXiv prepr. ArXiv170205970, 2017, https://arxiv.org/abs/1702.05970. (Accessed 27 February 2017).

[107] K. Men, J. Dai, Y. Li, Automatic segmentation of the clinical target volume and organs at risk in the planning CT for rectal cancer using deep dilated convolutional neural networks, Med. Phys. (2017), https://doi.org/10.1002/mp.12602.

[108] Y. Yuan, M. Chao, Y.-C. Lo, Automatic skin lesion segmentation using deep fully convolutional networks with jaccard distance, IEEE Trans. Med. Imag. 36 (2017) 1876–1886, https://doi.org/10.1109/TMI.2017.2695227.

[109] S. Trebeschi, J.J.M. van Griethuysen, D.M.J. Lambregts, M.J. Lahaye, C. Parmer, F.C.H. Bakers, N.H.G.M. Peters, R.G.H. Beets-Tan, H.J.W.L. Aerts, Deep learning for fully-automated localization and segmentation of rectal cancer on multiparametric MR, Sci. Rep. 7 (2017), https://doi.org/10.1038/s41598-017-05728-9.

[110] K.H. Cha, L.M. Hadjiiski, R.K. Samala, H.-P. Chan, R.H. Cohan, E.M. Caoili, C. Paramagul, A. Alva, A.Z. Weizer, Bladder cancer segmentation in CT for treatment response assessment: application of deep-learning convolution neural network—a pilot study, Tomogr. J. Imaging Res 2 (2016) 421–429, https://doi.org/10.18383/j.tom.2016.00184.

[111] R. Vivanti, A. Szeskin, N. Lev-Cohain, J. Sosna, L. Joskowicz, Automatic detection of new tumors and tumor burden evaluation in longitudinal liver CT scan studies, Int. J. Comput. Assist. Radiol. Surg 12 (2017) 1945–1957, https://doi.org/10.1007/s11548-017-1660-z.

[112] K. Men, X. Chen, Y. Zhang, T. Zhang, J. Dai, J. Yi, Y. Li, Deep deconvolutional neural network for target segmentation of nasopharyngeal cancer in planning computed tomography images, Front. Oncol 7 (2017), https://doi.org/10.3389/fonc.2017.00315.

[113] Y. Wang, C. Zu, G. Hu, Y. Luo, Z. Ma, K. He, X. Wu, J. Zhou, Automatic tumor segmentation with deep convolutional neural networks for radiotherapy applications, Neural Process. Lett. (2018) 1–12, https://doi.org/10.1007/s11063-017-9759-3.

[114] C.E. Cardenas, R.E. McCarroll, L.E. Court, B. Elgohari, H. Elhalawani, C.D. Fuller, M. Jomaa, M.A.M. Meheissen, A.S.R. Mohamed, A. Rao, B. Williams, A. Wong, J. Yang, M. Aristophanous, Deep learning algorithm for auto-delineation of high-risk oropharyngeal clinical target volumes with built-in dice similarity coefficient parameter optimization function, Int. J. Radiat. Oncol (2018), https://doi.org/10.1016/j.ijrobp.2018.01.114.

[115] M. Hatt, B. Laurent, A. Ouahabi, H. Fayad, S. Tan, L. Li, W. Lu, V. Jaouen, C. Tauber, J. Czakon, F. Drapejkowski, W. Dyrka, S. Camarasu-Pop, F. Cervenansky, P. Girard, T. Glatard, M. Kain, Y. Yao, C. Barillot, A. Kirov, D. Visvikis, The first MICCAI challenge on PET tumor segmentation, Med. Image Anal. 44 (2018) 177–195, https://doi.org/10.1016/j.media.2017.12.007.

[116] R. Anirudh, J.J. Thiagarajan, T. Bremer, H. Kim, Lung nodule detection using 3D convolutional neural networks trained on weakly labeled data, in: G.D. Tourassi, S.G. Armato (Eds.), 2016, p. 978532, https://doi.org/10.1117/12.2214876.

[117] H.R. Roth, L. Lu, J. Liu, J. Yao, A. Seff, K. Cherry, L. Kim, R.M. Summers, Improving computer-aided detection using convolutional neural networks and random view aggregation, IEEE Trans. Med. Imag. 35 (2016) 1170–1181, https://doi.org/10.1109/TMI.2015.2482920.

[118] H.C. Shin, H.R. Roth, M. Gao, L. Lu, Z. Xu, I. Nogues, J. Yao, D. Mollura, R.M. Summers, Deep convolutional neural networks for computer-aided detection: CNN architectures, dataset characteristics and transfer learning, IEEE Trans. Med. Imag. 35 (2016) 1285–1298, https://doi.org/10.1109/TMI.2016.2528162.

[119] A. Teramoto, H. Fujita, O. Yamamuro, T. Tamaki, Automated detection of pulmonary nodules in PET/CT images: ensemble false-positive reduction using a convolutional neural network technique, Med. Phys. 43 (2016) 2821–2827, https://doi.org/10.1118/1.4948498.

[120] I. Ali, G.R. Hart, G. Gunabushanam, Y. Liang, W. Muhammad, B. Nartowt, M. Kane, X. Ma, J. Deng, Lung nodule detection via deep reinforcement learning, Front. Oncol 8 (2018), https://doi.org/10.3389/fonc.2018.00108.

[121] Y. Zhu, L. Wang, M. Liu, C. Qian, A. Yousuf, A. Oto, D. Shen, MRI-based prostate cancer detection with high-level representation and hierarchical classification, Med. Phys. 44 (2017) 1028–1039, https://doi.org/10.1002/mp.12116.

[122] Max Loschs, Thesis: detection and segmentation of brain metastases with deep convolutional networks. http://www.diva-portal.se/smash/get/diva2:853460/FULLTEXT01.pdf, 2015. (Accessed 26 October 2016).

[123] A. Mastmeyer, G. Pernelle, R. Ma, L. Barber, T. Kapur, Accurate model-based segmentation of gynecologic brachytherapy catheter collections in MRI-images, Med. Image Anal. 42 (2017) 173–188, https://doi.org/10.1016/j.media.2017.06.011.

[124] S. Belharbi, C. Chatelain, R. Hérault, S. Adam, S. Thureau, M. Chastan, R. Modzelewski, Spotting L3 slice in CT scans using deep convolutional network and transfer learning, Comput. Biol. Med. 87 (2017) 95–103, https://doi.org/10.1016/j.compbiomed.2017.05.018.

[125] B.D. de Vos, M.A. Viergever, P.A. de Jong, I. Išgum, Automatic slice identification in 3D medical images with a ConvNet regressor, in: Deep Learn. Data Labeling Med. Appl, Springer, Cham, 2016, pp. 161–169, https://doi.org/10.1007/978-3-319-46976-8_17.

[126] H.R. Roth, J. Yao, L. Lu, J. Stieger, J.E. Burns, R.M. Summers, Detection of sclerotic spine metastases via random aggregation of deep convolutional neural network classifications, in: J. Yao, B. Glocker, T. Klinder, S. Li (Eds.), Recent Adv. Comput. Methods Clin. Appl. Spine Imaging, Springer International Publishing, Cham, 2015, pp. 3–12. http://link.springer.com/10.1007/978-3-319-14148-0_1. (Accessed 16 January 2017).

[127] D. Forsberg, E. Sjöblom, J.L. Sunshine, Detection and labeling of vertebrae in MR images using deep learning with clinical annotations as training data, J. Digit. Imag. 30 (2017) 406–412, https://doi.org/10.1007/s10278-017-9945-x.

[128] J. Hetherington, V. Lessoway, V. Gunka, P. Abolmaesumi, R. Rohling, SLIDE: automatic spine level identification system using a deep convolutional neural network, Int. J. Comput. Assist. Radiol. Surg (2017) 1–10, https://doi.org/10.1007/s11548-017-1575-8.

[129] J. Hetherington, M. Pesteie, V.A. Lessoway, P. Abolmaesumi, R.N. Rohling, Identification and Tracking of Vertebrae in Ultrasound Using Deep Networks with Unsupervised Feature Learning, 2017, https://doi.org/10.1117/12.2252641, p. 101350K–101350K–7.

[130] Y. Zheng, D. Liu, B. Georgescu, H. Nguyen, D. Comaniciu, 3D deep learning for efficient and robust landmark detection in volumetric data, in: Int. Conf. Med. Image Comput. Comput.-Assist. Interv, Springer, 2015, pp. 565–572. http://link.springer.com/chapter/10.1007/978-3-319-24553-9_69. (Accessed 20 July 2017).

[131] F.C. Ghesu, B. Georgescu, T. Mansi, D. Neumann, J. Hornegger, D. Comaniciu, An artificial agent for anatomical landmark detection in medical images, in: Int. Conf. Med. Image Comput. Comput.-Assist. Interv, Springer, 2016, pp. 229–237. http://link.springer.com/chapter/10.1007/978-3-319-46726-9_27. (Accessed 24 July 2017).

[132] J. Zhang, M. Liu, D. Shen, Detecting anatomical landmarks from limited medical imaging data using two-stage task-oriented deep neural networks, IEEE Trans. Image Process. Publ. IEEE Signal Process. Soc. 26 (2017) 4753–4764, https://doi.org/10.1109/TIP.2017.2721106.

[133] A. Esteva, B. Kuprel, R.A. Novoa, J. Ko, S.M. Swetter, H.M. Blau, S. Thrun, Dermatologist-level classification of skin cancer with deep neural networks, Nature 542 (2017) 115–118, https://doi.org/10.1038/nature21056.

[134] K.-L. Hua, C.-H. Hsu, S.C. Hidayati, W.-H. Cheng, Y.-J. Chen, Computer-aided classification of lung nodules on computed tomography images via deep learning technique, OncoTargets Ther. 8 (2015) 2015–2022, https://doi.org/10.2147/OTT.S80733.

[135] D. Kumar, A. Wong, D.A. Clausi, Lung nodule classification using deep features in CT images, in: Comput. Robot Vis. CRV 2015 12th Conf. on, IEEE, 2015, pp. 133–138. http://ieeexplore.ieee.org/abstract/document/7158331/. (Accessed 6 February 2017).

[136] Q. Song, L. Zhao, X. Luo, X. Dou, Using deep learning for classification of lung nodules on computed tomography images, J. Healthc. Eng (2017), https://doi.org/10.1155/2017/8314740 (2017).

[137] W. Sun, B. Zheng, W. Qian, Automatic feature learning using multichannel ROI based on deep structured algorithms for computerized lung cancer diagnosis, Comput. Biol. Med. 89 (2017) 530–539, https://doi.org/10.1016/j.compbiomed.2017.04.006.

[138] H. Wang, Z. Zhou, Y. Li, Z. Chen, P. Lu, W. Wang, W. Liu, L. Yu, Comparison of machine learning methods for classifying mediastinal lymph node metastasis of non-small cell lung cancer from 18 F-FDG PET/CT images, EJNMMI Res. 7 (2017) 11, https://doi.org/10.1186/s13550-017-0260-9.

[139] T. Kooi, B. van Ginneken, N. Karssemeijer, A. den Heeten, Discriminating solitary cysts from soft tissue lesions in mammography using a pretrained deep convolutional neural network, Med. Phys. 44 (2017) 1017–1027, https://doi.org/10.1002/mp.12110.

[140] A. Akselrod-Ballin, L. Karlinsky, S. Alpert, S. Hasoul, R. Ben-Ari, E. Barkan, A region based convolutional network for tumor detection and classification in breast mammography, in: Deep Learn. Data Labeling Med. Appl, Springer, Cham, 2016, pp. 197–205, https://doi.org/10.1007/978-3-319-46976-8_21.

[141] Q. Chen, X. Xu, S. Hu, X. Li, Q. Zou, Y. Li, A Transfer Learning Approach for Classification of Clinical Significant Prostate Cancers from MpMRI Scans, 2017, https://doi.org/10.1117/12.2279021, p. 101344F–101344F–4.

[142] I. Banerjee, A. Crawley, M. Bhethanabotla, H.E. Daldrup-Link, D.L. Rubin, Transfer learning on fused multiparametric MR images for classifying histopathological subtypes of rhabdomyosarcoma, Comput. Med. Imaging Graph. Off. J. Comput. Med. Imaging Soc (2017), https://doi.org/10.1016/j.compmedimag.2017.05.002.

[143] X. Yang, R. Kwitt, M. Niethammer, Fast predictive image registration, in: Deep Learn. Data Labeling Med. Appl, Springer, Cham, 2016, pp. 48–57, https://doi.org/10.1007/978-3-319-46976-8_6.

[144] S. Miao, Z.J. Wang, Y. Zheng, R. Liao, Real-time 2D/3D registration via CNN regression, in: Biomed. Imaging ISBI 2016 IEEE 13th Int. Symp. on, IEEE, 2016, pp. 1430–1434. http://ieeexplore.ieee.org/abstract/document/7493536/. (Accessed 15 February 2017).

[145] B. Hou, A. Alansary, S. McDonagh, A. Davidson, M. Rutherford, J.V. Hajnal, D. Rueckert, B. Glocker, B. Kainz, Predicting Slice-To-Volume Transformation in Presence of Arbitrary Subject Motion, ArXiv170208891 Cs, 2017, http://arxiv.org/abs/1702.08891. (Accessed 29 March 2017).

[146] G. Wu, M. Kim, Q. Wang, B.C. Munsell, D. Shen, Scalable high-performance image registration framework by unsupervised deep feature representations learning, IEEE Trans. Biomed. Eng. 63 (2016) 1505–1516, https://doi.org/10.1109/TBME.2015.2496253.

[147] K. Ma, J. Wang, V. Singh, B. Tamersoy, Y.-J. Chang, A. Wimmer, T. Chen, Multimodal image registration with deep context reinforcement learning, in: Med. Image Comput. Comput. Assist. Interv. – MICCAI 2017, Springer, Cham, 2017, pp. 240–248, https://doi.org/10.1007/978-3-319-66182-7_28.

[148] S. Miao, S. Piat, P. Fischer, A. Tuysuzoglu, P. Mewes, T. Mansi, R. Liao, Dilated FCN for Multi-Agent 2d/3d Medical Image Registration, ArXiv171201651 Cs, 2017, http://arxiv.org/abs/1712.01651.

[149] D. Nguyen, T. Long, X. Jia, W. Lu, X. Gu, Z. Iqbal, S. Jiang, Dose Prediction with U-net: a Feasibility Study for Predicting Dose Distributions from Contours Using Deep Learning on Prostate IMRT Patients, 2017. ArXiv Prepr. ArXiv170909233.

[150] M. Mardani, P. Dong, L. Xing, Deep-learning based prediction of achievable dose for personalizing inverse treatment planning, Int. J. Radiat. Oncol 96 (2016) E419–E420, https://doi.org/10.1016/j.ijrobp.2016.06.1685.

[151] M. Mardani Korani, P. Dong, L. Xing, MO-G-201-03: deep-learning based prediction of achievable dose for personalizing inverse treatment planning, Med. Phys. 43 (2016) 3724, https://doi.org/10.1118/1.4957369.

[152] O. Ogunmolu, X. Gu, S. Jiang, N. Gans, Nonlinear Systems Identification Using Deep Dynamic Neural Networks, ArXiv prepr. ArXiv161001439, 2016, https://arxiv.org/abs/1610.01439. (Accessed 15 February 2017).

[153] T. Terunuma, A. Tokui, T. Sakae, Novel real-time tumor-contouring method using deep learning to prevent mistracking in X-ray fluoroscopy, Radiol. Phys. Technol (2017) 1–11, https://doi.org/10.1007/s12194-017-0435-0.

[154] Park, Intra- and inter-fractional variation prediction of lung tumors using fuzzy deep learning, IEEE J. Transl. Eng. Health Med 4 (2016), https://doi.org/10.1109/JTEHM.2016.2516005.

[155] A. Santhanam, Y. Min, P. Beron, N. Agazaryan, P. Kupelian, D. Low, SU-D-201-05: on the automatic recognition of patient safety hazards in a radiotherapy setup using a novel 3D camera system and a deep learning framework, Med. Phys. 43 (2016) 3334–3335, https://doi.org/10.1118/1.4955617.

[156] S. Aneja, U. Shaham, R.J. Kumar, N. Pirakitikulr, S.K. Nath, J.B. Yu, D.J. Carlson, R.H. Decker, Deep neural network to predict local failure following stereotactic body radiation therapy: integrating imaging and clinical data to predict outcomes, Int J Radiat Oncol Biol. 99 (2017) S47, https://doi.org/10.1016/j.ijrobp.2017.06.120.

[157] H. Li, H. Zhong, P.J. Boimel, E. Ben-Josef, Y. Xiao, Y. Fan, Deep convolutional neural networks for imaging based survival analysis of rectal cancer patients, Int J Radiat Oncol Biol. 99 (2017) S183, https://doi.org/10.1016/j.ijrobp.2017.06.458.

[158] X. Qi, J. Neylon, A. Santhanam, Dosimetric predictors for quality of life after prostate stereotactic body radiation therapy via deep learning network, Int J Radiat Oncol Biol. 99 (2017) S167, https://doi.org/10.1016/j.ijrobp.2017.06.384.

[159] X. Zhen, J. Chen, Z. Zhong, B.A. Hrycushko, K. Albuquerque, L. Zhou, S.B. Jiang, X. Gu, Deep convolutional neural networks with transfer learning for rectum toxicity prediction in combined brachytherapy and external beam radiation therapy for cervical cancer, Int J Radiat Oncol Biol. 99 (2017) S168, https://doi.org/10.1016/j.ijrobp.2017.06.386.

[160] A. Jochems, T.M. Deist, I. El Naqa, M. Kessler, C. Mayo, J. Reeves, S. Jolly, M. Matuszak, R. Ten Haken, J. van Soest, C. Oberije, C. Faivre-Finn, G. Price, D. de Ruysscher, P. Lambin, A. Dekker, Developing and validating a survival prediction model for NSCLC patients through distributed learning across 3 countries, Int. J. Radiat. Oncol 99 (2017) 344–352, https://doi.org/10.1016/j.ijrobp.2017.04.021.

[161] H.-H. Tseng, Y. Luo, S. Cui, J.-T. Chien, R.K. Ten Haken, I.E. Naqa, Deep reinforcement learning for automated radiation adaptation in lung cancer, Med. Phys. 44 (2017) 6690–6705, https://doi.org/10.1002/mp.12625.

[162] A. Qayyum, S.M. Anwar, M. Awais, M. Majid, Medical image retrieval using deep convolutional neural network, Neurocomputing 266 (2017) 8–20, https://doi.org/10.1016/j.neucom.2017.05.025.

[163] Y. Wu, M. Jiang, J. Lei, H. Xu, Named entity recognition in Chinese clinical text using deep neural network, Stud. Health Technol. Inf. 216 (2015) 624–628.

[164] X. Lv, Y. Guan, J. Yang, J. Wu, Clinical relation extraction with deep learning, Int. J. Hybrid Inf. Technol 9 (2016) 237–248, https://doi.org/10.14257/ijhit.2016.9.7.22.

[165] J.M. Edmund, T. Nyholm, A review of substitute CT generation for MRI-only radiation therapy, Radiat. Oncol. Lond. Engl 12 (2017) 28, https://doi.org/10.1186/s13014-016-0747-y.

[166] E. Persson, C. Gustafsson, F. Nordström, M. Sohlin, A. Gunnlaugsson, K. Petruson, N. Rintelä, K. Hed, L. Blomqvist, B. Zackrisson, T. Nyholm, L.E. Olsson, C. Siversson, J. Jonsson, MR-opera: a multicenter/multivendor validation of magnetic resonance imaging–only prostate treatment planning using synthetic computed tomography images, Int. J. Radiat. Oncol 99 (2017) 692–700, https://doi.org/10.1016/j.ijrobp.2017.06.006.

[167] M.L. Nguyen, B. Willows, R. Khan, A. Chi, L. Kim, S.G. Nour, T. Sroka, C. Kerr, J. Godinez, M. Mills, U. Karlsson, G. Altdorfer, N.P. Nguyen, G. Jendrasiak, The potential role of magnetic resonance spectroscopy in image-guided radiotherapy, Front. Oncol 4 (2014), https://doi.org/10.3389/fonc.2014.00091.

[168] D. Giantsoudi, B. De Man, J. Verburg, A. Trofimov, Y. Jin, G. Wang, L. Gjesteby, H. Paganetti, Metal artifacts in computed tomography for radiation therapy planning: dosimetric effects and impact of metal artifact reduction, Phys. Med. Biol. 62 (2017) R49–R80, https://doi.org/10.1088/1361-6560/aa5293.

[169] D.G. Kovacs, L.A. Rechner, A.L. Appelt, A.K. Berthelsen, J.C. Costa, J. Friborg, G.F. Persson, J.P. Bangsgaard, L. Specht, M.C. Aznar, Metal artefact reduction for accurate tumour delineation in radiotherapy, Radiother. Oncol. 126 (2018) 479–486, https://doi.org/10.1016/j.radonc.2017.09.029.

[170] D.C. Alexander, D. Zikic, A. Ghosh, R. Tanno, V. Wottschel, J. Zhang, E. Kaden, T.B. Dyrby, S.N. Sotiropoulos, H. Zhang, A. Criminisi, Image quality transfer and applications in diffusion MRI, Neuroimage 152 (2017) 283–298, https://doi.org/10.1016/j.neuroimage.2017.02.089.

[171] G.T.Y. Chen, G.C. Sharp, S. Mori, A review of image-guided radiotherapy, Radiol. Phys. Technol 2 (2009) 1–12, https://doi.org/10.1007/s12194-008-0045-y.

[172] S.G. Tejinder Kataria, Image guided radiation therapy, J. Nucl. Med. Radiat. Ther. 05 (2014), https://doi.org/10.4172/2155-9619.1000179.

[173] D.A. Jaffray, Image-guided radiotherapy: from current concept to future perspectives, Nat. Rev. Clin. Oncol. 9 (2012) 688–699, https://doi.org/10.1038/nrclinonc.2012.194.

[174] I. Arivarasan, C. Anuradha, S. Subramanian, A. Anantharaman, V. Ramasubramanian, Magnetic resonance image guidance in external beam radiation therapy planning and delivery, Jpn. J. Radiol. 35 (2017) 417–426, https://doi.org/10.1007/s11604-017-0656-5.

[175] J. Simon, F. Eschwege, L.E. Hajj, V. Marchesi, A. Noel, M. Levitchi, C. Marchal, P. Gourmelon, D. Peiffert, Epinal #2: 409 patients overexposed during radiotherapy for prostate cancer after daily use of portal imaging controls, Int. J. Radiat. Oncol. Biol. Phys. 78 (2010) S361, https://doi.org/10.1016/j.ijrobp.2010.07.852.

[176] D.L. Pham, C. Xu, J.L. Prince, Current methods in medical image segmentation, Annu. Rev. Biomed. Eng. 2 (2000) 315–337, https://doi.org/10.1146/annurev.bioeng.2.1.315.

[177] D. Whitey, Z. Koles, A review of medial image segmentation, Int. J. Bioelectromagn 10 (2008) 125–148.

[178] Z. Akkus, A. Galimzianova, A. Hoogi, D.L. Rubin, B.J. Erickson, Deep learning for brain MRI segmentation: state of the art and future directions, J. Digit. Imag. 30 (2017) 449–459, https://doi.org/10.1007/s10278-017-9983-4.

[179] B.H. Menze, A. Jakab, S. Bauer, J. Kalpathy-Cramer, K. Farahani, J. Kirby, Y. Burren, N. Porz, J. Slotboom, R. Wiest, L. Lanczi, E. Gerstner, M.A. Weber, T. Arbel, B.B. Avants, N. Ayache, P. Buendia, D.L. Collins, N. Cordier, J.J. Corso, A. Criminisi, T. Das, H. Delingette, ??a??atay Demiralp, C.R. Durst, M. Dojat, S. Doyle, J. Festa, F. Forbes, E. Geremia, B. Glocker, P. Golland, X. Guo, A. Hamamci, K.M. Iftekharuddin, R. Jena, N.M. John, E. Konukoglu, D. Lashkari, J.A. Mariz, R. Meier, S. Pereira, D. Precup, S.J. Price, T.R. Raviv, S.M.S. Reza, M. Ryan, D. Sarikaya, L. Schwartz, H.C. Shin, J. Shotton, C.A. Silva, N. Sousa, N.K. Subbanna, G. Szekely, T.J. Taylor, O.M. Thomas, N.J. Tustison, G. Unal, F. Vasseur, M. Wintermark, D.H. Ye, L. Zhao, B. Zhao, D. Zikic, M. Prastawa, M. Reyes, K. Van Leemput, The multimodal brain tumor image segmentation benchmark (BRATS), IEEE Trans. Med. Imag. 34 (2015) 1993–2024, https://doi.org/10.1109/TMI.2014.2377694.

[180] MICCAI BRATS - The Multimodal Brain Tumor Segmentation Challenge. https://www.med.upenn.edu/sbia/brats2018.html.

[181] A. Işın, C. Direkoğlu, M. Şah, Review of MRI-based brain tumor image segmentation using deep learning methods, Procedia Comput. Sci. 102 (2016) 317–324, in: https://doi.org/10.1016/j.procs.2016.09.407.

[182] M. Shahedi, D.W. Cool, G.S. Bauman, M. Bastian-Jordan, A. Fenster, A.D. Ward, Accuracy validation of an automated method for prostate segmentation in magnetic resonance imaging, J. Digit. Imag. (2017), https://doi.org/10.1007/s10278-017-9964-7.

[183] J. Ferlay, I. Soerjomataram, R. Dikshit, S. Eser, C. Mathers, M. Rebelo, D.M. Parkin, D. Forman, F. Bray, Cancer incidence and mortality worldwide: sources, methods and major patterns in GLOBOCAN 2012, Int. J. Canc. 136 (2015) E359–E386, https://doi.org/10.1002/ijc.29210.

[184] A. Mehrtash, M. Pesteie, J. Hetherington, P.A. Behringer, T. Kapur, W.M. Wells, R. Rohling, A. Fedorov, P. Abolmaesumi, DeepInfer: open-source deep learning deployment toolkit for image-guided therapy, Proc. SPIE-Int. Soc. Opt. Eng. 10135 (2017), https://doi.org/10.1117/12.2256011.

[185] C. Chu, J. De Fauw, N. Tomasev, B.R. Paredes, C. Hughes, J. Ledsam, T. Back, H. Montgomery, G. Rees, R. Raine, others, Applying machine learning to automated segmentation of head and neck tumour volumes and organs at risk on radiotherapy planning CT and MRI scans, F1000Research 5 (2016). https://f1000research.com/articles/5-2104/v1. (Accessed 16 January 2017).

[186] Y. Yuan, M. Chao, Y.C. Lo, Automatic skin lesion segmentation using deep fully convolutional networks with jaccard distance, IEEE Trans. Med. Imaging. PP (2017), https://doi.org/10.1109/TMI.2017.2695227, 1–1.

[187] Y. Yuan, Y.C. Lo, Improving dermoscopic image segmentation with enhanced convolutional-deconvolutional networks, IEEE J. Biomed. Health Inform. PP (2017), https://doi.org/10.1109/JBHI.2017.2787487, 1–1.

[188] D. Fontanarosa, S. van der Meer, J. Bamber, E. Harris, T. O'Shea, F. Verhaegen, Review of ultrasound image guidance in external beam radiotherapy: I. Treatment planning and inter-fraction motion management, Phys. Med. Biol. 60 (2015), https://doi.org/10.1088/0031-9155/60/3/R77. R77.

[189] T. O'Shea, J. Bamber, D. Fontanarosa, S. van der Meer, F. Verhaegen, E. Harris, Review of ultrasound image guidance in external beam radiotherapy part II: intra-fraction motion management and novel applications, Phys. Med. Biol. 61 (2016), https://doi.org/10.1088/0031-9155/61/8/R90. R90.

[190] S.A. Mason, T.P. O'Shea, I.M. White, S. Lalondrelle, K. Downey, M. Baker, C.F. Behrens, J.C. Bamber, E.J. Harris, Towards ultrasound-guided adaptive radiotherapy for cervical cancer: evaluation of Elekta's semiautomated uterine segmentation method on 3D ultrasound images, Med. Phys. 44 (2017) 3630–3638, https://doi.org/10.1002/mp.12325.

[191] S. Nouranian, M. Ramezani, I. Spadinger, W.J. Morris, S.E. Salcudean, P. Abolmaesumi, Learning-based multi-label segmentation of transrectal ultrasound images for prostate brachytherapy, IEEE Trans. Med. Imag. 35 (2016) 921–932, https://doi.org/10.1109/TMI.2015.2502540.

[192] K. Doi, Computer-aided diagnosis in medical imaging: historical review, current status and future potential, Comput. Med. Imaging Graph. Off. J. Comput. Med. Imaging Soc. 31 (2007) 198–211, https://doi.org/10.1016/j.compmedimag.2007.02.002.

[193] I.R.S. Valente, P.C. Cortez, E.C. Neto, J.M. Soares, V.H.C. de Albuquerque, J.M.R. Tavares, Automatic 3D pulmonary nodule detection in CT images: a survey, Comput. Meth. Progr. Biomed. 124 (2016) 91–107.

[194] V.J. Mar, R.A. Scolyer, G.V. Long, Computer-assisted diagnosis for skin cancer: have we been outsmarted?, Lancet Lond, Englera 389 (2017) 1962–1964, https://doi.org/10.1016/S0140-6736(17)31285-0.

[195] S.G. Armato, K. Drukker, F. Li, L. Hadjiiski, G.D. Tourassi, R.M. Engelmann, M.L. Giger, G. Redmond, K. Farahani, J.S. Kirby, L.P. Clarke, LUNGx Challenge for computerized lung nodule classification, J. Med. Imaging 3 (2016), https://doi.org/10.1117/1.JMI.3.4.044506, 044506.

[196] L. Sunwoo, Y.J. Kim, S.H. Choi, K.-G. Kim, J.H. Kang, Y. Kang, Y.J. Bae, R.-E. Yoo, J. Kim, K.J. Lee, others, Computer-aided detection of brain metastasis on 3D MR imaging: observer performance study, PLoS One 12 (2017), e0178265.

[197] S. Belharbi, C. Chatelain, R. Hérault, S. Adam, S. Thureau, M. Chastan, R. Modzelewski, Spotting L3 slice in CT scans using deep convolutional network and transfer learning, Comput. Biol. Med. (2017), https://doi.org/10.1016/j.compbiomed.2017.05.018.

[198] K.K. Brock, S. Mutic, T.R. McNutt, H. Li, M.L. Kessler, Use of image registration and fusion algorithms and techniques in radiotherapy: report of the AAPM radiation therapy committee task group No. 132, Med. Phys. 44 (2017) e43–e76, https://doi.org/10.1002/mp.12256.

[199] M.A. Viergever, J.B.A. Maintz, S. Klein, K. Murphy, M. Staring, J.P.W. Pluim, A survey of medical image registration – under review, Med. Image Anal. 33 (2016) 140–144, https://doi.org/10.1016/j.media.2016.06.030.

[200] S. Wang, D. Zheng, C. Zhang, R. Ma, N.R. Bennion, Y. Lei, X. Zhu, C.A. Enke, S. Zhou, Automatic planning on hippocampal avoidance whole-brain radiotherapy, Med. Dosim. 42 (2017) 63–68, https://doi.org/10.1016/j.meddos.2016.12.002.

[201] K. Nawa, A. Haga, A. Nomoto, R.A. Sarmiento, K. Shiraishi, H. Yamashita, K. Nakagawa, Evaluation of a commercial automatic treatment planning system for prostate cancers, Med. Dosim. 42 (2017) 203–209, https://doi.org/10.1016/j.meddos.2017.03.004.

[202] C. Schubert, O. Waletzko, C. Weiss, D. Voelzke, S. Toperim, A. Roeser, S. Puccini, M. Piroth, C. Mehrens, J.-D. Kueter, K. Hierholz, K. Gerull, A. Fogliata, A. Block, L. Cozzi, Intercenter validation of a knowledge based model for automated planning of volumetric modulated arc therapy for prostate cancer. The experience of the German RapidPlan Consortium, PLoS One 12 (2017), e0178034, https://doi.org/10.1371/journal.pone.0178034.

[203] R.A. Mitchell, P. Wai, R. Colgan, A.M. Kirby, E.M. Donovan, Improving the efficiency of breast radiotherapy treatment planning using a semi-automated approach, J. Appl. Clin. Med. Phys. 18 (2017) 18–24, https://doi.org/10.1002/acm2.12006.

[204] C. McIntosh, M. Welch, A. McNiven, D.A. Jaffray, T.G. Purdie, Fully automated treatment planning for head and neck radiotherapy using a voxel-based dose prediction and dose mimicking method, Phys. Med. Biol. 62 (2017) 5926–5944, https://doi.org/10.1088/1361-6560/aa71f8.

[205] J. Fan, J. Wang, Z. Zhang, W. Hu, Iterative dataset optimization in automated planning: implementation for breast and rectal cancer radiotherapy, Med. Phys. 44 (2017) 2515–2531, https://doi.org/10.1002/mp.12232.

[206] J.J. Boutilier, T. Craig, M.B. Sharpe, T.C.Y. Chan, Sample size requirements for knowledge-based treatment planning, Med. Phys. 43 (2016) 1212–1221, https://doi.org/10.1118/1.4941363.

[207] H. Wang, P. Dong, H. Liu, L. Xing, Development of an autonomous treatment planning strategy for radiation therapy with effective use of population-based prior data, Med. Phys. 44 (2017) 389–396, https://doi.org/10.1002/mp.12058.

[208] D. Yan, F. Vicini, J. Wong, A. Martinez, Adaptive radiation therapy, Phys. Med. Biol. 42 (1997) 123–132.

[209] A.J. McPartlin, X.A. Li, L.E. Kershaw, U. Heide, L. Kerkmeijer, C. Lawton, U. Mahmood, F. Pos, N. van As, M. van Herk, D. Vesprini, J. van der Voort van Zyp, A. Tree, A. Choudhury, MRI-guided prostate adaptive radiotherapy – a systematic review, Radiother. Oncol. 119 (2016) 371–380, https://doi.org/10.1016/j.radonc.2016.04.014.

[210] E. Colvill, J. Booth, S. Nill, M. Fast, J. Bedford, U. Oelfke, M. Nakamura, P. Poulsen, E. Worm, R. Hansen, T. Ravkilde, J. Scherman Rydh?g, T. Pommer, P. Munck af Rosenschold, S. Lang, M. Guckenberger, C. Groh, C. Herrmann, D. Verellen, K. Poels, L. Wang, M. Hadsell, T. Sothmann, O. Blanck, P. Keall, A dosimetric comparison of real-time adaptive and non-adaptive radiotherapy: a multi-institutional study encompassing robotic, gimbaled, multileaf collimator and couch tracking, Radiother. Oncol. 119 (2016) 159–165, https://doi.org/10.1016/j.radonc.2016.03.006.

[211] S. Lim-Reinders, B.M. Keller, S. Al-Ward, A. Sahgal, A. Kim, Online adaptive radiation therapy, Int. J. Radiat. Oncol 99 (2017) 994–1003, https://doi.org/10.1016/j.ijrobp.2017.04.023.

[212] L.P. Muren, N. Jornet, D. Georg, R. Garcia, D.I. Thwaites, Improving radiotherapy through medical physics developments, Radiother. Oncol. 117 (2015) 403–406, https://doi.org/10.1016/j.radonc.2015.11.008.

[213] D.T. Nguyen, R. O'Brien, J.-H. Kim, C.-Y. Huang, L. Wilton, P. Greer, K. Legge, J.T. Booth, P.R. Poulsen, J. Martin, P.J. Keall, The first clinical implementation of a real-time six degree of freedom target tracking system during radiation therapy based on Kilovoltage Intrafraction Monitoring (KIM), Radiother. Oncol. 123 (2017) 37–42, https://doi.org/10.1016/j.radonc.2017.02.013.

[214] M. Glitzner, M.F. Fast, B.D. de Senneville, S. Nill, U. Oelfke, J.J.W. Lagendijk, B.W. Raaymakers, S.P.M. Crijns, Real-time auto-adaptive margin generation for MLC-tracked radiotherapy, Phys. Med. Biol. 62 (2017) 186–201, https://doi.org/10.1088/1361-6560/62/1/186.

[215] T. Lin, Y. Lin, Markerless tumor gating and tracking for lung cancer radiotherapy based on machine learning techniques, in: Artif. Intell. Decis. Support Syst. Diagn. Med. Imaging, Springer, Cham, 2018, pp. 337–359, https://doi.org/10.1007/978-3-319-68843-5_12.

[216] O.P. Ogunmolu, X. Gu, S. Jiang, N.R. Gans, A real-time, soft robotic patient positioning system for maskless head-and-neck cancer radiotherapy: an initial investigation, in: 2015 IEEE Int. Conf. Autom. Sci. Eng. CASE, 2015, pp. 1539–1545, https://doi.org/10.1109/CoASE.2015.7294318.

[217] O.P. Ogunmolu, X. Gu, S. Jiang, N.R. Gans, Vision-based control of a soft robot for maskless head and neck cancer radiotherapy, in: 2016 IEEE Int. Conf. Autom. Sci. Eng. CASE, 2016, pp. 180–187, https://doi.org/10.1109/COASE.2016.7743378.

[218] M. Schwarz, G.M. Cattaneo, L. Marrazzo, Geometrical and dosimetrical uncertainties in hypofractionated radiotherapy of the lung: a review, Phys. Med. 36 (2017) 126–139, https://doi.org/10.1016/j.ejmp.2017.02.011.

[219] J.-E. Bibault, P. Giraud, A. Burgun, Big Data and machine learning in radiation oncology: state of the art and future prospects, Canc. Lett. 382 (2016) 110–117, https://doi.org/10.1016/j.canlet.2016.05.033.

[220] O. Ylijoki, J. Porras, Perspectives to definition of big data: a mapping study and discussion, J. Innovat. Manag. 4 (2016) 69–91.

[221] G.S. Birkhead, M. Klompas, N.R. Shah, Uses of electronic health records for public health surveillance to advance public health, Annu. Rev. Publ. Health 36 (2015) 345–359, https://doi.org/10.1146/annurev-publhealth-031914-122747.

[222] Ö. Uzuner, B.R. South, S. Shen, S.L. DuVall, 2010 i2b2/VA challenge on concepts, assertions, and relations in clinical text, J. Am. Med. Inform. Assoc. JAMIA 18 (2011) 552–556, https://doi.org/10.1136/amiajnl-2011-000203.

[223] J. Kang, R. Schwartz, J. Flickinger, S. Beriwal, Machine learning approaches for predicting radiation therapy outcomes: a Clinician's perspective, Int J Radiat Oncol Biol. 93 (2015) 1127–1135, https://doi.org/10.1016/j.ijrobp.2015.07.2286.

[224] S. Lee, K.H. Kim, C.S. Woo, J.B. Shim, Y.J. Cao, K.H. Chang, C.Y. Kim, Predictive solution for radiation toxicity based on big data, in: Radiotherapy, InTech, 2017. https://www.intechopen.com/books/radiotherapy/predictive-solution-for-radiation-toxicity-based-on-big-data. (Accessed 24 May 2017).

[225] C.M. Lynch, V.H. van Berkel, H.B. Frieboes, Application of unsupervised analysis techniques to lung cancer patient data, PLoS One 12 (2017), e0184370.

[226] S.K. Das, S. Zhou, J. Zhang, F.-F. Yin, M.W. Dewhirst, L.B. Marks, Predicting lung radiotherapy-induced pneumonitis using a model combining parametric lyman probit withnonparametric decision trees, Int J Radiat Oncol Biol. 68 (2007) 1212–1221, https://doi.org/10.1016/j.ijrobp.2007.03.064.

[227] G. Cosma, D. Brown, M. Archer, M. Khan, A.G. Pockley, A survey on computational intelligence approaches for predictive modeling in prostate cancer, Expert Syst. Appl. 70 (2017) 1–19, https://doi.org/10.1016/j.eswa.2016.11.006.

[228] J.A. Dean, K.H. Wong, L.C. Welsh, A.-B. Jones, U. Schick, K.L. Newbold, S.A. Bhide, K.J. Harrington, C.M. Nutting, S.L. Gulliford, Normal tissue complication probability (NTCP) modelling using spatial dose metrics and machine learning methods for severe acute oral mucositis resulting from head and neck radiotherapy, Radiother. Oncol. J. Eur. Soc. Ther. Radiol. Oncol 120 (2016) 21–27, https://doi.org/10.1016/j.radonc.2016.05.015.

[229] J. Coates, L. Souhami, I. El Naqa, Big data analytics for prostate radiotherapy, Front. Oncol 6 (2016), https://doi.org/10.3389/fonc.2016.00149.

[230] B. Salazar, E. Balczewski, C. Ung, S. Zhu, Neuroblastoma, a paradigm for big data science in pediatric oncology, Int. J. Mol. Sci. 18 (2016) 37, https://doi.org/10.3390/ijms18010037.

[231] R.S. Muthalaly, Using Deep Learning to Predict the Mortality of Leukemia Patients, Queen's University, Kingston, Ont, 2017. http://qspace.library.queensu.ca/handle/1974/15929. (Accessed 12 July 2017).

[232] A. Nguyen, J. Yosinski, J. Clune, Deep neural networks are easily fooled: high confidence predictions for unrecognizable images, in: Proc. IEEE Conf. Comput. Vis. Pattern Recognit, 2015, pp. 427–436.

[233] M. Havaei, N. Guizard, H. Larochelle, P.-M. Jodoin, Deep learning trends for focal brain pathology segmentation in MRI, in: Mach. Learn. Health Inform, Springer, Cham, 2016, pp. 125–148, https://doi.org/10.1007/978-3-319-50478-0_6.

[234] S.H. Benedict, K. Hoffman, M.K. Martel, A.P. Abernethy, A.L. Asher, J. Capala, R.C. Chen, B. Chera, J. Couch, J. Deye, J.A. Efstathiou, E. Ford, B.A. Fraass, P.E. Gabriel, V. Huser, B.D. Kavanagh, D. Khuntia, L.B. Marks, C. Mayo, T. McNutt, R.S. Miller, K.L. Moore, F. Prior, E. Roelofs, B.S. Rosenstein, J. Sloan, A. Theriault, B. Vikram, Overview of the american society for radiation oncology–national institutes of health–american association of Physicists in medicine workshop 2015: exploring opportunities for radiation oncology in the era of big data, Int J Radiat Oncol Biol. 95 (2016) 873–879, https://doi.org/10.1016/j.ijrobp.2016.03.006.

3. Détection et segmentation des métastases cérébrales par réseau de neurone convolutionnel

La détection/segmentation automatique d'organes ou de lésions tumorales sur imagerie médicale est aujourd'hui un sujet de recherche majeur. De nombreuses méthodes ont été développées avec plus ou moins de succès, qui concernent aujourd'hui toutes les localisations anatomiques et toutes les modalités d'imagerie.

Il y a cependant peu de travaux à ce jour sur la détection et la segmentation automatiques des métastases cérébrales. Ces lésions ont pourtant une incidence importante, pouvant affecter un tiers des patients atteints d'un cancer. La radiothérapie stéréotaxique est aujourd'hui un traitement établi pour ces métastases, seule ou en complément de la chirurgie. Il est donc important que ces lésions soient précisément détectées et segmentées.

Nous avons adapté DeepMedic, un CNN développé à l'origine pour la segmentation de lésions cérébrales de type gliome (Kamnitas et al., 2017), à la détection et à la segmentation de métastases cérébrales. Ce travail est présenté dans la publication suivante (Charron et al., 2018)

Computers in Biology and Medicine 95 (2018) 43–54

Contents lists available at ScienceDirect

Computers in Biology and Medicine

journal homepage: www.elsevier.com/locate/compbiomed

Automatic detection and segmentation of brain metastases on multimodal MR images with a deep convolutional neural network

Odelin Charron [a], Alex Lallement [b], Delphine Jarnet [a], Vincent Noblet [b], Jean-Baptiste Clavier [a], Philippe Meyer [a,b,*]

[a] Department of Medical Physics, Paul Strauss Center, Strasbourg, France
[b] ICube-UMR 7357, Strasbourg, France

ARTICLE INFO

Keywords:
Brain metastases
Magnetic resonance imaging
Convolutional neural network
Detection
Segmentation

ABSTRACT

Stereotactic treatments are today the reference techniques for the irradiation of brain metastases in radiotherapy. The dose per fraction is very high, and delivered in small volumes (diameter <1 cm). As part of these treatments, effective detection and precise segmentation of lesions are imperative. Many methods based on deep-learning approaches have been developed for the automatic segmentation of gliomas, but very little for that of brain metastases. We adapted an existing 3D convolutional neural network (DeepMedic) to detect and segment brain metastases on MRI. At first, we sought to adapt the network parameters to brain metastases. We then explored the single or combined use of different MRI modalities, by evaluating network performance in terms of detection and segmentation. We also studied the interest of increasing the database with virtual patients or of using an additional database in which the active parts of the metastases are separated from the necrotic parts. Our results indicated that a deep network approach is promising for the detection and the segmentation of brain metastases on multimodal MRI.

1. Introduction

Brain metastases (BM) have a high incidence and affect up to one third of patients with cancer. Most common primary tumors are breast, lung, or melanoma. The majority of the patients have one, two or three metastases, respectively 49%, 21% and 10% [1]. Median survival of patients with BM is inferior to 12 months. Historically, treatment is based on corticoids and whole brain irradiation allowing a 3–6 months median survival. Surgery is a local treatment indicated in case of emergency or when a pathological diagnosis is mandatory. Locoregional relapse after surgery only is high (up to 85%) [2] so radiotherapy is added as an adjuvant treatment. Stereotactic radiotherapy (SRT) or radiosurgery is an established treatment for brain metastases, exclusively or after surgery. It is a highly conformal irradiation of a small volume of tumor with high dose per fraction. SRT reduces the irradiated volume of normal tissue, minimizing the complication probability while maintaining excellent tumor control. Thus, precise determination of the number of lesions and of the tumors boundaries is of great importance to minimize radiation necrosis risk in surrounding tissue [3]. Target segmentation for BM is performed manually by the radiation oncologist on magnetic resonance images (MRI). Inter-observer variability in target volume delineation is the most important contributor to uncertainty in radiation treatment planning. Age and experience of the physician could influence the delineation process, and therefore the survival outcomes.

Automatic detection and segmentation of organs or tumor lesions on medical images became today a major research subject in the medical field [4–9]. Numerous methods have been developed, which concern all the anatomical localizations and medical imaging modalities [10–12]. However, there have been relatively few studies to date on BM automatic detection and segmentation. In its review of BM detection methods dated 2016, Perez et al. identified 10 published works [13]. These studies, which uses hand-crafted templates or blob based complex procedures, had in common a recall rate that seems difficult to improve without making the feature extraction methods even more complex. One way to overcome this issue is to use deep learning (DL) methods, which perform an automated data-oriented feature extraction and can thus learn directly the most relevant feature representation from the input images. These methods have supplanted other machine learning methods for applications such as recognition in computer vision [14]. They can be considered today as the current state-of-the-art for many medical image

* Corresponding author. 3 rue de la porte de l'hôpital, 67000 Strasbourg, France.
E-mail address: pmeyer@strasbourg.unicancer.fr (P. Meyer).

https://doi.org/10.1016/j.compbiomed.2018.02.004
Received 22 November 2017; Received in revised form 6 February 2018; Accepted 7 February 2018

applications [15], such as for example glioma segmentation [16]. Losch et al. were the first to our knowledge to date that investigated the use of deep networks to detect and segment BM [17]. They explored several network depths, spatial inputs and pathways, and stated that their network detection performances are comparable to the conventional state-of-the-art ones. They hypothesized that the results could be much better, by improving the architectural aspect alone or the database quality. Liu et al. proposed a convolutional neural network (CNN) based algorithm to segment BM, trained on both gliomas and BM patients [18]. However, they didn't quantify the detection performances of their algorithm, which seems to us to be a crucial parameter for cerebral metastases which are sometimes very small and which can be missed by radiation oncologist. Furthermore, the BM dataset they used was composed of mono-modal MRI, namely T1-weighted MRI with Gadolinium contrast.

In this study, we mainly studied the influence of MRI modalities and the impact of the number of segmented classes, both on the detection and segmentation of brain metastases. To do this, we used the DeepMedic [12] neural network, which has already proven itself in the segmentation and detection of gliomas and brain white matter lesion [19]. We first investigated the behavior of this deep network with respect to BM when modifying parameters such as number of epochs, segments or batch size. Once the choice of parameters adapted to BM has been made, we explored and compared the use of mono and multimodal MRI dataset. We also evaluated the effect of using virtual patients and an advanced segmentation maps which distinguish the active part from the necrotic part of the metastasis. We finally compared the detection and segmentation performances of this network with published data.

2. Material and methods

2.1. Database

2.1.1. Patients

In the radiotherapy department of Paul Strauss Center (Strasbourg, France), BM are treated with SRT techniques since 2010, and are in 2016 the second most frequent disease treated with up to 200 patients/year. Treatments are performed with non-invasive stereotactic frame (Brainlab, Germany) in stereotactic radiotherapy with dynamic conformal arc or volumetric modulation arctherapy on a Novalis Tx (Varian, USA).

In order to retrospectively build a consistent database (DB) from this mass of data, only those patients for whom it was their first cranial irradiation (neither surgery nor prior radiation therapy), and which MRI was performed a week before radiotherapy treatment using the same 1.5T machine have been selected. It should be noted that since primary sites are heterogeneous (breast, lung, …), the spatial distribution of BM within the brain structures is not controlled.

Each retained patient is thus characterized by a set of 3 DICOM MRI whose characteristics are:

- T1-weighted 3D MRI with Gadolinium injection (3DT1Gd), with a resolution of 0.82*0.82*1.02 mm^3,
- T2-weighted 2D Fluid Attenuated Inversion Recovery MRI (2DFLAIR), with a resolution 0.82*0.82*3 mm^3,
- T1-weighted 2D MRI (2DT1), with a resolution of 0.82*0.82*3 mm^3.

The DB is therefore composed of 182 patients (and their corresponding 3 DICOM MRI) and has been split into training, validation and test databases comprising 146, 18 and 18 patients respectively. In order to have a selective test database, we chose to include a stroke patient, a leukosis patient (see Appendix 1), a cavernoma patient and a patient with artifacts due to movement during acquisition.

2.1.2. Brain metastases

The BM segmentation was carried out manually by up to 4 radiation oncologists using the iPlan software (Brainlab, Germany). Since the original segmentation was done for stereotactic radiotherapy treatment, only the metastases to be irradiated were segmented. In order to use the BM segmentation as ground truth in this study, each of the 182 patients of the DB was checked one by one by an experienced radiation oncologist, in particular to ensure that the DB did not contains unsegmented metastasis.

This segmentation was performed slice by slice on 3DT1Gd imaging. Via the enhancement of edema, 2D FLAIR images can help to guide the eye of the radiation oncologist, especially when the Gadolinium does not reach the BM. 2DT1 imaging sometimes allows to raise any doubts about the nature of the lesion. Fig. 1 illustrates the visualization difference for a BM on 3DT1Gd, 2DFLAIR and 2DT1 MRI modalities.

On each 3DT1Gd MRI slice where the BM is visible, the radiation oncologist segmented the gross tumor volume, which is the outline of the metastasis, saved in DICOM RT-Struct format [20,21]. 412 BM were segmented for the 182 patients, and their contours included in the DB. The minimum and maximum diameter of the metastasis population was 1.65 and 27 mm (median = 7 mm, mean = 8.1 mm), respectively. The minimum and maximum volume of the metastasis population was 0.01 and 37 cm^3 respectively (median = 0.5 cm^3, mean = 2.4 cm^3). Fig. 2 illustrates the distribution of the diameters and volumes of the BM included in the DB of our study.

In order to refine our knowledge of the metastasis population, we established their spatial distribution within the brain (see Fig. 3). The majority of them are cerebellar or in the frontal lobe.

2.1.2.1. Virtual patients. We also evaluated the influence of the artificial increase of our training database with virtual patients. The approach chosen is a linear registration of patients by rotation, performed with FSL FLIRT [22]. In order to obtain a significant additional number of metastases, 49 patients with at least 3 metastases were selected from the training database, for potentially more than 1200 virtual patients. The histogram of the rotations is given in Fig. 4: they are often small (less than 5°), the patients being constrained by the contention equipment and the MRI antenna. To clean data, we chose to exclude virtual patients with a rotation judged to be too weak, using the median of the angles. We also rejected those with aberrant angle values that may result from poor registration. With the additional constraint of not having more than twice the same original patient, we created 62 virtual patients with 189 metastases who were incorporated in the training database.

2.1.2.2. Simple and advanced segmentation maps. The original simple map (SM) was composed of the image voxels, equal to 1 or 0 respectively if they were or were not contained inside the BM contour.

To study the impact of the number of classes on the quality of segmentation and detection, we generated another segmentation map by separating the active from the necrotic part of the BM (see Fig. 5). The necrotic part is less hyper-intense than the active part, ranging from the intensity of healthy tissue to a flagrant hypo-intensity. In this advanced map (AM), the voxels are equal to 2 if they are contained in the active part of the BM, 1 in the necrotic part, and 0 in the healthy tissues.

Table 1 summarizes the composition of the different DB used in this study.

2.2. The deep network

We chose to use the DeepMedic network, proposed by Kamnitsas et al. [12], because it implements an efficient 3D segmentation of volumetric medical image data. This CNN, whose source code is made publicly available [23], obtained top ranking performance on the public benchmarks BRATS 2015 and ISLES 2015. It is a multi-scale 3D CNN with two convolutional pathways and 11 layers, followed by an independent post-processing phase [13] (which we did not used in this study). The first path is adapted to a precise segmentation and the second one to a smoother segmentation taking into account the neighborhood.

During the learning process, some patients are randomly selected at

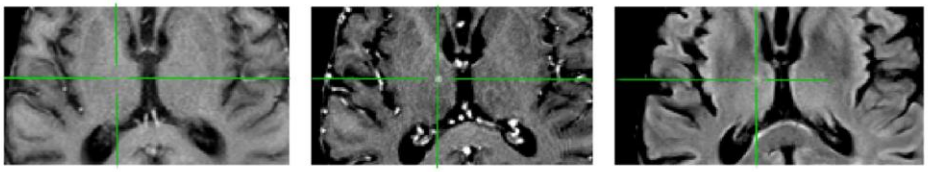

Fig. 1. From left to right: cerebral metastasis visualized on 2DT1, 3DT1Gd and 2DFLAIR MRI.

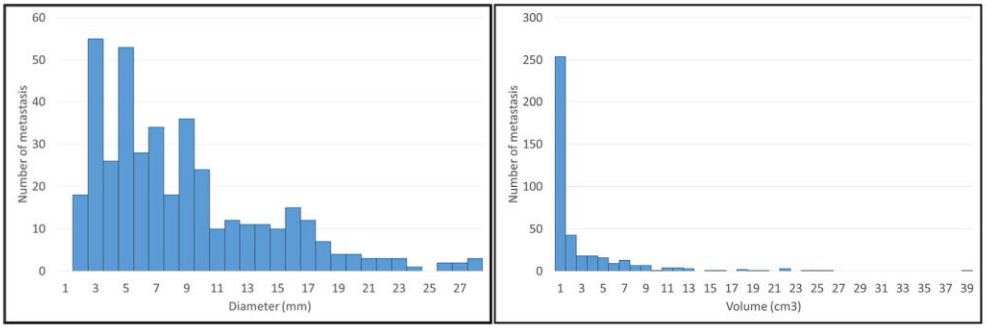

Fig. 2. Histogram of the brain metastasis diameters and volumes included in our database.

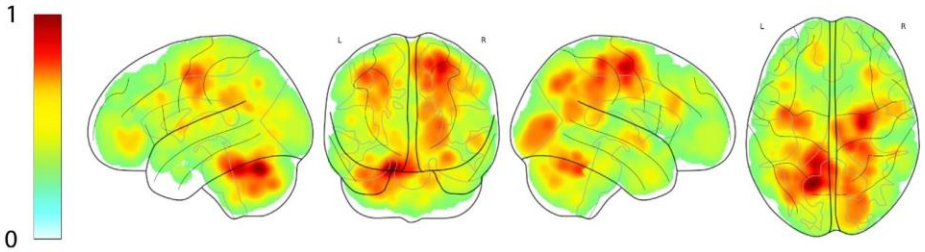

Fig. 3. From left to right: projection of the probability distribution of the cerebral metastases on the left sagittal, coronal, right sagittal and axial planes. In blue: low probability of presence. In red: high probability of presence. (For interpretation of the references to colour in this figure legend, the reader is referred to the Web version of this article.)

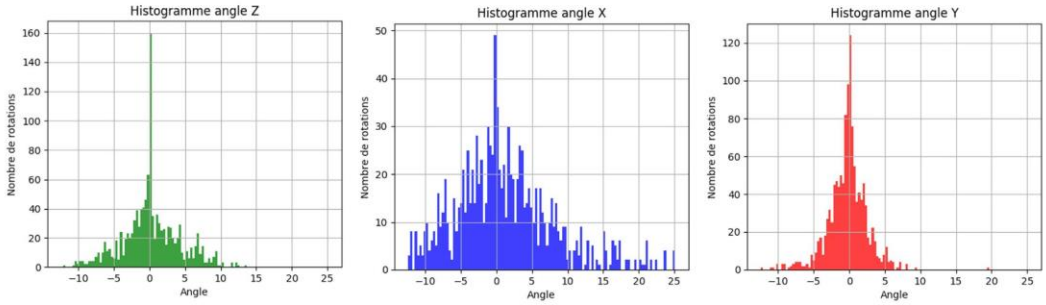

Fig. 4. Histogram of registration angles for the creation of virtual patients. X, Y and Z are respectively the angles around the sagittal, transverse and coronal planes.

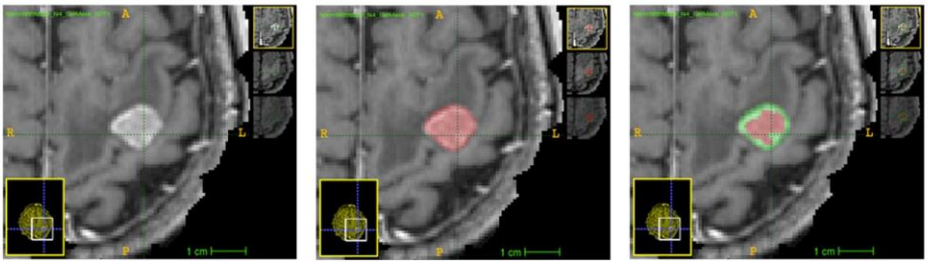

Fig. 5. From left to right: axial view of the 3DT1Gd image without segmentation, SM with the metastases segmented in red, and AM with active part of the metastases segmented in green and the necrotic part in red. (For interpretation of the references to colour in this figure legend, the reader is referred to the Web version of this article.)

Table 1
Composition of the different databases (noted 3_{T1} to $3_{T1}2_{FL}2^{A}_{T1}$) tested in this study. SM: standard map. AM: advanced map.

		3_{T1}	2_{FL}	2_{T1}	$3_{T1}2_{FL}$	$3_{T1}2_{T1}$	$3_{T1}2_{FL}2_{T1}$	3^{V}_{T1}	$3_{T1}2^{V}_{FL}$	$3_{T1}2_{FL}2^{V}_{T1}$	$3_{T1}2^{A}_{FL}$	$3_{T1}2^{A}_{T1}$	$3_{T1}2_{FL}2^{A}_{T1}$
Real patients (SM)	3DT1Gd	X			X	X	X	X	X	X			
	2DFLAIR		X		X		X		X	X			
	2DT1			X		X	X			X			
Virtual patients	3DT1Gd							X	X	X			
	2DFLAIR								X	X			
	2DT1									X			
Real patients (AM)	3DT1Gd										X	X	X
	2DFLAIR										X		X
	2DT1											X	X

each epoch. Likewise, the whole image is not used: it is cut into segments, whose size is parameterizable. At each sub-epoch, a certain number of segments are randomly selected. Moreover, DeepMedic uses a batch processing of these segments (size of the batch defined by the "batch-size") to improve the computation time and enhance parallel computations.

2.3. Pre-processing

The DICOM MRI were anonymized and converted into Nifti format with the dcm2nii software. The same operation was performed for the DICOM-RT structure set files using Plastimatch [24]. The three modalities 3DT1Gd, 2DFLAIR and 2DT1 have different spatial resolution, so the images were resampled with a tri-linear interpolation to fit the 3DT1Gd imaging resolution. The 2DT1 and 2DFLAIR MRI were registered on the 3DT1Gd MRI with FSL-FLIRT, and the BM contours transposed into the 3DT1Gd MRI coordinate system. Rigid transformation was preferred, since there should be no elastic deformation between the three MRI modalities, which were acquired at intervals of several seconds. Due to the privacy problems associated with the possibility of reconstructing the patient's face, the brain was segmented using the Brain Extraction Tool (BET) algorithm of Smith et al. [25]. All pixels outside the brain were removed. This segmentation also allowed to filter certain structures such as the eyes, the nerves, the face or the fat, which can decrease the CNN performances. We applied BET on the 2DT1 image, to avoid the segmentation difficulties associated with gadolinium injection. The inhomogeneity of the B0 field and of the RF pulse was corrected by the standard non-uniform intensity normalization algorithm N4 [26] (see Fig. 6). The data was normalized so that the average intensity of the voxels is equal to 0 and the standard deviation equal to 1. Hyper-intense pixels at 99% were thresholded.

2.4. Experiments

A flow-chart showing steps applied in this work is given in Fig. 7. The first step is to determine the value of the network parameters allowing a

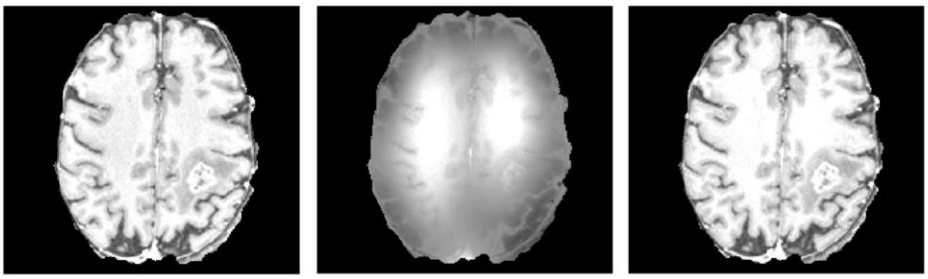

Fig. 6. Left: axial slice of the MRI 3DT1 of a patient of this study before correction by the standard non-uniform intensity normalization algorithm N4. Middle: the same axial slice illustrating the correction by N4. Right: the same axial slice after correction by N4.

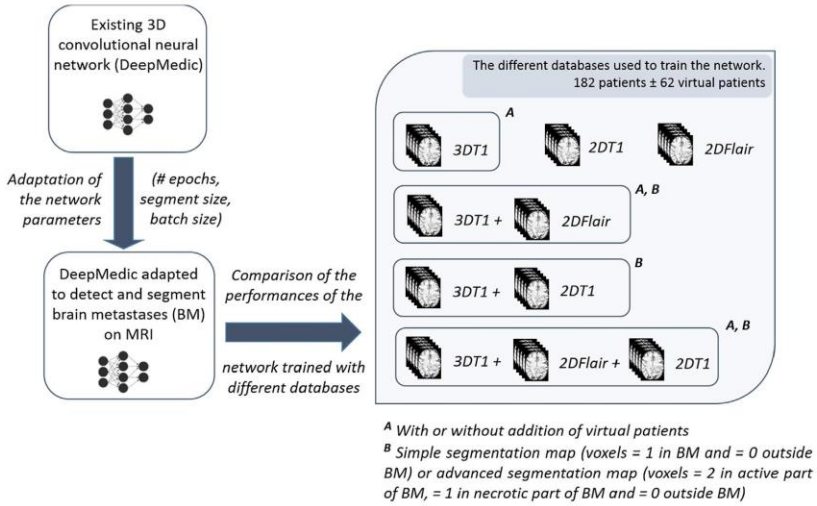

Fig. 7. Flow-chart showing steps applied in this work.

correct detection and segmentation of metastases (rather than gliomas) within a reasonable time frame. The second step is to examine the impact of choice of modalities, virtual patients and number of classes.

Network performance was evaluated by varying:

- the number of epochs on the DB 3_{T1}, 2_{FL}, 2_{T1}, $3_{T1}2_{FL}$, $3_{T1}2_{T1}$ and $3_{T1}2_{FL}2_{T1}$,
- the segment size: $20 \times 20 \times 20\,mm^3$, $22 \times 22 \times 22\,mm^3$, $24 \times 24 \times 24\,mm^3$ et $25 \times 25 \times 25\,mm^3$ (on DB 3_{T1}, batch size = 40),
- the batch size: 10 and 40 (on DB 3_{T1}, segment size = $24 \times 24 \times 24\,mm^3$).

Given the results obtained, we set the following network configuration: batch size 10, segment size $24 \times 24 \times 24\,mm^3$, 30 epochs, 20 sub-epochs, 1000 segments and 50 patients/epochs. The corresponding learning time was about 30 h, and that of detection and segmentation for a patient about 20 min (intel Xeon processor and NVIDIA 1080 graphics card with8 GB RAM).

With this network configuration, segmentation and detection performance were quantified by varying:

- the imaging modalities included in the DB 3_{T1}, 2_{FL}, 2_{T1}, $3_{T1}2_{FL}$, $3_{T1}2_{T1}$ and $3_{T1}2_{FL}2_{T1}$,
- the segmentation map: SM or AM for the DB $3_{T1}2_{FL}$, $3_{T1}2_{T1}$ and $3_{T1}2_{FL}2_{T1}$,
- the inclusion or not of virtual patients in DB 3_{T1}, $3_{T1}2_{FL}$ and $3_{T1}2_{FL}2_{T1}$,

Finally, we quantified the utility of a simple post-processing by rejecting any structure generated by the network with a volume less than $4\,mm^3$.

2.5. Quality measures

The performance of the network was evaluated both on detection and segmentation. Detection is defined as the network ability to detect a metastasis segmented by the physician. Segmentation is defined as its ability to provide a contour identical to that of the radiation oncologist.

Detection performance of the network was quantified by:

- the sensitivity Sd = TPm/(TPm + FNm) where TPm is the number of metastases correctly detected and FNm the number of undetected metastases,
- the number of false positives FPm where FPm is the number of falsely detected metastases.

Segmentation performance of the network was quantified by:

- The Dice Similarity Coefficient DSC = (2xTPv)/(2xTPv + FPv + FNv) where TPv is the number of voxels correctly detected, Fpv the number of voxels falsely detected, and FNv the number of voxels not detected.

Note that more detailed results on segmentation performances are given in appendix 2:

- the sensitivity Ss = TPv/(TPv + FNv),
- the Precision Ps = TPv/(TPv + FPv).

The results are given as an average of the results on the 18 patients of the test DB.

3. Results

The detailed results are given in Appendix 2.

Table 2 gives the mean of all patients of the sensitivity scores Sd, the number of false positives Fp and the Dice DSC index by varying the segment and the batch size.

Table 3 gives the average of all patients of the sensitivity scores Sd, the number of false positives Fp and the Dice DSC index for the different databases and a fixed network configuration detailed in the previous section.

Table 4 gives the same results as Table 3, with an additional post-processing step consisting of rejecting structures whose volume is less than $4\,mm^3$.

Table 2
Mean of all patients of the sensitivity scores Sd, the number of false positives Fp and the Dice index DSC by varying the segment and the batch size. Results obtained on DB 3_{T1}. Batch size = 40 when segment size varies. Segment size = 24 × 24 × 24 mm^3 when batch size varies. Best results in bold.

	Segment size				Batch size	
	20*20*20 mm^3	22*22*22 mm^3	24*24*24 mm^3	25*25*25 mm^3	10	40
Sd	**1.00**	**1.00**	**1.00**	0.97	0.91	0.91
Fp	117.9	37.3	19.4	11.8	**9.7**	42.1
DSC	0.49	0.68	0.75	**0.77**	0.76	0.63

Table 3
Mean of all patients of the sensitivity scores Sd, the number of false positives Fp and the index Dice DSC as a function of the database used to train the network. Best results in bold.

	DataBase											
	3_{T1}	2_{FL}	2_{T1}	$3_{T1}2_{FL}$	$3_{T1}2_{T1}$	$3_{T1}2_{FL}2_{T1}$	3^{V}_{T1}	$3_{T1}2^{V}_{FL}$	$3_{T1}2_{FL}2^{V}_{T1}$	$3_{T1}2^{A}_{FL}$	$3_{T1}2^{A}_{T1}$	$3_{T1}2_{FL}2^{A}_{T1}$
Sd	0.92	0.84	0.67	0.96	0.90	0.93	0.93	0.97	0.92	**0.98**	0.91	0.94
Fp	10.5	30.7	46.6	9.6	15.2	**7.8**	9.3	10.7	**7.8**	14.2	13.8	12.7
DSC	0.77	0.45	0.25	0.77	0.77	**0.79**	0.78	0.77	0.78	0.77	**0.79**	0.77

Table 4
Mean of all patients of the sensitivity scores Sd, the number of false positives Fp and the index Dice DSC as a function of the database used to train the network, after a post-processing step consisting of rejecting the structures <4 mm^3. Best results in bold.

	DataBase											
	3_{T1}	2_{FL}	2_{T1}	$3_{T1}2_{FL}$	$3_{T1}2_{T1}$	$3_{T1}2_{FL}2_{T1}$	3^{V}_{T1}	$3_{T1}2^{V}_{FL}$	$3_{T1}2_{FL}2^{V}_{T1}$	$3_{T1}2^{A}_{FL}$	$3_{T1}2^{A}_{T1}$	$3_{T1}2_{FL}2^{A}_{T1}$
Sd	0.92	0.84	0.64	0.96	0.90	0.93	0.93	0.97	0.92	**0.98**	0.91	0.91
Fp	6.0	17.8	25.9	5.6	7.6	**4.4**	5.3	5.9	4.6	7.2	6.8	6.8
DSC	0.77	0.46	0.25	0.77	0.77	**0.79**	0.78	0.78	0.78	0.77	**0.79**	0.77

4. Discussion

4.1. Number of epochs, segment size and batch size

35 epochs are performed by default in DeepMedic, which is originally optimized for the BRATS DB. For our learning DB, the performance of the network reached a threshold at 30 epochs without generating over-learning (data not shown). The simpler BM geometry, compared to gliomas, may explain this need for fewer iterations.

The size of the segments had an important impact on the performance of the network, since the proportion of metastases in the segment (see Fig. 8) and consequently their representation within the network depends on it. We observed (Table 2) that when the segment size increased from 20*20*20 mm^3 to 25*25* 25 mm^3, the mean sensitivity Sd decreased substantially (1–0.97), the mean number of false positive FPm decreased (117.9–11.8), and the average DSC index increased (0.49–0.77). These results can be explained by the fact that some filamentous structures such as blood vessels (also hyper-intense) are truncated with smaller segments. This truncated representation of these structures makes them similar to metastases and the number of false positives increases.

According to the DeepMedic authors, a high batch size should give better results, the data being better represented. Surprisingly, we observed lower performances with a batch size equal to 40 compared to a batch size equal to 10 (Table 2). The sensitivity Sd remained stable, but the mean number of false positives FPm increased from 9 to 41.5, and the average DSC index decreased from 0.76 to 0.63. An explanation could perhaps be the inhomogeneity of the data: if the sample size is sufficiently small, the probability of having only small or large metastases is higher. The network will only train on one type of data at a time, which might be favoring a neural path adapted to one type of metastasis, rather than seeking to establish a global path allowing to segment any type of the metastasis.

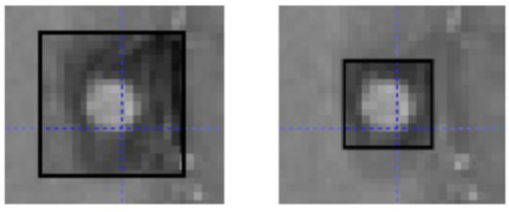

Fig. 8. Illustration of the influence of the segment size. On the left, a segment size of 25*25*25 mm^3; on the right a segment size of 15*15*15 mm^3.

4.2. MRI modalities

When comparing between databases with single imaging modalities (DB 3_{T1}, 2_{FL}, 2_{T1}), we observed as expected that the performance of the network was better with the 3DT1Gd MRI than with 2DT1 and 2DFLAIR. This can be explained by the higher spatial resolution of the 3DT1Gd image, as well as the Gadolinium injection. In the case of the use of a single modality in the database, the 3DT1Gd modality thus makes it possible to obtain the best network performance, in terms of detection quality as well as segmentation.

However, the combined use of different MRI modalities outperformed the performances of the network when using single modalities. More particularly, when comparing the performance of the network using 3DT1Gd/2DFLAIR (DB $3_{T1}2_{FL}$) or 3DT1Gd/2DT1 (DB $3_{T1}2_{T1}$), sensitivity and number of false positives were in favor of DB $3_{T1}2_{FL}$ versus DB $3_{T1}2_{T1}$ (respectively Sd = 0.96 Vs 090 and FPm = 9.6 Vs 15.2). The average segmentation score was identical in both cases (DSC = 0.77). However, the standard deviation of the false positive number FPm was higher with the 3DT1Gd/2DFLAIR DB than with the 3DT1Gd/2DT1 (see appendix 2). Indeed, the number of false positives was very high for several patients using the DB $3_{T1}2_{FL}$. One possible explanation is the presence of some patients with leukoaraiosis, which results in hyper-intense spots having the same characteristics as a BM on 2DFLAIR images, and which does not appear on the 3DT1Gd and 2DT1 modalities.

Among the 6 configurations tested, the simultaneous use of the 3

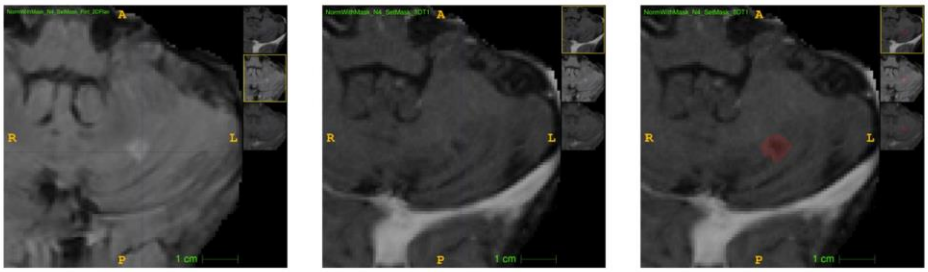

Fig. 9. Case where the cerebral metastasis did not take the contrast on 3DT1Gd image. From left to right: 2DFLAIR, 3DT1Gd without segmentation and with segmentation by the physician.

imaging modalities (DB $3_{T1}2_{FL}2_{T1}$) gave the best DSC segmentation (0.79) and number of false positives detected per patient results (7.8). However, the detection sensitivity score Sd was lower than that obtained using only the 2 imaging modalities 3DT1Gd/2DFLAIR (DB $3_{T1}2_{FL}$). This can be explained because in some cases, MRI is acquired too soon after the injection of Gadolinium. The contrast medium does not have time to reach the BM which then remain non-hyper-intense in both 3DT1Gd and 2DT1 images (see Fig. 9). The percentage of images on which the metastasis is not visible therefore increases from 50% with DB $3_{T1}2_{FL}$ to 66% with DB $3_{T1}2_{FL}2_{T1}$, which may explain the detection sensitivity decrease in network performance.

4.3. Simple and advanced segmentation maps

The use of the advanced segmentation map describing the active and necrotic parts of the metastasis allowed a slight gain in detection sensitivity Sd, compared to the use of simple segmentation maps. This gain, however, depended on the performance of the network not to generate false positives. This improvement in sensitivity to the detriment of the detection of false positives could partly be explained by the new weighting of the classes: when learning with two classes (healthy background and metastasis), they have the same probability of appearance at the creation of the segments (50% background, 50% metastasis). When using three classes, the background is only 33%, and the metastasis is 67% (active + necrotic). This change in weighting is, however, more complex than simply changing the weighting between two classes. Indeed, small metastases are composed only of an active tumor part, whereas necrosis appears on the larger metastases. This means that large metastases have a probability of occurrence greater than 33%, whereas small metastases have a probability of occurrence of less than 33%. One way to explore would be to compensate for this weight change manually (permitted by DeepMedic).

4.4. Limited dataset

It is useful to clarify a point about the number of patients included in our dataset. This number may seem limited, even if we have the third most important database compared to the other eleven studies listed in Table 5. Indeed, collecting more properly labelled data is difficult. We initially recovered several hundred of patients treated during 6 years with stereotactic cranial radiotherapy at the Paul Strauss Cancer center, which is one of the French centers having the biggest activity in this area. We chose to exclude patients previously treated with radiotherapy or surgery, to reduce potential learning bias. Note that in the majority of other studies, the authors do not specify if patients were previously treated or not. We have also excluded other patients for technical reasons. This work was very time-consuming: one by one, each patient has to be manually restored and opened on the manufacturer's software (iPlan, which does not have an archiving system), then exported individually to obtain the DICOM files. The constitution of our database composed of 182 patients required nearly 3 months of work.

For this reason, we cannot include significantly more patients unless we wait several more years. For this reason, we tested the use of virtual patients, which allowed to increase the volume of patients in our initial database.

4.5. Virtual patients

Of the 3 DB configurations tested (3_{T1}, 2_{FL}, 2_{T1}), the inclusion of virtual patients did not seem to have a significant impact on network performance, regardless of the indicator. Several explanations can be found. The increase in the number of patients allowed by the addition of virtual patients (from 182 to 244) may not be sufficient. Another explanation could be the choice of patients (with more than 3 metastases). Indeed, patients with more than 3 metastases often have a lot of small metastases that are sometimes confused by the network with leukoaraiosis, which favors the increase in the false positives detection.

4.6. Comparison with other studies

With simple enhancements filters combined with a linear discriminant analysis to distinguish from false positives, Sugimoto et al. obtained a sensitivity of 76.4% with 9.4 average number of false positive per case to detect BM on T1 weighted MRI (results and database characteristics are given in Table 5, as for the following studies) [27]. Ambrosini et al. developed a 3D template-based matching BM detection algorithm also using T1 weighted MRI, requiring a processing time of 30 min per brain [28]. They used a 3D spherical template, taking into account notably the nature of metastases borders. One of the limitations of this method was the hypothesis of the spherically and the intensity homogeneity of the BMs, which, although it remained true in many cases, can sometimes be totally erroneous because for example of necrotic regions. To fix these issues, Farjam et al. developed the same kind of 3D spherical mask intended to be used with T1 weighted MRI, including in particular a necrotic region [29]. Perez et al. also proposed a 3D template based matching algorithm with 3D varying ellipsoidal radii templates, combined with a false positive rate reduction technique based on the measurement of the object elongation [30]. Using contrast-enhanced MR black-blood imaging sequence represent another way to reduce the false-positive rate due especially to small blood vessels confused with metastases by detection algorithms [31]. Always with a 3D spherical template matching, combined with an artificial neural network to discriminate false positives, they obtained significantly better results than those obtained with classical T1 weighted MRI. Kwon et al. also used MR black-blood imaging and developed a new size and shape selective detection method, but they did not clearly quantify the performance of the algorithm [32]. Yu et al. developed a

Table 5
Overview of database characteristics and algorithm performance of papers which investigated computer-aided detection of brain metastases. Unless otherwise stated, T1 weighted MRI are used. More detailed results (such as Receiver Operating Curves) can sometimes be found in the publications. In bold: deep-learning based methods. In italic: with a 4 mm^3 threshold post-processing.

	#Patients (Training/test data)	#Méta. (Training/test data)	Diameter (mm) [Min-Max]	Sensitivity Sd (%)	False positive rate FP	Dice DSC
Sugimoto [27]	-/34	-/365	[2.6–49.4] Mean = 7.2	76.4	9.4/patient	
Ambrosini [28]	9/22	124/79	[3–45] Median = 7	89.9	0.22/slice	
Farjam [29]	9/20	60/186	[NA- 5]	93.5	0.024/slice	
Yang[a] [31]	7/19	33/57	[1–6] Median = 3.8	81.1	0.42/patient	
Yu [33]	-/20	-/85	[2–38]	95.3 87.4	10.4/patient 3.7/patient	
Perez [13]	8/11	20/42	[2.5–44.1] Mean = 7.8	88.1	0.05/slice	
Sunwoo [34]	80/30	450/134	[1–16] Median = 4.5	87.3	302.4/patient	
Nie[b] [35]	–	–	[NA-8]	81.5	0.45/slice	
Takenaga [36]	13	97	[2.5–37.7]	80.4	5.6/patient	
Losch [17]	**440[c]/50**	**1675[d]**	**NA**	**82.8**	**7.7/patient**	**0.662**
Liu [18]	**490[e]**	**NA**	**NA**	-	-	**0.67**
This study	**164[f]/18**	**374/38**	**[1.6–27]** **Median = 7.0** **Mean = 8.1**	**93** **98** ***93*** ***98***	**7.8/patient** **14.2/patient** ***4.4/patient*** ***7.2/patient***	**0.77** **0.77** ***0.77*** ***0.79***

[a] MR black-blood.
[b] Results are taken from the review of Perez.
[c] Including 49 patients for validation data.
[d] For training, validation and test data.
[e] Including 265 gliomas patients from BRATS.
[f] Including 18 patients for validation data.

3D blob model to detect and segment BM and other brain tumors [33]. Applied to T1 MRI, their method tested the compactness of the 3D blobs and the brain asymmetry, and run in less than 3 min per brain. Sunwoo et al. developed a CAD software based on various spherical template-matching models to detect small BM and K-means clustering to detect the largest BM, associating with an artificial neural network to discriminate the false positive [34]. Sunwoo et al. were the only ones who have tested their CAD system under real clinical conditions for the detection of BM, quantifying its contribution as a second reader in the exercise of 4 radiologists. Their proposed method required 4 min to process per MRI, and the authors demonstrated that it helps radiologists to improve their diagnostic performance, especially for less-experienced reviewers.

To our knowledge, there is no public DB for BM, the DB used in the above studies being all different. Furthermore, the number of metastases included in the training and test DB was either undefined or sometimes very low (<100). Finally, some studies aimed to detect only small metastases (whose diameter is less than 8 mm). It is therefore difficult to compare our results with those published in the literature. Taking into account these precautions, our sensitivity and false positive detection scores are among the most interesting, as we detect all metastasis size and that our database is one of the largest. Our best FP/Sd scores were respectively 7.8/93% and 14.2/98%, depending on whether the focus is on the number of false positives or on detection performance. Moreover, the advantage of the DL is that it can associate detection and segmentation, unlike the other published methods.

When adding a simple post-processing step consisting in rejecting all structures with a volume less than 4 mm^3, we obtained better results, even more so without equivalent in the literature. This threshold allowed to reduce the number of FP per patient by a factor about 2, without compromising the detection sensitivity Sd. As a result, our best FP/Sd scores were respectively 4.4/93% and 7.2/98%, depending on whether the focus is on the number of false positives or on detection performance.

4.7. Work's novelty

We first wanted to show that it is possible to use an existing architecture, developed for neighboring but not equivalent needs (gliomas), and to obtain excellent results by re-training the network with data specific to our problem (brain metastases). This had never been done for brain metastases. In addition, compared to the existing work on brain metastases (deep-learning based or not), we are among the only ones to use multimodal MRIs, with up to 3 simultaneous modalities, whereas the vast majority of work used only 3DT1. We have shown the performance improvement of the algorithm by using multimodal images, and especially by associating 3DT1 and 2DFLAIR image. We are also the only ones to have studied the influence of adding virtual patients for BM detection. Finally, we seem to have put forward a certain number of new elements in the detection of metastases, such as the use of advanced segmentation maps to better differentiate necrotic and active parts, the clear and precise presentation of the distribution of metastases of our database, and the difficulty of differentiating brain metastases with other diseases such as leukoaraiosis or cavernomas.

5. Conclusion

We adapted an existing 3D CNN (DeepMedic) to detect and segment brain metastases on MRI. We showed that the simultaneous use of different MRI modalities (3DT1Gd/2DFLAIR/2DT1 or 3DT1Gd/2DFLAIR) outperforms the deep network algorithm performance than when using single MRI modalities. The use of a segmentation map differentiating the active part from the necrotic part of a metastasis did not improve the performance of the network. Our results showed that a deep network approach is promising for the detection and the segmentation of brain metastases on MRI. Nevertheless, if the use of an existing network already allowed us to obtain a 98% sensitivity with only 7.2 false positive per patient, it is reasonable to think that it is still possible to improve these results significantly. Indeed, our approach suffered from

two major limitations: the small size of the dataset and the use of model developed for brain lesions other than brain metastases. We plan to address these limitations in a future work, notably by developing a deep model adapted to the specific problem of the brain metastases. We already tried to increase the dataset size by adding virtual patients, without significant results on the performances of the algorithm. This increase was however limited, and we will study a more massive use of virtual patients. The last step will be to test the contribution of this algorithm by integrating it into our hospital workflow for the treatment of patients with stereotactic radiotherapy. The objective will be to quantify two main indicators: the possible time saving, as well as the possible detection of metastases not detected by the radiation oncologist.

Funding

This research did not receive any specific grant from funding agencies in the public, commercial, or not-for-profit sectors.

Conflict of interest

None declared.

Appendix 1. Leukoaraiosis and cavernomas

Differential diagnostics for brain metastases imaging are leukoaraiosis or cavernomas. Leukoaraiosis corresponds to vascular alterations (micro-angiosclerosis) with fibrohyaline thickening, in the white matter of the brain (see Fig. a1). The presentation is a kind of the FLAIR hypersignal without taking contrast. Cerebral cavernomas are vascular malformations consisting of groups of small vessels consisting of a single layer of epithelium, with no other tissue usually present in the vessel. Their variable MRI presentation can sometimes create images close to those of brain metastases (see Fig. a2).

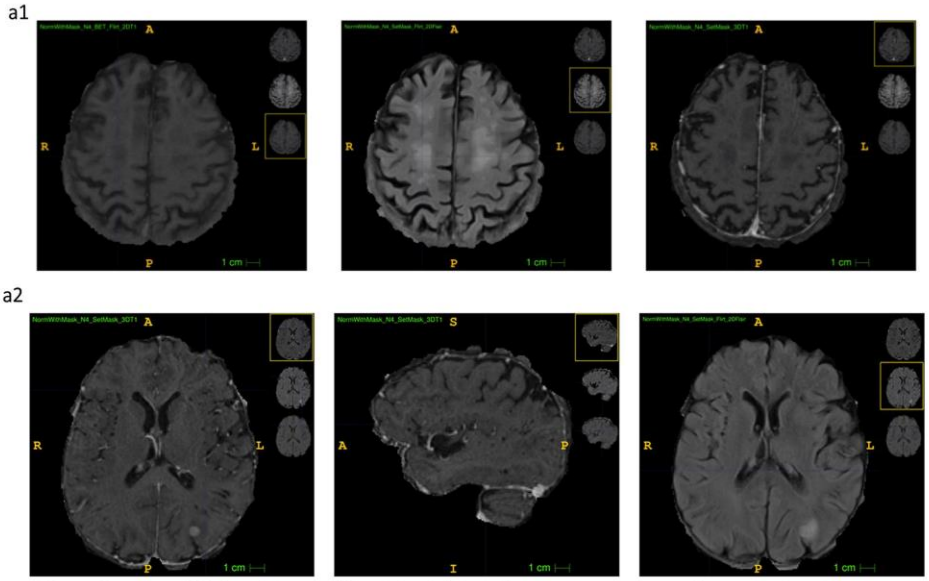

Fig. a1. **a1**. Axial view of a patient with leukoaraiosis. From left to right: axial views of 2DT1, 2DFLAIR and 3DT1Gd MRI. **a2**. Patient with cavernomas. From left to right: axial view of 3DT1 MRI, sagittal and axial view of 2DFLAIR MRI.

Appendix 2. Detailed results

Segment size

The network performance observed by varying the segments size is given in Table a1.

Table a1
Performance of the network by varying the size of the segments. Results obtained on DB 3_{T1}, with a batch size = 40. STD = Standard Deviation.

		Segment size		
		$20*20*20$ mm^3	$22*22*22$ mm^3	$25*25*25$ mm^3
Detection Sensitivity Sd	Min	1.00	1.00	0.67
	Max	1.00	1.00	1.00
	Mean	1.00	1.00	0.97

(*continued on next page*)

Table a1 (*continued*)

		Segment size		
		20*20*20 mm^3	22*22*22 mm^3	25*25*25 mm^3
	Median	1.00	1.00	1.00
	STD	0.00	0.00	0.09
False Positive FPm	Min	63.0	14.0	2.0
	Max	205.0	61.0	29.0
	Mean	117.9	37.3	11.8
	Median	112.0	31.0	9.2
	STD	43.7	15.3	8.3
Dice Similarity Coefficient DSC	Min	0.07	0.16	0.19
	Max	0.79	0.89	0.93
	Mean	0.49	0.68	0.77
	Median	0.50	0.71	0.83
	STD	0.20	0.21	0.19

Batch size

The network performance observed by varying the batch size is given in Table a2.

Table a2
Performance of the network by varying the size of the segments. Results obtained on DB 3_{T1}, with a segment size = 24*24*24 mm^3. STD = Standard Deviation.

		Batch Size	
		40	10
Detection Sensitivity Sd	Min	0.00	0.00
	Max	1.00	1.00
	Mean	0.91	0.91
	Median	1.00	1.00
	STD	0.24	0.24
False Positive FPm	Min	13.0	2.0
	Max	86.0	31.0
	Mean	42.1	9.7
	Median	41.5	9.0
	STD	23.0	6.9
Dice Similarity Coefficient DSC	Min	0.00	0.00
	Max	0.91	0.92
	Mean	0.63	0.76
	Median	0.72	0.82
	STD	0.26	0.22
Segmentation Sensitivity Ss	Min	0,00	0,00
	Max	0,98	0,98
	Mean	0,83	0,82
	Median	0,89	0,89
	STD	0,22	0,23
Segmentation Precision Ps	Min	0,00	0,00
	Max	0,90	0,92
	Mean	0,55	0,74
	Median	0,69	0,82
	STD	0,28	0,22

MRI modalities

The network performance obtained by varying the MRI imaging modalities included in the database is given in Table a3.

Table a3
Performance of the network by varying the MRI modalities included in the database. STD = Standard Deviation.

		Database					
		3_{T1}	2_{FL}	2_{T1}	$3_{T1}2_{FL}$	$3_{T1}2_{T1}$	$3_{T1}2_{FL}2_{T1}$
Detection Sensitivity Sd	Min	0.00	0.00	0.00	0.67	0.00	0.22
	Max	1.00	1.00	1.00	1.00	1.00	1.00
	Mean	0.92	0.84	0.67	0.96	0.90	0.93
	Median	1.00	1.00	1.00	1.00	1.00	1.00
	STD	0.24	0.31	0.41	0.10	0.26	0.20
False Positive FPm	Min	1.0	12.0	20.0	0.0	3.0	0.0
	Max	30.0	62.0	86.0	41.0	39.0	22.0
	Mean	10.5	30.7	46.6	9.64	15.17	7.81
	Median	8.25	28.0	41.0	6.50	13.0	4.17
	STD	7.56	14.0	23.1	10.24	10.0	7.38
Dice Similarity Coefficient DSC	Min	0.00	0.00	0.00	0.30	0.00	0.00

(*continued on next page*)

Table a3 (*continued*)

		Database					
		3_{T1}	2_{FL}	2_{T1}	$3_{T1}2_{FL}$	$3_{T1}2_{T1}$	$3_{T1}2_{FL}2_{T1}$
	Max	0.93	0.91	0.88	0.93	0.94	0.94
	Mean	0.77	0.45	0.25	0.77	0.77	0.79
	Median	0.83	0.46	0.17	0.84	0.84	0.84
	STD	0.21	0.28	0.26	0.17	0.22	0.21
Segmentation Sensitivity Ss	Min	0,00	0,00	0,00	0,20	0,00	0,00
	Max	0,98	0,96	0,95	0,97	0,98	0,97
	Mean	0,83	0,53	0,31	0,81	0,83	0,81
	Median	0,89	0,54	0,24	0,88	0,88	0,89
	STD	0,22	0,31	0,32	0,20	0,22	0,23
Segmentation Precision Ps	Min	0,00	0,00	0,00	0,47	0,00	0,10
	Max	0,94	0,91	0,82	0,94	0,92	0,95
	Mean	0,74	0,46	0,26	0,76	0,73	0,79
	Median	0,82	0,41	0,15	0,81	0,81	0,86
	STD	0,22	0,30	0,26	0,15	0,23	0,20

Simple and advanced segmentation map

The network performance obtained by varying the segmentation map (simple or advanced) used in the database 2a, 2b and 3 is given in Table a4.

Table a4
Performance of the network by varying the segmentation map (simple or advanced) for the database $3_{T1}2_{FL}$, $3_{T1}2_{T1}$ and $3_{T1}2_{FL}2_{T1}$. STD = Standard Deviation.

		Database					
		$3_{T1}2_{FL}$	$3_{T1}2^{A}_{FL}$	$3_{T1}2_{T1}$	$3_{T1}2^{A}_{T1}$	$3_{T1}2_{FL}2_{T1}$	$3_{T1}2_{FL}2^{A}_{T1}$
Detection Sensibility Sd	Min	0.67	0.67	0.00	0.00	0.22	0.22
	Max	1.00	1.00	1.00	1.00	1.00	1.00
	Mean	0.96	0.98	0.90	0.91	0.93	0.94
	Median	1.00	1.00	1.00	1.00	1.00	1.00
	STD	0.10	0.08	0.26	0.25	0.20	0.19
False Positive FPm	Min	0.0	1.00	3.00	1.00	0.00	1.00
	Max	41.00	54.00	39.00	34.00	22.0	35.00
	Mean	9.64	14.19	15.17	13.78	7.81	12.74
	Median	6.50	9.67	13.00	11.00	4.17	7.00
	STD	10.24	13.48	10.02	9.71	7.38	11.41
Dice Similarity Coefficient DSC	Min	0.30	0.31	0.00	0.00	0.00	0.00
	Max	0.93	0.94	0.94	0.94	0.94	0.94
	Mean	0.77	0.77	0.77	0.79	0.79	0.77
	Median	0.84	0.81	0.84	0.84	0.84	0.84
	STD	0.17	0.16	0.22	0.21	0.21	0.22
Segmentation Sensitivity Ss	Min	0,20	0,24	0,00	0,00	0,00	0,00
	Max	0,97	0,98	0,98	0,98	0,97	0,97
	Mean	0,81	0,83	0,83	0,84	0,81	0,81
	Median	0,88	0,89	0,88	0,88	0,89	0,89
	STD	0,20	0,18	0,22	0,22	0,23	0,23
Segmentation Precision Ps	Min	0,47	0,35	0,00	0,00	0,10	0,01
	Max	0,94	0,94	0,92	0,93	0,95	0,94
	Mean	0,76	0,75	0,73	0,76	0,79	0,75
	Median	0,81	0,80	0,81	0,84	0,86	0,84
	STD	0,15	0,17	0,23	0,22	0,20	0,23

Virtual patients

The network performance obtained by adding virtual patients in the database 3_{T1}, $3_{T1}2_{FL}$ and $3_{T1}2_{FL}2_{T1}$ is given in Table a5.

Table a5
Performance of the network obtained by adding virtual patients in the database 3_{T1}, $3_{T1}2_{FL}$ and $3_{T1}2_{FL}2_{T1}$. STD = Standard deviation.

		Database					
		3_{T1}	3^{V}_{T1}	$3_{T1}2_{FL}$	$3_{T1}2^{V}_{FL}$	$3_{T1}2_{FL}2_{T1}$	$3_{T1}2_{FL}2^{V}_{T1}$
Detection Sensibility Sd	Min	0.00	0.00	0.67	0.67	0.22	0.00
	Max	1.00	1.00	1.00	1.00	1.00	1.00
	Mean	0.92	0.93	0.96	0.97	0.93	0.92
	Median	1.00	1.00	1.00	1.00	1.00	1.00
	STD	0.24	0.24	0.10	0.09	0.20	0.24
False Positive FPm	Min	1.0	1.0	0.0	0.0	0.0	0.0
	Max	30.0	32.0	41.0	46.0	22.0	24.0
	Mean	10.50	9.31	9.64	10.67	7.81	7.78
	Median	8.25	7.00	6.50	5.50	4.17	4.75
	STD	7.56	7.77	10.24	11.69	7.38	7.86

(*continued on next page*)

Table a5 (*continued*)

		Database					
		3_{T1}	3^{V}_{T1}	$3_{T1}2_{FL}$	$3_{T1}2^{V}_{FL}$	$3_{T1}2_{FL}2_{T1}$	$3_{T1}2_{FL}2^{V}_{T1}$
Dice Similarity Coefficient DSC	Min	0.00	0.00	0.30	0.38	0.00	0.00
	Max	0.93	0.93	0.93	0.94	0.94	0.94
	Mean	0.77	0.78	0.77	0.77	0.79	0.78
	Median	0.83	0.84	0.84	0.83	0.84	0.84
	STD	0.21	0.21	0.17	0.15	0.21	0.21
Segmentation Sensitivity Ss	Min	0,00	0,00	0,20	0,26	0,00	0,00
	Max	0,98	0,98	0,97	0,97	0,97	0,97
	Mean	0,83	0,81	0,81	0,81	0,81	0,80
	Median	0,89	0,89	0,88	0,88	0,89	0,87
	STD	0,22	0,23	0,20	0,19	0,23	0,22
Segmentation Precision Ps	Min	0,00	0,00	0,47	0,45	0,10	0,00
	Max	0,94	0,94	0,94	0,94	0,95	0,95
	Mean	0,74	0,76	0,76	0,77	0,79	0,77
	Median	0,82	0,83	0,81	0,82	0,86	0,86
	STD	0,22	0,23	0,15	0,15	0,20	0,23

References

[1] J.Y. Delattre, G. Krol, H.T. Thaler, J.B. Posner, Distribution of brain metastases, Arch. Neurol. 45 (1988) 741–744.

[2] S.R. Smalley, M.F. Schray, E.R. Laws, J.R. O'Fallon, Adjuvant radiation therapy after surgical resection of solitary brain metastasis: association with pattern of failure and survival, Int. J. Radiat. Oncol. Biol. Phys. 13 (1987) 1611–1616.

[3] E. Le Rhun, F. Dhermain, G. Vogin, N. Reyns, P. Metellus, Radionecrosis after stereotactic radiotherapy for brain metastases, Expert Rev. Neurother. 16 (2016) 903–914, https://doi.org/10.1080/14737175.2016.1184572.

[4] E. Goceri, C. Songül, Computer-based segmentation, change detection and quantification for lesions in multiple sclerosis, in: 2017 Int. Conf. Comput. Sci. Eng. UBMK, 2017, pp. 177–182, https://doi.org/10.1109/UBMK.2017.8093371.

[5] E. Dura, J. Domingo, E. Göçeri, L. Martí-Bonmatí, A method for liver segmentation in perfusion MR images using probabilistic atlases and viscous reconstruction, Pattern Anal. Appl. (2017) 1–13, https://doi.org/10.1007/s10044-017-0666-z.

[6] É. Grossiord, H. Talbot, N. Passat, M. Meignan, L. Najman, Automated 3D lymphoma lesion segmentation from PET/CT characteristics, in: 2017 IEEE 14th Int. Symp. Biomed. Imaging ISBI 2017, 2017, pp. 174–178, https://doi.org/10.1109/ISBI.2017.7950495.

[7] M. Moghbel, S. Mashohor, R. Mahmud, M.I.B. Saripan, Review of liver segmentation and computer assisted detection/diagnosis methods in computed tomography, Artif. Intell. Rev. (2017) 1–41, https://doi.org/10.1007/s10462-017-9550-x.

[8] E. Goceri, E. Dura, M. Gunay, Review on machine learning based lesion segmentation methods from brain MR images, in: 2016 15th IEEE Int. Conf. Mach. Learn. Appl. ICMLA, 2016, pp. 582–587, https://doi.org/10.1109/ICMLA.2016.0102.

[9] Z. Akkus, A. Galimzianova, A. Hoogi, D.L. Rubin, B.J. Erickson, Deep learning for brain MRI segmentation: state of the art and future directions, J. Digit. Imag. 30 (2017) 449–459, https://doi.org/10.1007/s10278-017-9983-4.

[10] G. Litjens, T. Kooi, B.E. Bejnordi, A.A.A. Setio, F. Ciompi, M. Ghafoorian, J.A.W.M. van der Laak, B. van Ginneken, C.I. Sánchez, A survey on deep learning in medical image analysis, Med. Image Anal. 42 (2017) 60–88, https://doi.org/10.1016/j.media.2017.07.005.

[11] D.L. Pham, C. Xu, J.L. Prince, Current methods in medical image segmentation, Annu. Rev. Biomed. Eng. 2 (2000) 315–337, https://doi.org/10.1146/annurev.bioeng.2.1.315.

[12] D. Whitey, Z. Koles, A review of medial image segmentation, Int. J. Bioelectromagn. 10 (2008) 125–148.

[13] U. Perez, E. Arana, D. Moratal, Brain metastases detection algorithms in magnetic resonance imaging, IEEE Lat. Am. Trans. 14 (2016) 1109–1114, https://doi.org/10.1109/TLA.2016.7459586.

[14] Y. LeCun, Y. Bengio, G. Hinton, Deep learning, Nature 521 (2015) 436–444, https://doi.org/10.1038/nature14539.

[15] E. Goceri, N. Goceri, Deep learning in medical image analysis: recent advances and future trends, in: Int. Conf. Comput. Graph. Vis. Comput. Vis. Image Process. CGVCVIP 2017, Lisbon, Portugal, 2017, pp. 305–310.

[16] A. Işın, C. Direkoğlu, M. Şah, Review of MRI-based brain tumor image segmentation using deep learning methods, Procedia Comput. Sci. 102 (2016) 317–324, https://doi.org/10.1016/j.procs.2016.09.407.

[17] Max Loschs, Thesis: Detection and Segmentation of Brain Metastases with Deep Convolutional Networks, 2015. http://www.diva-portal.se/smash/get/diva2:853460/FULLTEXT01.pdf. (Accessed 26 October 2016).

[18] Y. Liu, S. Stojadinovic, B. Hrycushko, Z. Wardak, S. Lau, W. Lu, Y. Yan, S.B. Jiang, X. Zhen, R. Timmerman, L. Nedzi, X. Gu, A deep convolutional neural network-based automatic delineation strategy for multiple brain metastases stereotactic radiosurgery, PLoS One 12 (2017), e0185844, https://doi.org/10.1371/journal.pone.0185844.

[19] A. López-Zorrilla, M. de Velasco-Vázquez, O. Serradilla-Casado, L. Roa-Barco, M. Graña, D. Chyzhyk, C.C. Price, Brain white matter lesion segmentation with 2D/3D CNN, in: J.M. Ferrández Vicente, J.R. Álvarez-Sánchez, F. de la Paz López, J. Toledo Moreo, H. Adeli (Eds.), Nat. Artif. Comput. Biomed. Neurosci, Springer International Publishing, Cham, 2017, pp. 394–403, https://doi.org/10.1007/978-3-319-59740-9_39.

[20] M.Y.Y. Law, B. Liu, DICOM-RT and its utilization in radiation therapy, RadioGraphics 29 (2009) 655–667, https://doi.org/10.1148/rg.293075172.

[21] DICOM Homepage. (n.d.). http://dicom.nema.org/. (Accessed 29 September 2017).

[22] M. Jenkinson, P. Bannister, M. Brady, S. Smith, Improved optimization for the robust and accurate linear registration and motion correction of brain images, NeuroImage 17 (2002) 825–841, https://doi.org/10.1006/nimg.2002.1132.

[23] Kamnitsask/deepmedic, GitHub. (n.d.). https://github.com/Kamnitsask/deepmedic. (Accessed 28 April 2017).

[24] P. Zaffino, P. Raudaschl, K. Fritscher, G.C. Sharp, M.F. Spadea, Technical Note: plastimatch mabs, an open source tool for automatic image segmentation, Med. Phys. 43 (2016) 5155, https://doi.org/10.1118/1.4961121.

[25] S.M. Smith, Fast robust automated brain extraction, Hum. Brain Mapp. 17 (2002) 143–155, https://doi.org/10.1002/hbm.10062.

[26] N.J. Tustison, B.B. Avants, P.A. Cook, Y. Zheng, A. Egan, P.A. Yushkevich, J.C. Gee, N4ITK: improved N3 bias correction, IEEE Trans. Med. Imag. 29 (2010) 1310–1320, https://doi.org/10.1109/TMI.2010.2046908.

[27] T. Sugimoto, S. Katsuragawa, T. Hirai, R. Murakami, Y. Yamashita, Computerized detection of metastatic brain tumors on contrast-enhanced 3D MR images by using a selective enhancement filter, in: World Congr. Med. Phys. Biomed. Eng. Sept. 7-12 2009 Munich Ger, Springer, 2009, pp. 2070–2072. https://link.springer.com/chapter/10.1007/978-3-642-03882-2_549. (Accessed 25 July 2017).

[28] R.D. Ambrosini, P. Wang, W.G. O'Dell, Computer-aided detection of metastatic brain tumors using automated three-dimensional template matching: CAD of brain metastases, J. Magn. Reson. Imag. 31 (2010) 85–93, https://doi.org/10.1002/jmri.22009.

[29] R. Farjam, H.A. Parmar, D.C. Noll, C.I. Tsien, Y. Cao, An approach for computer-aided detection of brain metastases in post-Gd T1-W MRI, Magn. Reson. Imag. 30 (2012) 824–836, https://doi.org/10.1016/j.mri.2012.02.024.

[30] Ú. Pérez-Ramírez, E. Arana, D. Moratal, Brain metastases detection on MR by means of three-dimensional tumor-appearance template matching: method for brain metastases detection, J. Magn. Reson. Imag. 44 (2016) 642–652, https://doi.org/10.1002/jmri.25207.

[31] S. Yang, Y. Nam, M.-O. Kim, E.Y. Kim, J. Park, D.-H. Kim, Computer-aided detection of metastatic brain tumors using magnetic resonance black-blood imaging, Invest. Radiol. 48 (2013) 113–119.

[32] H. Kwon, Y.M. Jung, J. Park, J.K. Seo, A new computer-aided method for detecting brain metastases on contrast-enhanced MR images, Inverse Probl. Imag. 8 (2014) 491–505, https://doi.org/10.3934/ipi.2014.8.491.

[33] C.-P. Yu, G. Ruppert, R. Collins, D. Nguyen, A. Falcao, Y. Liu, 3D Blob Based Brain Tumor Detection and Segmentation in MR Images, 2014, pp. 1192–1197, https://doi.org/10.1109/ISBI.2014.6868089.

[34] L. Sunwoo, Y.J. Kim, S.H. Choi, K.-G. Kim, J.H. Kang, Y. Kang, Y.J. Bae, R.-E. Yoo, J. Kim, K.J. Lee, et al., Computer-aided detection of brain metastasis on 3D MR imaging: observer performance study, PLoS One 12 (2017), e0178265.

[35] D. Nie, X. Cao, Y. Gao, L. Wang, D. Shen, Estimating CT image from MRI data using 3D fully convolutional networks, in: Deep Learn. Data Labeling Med. Appl, Springer, Cham, 2016, pp. 170–178, https://doi.org/10.1007/978-3-319-46976-8_18.

[36] T. Takenaga, Y. Uchiyama, T. Hirai, H. Nakamura, Y. Kai, S. Katsuragawa, J. Shiraishi, Computer-aided detection of metastatic brain tumors in magnetic resonance images, Nihon Hoshasen Gijutsu Gakkai Zasshi 69 (2013) 632–640, https://doi.org/10.6009/jjrt.2013_JSRT_69.6.632.

CONCLUSIONS DU CHAPITRE I.B

Nous avons commencé à nous intéresser aux applications potentielles du *deep learning* pour la radiothérapie en 2016, en collaboration avec l'équipe Modèles Image Vision (MIV) du laboratoire ICube. Nos premiers travaux ont consisté à développer un algorithme de détection et de segmentation des métastases cérébrales sur IRM, dans le cadre de traitements stéréotaxiques. Nous avons également effectué une revue des publications dans lesquelles une méthode de *deep learning* a été utilisée lors d'une étape de prise en charge d'un patient de radiothérapie. A l'IRC, le développement d'applications par *deep learning* dédiées à la radiothérapie constituera un de nos axes centraux de recherche.

C. PROJET DE RECHERCHE

1. Contexte

Contexte global

La radiothérapie, modalité thérapeutique incontournable dans le traitement du cancer, est une discipline dont la complexité s'est accélérée depuis les années 2000. Cette complexification a eu comme parallèle la nécessité d'augmenter les effectifs de physiciens médicaux.

En France, pour assurer la sécurité des traitements, les effectifs de promotion des physiciens médicaux ont été multipliés par quatre entre 2003 et 2010, le nombre de physiciens médicaux en exercice passant de 337 à 546 entre 2006 et 2013 (Observatoire National de la Radiothérapie, INCA). L'activité clinique est le quotidien de la grande majorité de ces physiciens médicaux, et laisse peu de temps à la recherche. La situation évolue cependant : d'après une enquête sur l'activité de recherche des physiciens médicaux présentée lors des journées scientifiques de la SFPM en 2016, 14 services de physique médicale déclarent avoir un temps officiellement dédié à la recherche. Avant 2011, ce nombre n'était que de quatre, preuve que les équipes se réorganisent, et que les activités de recherche de physique médicale sont progressivement intégrées aux activités cliniques des établissements.

Contexte local : l'Institut Régional du Cancer (IRC)

Portés par la volonté du Ministère de la Santé, sous l'impulsion de l'Agence Régionale de Santé d'Alsace, le CPS et le CHU se sont rapprochés afin de constituer l'Institut Régional du Cancer (IRC). Un nouveau bâtiment, dont la construction s'achève sur le site de Hautepierre, rassemble les services d'oncologie et d'hématologie adultes des deux établissements, ainsi que le plateau technique de radiothérapie et de médecine nucléaire. Les premiers patients devraient être pris en charge en septembre 2018. L'objectif assumé est d'en faire un pôle de référence et de recours en cancérologie, constituant la tête du réseau régional du cancer et assurant des missions de recherche et d'enseignement. Concernant la radiothérapie, nous disposons de six bunkers où seront installées les technologies d'accélérateurs parmi les plus récentes en radiothérapie (trois tomothérapies dont une Radixact, un Truebeam STX, un Novalis TX et un Clinac). Le plateau technique de médecine nucléaire sera conséquent, puisqu'il devrait accueillir 2 PET-SCAN, 4 gamma-caméras et à terme 1 PET-IRM.

Le département de physique médicale du CPS intègrera l'IRC, et aura comme responsabilité le plateau de médecine nucléaire et de radiothérapie. Nous préparons ce projet complexe depuis plusieurs années. Lorsque nous prendrons possession des locaux de l'IRC, notre principale tâche sera d'assurer la transition du CPS vers l'IRC, en maintenant la file active de patients. Nous mettrons en place des technologies de machines de radiothérapie innovantes, des outils informatiques novateurs et de nouvelles méthodologies de gestion du parcours du patient. Notre but est de proposer aux patients qui seront pris en charge à l'IRC des traitements performants et sécurisés, tout en optimisant nos ressources et méthodes de travail.

Le développement des activités de recherche en physique médicale à l'IRC

En parallèle, le développement d'une plateforme de recherche en physique médicale au sein de l'IRC est un des axes prioritaires du département de physique médicale et du projet médical de l'IRC. Dans un premier temps, cette plateforme aura comme but le développement de projets autour des patients

traités en radiothérapie. Dans un second temps, la médecine nucléaire fera partie des axes de recherche, en fonction des convergences qui seront trouvées avec nos homologues du CHU. Pour ce faire, nous souhaitons nous appuyer sur les collaborations entreprises ces dernières années avec des structures de recherche strasbourgeoises : les équipes DeSIs et RAMSES de l'IPHC, l'équipe MIV du laboratoire ICUBE, l'IHU, AERIAL, ou encore des structures privées comme Fibermetrix et Eurorad. La formalisation de ces collaborations devra permettre à ces équipes un accès plus simple aux installations de radiothérapie, une meilleure communication et des échanges facilités entre acteurs de terrain et équipes de recherche, ainsi qu'une visibilité plus forte de l'IRC. Cette plateforme sera également l'occasion de renforcer nos liens avec les équipes de physique médicale alsaciennes et du grand Est, avec lesquelles nous échangeons régulièrement.

Notre ambition est donc d'inscrire dans la durée nos activités de recherche, en franchissant un palier par rapport à notre fonctionnement actuel. Cette HDR fait partie intégrante de ce projet. Outre un objectif personnel, l'HDR est une ambition collective du département de physique médicale, qui doit nous aider à développer nos activités de recherche pour l'IRC. En plus des stagiaires actuels (master 2 et DQPRM), notre objectif est d'accueillir des doctorants et des étudiants post-docs, qui constitueront le pilier de notre projet de recherche en physique médicale. En termes d'organisation, je maintiendrai mon implication dans la routine des traitements de radiothérapie, cette implication étant à mon sens nécessaire à l'émergence de projets connectés à la réalité des besoins du terrain. Un profil de poste officiellement dédié à la recherche sera néanmoins souhaitable à court terme. Les techniques de radiothérapie modernes nécessitant aujourd'hui des compétences multiples, l'ensemble des physiciens médicaux seront impliqués dans les projets de recherche du service, centralisés autour du physicien HDR. Cette démarche est soutenue par le Dr Phys. Christophe Mazzara, responsable du département de physique médicale du CPS, ainsi que par le Dr Pierre Salze, responsable du département de radiothérapie du CPS, et par la direction du CPS.

2. Thématiques à court et moyen terme

Tomothérapie

Nous continuerons à affirmer notre maitrise de la tomothérapie, pour assurer un meilleur traitement au patient. Nous poursuivrons dans un premier temps l'étude des traitements mammaires (voir paragraphes suivants). La nouvelle tomothérapie Radixact, dont sera équipé l'IRC, ouvrira de nouvelles perspectives de recherche appliquée, notamment sur l'utilisation de l'imagerie qui sera novatrice par rapport aux tomothérapies actuelles, et qu'il faudra caractériser. Il sera également nécessaire d'explorer les nouvelles limites de la machine, dont le bras tournera plus vite et le débit sera plus élevé : nous étudierons l'impact de ces améliorations techniques sur la capacité de la machine à délivrer correctement les traitements, via des mesures par le détecteur intégré à la tomothérapie. Nous développerons une stratégie d'utilisation du module Delivery Analysis, dans le but d'automatiser le contrôle qualité et la prévention de modifications en cours de traitement. Cela pourra passer par l'extraction de données et le développement de nouveaux algorithmes d'analyse des données fournies par le module. La machine Radixact sera en outre accompagnée de nouveaux outils informatiques, qui faciliteront les techniques de radiothérapie adaptative. Il s'agira d'une révolution massive, puisque ces outils pourront être utilisés sur tous les patients traités sur les trois tomothérapies de l'IRC. Nous nous engagerons sur cette voie incontournable, dont la mise en œuvre n'est toujours pas effective en routine dans les services de radiothérapie. Ce travail nécessitera de collaborer étroitement avec les

radiothérapeutes de l'IRC, puisqu'il faudra évaluer l'apport clinique de cette technologie pour le patient. Une recherche de financement de thèse sur ce sujet est en cours.

Intelligence artificielle et deep learning

Nos travaux sur l'utilisation du *deep learning* en radiothérapie n'en sont qu'à leurs débuts. J'ai intégré l'équipe Modèles, Images, Visions (MIV) du laboratoire ICube en 2017, avec l'objectif d'appliquer ces modèles dans les processus de radiothérapie. Trois stages de master 2 sont d'ores et déjà prévus, financés notamment dans le cadre d'un appel à projet interne du laboratoire que j'ai décroché pour 2018-2019 (projet A_PART – Apprentissage Profond Appliqué à la RadioThérapie). L'algorithme que nous avons développé pour la détection des métastases cérébrales sera d'abord amélioré, puis testé en conditions cliniques en 2018. Cette évaluation aura pour objectif de quantifier et de comparer les performances de radiothérapeutes expérimentés et novices, avec et sans l'utilisation de cet algorithme. En parallèle, nous développerons des outils qui faciliteront l'interprétation du comportement d'un réseau de neurones convolutionnels. Ces outils permettront de visualiser les cartes d'activation des différentes couches (réseaux *deconvnet*), d'occlure ou de dégrader une fraction de l'entrée. Nous les utiliserons en 2019 pour débruiter des images de positionnement de radiothérapie de type CBCT ou MVCT, dont la qualité est relativement faible par rapport à celle de modalités diagnostiques. Nous utiliserons pour cela un réseau GAN, que nous entrainerons avec notre base de données constituée pour partie de plusieurs dizaines de milliers d'images MVCT de repositionnement. D'autres applications du *deep learning* sont prévues, notamment sur la modélisation des effets cliniques. Nous sommes enfin en phase d'évaluation d'un projet sur l'utilisation d'une technologie *deep learning* pour une application particulière en radiothérapie (confidentielle) avec la SATT Conectus Alsace. Cette application pourrait trouver sa place dans le projet PMRT décrit dans le paragraphe suivant.

Modélisation des effets cliniques/Big Data

L'utilisation des donnés massives de radiothérapie pour modéliser les traitements est un axe sur lequel nous continuerons à nous impliquer, notamment dans le développement de la PMRT (Plateforme de Modélisation en RadioThérapie). Ce projet ambitieux, initié en 2013 par le LPC de Caen, associe une dizaine de laboratoires français. Son objectif est la création d'un outil d'aide à la décision basé sur la prédiction statistique d'effets cliniques, pour aider le radiothérapeute vers une individualisation du traitement. Pour cela, il faut modéliser, évaluer et comparer des traitements en intégrant dans le modèle la phase physique (dosimétrie, contourage), la biologie (organes sains, tumeur), les données du patient (données de santé, imagerie, effets cliniques…) et celles du traitement (dosimétrie, fractionnement, …). Un des problèmes initiaux est de collecter efficacement, de standardiser et de conserver ces données. Nous avons entamé la phase de standardisation et de conservation des données, en collaboration avec nos radiothérapeutes et informaticiens : la nomenclature des organes à risque, des volumes cibles et des effets cliniques a été normalisée, afin de permettre une récupération et un stockage automatique des doses délivrées et du suivi du patient. Nous développons en collaboration avec les fabricants de réseau R&V des modules permettant de récupérer plus facilement les données cliniques du patient. Nous avons également développé des outils d'extraction automatique des données dosimétriques. Des contacts sont en cours avec d'autres centres de radiothérapie français, dans le but d'étendre cette standardisation et de créer une base de données itérative qui alimentera automatiquement la PMRT. Nous sommes en phase de validation des

outils qui ont été développés sur une base de données de patients traités au CPS pour des cancers ORLs.

Mesure des neutrons

En collaboration avec le laboratoire DeSIs de l'IPHC, notre démarche actuelle est de construire une plateforme de modélisation Monte-Carlo des accélérateurs du CPS, ainsi que de leurs systèmes d'imagerie associés. En 2017, nous avons déjà modélisé les traitements à champs fixes, IMRT statiques et VMAT (VoluMetric ArcTherapy) du Novalis TX sur GATE. Ces modélisations sont nécessaires à la poursuite du développement du nouveau détecteur CMOS AlphaRad pour la dosimétrie des neutrons thermiques et rapides en radiothérapie, dont nous avons récemment montré la faisabilité. Il est prévu d'intégrer ces détecteurs dans des fantômes anthropomorphiques, en vue de valider les simulations Monte-Carlo. Nous souhaitons également étudier l'intérêt du détecteur AlphaRad pour comparer la dose hors-champ globale (imagerie + neutrons secondaires) en radiothérapie, mais aussi en protonthérapie. A terme, les doses délivrées par les neutrons secondaires lors de traitements de protonthérapie pourront être inclus aux calculs de modèles de la plateforme PMRT.

Mouvements/modifications anatomiques du patient

La prise en compte des mouvements ou des modifications anatomiques du patient lors de l'irradiation est aujourd'hui une thématique importante en radiothérapie. Nous avons entamé sur ce sujet un travail préliminaire avec l'IHU sur une technologie de visualisation 3D de la surface externe du patient sur la table de traitement, avec corrélation aux mouvements internes de ses organes. En fonction de l'avancée de la phase préliminaire, nous pourrions envisager une seconde phase en milieu clinique. Des projets d'outils de positionnement en réalité augmentée permettant de confronter la position effective du patient sur la table de traitement avec celle de simulation pourraient également faire partie des voies de recherche.

Les modèles Monte-Carlo décrits dans le paragraphe précédent vont être prochainement utilisés dans le cadre d'un stage de Master 2 pour l'amélioration de la prise en charge des traitements mammaires par VMAT et tomothérapie. Notre objectif est de déterminer les paramètres d'irradiation permettant d'assurer une couverture cutanée optimale, et de mieux gérer les mouvements respiratoires et les modifications anatomiques en cours de traitement. Des modélisations Monte-Carlo de traitements mammaires VMAT sur fantômes numériques mobiles ou scanners 4D seront effectuées. Les simulations seront comparées aux calculs TPS et à des mesures par film gafchromic. Cette étude sera complétée avec des irradiations tomothérapie et VMAT-FFF, dont les modélisations seront fournies par des centres partenaires.

Objectifs à long terme

Notre objectif principal à long terme est de développer des compétences sur la gestion des données massives numériques, avec l'ambition de devenir leader. Ce thème est fortement transversal et en pleine expansion ; il pourrait être un élément fédérateur de l'IRC. Les différents axes de recherche évoqués dans les paragraphes précédents et sur lesquels nous travaillerons dans l'avenir vont dans ce sens. Cette amélioration ne pourra se faire efficacement qu'à la condition que les immenses bases de

données d'imagerie, techniques et cliniques soient mieux normalisées, plus facilement accessibles et mieux analysées. Nous apporterons notre contribution à cette évolution.

Nous affirmerons nos collaborations avec les laboratoires et entreprises strasbourgeoises et alsaciennes. De cette manière, nous souhaitons que l'investissement du département de physique médicale dans la recherche soit un facteur qui appuiera la présence de l'IRC en tant qu'acteur du pôle de compétitivité de la région Alsace dédié aux innovations thérapeutiques. Enfin, d'un point de vue clinique plus concret, notre objectif à long terme est de mettre à profit nos activités de recherche pour maintenir constamment la radiothérapie de l'IRC à la pointe des techniques, et assurer aux patients alsaciens des traitements performants.

REFERENCES

Accuray, 2013a. ETT.700456.A 1c Physics Course. Beamline Components.

Accuray, 2013b. 002 ETT.700230.B PS 5.0 2.0 Tomo Conventional.

Accuray, 2013c. ETT.700502.A Planning Course. Geometry Overview.

Ajani, B., Krishnan, K., n.d. Prostate segmentation in MR using 3D CNN with mean surface distance minimization loss.

Akkus, Z., Galimzianova, A., Hoogi, A., Rubin, D.L., Erickson, B.J., 2017. Deep Learning for Brain MRI Segmentation: State of the Art and Future Directions. J. Digit. Imaging 30, 449–459. https://doi.org/10.1007/s10278-017-9983-4

Akselrod-Ballin, A., Karlinsky, L., Alpert, S., Hasoul, S., Ben-Ari, R., Barkan, E., 2016. A Region Based Convolutional Network for Tumor Detection and Classification in Breast Mammography, in: Deep Learning and Data Labeling for Medical Applications, Lecture Notes in Computer Science. Springer, Cham, pp. 197–205. https://doi.org/10.1007/978-3-319-46976-8_21

Alexander, D.C., Zikic, D., Ghosh, A., Tanno, R., Wottschel, V., Zhang, J., Kaden, E., Dyrby, T.B., Sotiropoulos, S.N., Zhang, H., Criminisi, A., 2017. Image quality transfer and applications in diffusion MRI. NeuroImage 152, 283–298. https://doi.org/10.1016/j.neuroimage.2017.02.089

Aneja, S., Shaham, U., Kumar, R.J., Pirakitikulr, N., Nath, S.K., Yu, J.B., Carlson, D.J., Decker, R.H., 2017. Deep Neural Network to Predict Local Failure Following Stereotactic Body Radiation Therapy: Integrating Imaging and Clinical Data to Predict Outcomes. Int J Radiat Oncol Biol 99, S47. https://doi.org/10.1016/j.ijrobp.2017.06.120

Anirudh, R., Thiagarajan, J.J., Bremer, T., Kim, H., 2016. Lung nodule detection using 3D convolutional neural networks trained on weakly labeled data, in: Tourassi, G.D., Armato, S.G. (Eds.), . p. 978532. https://doi.org/10.1117/12.2214876

Antoni, D., Natarajan-Ame, S., Meyer, P., Niederst, C., Bourahla, K., Noel, G., 2013. Contribution of three-dimensional conformal intensity-modulated radiation therapy for women affected by bulky stage II supradiaphragmatic Hodgkin disease. Radiat. Oncol. 8. https://doi.org/10.1186/1748-717X-8-112

Aoulad, N., Massabeau, C., de Lafontan, B., Vieillevigne, L., Hangard, G., Ciprian, C., Chaltiel, L., Moyal, É., Izar, F., 2017. Toxicité aiguë de la tomothérapie des cancers mammaires. Cancer/Radiothérapie 21, 180–189. https://doi.org/10.1016/j.canrad.2016.11.008

Arbor, N., Higueret, S., Elazhar, H., Combe, R., Meyer, P., Dehaynin, N., Taupin, F., Husson, D., 2017. Real-time detection of fast and thermal neutrons in radiotherapy with CMOS sensors. Phys. Med. Biol. 62, 1920–1934. https://doi.org/10.1088/1361-6560/aa5bc9

Arivarasan, I., Anuradha, C., Subramanian, S., Anantharaman, A., Ramasubramanian, V., 2017. Magnetic resonance image guidance in external beam radiation therapy planning and delivery. Jpn. J. Radiol. 35, 417–426. https://doi.org/10.1007/s11604-017-0656-5

Armato, S.G., Drukker, K., Li, F., Hadjiiski, L., Tourassi, G.D., Engelmann, R.M., Giger, M.L., Redmond, G., Farahani, K., Kirby, J.S., Clarke, L.P., 2016. LUNGx Challenge for computerized lung nodule classification. J. Med. Imaging 3, 044506. https://doi.org/10.1117/1.JMI.3.4.044506

Ashfaq, A., 2016. Segmentation of Cone Beam CT in Stereotactic Radiosurgery (TRITA-STH, 2016:104). KTH, School of Technology and Health (STH).

Bahrami, K., Shi, F., Rekik, I., Shen, D., 2016. Convolutional Neural Network for Reconstruction of 7T-like Images from 3T MRI Using Appearance and Anatomical Features, in: Deep Learning and Data Labeling for Medical Applications, Lecture Notes in Computer Science. Springer, Cham, pp. 39–47. https://doi.org/10.1007/978-3-319-46976-8_5

Banerjee, I., Crawley, A., Bhethanabotla, M., Daldrup-Link, H.E., Rubin, D.L., 2017. Transfer learning on fused multiparametric MR images for classifying histopathological subtypes of rhabdomyosarcoma. Comput. Med. Imaging Graph. Off. J. Comput. Med. Imaging Soc. https://doi.org/10.1016/j.compmedimag.2017.05.002

Baudou, J., 2011. L'encyclopédie du fantastique, Fetjaine. ed.

Beavis, A.W., 2004. Is tomotherapy the future of IMRT? Br. J. Radiol. 77, 285–295. https://doi.org/10.1259/bjr/22666727

Belharbi, S., Chatelain, C., Hérault, R., Adam, S., Thureau, S., Chastan, M., Modzelewski, R., 2017a. Spotting L3 slice in CT scans using deep convolutional network and transfer learning. Comput. Biol. Med. 87, 95–103. https://doi.org/10.1016/j.compbiomed.2017.05.018

Belharbi, S., Chatelain, C., Hérault, R., Adam, S., Thureau, S., Chastan, M., Modzelewski, R., 2017b. Spotting L3 slice in CT scans using deep convolutional network and transfer learning. Comput. Biol. Med. https://doi.org/10.1016/j.compbiomed.2017.05.018

Ben-Cohen, A., Diamant, I., Klang, E., Amitai, M., Greenspan, H., 2016. Fully Convolutional Network for Liver Segmentation and Lesions Detection, in: Deep Learning and Data Labeling for Medical Applications, Lecture Notes in Computer Science. Springer, Cham, pp. 77–85. https://doi.org/10.1007/978-3-319-46976-8_9

Benedict, S.H., Naqa, I.E., Klein, E.E., 2016. Introduction to Big Data in Radiation Oncology: Exploring Opportunities for Research, Quality Assessment, and Clinical Care. Int. J. Radiat. Oncol. • Biol. • Phys. 95, 871–872. https://doi.org/10.1016/j.ijrobp.2015.12.358

Beneyton, V., Niederst, C., Vigneron, C., Meyer, P., Becmeur, F., Marcellin, L., Lutz, P., Noel, G., 2012. Comparison of the dosimetries of 3-dimensions Radiotherapy (3D-RT) with linear accelerator and intensity modulated radiotherapy (IMRT) with helical tomotherapy in children irradiated for neuroblastoma. BMC Med. Phys. 12. https://doi.org/10.1186/1756-6649-12-2

Beneyton, V., Quetin, P., Meyer, P., Niederst, C., Lutz, P., Noël, G., 2009a. Radiothérapie dans la prise en charge des neuroblastomes rétropéritonéaux de l'enfant : une place pour la tomothérapie ? Cancer/Radiothérapie 13, 656–657. https://doi.org/10.1016/j.canrad.2009.08.035

Beneyton, V., Quetin, P., Meyer, P., Niederst, C., Lutz, P., Noel, G., 2009b. Place de la tomothérapie dans l'irradiation des tumeurs du tronc de l'enfant. Cancer/Radiothérapie 13, 655–656. https://doi.org/10.1016/j.canrad.2009.08.032

Bibault, J.-E., Dussart, S., Pommier, P., Morelle, M., Huguet, M., Boisselier, P., Coche-Dequeant, B., Alfonsi, M., Bardet, E., Rives, M., Calugaru, V., Chajon, E., Noel, G., Mecellem, H., Servagi Vernat, S., Perrier, L., Giraud, P., 2017. Clinical Outcomes of Several IMRT Techniques for Patients With Head and Neck Cancer: A Propensity Score–Weighted Analysis. Int. J. Radiat. Oncol. 99, 929–937. https://doi.org/10.1016/j.ijrobp.2017.06.2456

Bibault, J.-E., Giraud, P., Burgun, A., 2016. Big Data and machine learning in radiation oncology: State of the art and future prospects. Cancer Lett. 382, 110–117. https://doi.org/10.1016/j.canlet.2016.05.033

Birkhead, G.S., Klompas, M., Shah, N.R., 2015. Uses of Electronic Health Records for Public Health Surveillance to Advance Public Health. Annu. Rev. Public Health 36, 345–359. https://doi.org/10.1146/annurev-publhealth-031914-122747

Boden, M.A., 1977. Artificial Intelligence and Natural Man. Basic Books.

Bourgier, C., Fenoglietto, P., Lemanski, C., Ducteil, A., Charissoux, M., Draghici, R., Azria, D., 2016. Techniques d'irradiation du cancer du sein en 2016 : intérêt et indications de la radiothérapie conformationnelle avec modulation d'intensité. Cancer/Radiothérapie, 27e Congrès national de la Société française de radiothérapie oncologique 20, 572–575. https://doi.org/10.1016/j.canrad.2016.07.067

Boutilier, J.J., Craig, T., Sharpe, M.B., Chan, T.C.Y., 2016. Sample size requirements for knowledge-based treatment planning. Med. Phys. 43, 1212–1221. https://doi.org/10.1118/1.4941363

Brahme, A., Roos, J.-E., Lax, I., 1982. Solution of an integral equation encountered in rotation therapy. Phys. Med. Biol. 27, 1221. https://doi.org/10.1088/0031-9155/27/10/002

Brock, K.K., Mutic, S., McNutt, T.R., Li, H., Kessler, M.L., 2017. Use of image registration and fusion algorithms and techniques in radiotherapy: Report of the AAPM Radiation Therapy Committee Task Group No. 132. Med. Phys. 44, e43–e76. https://doi.org/10.1002/mp.12256

Buchanan, B.G., 2005. A (very) brief history of artificial intelligence. Ai Mag. 26, 53.

Cha, K.H., Hadjiiski, L.M., Samala, R.K., Chan, H.-P., Cohan, R.H., Caoili, E.M., Paramagul, C., Alva, A., Weizer, A.Z., 2016. Bladder Cancer Segmentation in CT for Treatment Response Assessment: Application of Deep-Learning Convolution Neural Network—A Pilot Study. Tomogr. J. Imaging Res. 2, 421–429. https://doi.org/10.18383/j.tom.2016.00184

Chargari, C., Cosset, J.-M., 2013. Le problème des faibles doses en radiothérapie: quel risque de carcinogenèse radio-induite? Bull. Cancer (Paris) 100, 1333–1342.

Chargari, C., Goodman, K.A., Diallo, I., Guy, J.-B., Rancoule, C., Cosset, J.-M., Deutsch, E., Magne, N., 2016. Risk of second cancers in the era of modern radiation therapy: does the risk/benefit analysis overcome theoretical models? Cancer Metastasis Rev. 35, 277–288. https://doi.org/10.1007/s10555-016-9616-2

Charron, O., Lallement, A., Jarnet, D., Noblet, V., Clavier, J.-B., Meyer, P., 2018. Automatic detection and segmentation of brain metastases on multimodal MR images with a deep convolutional neural network. Comput. Biol. Med. 95, 43–54. https://doi.org/10.1016/j.compbiomed.2018.02.004

Chen, G.T.Y., Sharp, G.C., Mori, S., 2009. A review of image-guided radiotherapy. Radiol. Phys. Technol. 2, 1–12. https://doi.org/10.1007/s12194-008-0045-y

Chen, H., Zhang, Y., Zhang, W., Liao, P., Li, K., Zhou, J., Wang, G., 2017. Low-dose CT via convolutional neural network. Biomed. Opt. Express 8, 679–694. https://doi.org/10.1364/BOE.8.000679

Chen, M., Chen, Y., Chen, Q., Lu, W., 2011. Theoretical analysis of the thread effect in helical TomoTherapy. Med. Phys. 38, 5945–5960. https://doi.org/10.1118/1.3644842

Chen, Q., Chen, M., Lu, W., 2011. Ultrafast convolution/superposition using tabulated and exponential kernels on GPU. Med. Phys. 38, 1150–1161. https://doi.org/10.1118/1.3551996

Chen, Q., Xu, X., Hu, S., Li, X., Zou, Q., Li, Y., 2017. A transfer learning approach for classification of clinical significant prostate cancers from mpMRI scans. p. 101344F–101344F–4. https://doi.org/10.1117/12.2279021

Chrisley, R., Begeer, S., 2000. Artificial Intelligence: Critical Concepts. Taylor & Francis.

Christ, P.F., Ettlinger, F., Grün, F., Elshaera, M.E.A., Lipkova, J., Schlecht, S., Ahmaddy, F., Tatavarty, S., Bickel, M., Bilic, P., others, 2017. Automatic Liver and Tumor Segmentation of CT and MRI Volumes using Cascaded Fully Convolutional Neural Networks. ArXiv Prepr. ArXiv170205970.

Chu, C., De Fauw, J., Tomasev, N., Paredes, B.R., Hughes, C., Ledsam, J., Back, T., Montgomery, H., Rees, G., Raine, R., others, 2016. Applying machine learning to automated segmentation of head and neck tumour volumes and organs at risk on radiotherapy planning CT and MRI scans. F1000Research 5.

Coates, J., Souhami, L., El Naqa, I., 2016. Big Data Analytics for Prostate Radiotherapy. Front. Oncol. 6. https://doi.org/10.3389/fonc.2016.00149

Colvill, E., Booth, J., Nill, S., Fast, M., Bedford, J., Oelfke, U., Nakamura, M., Poulsen, P., Worm, E., Hansen, R., Ravkilde, T., Scherman Rydh?g, J., Pommer, T., Munck af Rosenschold, P., Lang, S., Guckenberger, M., Groh, C., Herrmann, C., Verellen, D., Poels, K., Wang, L., Hadsell, M., Sothmann, T., Blanck, O., Keall, P., 2016. A dosimetric comparison of real-time adaptive and non-adaptive radiotherapy: A multi-institutional study encompassing robotic, gimbaled, multileaf collimator and couch tracking. Radiother. Oncol. 119, 159–165. https://doi.org/10.1016/j.radonc.2016.03.006

Cosma, G., Brown, D., Archer, M., Khan, M., Pockley, A.G., 2017. A survey on computational intelligence approaches for predictive modeling in prostate cancer. Expert Syst. Appl. 70, 1–19. https://doi.org/http://dx.doi.org/10.1016/j.eswa.2016.11.006

Court, L.E., Balter, P., Mohan, R., 2015. Principles of IMRT, in: Nishimura, Y., Komaki, R. (Eds.), Intensity-Modulated Radiation Therapy. Springer Japan, Tokyo, pp. 15–42. https://doi.org/10.1007/978-4-431-55486-8_2

Crevier, D., 1993. Ai: The Tumultuous History Of The Search For Artificial Intelligence, First Edition edition. ed. Basic Books, New York, NY.

Dalmış, M.U., Litjens, G., Holland, K., Setio, A., Mann, R., Karssemeijer, N., Gubern-Mérida, A., 2017. Using deep learning to segment breast and fibroglandular tissue in MRI volumes. Med. Phys. 44, 533–546. https://doi.org/10.1002/mp.12079

Das, S.K., Zhou, S., Zhang, J., Yin, F.-F., Dewhirst, M.W., Marks, L.B., 2007. Predicting Lung Radiotherapy-Induced Pneumonitis Using a Model Combining Parametric Lyman Probit Withnonparametric Decision Trees. Int J Radiat Oncol Biol 68, 1212–1221. https://doi.org/10.1016/j.ijrobp.2007.03.064

de Brebisson, A., Montana, G., 2015. Deep neural networks for anatomical brain segmentation, in: Proceedings of the IEEE Conference on Computer Vision and Pattern Recognition Workshops. pp. 20–28.

De Kerf, G., Van Gestel, D., Mommaerts, L., Van den Weyngaert, D., Verellen, D., 2015. Evaluation of the optimal combinations of modulation factor and pitch for Helical TomoTherapy plans made with TomoEdge using Pareto optimal fronts. Radiat. Oncol. Lond. Engl. 10. https://doi.org/10.1186/s13014-015-0497-2

Dean, J.A., Wong, K.H., Welsh, L.C., Jones, A.-B., Schick, U., Newbold, K.L., Bhide, S.A., Harrington, K.J., Nutting, C.M., Gulliford, S.L., 2016. Normal tissue complication probability (NTCP) modelling using spatial dose metrics and machine learning methods for severe acute oral mucositis resulting from head and neck radiotherapy. Radiother. Oncol. J. Eur. Soc. Ther. Radiol. Oncol. 120, 21–27. https://doi.org/10.1016/j.radonc.2016.05.015

Diagne, R., 2006. DESCARTES ET LA METTRIE : DE LA VIE AU VIVANT. - Ethiop. - Rev. Negro-Afr. Litt. Philos.

Dodge, S., Karam, L., 2017. A Study and Comparison of Human and Deep Learning Recognition Performance Under Visual Distortions. ArXiv170502498 Cs.

Doi, K., 2007. Computer-Aided Diagnosis in Medical Imaging: Historical Review, Current Status and Future Potential. Comput. Med. Imaging Graph. Off. J. Comput. Med. Imaging Soc. 31, 198–211. https://doi.org/10.1016/j.compmedimag.2007.02.002

Dolz, J., Betrouni, N., Quidet, M., Kharroubi, D., Leroy, H.A., Reyns, N., Massoptier, L., Vermandel, M., 2016. Stacking denoising auto-encoders in a deep network to segment the brainstem on {MRI} in brain cancer patients: A clinical study. Comput. Med. Imaging Graph. 52, 8–18. https://doi.org/http://dx.doi.org/10.1016/j.compmedimag.2016.03.003

Dolz, J., Desrosiers, C., Ayed, I.B., 2017. 3D fully convolutional networks for subcortical segmentation in MRI: A large-scale study. NeuroImage. https://doi.org/10.1016/j.neuroimage.2017.04.039

Dolz, Jose, Reyns, N., Betrouni, N., Kharroubi, D., Quidet, M., Massoptier, L., Vermandel, M., 2017. A deep learning classification scheme based on augmented-enhanced features to segment organs at risk on the optic region in brain cancer patients. ArXiv170310480 Cs.

Dong, C., Loy, C.C., He, K., Tang, X., 2016. Image Super-Resolution Using Deep Convolutional Networks. IEEE Trans. Pattern Anal. Mach. Intell. 38, 295–307. https://doi.org/10.1109/TPAMI.2015.2439281

Edmund, J.M., Nyholm, T., 2017. A review of substitute CT generation for MRI-only radiation therapy. Radiat. Oncol. Lond. Engl. 12, 28. https://doi.org/10.1186/s13014-016-0747-y

Esteva, A., Kuprel, B., Novoa, R.A., Ko, J., Swetter, S.M., Blau, H.M., Thrun, S., 2017. Dermatologist-level classification of skin cancer with deep neural networks. Nature 542, 115–118. https://doi.org/10.1038/nature21056

Ezzell, G.A., Galvin, J.M., Low, D., Palta, J.R., Rosen, I., Sharpe, M.B., Xia, P., Xiao, Y., Xing, L., Yu, C.X., 2003. Guidance document on delivery, treatment planning, and clinical implementation of IMRT: Report of the IMRT subcommittee of the AAPM radiation therapy committee. Med. Phys. 30, 2089–2115. https://doi.org/10.1118/1.1591194

Fact Sheets by Cancer [WWW Document], n.d. URL http://globocan.iarc.fr/Pages/fact_sheets_cancer.aspx (accessed 9.27.17).

Fan, J., Wang, J., Zhang, Z., Hu, W., 2017. Iterative dataset optimization in automated planning: Implementation for breast and rectal cancer radiotherapy. Med. Phys. 44, 2515–2531. https://doi.org/10.1002/mp.12232

Farah, J., Martinetti, F., Sayah, R., Lacoste, V., Donadille, L., Trompier, F., Nauraye, C., De Marzi, L., Vabre, I., Delacroix, S., Hérault, J., Clairand, I., 2014. Monte Carlo modeling of proton therapy installations: a global experimental method to validate secondary neutron dose calculations. Phys. Med. Biol. 59, 2747–2765. https://doi.org/10.1088/0031-9155/59/11/2747

Fechter, T., Adebahr, S., Baltas, D., Ayed, I.B., Desrosiers, C., Dolz, J., 2017a. A 3D fully convolutional neural network and a random walker to segment the esophagus in CT. ArXiv170406544 Cs.

Fechter, T., Adebahr, S., Baltas, D., Ben Ayed, I., Desrosiers, C., Dolz, J., 2017b. Esophagus segmentation in CT via 3D fully convolutional neural network and random walk. Med. Phys. 44, 6341–6352. https://doi.org/10.1002/mp.12593

Fontanarosa, D., Meer, S. van der, Bamber, J., Harris, E., O'Shea, T., Verhaegen, F., 2015. Review of ultrasound image guidance in external beam radiotherapy: I. Treatment planning and inter-fraction motion management. Phys. Med. Biol. 60, R77. https://doi.org/10.1088/0031-9155/60/3/R77

Forsberg, D., Sjöblom, E., Sunshine, J.L., 2017. Detection and Labeling of Vertebrae in MR Images Using Deep Learning with Clinical Annotations as Training Data. J. Digit. Imaging 30, 406–412. https://doi.org/10.1007/s10278-017-9945-x

Franco, P., Catuzzo, P., Cante, D., Porta, M., Sciacero, Pi., Girelli, G., Casanova Borca, V., Pasquino, M., Numico, G., Tofani, S., Meloni, T., Ricardi, U., Ozzello, F., 2011. TomoDirect: An efficient means to deliver radiation at static angles with tomotherapy. https://doi.org/10.1700/950.10404

Franco, P., Zeverino, M., Migliaccio, F., Cante, D., Sciacero, P., Casanova Borca, V., Torielli, P., Arrichiello, C., Girelli, G., La Porta, M.R., Tofani, S., Numico, G., Ricardi, U., 2014. Intensity-modulated and hypofractionated simultaneous integrated boost adjuvant breast radiation employing statics ports of tomotherapy (TomoDirect): a prospective phase II trial. J. Cancer Res. Clin. Oncol. 140, 167–177. https://doi.org/10.1007/s00432-013-1560-8

Garcia, R., Oozeer, R., Le Thanh, H., Chastel, D., Doyen, J.C., Chauvet, B., Reboul, F., 2002. Radiothérapie des cancers du poumon: le blocage en inspiration sous contrôle spirométrique. Cancer/Radiothérapie 6, 30–38.

Ghesu, F.C., Georgescu, B., Mansi, T., Neumann, D., Hornegger, J., Comaniciu, D., 2016. An artificial agent for anatomical landmark detection in medical images, in: International Conference on Medical Image Computing and Computer-Assisted Intervention. Springer, pp. 229–237.

Giantsoudi, D., De Man, B., Verburg, J., Trofimov, A., Jin, Y., Wang, G., Gjesteby, L., Paganetti, H., 2017. Metal artifacts in computed tomography for radiation therapy planning: dosimetric effects and impact of metal artifact reduction. Phys. Med. Biol. 62, R49–R80. https://doi.org/10.1088/1361-6560/aa5293

Gjesteby, L., Yang, Q., Xi, Y., Zhou, Y., Zhang, J., Wang, G., 2017. Deep learning methods to guide CT image reconstruction and reduce metal artifacts. p. 101322W–101322W–7. https://doi.org/10.1117/12.2254091

Glitzner, M., Fast, M.F., de Senneville, B.D., Nill, S., Oelfke, U., Lagendijk, J.J.W., Raaymakers, B.W., Crijns, S.P.M., 2017. Real-time auto-adaptive margin generation for MLC-tracked radiotherapy. Phys. Med. Biol. 62, 186–201. https://doi.org/10.1088/1361-6560/62/1/186

Globocan 2012 - Home [WWW Document], n.d. URL http://globocan.iarc.fr/Default.aspx (accessed 12.21.17).

Glorot, X., Bordes, A., Bengio, Y., 2011. Deep sparse rectifier neural networks, in: Proceedings of the Fourteenth International Conference on Artificial Intelligence and Statistics. pp. 315–323.

Gonzalez, V.J., Buchholz, D.J., Langen, K.M., Olivera, G.H., Chauhan, B., Meeks, S.L., Ruchala, K.J., Haimerl, J., Lu, W., Kupelian, P.A., 2006. Evaluation of two tomotherapy-based techniques for the delivery of whole-breast intensity-modulated radiation therapy. Int. J. Radiat. Oncol. 65, 284–290. https://doi.org/10.1016/j.ijrobp.2005.12.044

Goodfellow, I., Bengio, Y., Courville, A., 2016. Deep Learning [WWW Document]. MIT Press. URL http://www.deeplearningbook.org/

Gottschalk, B., 2006. Neutron dose in scattered and scanned proton beams: In regard to Eric J. Hall (Int J Radiat Oncol Biol Phys 2006;65:1–7). Int. J. Radiat. Oncol. • Biol. • Phys. 66, 1594. https://doi.org/10.1016/j.ijrobp.2006.08.014

Guarnieri, R.A., Pereira, E.B., Chou, S.C., 2006. Solar radiation forecast using artificial neural networks in South Brazil. Proc. 8th ICSHMO 24–28.

Guo, Y., Gao, Y., Shen, D., 2016. Deformable MR Prostate Segmentation via Deep Feature Learning and Sparse Patch Matching. IEEE Trans. Med. Imaging 35, 1077–1089. https://doi.org/10.1109/TMI.2015.2508280

Hall, E.J., 2006. Intensity-modulated radiation therapy, protons, and the risk of second cancers. Int. J. Radiat. Oncol. Biol. Phys. 65, 1–7. https://doi.org/10.1016/j.ijrobp.2006.01.027

Han, X., 2017. MR-based synthetic CT generation using a deep convolutional neural network method. Med. Phys. 44, 1408–1419. https://doi.org/10.1002/mp.12155

Hatt, M., Laurent, B., Ouahabi, A., Fayad, H., Tan, S., Li, L., Lu, W., Jaouen, V., Tauber, C., Czakon, J., Drapejkowski, F., Dyrka, W., Camarasu-Pop, S., Cervenansky, F., Girard, P., Glatard, T., Kain, M., Yao, Y., Barillot, C., Kirov, A., Visvikis, D., n.d. The first MICCAI challenge on PET tumor segmentation. Med. Image Anal. https://doi.org/10.1016/j.media.2017.12.007

Havaei, M., Davy, A., Warde-Farley, D., Biard, A., Courville, A., Bengio, Y., Pal, C., Jodoin, P.-M., Larochelle, H., 2017. Brain Tumor Segmentation with Deep Neural Networks. Med. Image Anal. 35, 18–31. https://doi.org/10.1016/j.media.2016.05.004

Havaei, M., Guizard, N., Larochelle, H., Jodoin, P.-M., 2016. Deep Learning Trends for Focal Brain Pathology Segmentation in MRI, in: Machine Learning for Health Informatics, Lecture Notes in Computer Science. Springer, Cham, pp. 125–148. https://doi.org/10.1007/978-3-319-50478-0_6

Hetherington, J., Lessoway, V., Gunka, V., Abolmaesumi, P., Rohling, R., 2017a. SLIDE: automatic spine level identification system using a deep convolutional neural network. Int. J. Comput. Assist. Radiol. Surg. 1–10. https://doi.org/10.1007/s11548-017-1575-8

Hetherington, J., Pesteie, M., Lessoway, V.A., Abolmaesumi, P., Rohling, R.N., 2017b. Identification and tracking of vertebrae in ultrasound using deep networks with unsupervised feature learning. p. 101350K–101350K–7. https://doi.org/10.1117/12.2252641

Hou, B., Alansary, A., McDonagh, S., Davidson, A., Rutherford, M., Hajnal, J.V., Rueckert, D., Glocker, B., Kainz, B., 2017. Predicting Slice-to-Volume Transformation in Presence of Arbitrary Subject Motion. ArXiv170208891 Cs.

Hsu, S.-H., Cao, Y., Huang, K., Feng, M., Balter, J.M., 2013. Investigation of a method for generating synthetic CT models from MRI scans of the head and neck for radiation therapy. Phys. Med. Biol. 58, 8419. https://doi.org/10.1088/0031-9155/58/23/8419

Hu, P., Wu, F., Peng, J., Bao, Y., Chen, F., Kong, D., 2016. Automatic abdominal multi-organ segmentation using deep convolutional neural network and time-implicit level sets. Int. J. Comput. Assist. Radiol. Surg. 1–13. https://doi.org/10.1007/s11548-016-1501-5

Hua, K.-L., Hsu, C.-H., Hidayati, S.C., Cheng, W.-H., Chen, Y.-J., 2015. Computer-aided classification of lung nodules on computed tomography images via deep learning technique. OncoTargets Ther. 8, 2015–2022. https://doi.org/10.2147/OTT.S80733

Ibragimov, Bulat, Toesca, D., Chang, D., Koong, A., Xing, L., 2017. Combining deep learning with anatomical analysis for segmentation of the portal vein for liver SBRT planning. Phys. Med. Biol. 62, 8943–8958. https://doi.org/10.1088/1361-6560/aa9262

Ibragimov, B., Toesca, D.A.S., Chang, D.T., Koong, A.C., Xing, L., 2017. Deep Learning-Based Autosegmentation of Portal Vein for Prediction of Central Liver Toxicity After SBRT. Int. J. Radiat. Oncol. Biol. Phys. 99, E672.

Ibragimov, B., Xing, L., 2017. Segmentation of organs-at-risks in head and neck CT images using convolutional neural networks. Med. Phys. 44, 547–557. https://doi.org/10.1002/mp.12045

INCA, 2016. PROTONTHÉRAPIE, INDICATIONS ET CAPACITÉ DE TRAITEMENT.

Institut National du Cancer, 2015. Observatoire national de la radiothérapie - Situation fin 2013 et évolution depuis 2009 - 2015.pdf.

Işın, A., Direkoğlu, C., Şah, M., 2016. Review of MRI-based Brain Tumor Image Segmentation Using Deep Learning Methods. Procedia Comput. Sci. 102, 317–324. https://doi.org/http://dx.doi.org/10.1016/j.procs.2016.09.407

Jaffray, D.A., 2012. Image-guided radiotherapy: from current concept to future perspectives. Nat. Rev. Clin. Oncol. 9, 688–699. https://doi.org/10.1038/nrclinonc.2012.194

Jeraj, R., Mackie, T.R., Balog, J., Olivera, G., Pearson, D., Kapatoes, J., Ruchala, K., Reckwerdt, P., 2004. Radiation characteristics of helical tomotherapy. Med. Phys. 31, 396–404. https://doi.org/10.1118/1.1639148

Jochems, A., Deist, T.M., El Naqa, I., Kessler, M., Mayo, C., Reeves, J., Jolly, S., Matuszak, M., Ten Haken, R., van Soest, J., Oberije, C., Faivre-Finn, C., Price, G., de Ruysscher, D., Lambin, P., Dekker, A., 2017. Developing and Validating a Survival Prediction Model for NSCLC Patients Through Distributed Learning Across 3 Countries. Int. J. Radiat. Oncol. 99, 344–352. https://doi.org/10.1016/j.ijrobp.2017.04.021

Jung, J.H., Cho, K.H., Kim, Y.H., Moon, S.K., Min, C.K., Kim, W.C., Kim, E.S., Chang, A.R., Kim, T.H., Yoon, J.-W., Suh, T.-S., Huh, H.D., 2012. Effect of jaw size in megavoltage CT on image quality and dose. Med. Phys. 39, 4976–83. https://doi.org/10.1118/1.4736951

Kamnitas, K., Ledig, C., Newcombe, V.F.J., Simpson, J.P., Kane, A.D., Menon, D.K., Rueckert, D., Glocker, B., 2017. Efficient Multi-scale 3D CNN with fully connected CRF for accurate Brain Lesion Segmentation.

Kamnitsas, K., Bai, W., Ferrante, E., McDonagh, S., Sinclair, M., Pawlowski, N., Rajchl, M., Lee, M., Kainz, B., Rueckert, D., Glocker, B., 2017a. Ensembles of Multiple Models and Architectures for Robust Brain Tumour Segmentation. ArXiv171101468 Cs.

Kamnitsas, K., Ferrante, E., Parisot, S., Ledig, C., Nori, A., Criminisi, A., Rueckert, D., Glocker, B., 2016. DeepMedic on Brain Tumor Segmentation. Athens Greece Proc BRATS-MICCAI.

Kamnitsas, K., Ledig, C., Newcombe, V.F.J., Simpson, J.P., Kane, A.D., Menon, D.K., Rueckert, D., Glocker, B., 2017b. Efficient multi-scale 3D CNN with fully connected CRF for accurate brain lesion segmentation. Med. Image Anal. 36, 61–78. https://doi.org/10.1016/j.media.2016.10.004

Kamnitsas, K., Ledig, C., Newcombe, V.F.J., Simpson, J.P., Kane, A.D., Menon, D.K., Rueckert, D., Glocker, B., 2017c. Efficient multi-scale 3D CNN with fully connected CRF for accurate brain lesion segmentation. Med. Image Anal. 36, 61–78. https://doi.org/10.1016/j.media.2016.10.004

Kang, J., Schwartz, R., Flickinger, J., Beriwal, S., 2015. Machine Learning Approaches for Predicting Radiation Therapy Outcomes: A Clinician's Perspective. Int J Radiat Oncol Biol 93, 1127–1135. https://doi.org/http://dx.doi.org/10.1016/j.ijrobp.2015.07.2286

Keller, H., Glass, M., Hinderer, R., Ruchala, K., Jeraj, R., Olivera, G., Mackie, T.R., 2002. Monte Carlo study of a highly efficient gas ionization detector for megavoltage imaging and image-guided radiotherapy. Med. Phys. 29, 165–175. https://doi.org/10.1118/1.1445414

Kim, M., Wu, G., Shen, D., 2013. Unsupervised Deep Learning for Hippocampus Segmentation in 7.0 Tesla MR Images, in: Proceedings of the 4th International Workshop on Machine Learning in Medical Imaging - Volume 8184. Springer-Verlag New York, Inc., New York, NY, USA, pp. 1–8. https://doi.org/10.1007/978-3-319-02267-3_1

Kissick, M.W., Fenwick, J., James, J.A., Jeraj, R., Kapatoes, J.M., Keller, H., Mackie, T.R., Olivera, G., Soisson, E.T., 2005. The helical tomotherapy thread effect. Med. Phys. 32, 1414–1423. https://doi.org/10.1118/1.1896453

Kooi, T., van Ginneken, B., Karssemeijer, N., den Heeten, A., 2017. Discriminating solitary cysts from soft tissue lesions in mammography using a pretrained deep convolutional neural network. Med. Phys. 44, 1017–1027. https://doi.org/10.1002/mp.12110

Krizhevsky, A., Sutskever, I., Hinton, G.E., 2012. Imagenet classification with deep convolutional neural networks, in: Advances in Neural Information Processing Systems. pp. 1097–1105.

Kumar, D., Wong, A., Clausi, D.A., 2015. Lung nodule classification using deep features in CT images, in: Computer and Robot Vision (CRV), 2015 12th Conference on. IEEE, pp. 133–138.

Kushibar, K., Valverde, S., Gonzalez-Villa, S., Bernal, J., Cabezas, M., Oliver, A., Llado, X., 2017. Automated sub-cortical brain structure segmentation combining spatial and deep convolutional features. ArXiv170909075 Cs.

Latty, D., Stuart, K.E., Wang, W., Ahern, V., 2015. Review of deep inspiration breath-hold techniques for the treatment of breast cancer. J. Med. Radiat. Sci. 62, 74–81. https://doi.org/10.1002/jmrs.96

Lecun, Y., 1985. Une procedure d'apprentissage pour reseau a seuil asymmetrique (A learning scheme for asymmetric threshold networks). Cognitiva 85, 599–604.

LeCun, Y., Bengio, Y., Hinton, G., 2015. Deep learning. Nature 521, 436–444. https://doi.org/10.1038/nature14539

Lee, H., Grosse, R., Ranganath, R., Ng, A.Y., 2009. Convolutional deep belief networks for scalable unsupervised learning of hierarchical representations, in: Proceedings of the 26th Annual International Conference on Machine Learning. ACM, pp. 609–616.

Lee, H.C., Kim, S.H., Suh, Y.J., Chung, M.J., Kang, D.G., Choi, H.J., Lee, J.H., 2014. A prospective cohort study on postoperative radiotherapy with TomoDirect using simultaneous integrated boost technique in early breast cancer. Radiat. Oncol. 9, 1.

Lee, J.-G., Jun, S., Cho, Y.-W., Lee, H., Kim, G.B., Seo, J.B., Kim, N., 2017. Deep Learning in Medical Imaging: General Overview. Korean J. Radiol. 18, 570. https://doi.org/10.3348/kjr.2017.18.4.570

Lee, S., Kim, K.H., Woo, C.S., Shim, J.B., Cao, Y.J., Chang, K.H., Kim, C.Y., 2017. Predictive Solution for Radiation Toxicity Based on Big Data, in: Radiotherapy. InTech.

Li, H., Zhong, H., Boimel, P.J., Ben-Josef, E., Xiao, Y., Fan, Y., 2017. Deep Convolutional Neural Networks for Imaging Based Survival Analysis of Rectal Cancer Patients. Int J Radiat Oncol Biol 99, S183. https://doi.org/10.1016/j.ijrobp.2017.06.458

Lim-Reinders, S., Keller, B.M., Al-Ward, S., Sahgal, A., Kim, A., 2017. Online Adaptive Radiation Therapy. Int. J. Radiat. Oncol. 99, 994–1003. https://doi.org/10.1016/j.ijrobp.2017.04.023

Litjens, G., Kooi, T., Bejnordi, B.E., Setio, A.A.A., Ciompi, F., Ghafoorian, M., van der Laak, J.A., van Ginneken, B., Sánchez, C.I., 2017a. A survey on deep learning in medical image analysis. ArXiv Prepr. ArXiv170205747.

Litjens, G., Kooi, T., Bejnordi, B.E., Setio, A.A.A., Ciompi, F., Ghafoorian, M., van der Laak, J.A.W.M., van Ginneken, B., Sánchez, C.I., 2017b. A survey on deep learning in medical image analysis. Med. Image Anal. 42, 60–88. https://doi.org/10.1016/j.media.2017.07.005

Liu, Y., Stojadinovic, S., Hrycushko, B., Wardak, Z., Lau, S., Lu, W., Yan, Y., Jiang, S.B., Zhen, X., Timmerman, R., Nedzi, L., Gu, X., 2017. A deep convolutional neural network-based automatic delineation strategy for multiple brain metastases stereotactic radiosurgery. PloS One 12, e0185844. https://doi.org/10.1371/journal.pone.0185844

Lu, F., Wu, F., Hu, P., Peng, Z., Kong, D., 2017. Automatic 3D liver location and segmentation via convolutional neural network and graph cut. Int. J. Comput. Assist. Radiol. Surg. 12, 171–182. https://doi.org/10.1007/s11548-016-1467-3

Lu, W., 2010. A non-voxel-based broad-beam (NVBB) framework for IMRT treatment planning. Phys. Med. Biol. 55, 7175–7210. https://doi.org/10.1088/0031-9155/55/23/002

Lu, W., Chen, M., 2010. Fluence-convolution broad-beam (FCBB) dose calculation. Phys. Med. Biol. 55, 7211–7229. https://doi.org/10.1088/0031-9155/55/23/003

Lustberg, T., van Soest, J., Gooding, M., Peressutti, D., Aljabar, P., van der Stoep, J., van Elmpt, W., Dekker, A., 2017. Clinical evaluation of atlas and deep learning based automatic contouring for lung cancer. Radiother. Oncol. J. Eur. Soc. Ther. Radiol. Oncol. https://doi.org/10.1016/j.radonc.2017.11.012

Lv, X., Guan, Y., Yang, J., Wu, J., 2016. Clinical Relation Extraction with Deep Learning. Int. J. Hybrid Inf. Technol. 9, 237–248. https://doi.org/10.14257/ijhit.2016.9.7.22

Lynch, C.M., van Berkel, V.H., Frieboes, H.B., 2017. Application of unsupervised analysis techniques to lung cancer patient data. PLOS ONE 12, e0184370.

Ma, K., Wang, J., Singh, V., Tamersoy, B., Chang, Y.-J., Wimmer, A., Chen, T., 2017. Multimodal Image Registration with Deep Context Reinforcement Learning, in: Medical Image Computing and Computer Assisted Intervention − MICCAI 2017, Lecture Notes in Computer Science. Presented at the International Conference on Medical Image Computing and Computer-Assisted Intervention, Springer, Cham, pp. 240–248. https://doi.org/10.1007/978-3-319-66182-7_28

Ma, L., Guo, R., Zhang, G., Tade, F., Schuster, D.M., Nieh, P., Master, V., Fei, B., 2017. Automatic segmentation of the prostate on CT images using deep learning and multi-atlas fusion. Presented at the Medical Imaging 2017: Image Processing, International Society for Optics and Photonics, p. 101332O. https://doi.org/10.1117/12.2255755

Mackie, T.R., 2006. History of tomotherapy. Phys. Med. Biol. 51, R427–R453. https://doi.org/10.1088/0031-9155/51/13/R24

Mackie, T.R., 2003. Intensity-modulated Radiation Therapy: The State of the Art : American Association of Physicists in Medicine 2003 Summer School Proceedings, Colorado College, Colorado Springs, Colorado, June 22-26, 2003. American Association of Physicists in Medicine.

Mackie, T.R., 1990. 6 - Applications of the Monte Carlo Method in Radiotherapy, in: Kase, K.R., Bjärngard, B.E., Attix, F.H. (Eds.), The Dosimetry of Ionizing Radiation. Academic Press, San Diego, pp. 541–620. https://doi.org/10.1016/B978-0-12-400403-0.50010-5

Mackie, T.R., Bielajew, A.F., Rogers, D.W.O., Battista, J.J., 1988. Generation of photon energy deposition kernels using the EGS Monte Carlo code. Phys. Med. Biol. 33, 1. https://doi.org/10.1088/0031-9155/33/1/001

Mackie, T.R., Holmes, T., Swerdloff, S., Reckwerdt, P., Deasy, J.O., Yang, J., Paliwal, B., Kinsella, T., 1993. Tomotherapy: A new concept for the delivery of dynamic conformal radiotherapy. Med. Phys. 20, 1709–1719. https://doi.org/10.1118/1.596958

Mackie, T.R., Scrimger, J.W., Battista, J.J., 1985. A convolution method of calculating dose for 15-MV x rays. Med. Phys. 12, 188–196. https://doi.org/10.1118/1.595774

Mahé, M.-A., Lisbona, A., Mazal, A., Kantor, G., Giraud, P., Caron, J., 2007. La tomothérapie hélicoïdale: un appareil dédié pour la RCMI. Oncologie 9, 447–450. https://doi.org/10.1007/s10269-007-0646-9

Mar, V.J., Scolyer, R.A., Long, G.V., 2017. Computer-assisted diagnosis for skin cancer: have we been outsmarted? Lancet Lond. Engl. 389, 1962–1964. https://doi.org/10.1016/S0140-6736(17)31285-0

Mardani Korani, M., Dong, P., Xing, L., 2016. MO-G-201-03: Deep-Learning Based Prediction of Achievable Dose for Personalizing Inverse Treatment Planning. Med. Phys. 43, 3724. https://doi.org/10.1118/1.4957369

Mardani, M., Dong, P., Xing, L., 2016. Deep-Learning Based Prediction of Achievable Dose for Personalizing Inverse Treatment Planning. Int. J. Radiat. Oncol. 96, E419–E420. https://doi.org/http://dx.doi.org/10.1016/j.ijrobp.2016.06.1685

Mason, S.A., O'Shea, T.P., White, I.M., Lalondrelle, S., Downey, K., Baker, M., Behrens, C.F., Bamber, J.C., Harris, E.J., 2017. Towards ultrasound-guided adaptive radiotherapy for cervical cancer: Evaluation of Elekta's semiautomated uterine segmentation method on 3D ultrasound images. Med. Phys. 44, 3630–3638. https://doi.org/10.1002/mp.12325

Mastmeyer, A., Pernelle, G., Ma, R., Barber, L., Kapur, T., 2017. Accurate model-based segmentation of gynecologic brachytherapy catheter collections in MRI-images. Med. Image Anal. 42, 173–188. https://doi.org/10.1016/j.media.2017.06.011

Max Loschs, 2015. Thesis: Detection and Segmentation of Brain Metastases with Deep Convolutional Networks.

McCarthy, J., Feigenbaum, E.A., 1990. In memoriam: Arthur samuel: Pioneer in machine learning. AI Mag. 11, 10.

McCarthy, J., Hayes, P., 1969. Some philosophical problems from the standpoint of artificial intelligence. Read. Plan. 393, 1–51.

McIntosh, C., Welch, M., McNiven, A., Jaffray, D.A., Purdie, T.G., 2017. Fully automated treatment planning for head and neck radiotherapy using a voxel-based dose prediction and dose mimicking method. Phys. Med. Biol. 62, 5926–5944. https://doi.org/10.1088/1361-6560/aa71f8

McPartlin, A.J., Li, X.A., Kershaw, L.E., Heide, U., Kerkmeijer, L., Lawton, C., Mahmood, U., Pos, F., van As, N., van Herk, M., Vesprini, D., van der Voort van Zyp, J., Tree, A., Choudhury, A., 2016. MRI-guided prostate adaptive radiotherapy – A systematic review. Radiother. Oncol. 119, 371–380. https://doi.org/10.1016/j.radonc.2016.04.014

Meeks, S.L., Harmon, J.F., Langen, K.M., Willoughby, T.R., Wagner, T.H., Kupelian, P. a, 2005. Performance characterization of megavoltage computed tomography imaging on a helical tomotherapy unit. Med. Phys. 32, 2673–2681. https://doi.org/10.1118/1.1990289

Mege, J.P., Wenzhao, S., Veres, A., Auzac, G., Diallo, I., Lefkopoulos, D., 2016. Evaluation of MVCT imaging dose levels during helical IGRT: Comparison between ion chamber, TLD, and EBT3 films. J. Appl. Clin. Med. Phys. 17, 143–157. https://doi.org/10.1120/jacmp.v17i1.5774

Mehrtash, A., Pesteie, M., Hetherington, J., Behringer, P.A., Kapur, T., Wells, W.M., Rohling, R., Fedorov, A., Abolmaesumi, P., 2017. DeepInfer: Open-Source Deep Learning Deployment Toolkit for Image-Guided Therapy. Proc. SPIE-- Int. Soc. Opt. Eng. 10135. https://doi.org/10.1117/12.2256011

Men, K., Chen, X., Zhang, Y., Zhang, T., Dai, J., Yi, J., Li, Y., 2017a. Deep Deconvolutional Neural Network for Target Segmentation of Nasopharyngeal Cancer in Planning Computed Tomography Images. Front. Oncol. 7. https://doi.org/10.3389/fonc.2017.00315

Men, K., Dai, J., Li, Y., 2017b. Automatic segmentation of the clinical target volume and organs at risk in the planning CT for rectal cancer using deep dilated convolutional neural networks. Med. Phys. https://doi.org/10.1002/mp.12602

Menze, B.H., Jakab, A., Bauer, S., Kalpathy-Cramer, J., Farahani, K., Kirby, J., Burren, Y., Porz, N., Slotboom, J., Wiest, R., Lanczi, L., Gerstner, E., Weber, M.A., Arbel, T., Avants, B.B., Ayache, N., Buendia, P., Collins, D.L., Cordier, N., Corso, J.J., Criminisi, A., Das, T., Delingette, H., Demiralp, ??a??atay, Durst, C.R., Dojat, M., Doyle, S., Festa, J., Forbes, F., Geremia, E., Glocker, B., Golland, P., Guo, X., Hamamci, A., Iftekharuddin, K.M., Jena, R., John, N.M., Konukoglu, E., Lashkari, D., Mariz, J.A., Meier, R., Pereira, S., Precup, D., Price, S.J., Raviv, T.R., Reza, S.M.S., Ryan, M., Sarikaya, D., Schwartz, L., Shin, H.C., Shotton, J., Silva, C.A., Sousa, N., Subbanna, N.K., Szekely, G., Taylor, T.J., Thomas, O.M., Tustison, N.J., Unal, G., Vasseur, F., Wintermark, M., Ye, D.H., Zhao, L., Zhao, B., Zikic, D., Prastawa, M., Reyes, M., Van Leemput, K., 2015. The Multimodal Brain Tumor Image Segmentation Benchmark (BRATS). IEEE Trans. Med. Imaging 34, 1993–2024. https://doi.org/10.1109/TMI.2014.2377694

Meyer, P., Bouhours, H., Dehaynin, N., Jarnet, D., Gantier, M., Karamanoukian, D., Niederst, C., 2015. The optimal tomotherapy treatment planning parameters for extremity soft tissue sarcomas. Phys. Med. 31. https://doi.org/10.1016/j.ejmp.2015.05.005

Meyer, P., Chami, S., Enderlin, E., Niederst, C., Jarnet, D., Guerra, R., Karamanoukian, D., Noel, G., 2011. The Impact of MVCT Imaging Frequency Reduction and Manual Registration Suppression on PTV Margins: A Retrospective Analysis on 259 Patients Treated on Helical Tomotherapy. Int. J. Radiat. Oncol. 81, S151–S152. https://doi.org/10.1016/j.ijrobp.2011.06.311

Meyer, P., Le Pennec, F., Hui, S.K., Dehaynin, N., Jarnet, D., Gantier, M., Niederst, C., Mazzara, C., Baudrier, E., Noblet, V., 2017. Megavoltage 2D topographic imaging: An attractive alternative to megavoltage CT for the localization of breast cancer patients treated with TomoDirect. Phys. Med. 39, 33–38. https://doi.org/10.1016/j.ejmp.2017.06.015

Meyer, P., Niederst, C., Scius, M., Jarnet, D., Dehaynin, N., Gantier, M., Waissi, W., Poulin, N., Karamanoukian, D., 2016. Is the lack of respiratory gating prejudicial for left breast TomoDirect treatments? Phys. Med. 32, 644–650. https://doi.org/10.1016/j.ejmp.2016.04.001

Meyer, P., Noblet, V., Mazzara, C., Lallement, A., 2018. Survey on deep learning for radiotherapy. Comput. Biol. Med. 98, 126–146. https://doi.org/10.1016/j.compbiomed.2018.05.018

Miao, S., Piat, S., Fischer, P., Tuysuzoglu, A., Mewes, P., Mansi, T., Liao, R., 2017. Dilated FCN for Multi-Agent 2D/3D Medical Image Registration. ArXiv171201651 Cs.

Miao, S., Wang, Z.J., Zheng, Y., Liao, R., 2016. Real-time 2D/3D registration via CNN regression, in: Biomedical Imaging (ISBI), 2016 IEEE 13th International Symposium on. IEEE, pp. 1430–1434.

MICCAI BRATS - The Multimodal Brain Tumor Segmentation Challenge [WWW Document], n.d. URL http://braintumorsegmentation.org/ (accessed 9.27.17).

Milletari, F., Ahmadi, S.-A., Kroll, C., Plate, A., Rozanski, V., Maiostre, J., Levin, J., Dietrich, O., Ertl-Wagner, B., Bötzel, K., Navab, N., 2017. Hough-CNN: Deep learning for segmentation of deep brain regions in MRI and ultrasound. Comput. Vis. Image Underst., Deep Learning for Computer Vision 164, 92–102. https://doi.org/10.1016/j.cviu.2017.04.002

Milletari, F., Navab, N., Ahmadi, S.A., 2016. V-Net: Fully Convolutional Neural Networks for Volumetric Medical Image Segmentation, in: 2016 Fourth International Conference on 3D Vision (3DV). Presented at the 2016 Fourth International Conference on 3D Vision (3DV), pp. 565–571. https://doi.org/10.1109/3DV.2016.79

Miotto, R., Wang, F., Wang, S., Jiang, X., Dudley, J.T., 2017. Deep learning for healthcare: review, opportunities and challenges. Brief. Bioinform. https://doi.org/10.1093/bib/bbx044

Mitchell, R.A., Wai, P., Colgan, R., Kirby, A.M., Donovan, E.M., 2017. Improving the efficiency of breast radiotherapy treatment planning using a semi-automated approach. J. Appl. Clin. Med. Phys. 18, 18–24. https://doi.org/10.1002/acm2.12006

Mitchell, T.M., 1997. Machine Learning, McGraw-Hill series in computer science. McGraw-Hill, New York.

Moeskops, P., Viergever, M.A., Mendrik, A.M., de Vries, L.S., Benders, M.J.N.L., Isgum, I., 2016. Automatic Segmentation of MR Brain Images With a Convolutional Neural Network. IEEE Trans. Med. Imaging 35, 1252–1261. https://doi.org/10.1109/TMI.2016.2548501

Mori, S., 2017. Deep architecture neural network-based real-time image processing for image-guided radiotherapy. Phys. Med. 40, 79–87. https://doi.org/10.1016/j.ejmp.2017.07.013

Murai, T., Shibamoto, Y., Manabe, Y., Murata, R., Sugie, C., Hayashi, A., Ito, H., Miyoshi, Y., 2013. Intensity-modulated radiation therapy using static ports of tomotherapy (TomoDirect): comparison with the TomoHelical mode. Radiat. Oncol. 8, 1.

Muren, L.P., Jornet, N., Georg, D., Garcia, R., Thwaites, D.I., 2015. Improving radiotherapy through medical physics developments. Radiother. Oncol. 117, 403–406. https://doi.org/10.1016/j.radonc.2015.11.008

Murphy, K.P., 2012. Machine learning: a probabilistic perspective, Adaptive computation and machine learning series. MIT Press, Cambridge, MA.

Muthalaly, R.S., 2017. Using Deep Learning to predict the mortality of Leukemia patients. Queen's University (Kingston, Ont.).

Naqa, I.E., Murphy, M.J., 2015. What Is Machine Learning?, in: Naqa, I.E., Li, R., Murphy, M.J. (Eds.), Machine Learning in Radiation Oncology. Springer International Publishing, pp. 3–11. https://doi.org/10.1007/978-3-319-18305-3_1

Natarajan, P., Frenzel, J.C., Smaltz, D.H., 2017. Demystifying Big Data and Machine Learning for Healthcare. CRC Press.

Nawa, K., Haga, A., Nomoto, A., Sarmiento, R.A., Shiraishi, K., Yamashita, H., Nakagawa, K., 2017. Evaluation of a commercial automatic treatment planning system for prostate cancers. Med. Dosim. 42, 203–209. https://doi.org/10.1016/j.meddos.2017.03.004

Newell, A., Simon, H., 1956. The logic theory machine–A complex information processing system. IRE Trans. Inf. Theory 2, 61–79. https://doi.org/10.1109/TIT.1956.1056797

Nguyen, A., Yosinski, J., Clune, J., 2015. Deep neural networks are easily fooled: High confidence predictions for unrecognizable images, in: Proceedings of the IEEE Conference on Computer Vision and Pattern Recognition. pp. 427–436.

Nguyen, D., Long, T., Jia, X., Lu, W., Gu, X., Iqbal, Z., Jiang, S., 2017. Dose Prediction with U-net: A Feasibility Study for Predicting Dose Distributions from Contours using Deep Learning on Prostate IMRT Patients. ArXiv Prepr. ArXiv170909233.

Nguyen, D.T., O'Brien, R., Kim, J.-H., Huang, C.-Y., Wilton, L., Greer, P., Legge, K., Booth, J.T., Poulsen, P.R., Martin, J., Keall, P.J., 2017. The first clinical implementation of a real-time six degree of freedom target tracking system during radiation therapy based on Kilovoltage Intrafraction Monitoring (KIM). Radiother. Oncol. 123, 37–42. https://doi.org/10.1016/j.radonc.2017.02.013

Nie, D., Cao, X., Gao, Y., Wang, L., Shen, D., 2016. Estimating CT Image from MRI Data Using 3D Fully Convolutional Networks, in: Carneiro, G., Mateus, D., Peter, L., Bradley, A., Tavares, J.M.R.S., Belagiannis, V., Papa, J.P., Nascimento, J.C., Loog, M., Lu, Z., Cardoso, J.S., Cornebise, J. (Eds.), Deep Learning and Data Labeling for Medical Applications, Lecture Notes in Computer Science. Presented at the International Workshop on Large-Scale Annotation of Biomedical Data and Expert Label Synthesis, Springer International Publishing, pp. 170–178. https://doi.org/10.1007/978-3-319-46976-8_18

Nouranian, S., Ramezani, M., Spadinger, I., Morris, W.J., Salcudean, S.E., Abolmaesumi, P., 2016. Learning-Based Multi-Label Segmentation of Transrectal Ultrasound Images for Prostate Brachytherapy. IEEE Trans. Med. Imaging 35, 921–932. https://doi.org/10.1109/TMI.2015.2502540

Ogunmolu, O., Gu, X., Jiang, S., Gans, N., 2016. Nonlinear Systems Identification Using Deep Dynamic Neural Networks. ArXiv Prepr. ArXiv161001439.

Ogunmolu, O.P., Gu, X., Jiang, S., Gans, N.R., 2016. Vision-based control of a soft robot for maskless head and neck cancer radiotherapy, in: 2016 IEEE International Conference on Automation Science and Engineering (CASE). Presented at the 2016 IEEE International Conference on Automation Science and Engineering (CASE), pp. 180–187. https://doi.org/10.1109/COASE.2016.7743378

Ogunmolu, O.P., Gu, X., Jiang, S., Gans, N.R., 2015. A real-time, soft robotic patient positioning system for maskless head-and-neck cancer radiotherapy: An initial investigation, in: 2015 IEEE International Conference on Automation Science and Engineering (CASE). Presented at the 2015 IEEE International Conference on Automation Science and Engineering (CASE), pp. 1539–1545. https://doi.org/10.1109/CoASE.2015.7294318

Olivera, G., Ruchala, K., Lu, W., Haimerl, J., Schnarr, E., Langen, K., Kupelian, P., Meeks, S., Mackie, T., 2005. SU-FF-T-363: Dynamic Tangents and Topotherapy: New Delivery Capabilities for Helical Tomotherapy. Med. Phys. 32, 2034–2034. https://doi.org/10.1118/1.1998092

O'Shea, T., Bamber, J., Fontanarosa, D., Meer, S. van der, Verhaegen, F., Harris, E., 2016. Review of ultrasound image guidance in external beam radiotherapy part II: intra-fraction motion management and novel applications. Phys. Med. Biol. 61, R90. https://doi.org/10.1088/0031-9155/61/8/R90

Park, 2016. Intra- and Inter-Fractional Variation Prediction of Lung Tumors Using Fuzzy Deep Learning. IEEE J. Transl. Eng. Health Med. 4. https://doi.org/10.1109/JTEHM.2016.2516005

Pereira, G.C., Traughber, M., Muzic, R.F., 2014. The Role of Imaging in Radiation Therapy Planning: Past, Present, and Future. BioMed Res. Int. 2014, 1–9. https://doi.org/10.1155/2014/231090

Persson, E., Gustafsson, C., Nordström, F., Sohlin, M., Gunnlaugsson, A., Petruson, K., Rintelä, N., Hed, K., Blomqvist, L., Zackrisson, B., Nyholm, T., Olsson, L.E., Siversson, C., Jonsson, J., 2017. MR-OPERA: A Multicenter/Multivendor Validation of Magnetic Resonance Imaging–Only Prostate Treatment Planning Using Synthetic Computed Tomography Images. Int. J. Radiat. Oncol. 99, 692–700. https://doi.org/10.1016/j.ijrobp.2017.06.006

Pham, D.L., Xu, C., Prince, J.L., 2000. Current methods in medical image segmentation. Annu. Rev. Biomed. Eng. 2, 315–337. https://doi.org/10.1146/annurev.bioeng.2.1.315

Pignataro, A., 2005. Le lien entre sensibilité et pensée dans la critique de l'automatisme animal de Descartes : Bayle, La Mettrie, Maupertuis. Cah. Antispécistes 26.

Qayyum, A., Anwar, S.M., Awais, M., Majid, M., 2017. Medical image retrieval using deep convolutional neural network. Neurocomputing 266, 8–20. https://doi.org/10.1016/j.neucom.2017.05.025

Qi, X., Neylon, J., Santhanam, A., 2017. Dosimetric Predictors for Quality of Life After Prostate Stereotactic Body Radiation Therapy via Deep Learning Network. Int. J. Radiat. Oncol. • Biol. • Phys. 99, S167. https://doi.org/10.1016/j.ijrobp.2017.06.384

Ravì, D., Wong, C., Deligianni, F., Berthelot, M., Andreu-Perez, J., Lo, B., Yang, G.Z., 2017a. Deep Learning for Health Informatics. IEEE J. Biomed. Health Inform. 21, 4–21. https://doi.org/10.1109/JBHI.2016.2636665

Ravì, D., Wong, C., Deligianni, F., Berthelot, M., Andreu-Perez, J., Lo, B., Yang, G.Z., 2017b. Deep Learning for Health Informatics. IEEE J. Biomed. Health Inform. 21, 4–21. https://doi.org/10.1109/JBHI.2016.2636665

Reynders, T., Tournel, K., De Coninck, P., Heymann, S., Vinh-Hung, V., Van Parijs, H., Duchateau, M., Linthout, N., Gevaert, T., Verellen, D., Storme, G., 2009. Dosimetric assessment of static and helical TomoTherapy in the clinical implementation of breast cancer treatments. Radiother. Oncol. 93, 71–79. https://doi.org/10.1016/j.radonc.2009.07.005

Ronneberger, O., Fischer, P., Brox, T., 2015. U-net: Convolutional networks for biomedical image segmentation, in: International Conference on Medical Image Computing and Computer-Assisted Intervention. Springer, pp. 234–241.

Rosenblatt, F., 1957. The perceptron, a perceiving and recognizing automaton. Cornell Aeronaut. Lab. - Rep. 85-460-1.

Roth, H.R., Lu, L., Liu, J., Yao, J., Seff, A., Cherry, K., Kim, L., Summers, R.M., 2016. Improving Computer-Aided Detection Using Convolutional Neural Networks and Random View Aggregation. IEEE Trans. Med. Imaging 35, 1170–1181. https://doi.org/10.1109/TMI.2015.2482920

Roth, H.R., Yao, J., Lu, L., Stieger, J., Burns, J.E., Summers, R.M., 2015. Detection of Sclerotic Spine Metastases via Random Aggregation of Deep Convolutional Neural Network Classifications, in: Yao, J., Glocker, B., Klinder, T., Li, S. (Eds.), Recent Advances in Computational Methods and Clinical Applications for Spine Imaging. Springer International Publishing, Cham, pp. 3–12.

Ruchala, K.J., Olivera, G.H., Kapatoes, J.M., Schloesser, E. a, Reckwerdt, P.J., Mackie, T.R., 2000. Megavoltage CT image reconstruction during tomotherapy treatments. Phys. Med. Biol. 45, 3545–62. https://doi.org/10.1088/0031-9155/45/12/303

Ruchala, K.J., Olivera, G.H., Schloesser, E. a, Mackie, T.R., 1999. Megavoltage CT on a tomotherapy system. Phys. Med. Biol. 44, 2597–2621. https://doi.org/10.1088/0031-9155/44/10/316

Rumelhart, D.E., Hinton, G.E., Williams, R.J., 1986. Learning representations by back-propagating errors. Nature 323, 323533a0. https://doi.org/10.1038/323533a0

Russakovsky, O., Deng, J., Su, H., Krause, J., Satheesh, S., Ma, S., Huang, Z., Karpathy, A., Khosla, A., Bernstein, M., Berg, A.C., Fei-Fei, L., 2015. ImageNet Large Scale Visual Recognition Challenge. Int. J. Comput. Vis. 115, 211–252. https://doi.org/10.1007/s11263-015-0816-y

Salazar, B., Balczewski, E., Ung, C., Zhu, S., 2016. Neuroblastoma, a Paradigm for Big Data Science in Pediatric Oncology. Int. J. Mol. Sci. 18, 37. https://doi.org/10.3390/ijms18010037

Samuel, A.L., 1959. Some Studies in Machine Learning Using the Game of Checkers. IBM J Res Dev 3, 210–229. https://doi.org/10.1147/rd.33.0210

Sánchez Mesa, J.A., Galán, C., Hervás, C., 2005. The use of discriminant analysis and neural networks to forecast the severity of the Poaceae pollen season in a region with a typical Mediterranean climate. Int. J. Biometeorol. 49, 355–362. https://doi.org/10.1007/s00484-005-0260-8

Santhanam, A., Min, Y., Beron, P., Agazaryan, N., Kupelian, P., Low, D., 2016. SU-D-201-05: On the Automatic Recognition of Patient Safety Hazards in a Radiotherapy Setup Using a Novel 3D Camera System and a Deep Learning Framework. Med. Phys. 43, 3334–3335. https://doi.org/10.1118/1.4955617

Schiopu, S.R.I., Habl, G., Häfner, M., Katayama, S., Herfarth, K., Debus, J., Sterzing, F., 2017. Craniospinal irradiation using helical tomotherapy for central nervous system tumors. J. Radiat. Res. (Tokyo) 58, 238–246. https://doi.org/10.1093/jrr/rrw095

Schmidt, M.A., Payne, G.S., 2015. Radiotherapy planning using MRI. Phys. Med. Biol. 60, R323–R361. https://doi.org/10.1088/0031-9155/60/22/R323

Schubert, C., Waletzko, O., Weiss, C., Voelzke, D., Toperim, S., Roeser, A., Puccini, S., Piroth, M., Mehrens, C., Kueter, J.-D., Hierholz, K., Gerull, K., Fogliata, A., Block, A., Cozzi, L., 2017. Intercenter validation of a knowledge based model for automated planning of volumetric modulated arc therapy for prostate cancer. The experience of the German RapidPlan Consortium. PLOS ONE 12, e0178034. https://doi.org/10.1371/journal.pone.0178034

Schwarz, M., Cattaneo, G.M., Marrazzo, L., 2017. Geometrical and dosimetrical uncertainties in hypofractionated radiotherapy of the lung: A review. Phys. Med. 36, 126–139. https://doi.org/10.1016/j.ejmp.2017.02.011

Scius, M., Meyer, P., Niederst, C., Dehaynin, N., Jarnet, D., Gantier, M., Karamanoukian, D., 2016. EP-1645: Optimal treatment parameters for left-sided whole breast cancer irradiation using TomoDirect. Radiother. Oncol. 119, S769–S769. https://doi.org/10.1016/S0167-8140(16)32896-1

Shahedi, M., Cool, D.W., Bauman, G.S., Bastian-Jordan, M., Fenster, A., Ward, A.D., 2017. Accuracy Validation of an Automated Method for Prostate Segmentation in Magnetic Resonance Imaging. J. Digit. Imaging. https://doi.org/10.1007/s10278-017-9964-7

Sharp, G., Fritscher, K.D., Pekar, V., Peroni, M., Shusharina, N., Veeraraghavan, H., Yang, J., 2014. Vision 20/20: Perspectives on automated image segmentation for radiotherapy. Med. Phys. 41. https://doi.org/10.1118/1.4871620

Shen, D., Wu, G., Suk, H.-I., 2017. Deep Learning in Medical Image Analysis. Annu. Rev. Biomed. Eng. 19, 221–248. https://doi.org/10.1146/annurev-bioeng-071516-044442

Shickel, Benjamin, Tighe, P., Bihorac, A., Rashidi, P., 2017a. Deep EHR: A Survey of Recent Advances on Deep Learning Techniques for Electronic Health Record (EHR) Analysis. ArXiv170603446 Cs.

Shickel, Benjamin, Tighe, P., Bihorac, A., Rashidi, P., 2017b. Deep EHR: A Survey of Recent Advances on Deep Learning Techniques for Electronic Health Record (EHR) Analysis. ArXiv170603446 Cs.

Shickel, B., Tighe, P.J., Bihorac, A., Rashidi, P., 2017. Deep EHR: A Survey of Recent Advances in Deep Learning Techniques for Electronic Health Record (EHR) Analysis. IEEE J. Biomed. Health Inform. PP, 1–1. https://doi.org/10.1109/JBHI.2017.2767063

Shin, H.-C., Roth, H.R., Gao, M., Lu, L., Xu, Z., Nogues, I., Yao, J., Mollura, D., Summers, R.M., 2016. Deep Convolutional Neural Networks for Computer-Aided Detection: CNN Architectures, Dataset Characteristics and Transfer Learning. ArXiv160203409 Cs.

Simon, J.-M., Eschwège, F., Hajj, L.E., Marchesi, V., Noel, A., Levitchi, M., Marchal, C., Gourmelon, P., Peiffert, D., 2010. Epinal 2 : 409 Patients overexposed during Radiotherapy for prostate cancer after daily use of portal imaging controls. Presented at the 29th Annual ESTRO Meeting (European Society for Therapeutic Radiology and Oncology), Elsevier, p. S626.

Simonyan, K., Zisserman, A., 2014. Very Deep Convolutional Networks for Large-Scale Image Recognition. ArXiv14091556 Cs.

Stimpel, B., Syben, C., Würfl, T., Mentl, K., Dörfler, A., Maier, A., 2017. MR to X-Ray Projection Image Synthesis. ArXiv171007498 Cs.

Sun, W., Zheng, B., Qian, W., 2017. Automatic feature learning using multichannel ROI based on deep structured algorithms for computerized lung cancer diagnosis. Comput. Biol. Med. 89, 530–539. https://doi.org/10.1016/j.compbiomed.2017.04.006

Sunwoo, L., Kim, Y.J., Choi, S.H., Kim, K.-G., Kang, J.H., Kang, Y., Bae, Y.J., Yoo, R.-E., Kim, J., Lee, K.J., others, 2017. Computer-aided detection of brain metastasis on 3D MR imaging: Observer performance study. PloS One 12, e0178265.

Suzuki, K., 2017. Overview of deep learning in medical imaging. Radiol. Phys. Technol. 1–17. https://doi.org/10.1007/s12194-017-0406-5

Tejinder Kataria, S.G., 2014. Image Guided Radiation Therapy. J. Nucl. Med. Radiat. Ther. 05. https://doi.org/10.4172/2155-9619.1000179

Teramoto, A., Fujita, H., Yamamuro, O., Tamaki, T., 2016. Automated detection of pulmonary nodules in PET/CT images: Ensemble false-positive reduction using a convolutional neural network technique. Med. Phys. 43, 2821–2827. https://doi.org/10.1118/1.4948498

Tomsej, M., 2006. Le système de tomothérapie hélicoïdale pour la radiothérapie modulée en intensité et guidée par l'image : développements récents et applications cliniques. Cancer/Radiothérapie 10, 288–295. https://doi.org/10.1016/j.canrad.2006.07.006

Trebeschi, S., van Griethuysen, J.J.M., Lambregts, D.M.J., Lahaye, M.J., Parmer, C., Bakers, F.C.H., Peters, N.H.G.M., Beets-Tan, R.G.H., Aerts, H.J.W.L., 2017. Deep Learning for Fully-Automated Localization and Segmentation of Rectal Cancer on Multiparametric MR. Sci. Rep. 7. https://doi.org/10.1038/s41598-017-05728-9

Trullo, Roger, Petitjean, C., Nie, D., Shen, D., Ruan, S., 2017. Joint Segmentation of Multiple Thoracic Organs in CT Images with Two Collaborative Deep Architectures, in: Deep Learning in Medical Image Analysis and Multimodal Learning for Clinical Decision Support, Lecture Notes in Computer Science. Springer, Cham, pp. 21–29. https://doi.org/10.1007/978-3-319-67558-9_3

Trullo, R., Petitjean, C., Ruan, S., Dubray, B., Nie, D., Shen, D., 2017. Segmentation of Organs at Risk in thoracic CT images using a SharpMask architecture and Conditional Random Fields, in: 2017 IEEE 14th International Symposium on Biomedical Imaging (ISBI 2017). Presented at the 2017 IEEE 14th International Symposium on Biomedical Imaging (ISBI 2017), pp. 1003–1006. https://doi.org/10.1109/ISBI.2017.7950685

Tsang, S.W.S., Collins, M., Wong, J.T.L., Chiu, G., 2017. A dosimetric comparison of craniospinal irradiation using TomoDirect radiotherapy, TomoHelical radiotherapy and 3D conventional radiotherapy. J. Radiother. Pract. 1–12. https://doi.org/10.1017/S1460396917000309

Tseng, H.-H., Luo, Y., Cui, S., Chien, J.-T., Ten Haken, R.K., Naqa, I.E., 2017. Deep reinforcement learning for automated radiation adaptation in lung cancer. Med. Phys. 44, 6690–6705. https://doi.org/10.1002/mp.12625

Turing, A.M., 1950. Computing machinery and intelligence. Mind 59, 433–460.

Uzuner, Ö., South, B.R., Shen, S., DuVall, S.L., 2011. 2010 i2b2/VA challenge on concepts, assertions, and relations in clinical text. J. Am. Med. Inform. Assoc. JAMIA 18, 552–556. https://doi.org/10.1136/amiajnl-2011-000203

Valente, I.R.S., Cortez, P.C., Neto, E.C., Soares, J.M., de Albuquerque, V.H.C., Tavares, J.M.R., 2016. Automatic 3D pulmonary nodule detection in CT images: a survey. Comput. Methods Programs Biomed. 124, 91–107.

Vandendorpe, B., Guilbert, P., Champagne, C., Antoni, T., Nguyen, T.D., Gaillot-Petit, N., Servagi Vernat, S., 2017. Techniques d'irradiation mammaire complexe : radiothérapie conformationelle tridimensionnelle mono-isocentrique et nomothérapie hélicoïdale. Cancer/Radiothérapie. https://doi.org/10.1016/j.canrad.2017.03.005

Vania, M., Mureja, D., Lee, D., 2017. Automatic Spine Segmentation using Convolutional Neural Network via Redundant Generation of Class Labels for 3D Spine Modeling. ArXiv171201640 Cs.

Veen, F. van, 2016. The Neural Network Zoo - http://www.asimovinstitute.org/neural-network-zoo/. Asimov Inst.

Viergever, M.A., Maintz, J.B.A., Klein, S., Murphy, K., Staring, M., Pluim, J.P.W., 2016. A survey of medical image registration – under review. Med. Image Anal. 33, 140–144. https://doi.org/10.1016/j.media.2016.06.030

Vigneron, C., Antoni, D., Coca, A., Entz-Werlé, N., Lutz, P., Spiegel, A., Jannier, S., Niederst, C., Jarnet, D., Meyer, P., Kehrli, P., Noël, G., 2016. Médullo de l'enfant : étude rétrospective portant sur 52 patients. Cancer/Radiothérapie 20, 104–108. https://doi.org/10.1016/j.canrad.2015.11.004

Vigneron, C., Schwartz, É., Trojé, C., Niederst, C., Meyer, P., Lutz, P., Entz Werlé, N., Noël, G., 2013. General anaesthesia in paediatric radiotherapy | Anesthésie générale en radiothérapie pédiatrique. Cancer/Radiotherapie 17, 534–537. https://doi.org/10.1016/j.canrad.2013.06.036

Vivanti, R., Szeskin, A., Lev-Cohain, N., Sosna, J., Joskowicz, L., 2017. Automatic detection of new tumors and tumor burden evaluation in longitudinal liver CT scan studies. Int. J. Comput. Assist. Radiol. Surg. 12, 1945–1957. https://doi.org/10.1007/s11548-017-1660-z

Vizier, A., 1996. Descartes et les automates. MLN 111, 688–708. https://doi.org/10.1353/mln.1996.0057

Vos, B.D. de, Viergever, M.A., Jong, P.A. de, Išgum, I., 2016. Automatic Slice Identification in 3D Medical Images with a ConvNet Regressor, in: Deep Learning and Data Labeling for Medical Applications, Lecture Notes in Computer Science. Springer, Cham, pp. 161–169. https://doi.org/10.1007/978-3-319-46976-8_17

Wachinger, C., Reuter, M., Klein, T., 2017. DeepNAT: Deep Convolutional Neural Network for Segmenting Neuroanatomy. NeuroImage. https://doi.org/10.1016/j.neuroimage.2017.02.035

Wang, H., Cai, Y., Zhang, Y., Pan, H., Lv, W., Han, H., 2015. Deep Learning for Image Retrieval: What Works and What Doesn't. IEEE, pp. 1576–1583. https://doi.org/10.1109/ICDMW.2015.121

Wang, Huan, Dong, P., Liu, H., Xing, L., 2017. Development of an autonomous treatment planning strategy for radiation therapy with effective use of population-based prior data. Med. Phys. 44, 389–396. https://doi.org/10.1002/mp.12058

Wang, Hongkai, Zhou, Z., Li, Y., Chen, Z., Lu, P., Wang, W., Liu, W., Yu, L., 2017. Comparison of machine learning methods for classifying mediastinal lymph node metastasis of non-small cell lung cancer from 18 F-FDG PET/CT images. EJNMMI Res. 7, 11. https://doi.org/10.1186/s13550-017-0260-9

Wang, S., Zheng, D., Zhang, C., Ma, R., Bennion, N.R., Lei, Y., Zhu, X., Enke, C.A., Zhou, S., 2017. Automatic planning on hippocampal avoidance whole-brain radiotherapy. Med. Dosim. 42, 63–68. https://doi.org/10.1016/j.meddos.2016.12.002

Whitey, D., Koles, Z., 2008. A review of medial image segmentation. Int. J. Bioelectromagn. 10, 125–148.

Wolterink, J.M., Dinkla, A.M., Savenije, M.H.F., Seevinck, P.R., Berg, C.A.T. van den, Išgum, I., 2017. Deep MR to CT Synthesis Using Unpaired Data, in: Simulation and Synthesis in Medical Imaging, Lecture Notes in Computer Science. Presented at the International Workshop on Simulation and Synthesis in Medical Imaging, Springer, Cham, pp. 14–23. https://doi.org/10.1007/978-3-319-68127-6_2

Wu, G., Kim, M., Wang, Q., Munsell, B.C., Shen, D., 2016. Scalable High-Performance Image Registration Framework by Unsupervised Deep Feature Representations Learning. IEEE Trans. Biomed. Eng. 63, 1505–1516. https://doi.org/10.1109/TBME.2015.2496253

Wu, Y., Jiang, M., Lei, J., Xu, H., 2015. Named Entity Recognition in Chinese Clinical Text Using Deep Neural Network. Stud. Health Technol. Inform. 216, 624–628.

Xiang, L., Wang, Q., Nie, D., Qiao, Y., Shen, D., 2017. Deep Embedding Convolutional Neural Network for Synthesizing CT Image from T1-Weighted MR Image. ArXiv Prepr. ArXiv170902073.

Yan, D., Vicini, F., Wong, J., Martinez, A., 1997. Adaptive radiation therapy. Phys. Med. Biol. 42, 123–132.

Yang, H., Yu, H., Wang, G., 2016. Deep Learning for the Classification of Lung Nodules. ArXiv Prepr. ArXiv161106651.

Yang, Q., Yan, P., Zhang, Y., Yu, H., Shi, Y., Mou, X., Kalra, M.K., Wang, G., 2017. Low Dose CT Image Denoising Using a Generative Adversarial Network with Wasserstein Distance and Perceptual Loss. ArXiv170800961 Cs.

Yang, X., Kwitt, R., Niethammer, M., 2016. Fast Predictive Image Registration, in: Deep Learning and Data Labeling for Medical Applications, Lecture Notes in Computer Science. Springer, Cham, pp. 48–57. https://doi.org/10.1007/978-3-319-46976-8_6

Ylijoki, O., Porras, J., 2016. Perspectives to definition of big data: a mapping study and discussion. J. Innov. Manag. 4, 69–91.

Yuan, Y., 2017. Hierarchical Convolutional-Deconvolutional Neural Networks for Automatic Liver and Tumor Segmentation. ArXiv171004540 Cs.

Yuan, Yading, Chao, M., Lo, Y.-C., 2017. Automatic Skin Lesion Segmentation Using Deep Fully Convolutional Networks With Jaccard Distance. IEEE Trans. Med. Imaging 36, 1876–1886. https://doi.org/10.1109/TMI.2017.2695227

Yuan, Y., Chao, M., Lo, Y.C., 2017. Automatic Skin Lesion Segmentation Using Deep Fully Convolutional Networks with Jaccard Distance. IEEE Trans. Med. Imaging PP, 1–1. https://doi.org/10.1109/TMI.2017.2695227

Yuan, Y., Lo, Y.-C., 2017. Improving Dermoscopic Image Segmentation with Enhanced Convolutional-Deconvolutional Networks. ArXiv170909780 Cs.

Zeiler, M.D., Fergus, R., 2014. Visualizing and understanding convolutional networks, in: European Conference on Computer Vision. Springer, pp. 818–833.

Zhang, H., Li, Liang, Qiao, K., Wang, L., Yan, B., Li, Lei, Hu, G., 2016. Image prediction for limited-angle tomography via deep learning with convolutional neural network. ArXiv Prepr. ArXiv160708707.

Zhang, J., Liu, M., Shen, D., 2017. Detecting Anatomical Landmarks From Limited Medical Imaging Data Using Two-Stage Task-Oriented Deep Neural Networks. IEEE Trans. Image Process. Publ. IEEE Signal Process. Soc. 26, 4753–4764. https://doi.org/10.1109/TIP.2017.2721106

Zhang, X., Penagaricano, J.A., Fan, J., Narayanasamy, G., Maraboyina, S., Xia, F., Loverd, P., Morrill, S., 2017. Total Body Irradiation Using Fixed-beam Tomotherapy in Patients With Width Larger Than 40cm. Int. J. Radiat. Oncol. • Biol. • Phys. 99, E710. https://doi.org/10.1016/j.ijrobp.2017.06.2311

Zhao, C., Carass, A., Lee, J., He, Y., Prince, J.L., 2017. Whole Brain Segmentation and Labeling from CT Using Synthetic MR Images, in: Machine Learning in Medical Imaging, Lecture Notes in Computer Science. Presented at the International Workshop on Machine Learning in Medical Imaging, Springer, Cham, pp. 291–298. https://doi.org/10.1007/978-3-319-67389-9_34

Zhen, X., Chen, J., Zhong, Z., Hrycushko, B.A., Albuquerque, K., Zhou, L., Jiang, S.B., Gu, X., 2017. Deep Convolutional Neural Networks With Transfer Learning for Rectum Toxicity Prediction in Combined Brachytherapy and External Beam Radiation Therapy for Cervical Cancer. Int J Radiat Oncol Biol, Proceedings of the American Society for Radiation Oncology 99, S168. https://doi.org/10.1016/j.ijrobp.2017.06.386

Zheng, Y., Liu, D., Georgescu, B., Nguyen, H., Comaniciu, D., 2015. 3D deep learning for efficient and robust landmark detection in volumetric data, in: International Conference on Medical Image Computing and Computer-Assisted Intervention. Springer, pp. 565–572.

Zhou, S.K., Greenspan, H., Shen, D., 2017. Deep Learning for Medical Image Analysis. Academic Press.

Zhou, X., Ito, T., Takayama, R., Wang, S., Hara, T., Fujita, H., 2016. Three-Dimensional CT Image Segmentation by Combining 2D Fully Convolutional Network with 3D Majority Voting, in: Deep Learning and Data Labeling for Medical Applications, Lecture Notes in Computer Science. Springer, Cham, pp. 111–120. https://doi.org/10.1007/978-3-319-46976-8_12

Zhu, Y., Wang, L., Liu, M., Qian, C., Yousuf, A., Oto, A., Shen, D., 2017. MRI-based prostate cancer detection with high-level representation and hierarchical classification. Med. Phys. 44, 1028–1039. https://doi.org/10.1002/mp.12116

Zhuge, Y., Krauze, A.V., Ning, H., Cheng, J.Y., Arora, B.C., Camphausen, K., Miller, R.W., 2017. Brain tumor segmentation using holistically nested neural networks in MRI images. Med. Phys. 44, 5234–5243. https://doi.org/10.1002/mp.12481

II. ACTIVITES PERSONNELLES

A. CURRICULUM VITAE

ETAT CIVIL

Philippe MEYER
Né le 23 mars 1976 à Saverne (Bas-Rhin)
Marié, 2 enfants

Profession : Personne spécialisée en radiophysique médicale au Centre Paul Strauss

Adresse professionnelle : Centre Paul Strauss
Département de physique médicale
3 rue de la porte de l'hôpital
67000 Strasbourg – France
Email : pmeyer@strasbourg.unicancer.fr
Tél : +33.388.258.544

EXPERIENCE PROFESSIONNELLE

Juin 2004-aujourd'hui Personne spécialisée en radiophysique médicale
Centre Paul Strauss, Strasbourg

Nov 2003-Juin 2004 Diplôme de Qualification en Physique Radiologique et Médicale (DQPRM) : Stage pratique
Centre Alexis Vautrin, Vandoeuvre lès Nancy

FORMATION UNIVERSITAIRE

1999-2003 Doctorat de physique, spécialité sciences médicales
Sujet : Contribution au principe d'optimisation de la radioprotection en radiologie.
Coordination du projet Européen Med-X-Test
Thèse soutenue le 27 juin 2003 au CNRS/Strasbourg
Laboratoire de Physique et Application des SEmiconducteurs (PHASE), CNRS UPR 292, Strasbourg – CHU, Université Louis Pasteur (ULP), Strasbourg

Sept 1999-Nov 1999 Préparation du Diplôme de Qualification en Physique Radiologique et Médicale (DQPRM) : Cours théoriques
INSTN, Saclay

1998-1999 DEA Rayonnements et Imagerie en Médecine
option 1 : physique radiologique et médicale
Université Paul Sabatier, Toulouse

Après un Bac C (1994, Bouxwiller) et un DUT Mesures Physique (1996, ULP Strasbourg), j'ai poursuivi mes études par une MST Physique Appliquée et Instrumentation (1998, ESIA Annecy). Après avoir effectué mon stage de maîtrise à l'Institut de REcherches Subatomiques sur le projet NEMO3, sous la direction de Mr Guyonnet (1998, IRES, Strasbourg), j'ai intégré le DEA Rayonnements et Imagerie en

Médecine (1999, UPS Toulouse), dont j'ai effectué le stage de recherche au laboratoire de Physique et Application des SEmiconducteurs (1999, PHASE, Strasbourg). J'ai ensuite suivi les cours théoriques du Diplôme de Qualification en Physique Radiologique et Médicale (DQPRM) à l'Institut National des Sciences et Techniques Nucléaires (1999, INSTN, Saclay), avant d'entamer une thèse codirigée par Messieurs Siffert (PHASE) et Constantinesco (CHU Strasbourg), intitulée « Contribution au principe d'optimisation de la radioprotection en radiologie » (2003). Après avoir travaillé durant 6 mois dans la société EURORAD (2003), j'ai effectué la formation pratique du DQPRM au Centre Alexis Vautrin (2004, Nancy), puis ai été embauché en tant que personne spécialisée en radiophysique médicale au Centre Paul Strauss en 2004.

IMPLICATIONS ANNEXES

Membre du Conseil Scientifique de la Société Française de Physique Médicale (SFPM) (depuis 2014)
Membre de la SFPM (depuis 2004)
Membre associé laboratoire ICUBE – Equipe Modèles, Images et Vision (depuis 2017)
Chairman de congrès : SFPM 2012 (Strasbourg)/SFPM 2016 (Nancy)

Reviewer dans *Radiation Physics and Chemistry*
Reviewer dans *Journal of Applied Clinical Medical Physics*

Coordonnateur des 2èmes Journée Tomothérapie Grand'Est (2016)
Coordonnateur du Conseil Scientifique des 51èmes Journées Scientifiques de la SFPM (Strasbourg, 2012)
Coordonnateur du Projet Européen MedXTest (2000-2003)

Formateur DES d'Oncologie : "Techniques Innovantes en Radiothérapie" (2016)
Formateur modules d'enseignement pour les internes de radiothérapie du CPS (depuis 2014)
Formateur EPU Metz et Formation en Cancérologie *Radioprotection des patients* (2007-2008 -2009)

Porteur du projet API ICUBE 2018 : « Apprentissage Profond en Radiothérapie »

FORMATIONS/CONGRES

2017	Journée utilisateur Grand'Est Tomotherapy (Metz)
2017	Congrès de la SFPM (Lyon)
2016	Congrès de la SFPM (Nancy)
2016	Journées de Lille : IRM et automatisation en radiothérapie (Lille)
2016	Journée utilisateur Grand'Est Tomotherapy (Strasbourg)
2015	Journée utilisateur Raysearch (Marseille)
2015	Traitement des seins par Tomothérapie (IEO Milan)
2015	TMI Workshop (Paris)
2014	Journée utilisateur Grand'Est Tomotherapy (Nancy)
2014	Congrès de l'American Society for Radiation Oncology (ASTRO) (San Francisco)
2013	EPU IMRT SFPM/AFCOR (Paris)
2012	Congrès de la SFPM (Strasbourg)
2012	Journées Utilisateur France Tomotherapy (Paris)
2011	Congrès de l'ASTRO (Miami)
2011	Journées Utilisateur Europe Tomotherapy (Heidelberg)
2010	Elekta RTP Software User Meeting (Split, Croatie)
2010	Congrès de la SFPM (Bordeaux)
2009	Congrès de l'ASTRO (Chicago)
2009	Brainlab academy (Paris)
2009	EPU Gestion des risques (Paris)

2009 Brainlab European RT User Meeting (Lyon)
2008 Congrès de la SFPM (Marseille)
2008 Journées utilisateurs Tomothérapie (Antalya, Turquie)
2008 EPU Radioprotection des patients (Metz)
2008 Formation physique Tomothérapie (Madison, USA)
2007 Congrès de la SFPM (St-Malo)
2006 Congrès de l'ESTRO (Leipzig, Allemagne)
2006 Journées utilisateurs Nucletron (Arcachon)
2006 Congrès de la SFPM (Lyon)
2006 EPU Assurance de qualité en imagerie médicale et radiothérapie : de la réglementation au patient (SFPM - Créteil)
2005 EPU Nouvelles installations en radiothérapie (SFPM - Ploermel)
2005 EPU Imagerie multimodale en radiothérapie : de l'acquisition aux contrôles de qualité (SFPM - Créteil)
2005 EPU Les nouvelles technologies des réseaux en radiothérapie (SFPM - La Clusaz)
2004 Congrès de la SFRO (Paris)
2003 Congrès de la SFPM (Reims)
2001 Congrès de la SFPM (Nantes)
2000 Congrès de la SFPM (Lille)

PRINCIPALES CONTRIBUTIONS TECHNIQUES ET CLINIQUES AU CPS

Mise en place de la technique d'irradiation par modulation d'intensité en TomoDirect (2015).
Installation de 2 projecteurs de sources pour curiethérapie PDR V3 Elekta + nouveau Treatment Planning System (TPS) Oncentra (2014)
Mise en place des irradiations médullaires totales sur tomothérapie - protocole TOMMY (2013)
Installation du Clinac IX et de la tomothérapie HD (2013)
Mise en place de la technique d'irradiation par modulation d'intensité à faisceaux fixes sur TPS Iplan (2012)
Mise en place de la technique d'irradiation stéréotaxique sur TPS Iplan (2011)
Installation du 1er Novalis Tx de France (2010).
Installation de la 4ème tomothérapie Hi-Art de France. Mise en place de la technique d'irradiation par modulation d'intensité par tomothérapie hélicoïdale (2008).
Mise en place du serveur CMS Direct (2007)
Mise en place du Record & Verify Mosaiq (2007)
Mise en place de la technique de curiethérapie de prostate par implants permanents à l'^{125}I (2004)
Participation aux protocoles d'essais cliniques : Concorde (2013-2016), ART ORL (2013-2015), DivMele (2013-2016), TOMMY (2013-), SpectroGlio (2012-), RCMI Pelvis (2011-2014), H10 (2006-), GSK EGF (2004-2010), HYPOG1 (2016-)

B. ACTIVITES D'ENCADREMENT ET D'ENSEIGNEMENT

ENSEIGNEMENT

Master 2 Master Physique des Rayonnements, Instrumentation, Détecteurs et Imagerie (PRIDI, ULP Strasbourg) : option dosimétrie (depuis 2011)
Master 2 Spécialité Physique Médicale (Rabat, Maroc, 2008)
Diplôme de Technicien Supérieur (DTS) Imagerie Médicale et Radiologie Thérapeutique (IMRT) : 1ère, 2ème et 3ème année (depuis 2006)

MASTER 2 PHYSIQUE

2017 Quentin Ricard (M2 Clermont Ferrand) : « Modélisation Monte-Carlo des traitements mammaires en VMAT sur Novalis TX » - Collaboration CPS-IPHC
2017 Odelin Charron (M2 Strasbourg) : « Détection et segmentation automatique des métastases cérébrales sur IRM par réseau de neurone convolutif » - Collaboration CPS-ICUBE
2016 Fabien Le Pennec (M2 Rennes) : « Imagerie topographique 2D pour les traitements des seins par TomoDirect » - Collaboration CPS-ICUBE
2015 Maximilien Scius (M2 Rennes) : «Comparaison dosimétrique du TomoDirect avec le RTC3D dans le traitement du cancer du sein seul »
2014 Hugo Bouhours (M2 Strasbourg) : « Détermination des paramètres optimaux de planification pour le traitement des sarcomes des membres en tomothérapie »
2014 Julie Kabil (M2 Strasbourg) : « Caractérisation des films Gafchromic EBT3 pour la vérification en routine des distributions de dose de 0 à 8 Gy en radiothérapie »
2012 Maximilien Barbier (M2 Strasbourg) : « Caractérisation de l'application TQA en tomothérapie »
2011 Sandra Chami (M2 Strasbourg) : « Evaluation de l'imagerie de repositionnement 3D pour les patients traités en Tomothérapie (2ème partie) »
2010 Nicolas Dehaynin (M2 Lyon) : « Caractérisation du système dosimétrique RPE/Alanine et applications en radiothérapie » - Collaboration AERIAL
2010 Elise Enderlin (M2 Lyon) : « Evaluation de l'imagerie de repositionnement MVCT pour les patients traités en tomothérapie (1ère partie) »
2009 Abdelati Nourreddine (M2 Rabat) : « Acceptance d'un système de dosimétrie par film gafchromique pour le contrôle des plans de traitement IMRT en Tomothérapie »
2008 Mickael Perdrieux (M2 Nantes) : « Etude des facteurs d'influence du contrôle qualité patient en IMRT par tomothérapie »
2007 Marion Bonfanti (M2 Toulouse) : « Participation à la mise en place d'un contrôle de qualité des méthodes de fusion d'image utilisées au centre Paul Strauss pour la préparation de plans de traitement en radiothérapie externe »
2002 Edwige Buffard (M2 Toulouse)
2001 Magalie Krieger (M2 Toulouse)

DQPRM

2017 Maude Bronnec et Arnaud Faure
2016 Maximilien SCIUS et Anis Ben Yahmed
2015 Matthieu Moreau
2014 Felix Werle et Romain Risso
2013 Laurent Bartolucci et Sandrine Oddo
2012 Pierre-Alexandre Rigaud et Alban Brisson
2011 Caroline Bonin, Elise Enderlin et Nicolas Dehaynin
2010 Reda Saidi et Mery Diagne
2009 Antoine Prieur

ENSEIGNEMENT

Master 2 Master Physique des Rayonnements, Instrumentation, Détecteurs et Imagerie (PRIDI, ULP Strasbourg) : option dosimétrie
Diplôme de Technicien Supérieur (DTS) Imagerie Médicale et Radiologie Thérapeutique (IMRT) : 1ère, 2ème et 3ème année
Master 2 Spécialité Physique Médicale (Rabat, Maroc, 2008)

C. PUBLICATIONS

REVUES AVEC ACTES

R1. Odelin Charron, Alex Lallement, Delphine Jarnet, Vincent Noblet, Jean-Baptiste Clavier, Philippe Meyer, *Automatic detection and segmentation of brain metastases on multimodal MR images with a deep convolutional neural network*. Computers in Biology and Medicine 95:43-54 (2018)

R2. Philippe Meyer, Vincent Noblet, Christophe Mazzara, Alex Lallement, *Survey on deep learning for radiotherapy,* Computers in Biology and Medicine 98:126-46 (2018)

R3. Werlé F, Dehaynin N, Niederst C, Jarnet D, Gantier M, Karamanoukian D, Philippe Meyer. *Detecting anomalies in a deliberately biased tomotherapy plan: Comparison of two patient-specific quality assurance processes involving ArcCHECK ® and Gafchromic ® EBT3 films*. Cancer/Radiothérapie 21(8):749-58 (2017)

R4. Nicolas Arbor, Stephane Higueret, Halima Elazhar, Rodolphe Combe, Philippe Meyer, Nicolas Dehaynin, Florence Taupin, Daniel Husson. *Real-time detection of fast and thermal neutrons in radiotherapy with CMOS Sensors*. Phys. Med. Biol. 62:1920-34 (2017)

R5. Philippe Meyer, Fabien Le Pennec, Susanta K. Hui, Nicolas Dehaynin, Delphine Jarnet, Matthieu Gantier, Claudine Niederst, Christophe Mazzara, Etienne Baudrier, Vincent Noblet. *MV2D topographic imaging: an attractive alternative to MVCT for the localization of breast patients treated with TomoDirect.* Physica Medica 39:33-38 (2017)

R6. Philippe Meyer, Claudine Niederst, Maximilien Scius, Delphine Jarnet, Nicolas Dehaynin, Matthieu Gantier, Waisse Waissi, Nicolas Poulin, Diran Karamanoukian: *Is the lack of respiratory gating prejudicial for left breast TomoDirect treatments?* Physica Medica 32: 644-650 (2016)

R7. C Vigneron, D Antoni, A Coca, N Entz-Werlé, P Lutz, A Spiegel, S Jannier, C Niederst, D Jarnet, P Meyer, P Kehrli, G Noël: *Pediatric medulloblastoma: Retrospective series of 52 patients*. Cancer/Radiothérapie 20(2) :104-108 (2016)

R8. Vigneron, C., D. Antoni, A. Coca, C. Niederst, D. Jarnet, P. Meyer, P. Kehrli, and G. Noël. *Médulloblastomes de l'adulte: étude rétrospective portant sur 21 patients* Cancer/Radiothérapie 20, no. 1: 14–17 (2016).

R9. Rouers, M., D. Antoni, A. Thompson, P. Truntzer, Q.C. Haoming, C. Bourrier, P. Meyer, et al. *Maxillary and Mandible Contouring in Patients with a Head and Neck Area Irradiation.* Practical Radiation Oncology 6, no. 3 (2016).

R10. Philippe Meyer, Hugo Bouhours, Nicolas Dehaynin, Delphine Jarnet, Matthieu Gantier, Diran Karamanoukian, Claudine Niederst. *The optimal tomotherapy treatment planning parameters for extremity soft tissue sarcomas.* Physica Medica 31 ; 542-552 (2015)

R11. S. Servagi-Vernat, P. Giraud, P. Fenoglietto, D. Azria, A. Lisbona, A. de La Rochefordière, S. Zefkili, P. Fau, M. Resbeut, S. Huger, D. Peiffert, P. Meyer, G. Noël, J. Mazurier, I. Latorzeff, M.-C. Biston, P. Pommier, D. Ledu, R. Garcia, B. Chauvet, P. Dudouet, S. Belhomme, G. Kantor, M.-A. Mahé: *Apport de la RCMI rotationnelle et de la tomothérapie hélicoïdale dans les cancers pelviens : étude dosimétrique prospective sur 51 patients*. Cancer/Radiothérapie 18(2) ; 111-118 (2014).

R12. C Vigneron, E Schwartz, C Trojé, C Niederst, P Meyer, P Lutz, N Entz Werlé, G Noël. *General anaesthesia in paediatric radiotherapy.* Cancer/Radiothérapie 17(5-6); 534-537 (2013)

R13. S Jaussaud, S Guihard, C Niederst, C Borel, P Meyer, P Hémar, P Schultz, G Noël, A Féki. *Constraints of the dentist are consistent with the results of an optimal irradiation with modulated intensity in N0 oropharyngeal cancer*. Cancer/Radiothérapie 17(4); 265-271 (2013)

R14. Delphine Antoni, Shanti Natarajan-Ame, Philippe Meyer, Claudine Niederst, Khalil Bourahla, Georges Noel: *Contribution of three-dimensional conformal intensity-modulated radiation therapy for women affected by bulky stage II supradiaphragmatic Hodgkin disease*. Radiation Oncology 8(1)-12 pages:112 (2013).

R15. Violaine Beneyton, Claudine Niederst, Céline Vigneron, Philippe Meyer, François Becmeur, Luc Marcellin, Patrick Lutz, Georges Noel. *Comparison of the dosimetries of 3-dimensions Radiotherapy (3D-RT) with linear accelerator and intensity modulated radiotherapy (IMRT) with helical tomotherapy in children irradiated for neuroblastoma.* BMC Medical Physics 12(1):2-9 pages (2012).

R16. V Beneyton, G Billaud, C Niederst, P Meyer, K Bourhala, C Schumacher, D Karamanoukian, G Noël. *Comparison of three dosimetric techniques for lung tumor irradiation*. Cancer/Radiothérapie 14(1):50-58 (2009).

R17. Y Métayer, P Meyer, C Brunaud, D Peiffert. *Quality control in pulsed dose rate brachytherapy*. Cancer/Radiothérapie 13(4):318-322 (2009)

R18. G Noël, C Schumacher, C Niederst, V Beneyton, P Meyer, D Karamanoukian. *New technologies in lung cancer radiotherapy*. Revue des Maladies Respiratoires 24(8 Pt 2):6S73-86 (2007).

R19. Philippe Meyer, E Buffard, L Mertz, C Kennel, A Constantinesco, P Siffert: *Evaluation of the use of six diagnostic X-ray spectra computer code.*. British Journal of Radiology 77(915):224-30 (2004).

R20. M. Jung, Philippe Meyer, J. Morel, C. Teissier, P. Siffert: *Diamond X-ray personal dosimetry. Numerical evaluation against silicon response*. Nuclear Instruments and Methods in Physics Research Section A Accelerators Spectrometers Detectors and Associated Equipment 511(3):417-424 (2003).

R21. Philippe Meyer, R Regal, M Jung, P Siffert, L Mertz, A Constantinesco: *Feasibility of a semiconductor dosimeter to monitor skin dose in interventional radiology.* Medical Physics 28(10):2002-6 (2001).

CONFERENCES AVEC ACTES

CA1. G Noel, N. Schreuder, P. Meyer, S.G. Price, A.G. Meek, and M.A. Fagundes. *Proton Therapy of Localized Left Breast Cancer Improves Cardiac and Left Lung Sparing Compared to Intensity Modulated Radiation Therapy With or Without Deep Inspiration Breath Hold*. International Journal of Radiation Oncology*Biology*Physics 96, no. 2: E60–61 (2016)

CA2. M Rouers, D. Antoni, F. Bornert, C. Laurel Wong, S. Dubourg, P. Truntzer, H. C. Qiu, P Meyer et al. *Ability to Deliver Safe Dental Care and Optimal Prosthetic Rehabilitation Are Correlating With Irradiation Doses in Maxillary and Mandible*. International Journal of Radiation Oncology*Biology*Physics, 96, no. 2, Supplement: E354–55 (2016)

CA3. Maximilien Scius, Philippe Meyer, Claudine Niederst, Delphine Jarnet, Nicolas Dehaynin, Matthieu Gantier, Diran Karamanoukian *Optimal treatment parameters for left-sided whole breast cancer irradiation using TomoDirect.* Radiother Oncol 119 : S769–S769 (2016*)*

CA4. R. Risso, D. Jarnet, M. Gantier, C. Niederst, N. Dehaynin, P. Meyer,D. Karamanoukian. *Study of the influence of the use of hidden isocenters in extracranial stereotactic treatments* Physica Medica 31 e23–e54 (2015)

CA5. F. Werle, N. Dehaynin, P. Meyer, C. Niederst, D. Jarnet, M. Gantier, D. Karamanoukian. *Detection of anomalies in an intentionally distorted tomotherapy treatment plan: Comparison of the ArcCHECK® detector (Sun Nuclear) and Gafchromic® EBT3 films (Ashland).* Physica Medica 31 : e23–e54 (2015)

CA6. J. Kabil, N. Dehaynin, S. Chiavassa, P. Meyer, C. Niederst, D. Jarnet, M. Gantier, D. Karamanoukian. *A single EBT3 gafchromic calibration curve for dose measurement from 0 to 8.5 Gy/fraction.* Physica Medica 30:e132-e133 (2014)

CA7. H. Bouhours, P. Meyer, C. Niederst, D. Jarnet, N. Dehaynin, M. Gantier, D. Karamanoukian. *Determination of the optimal planning parameters (pitch, MF and FW) for limb sarcoma treated with tomotherapy: A preliminary study*. Physica Medica 30:e144-e145 (2014).

CA8. M. Munier, T. Sohier, N. Muller, J.-M. Jung, F. Carbillet, S. Perlongo, P. Meyer, G. Noël. *A new scintillating fiber dosimeter for real-time measurement in radiology and radiotherapy.* Physica Medica 30:e129 (2014)

CA9. Bauer, N.; Clavier, J.; Meyer, P.; Noël, G.*Linac-based fractionated stereotactic radiotherapy (FSRT) for vestibular schwannomas: dosimetric comparison of dynamic conformal arc therapy and helical tomotherapy,* Journal of Radiosurgery & SBRT; Supplement 2.1, Vol. 2, p13 (2013)

CA10. P. Truntzer, C. Schumacher, G. Billaud, C. Bourrier, C. Renaud, C. Niederst, P. Meyer, G. Noël, *Étude comparative dosimétrique d'un plan d'irradiation conformationnelle tridimensionnelles sans et avec modulation d'intensité par un appareil de tomothérapie (Tomotherapy Hi-Art) dans l'irradiation des cancers bronchiques non à petites cellules de l'apex* Cancer/Radiothérapie 17,n 5-6, p620 (2013)

CA11. Kantor G, Bobin M, Sargos P, Antoine M, Lisbona A, Mahé M-A, et al*. Tomothérapie hélicoïdale de chordomes rachidiens : étude française multicentrique de faisabilité sur 30 cas*. Cancer/Radiothérapie 2013;17:593–4.

CA12. P. Koell, F. Kuntz, A. Strasser, P. Meyer, N. Dehaynin, G. Noël: *Electron paramagnetic resonance dosimetry with alanine pellets for radiation therapy applications: Calibration methods*. Physica Medica 29(1):43 (2013).

CA13. M. Chea, C. Llagostera, Philippe Meyer, K. Cristina, R. Itti, F. Culot, L. De Marzi, X. Cuenca, M. A. Mahé, J. J. Mazeron, A. Lisbona, C. Jenny: *Feasibility study of total marrow irradiation using helical tomotherapy*. Physica Medica 29(1):38-39 (2013).

CA14. P. Koell, Philippe Meyer, N. Dehaynin, F. Kuntz, G. Noël: *Étude de la modification de la dose lors de la mise en place de deux types de dosimètres en surface*. Cancer/Radiothérapie 17:592 (2013).

CA15. P. Meyer, S. Chami, E. Enderlin, C. Niederst, D. Jarnet, R. Guerra, D. Karamanoukian, G. Noel: *The Impact of MVCT Imaging Frequency Reduction and Manual Registration Suppression on PTV Margins: A Retrospective Analysis on 259 Patients Treated on Helical Tomotherapy*. International journal of radiation oncology, biology, physics; 81(2) (2011).

CA16. M. Ayadi, G. Delpon, F. Lafay, P. Meyer: *Evaluation of ABAS TM : multi-center study in the case of prostate cancer*. Physica Medica 27 (2011).

CA17. S. Chami, E. Enderlin, P. Meyer, C. Niederst, D. Jarnet, D. Karamanoukian, G. Noel: *Evaluation of set-up 3D images for patients treated in helical tomotherapy*. Physica Medica 27 (2011).

CA18. T. Garcia, P. Francois, J. Caron, G. Hangard, P. Meyer, C. Munos-Llagostera, N. Nomikossoff, N. Reynaert: *Validation of EPR/Alanine dosimetry for dose delivery verifications - Application to French Tomotherapy centers*. Physica Medica 27 (2011).

CA19. J.-B. Clavier, D. Atlani, P. Salze, Ben Abdelghani, C. Borel, D. Karamanoukian, P. Meyer, B. Perrin, G. Noel: *Radiochimiothérapie exclusive dans les cancers de l'oesophage : l'état nutritionnel initial est un facteur pronostique du devenir du patient*. JFHOD, Paris; (2011)

CA20. D. N. Antoni, P. Meyer, S. Ame, C. Niederst, K. Bourahla, D. Karamanoukian, G. Noel: *Contribution of Three-dimensional Conformational Radiotherapy with Modulation of Intensity (IMRT) for Women Affected by Stage II Supradiaphragmatic Hodgkin's Disease: A Dosimetric Study Comparing IMRT by Tomotherapy and a Three-dimensional Conformational Radiotherapy (3D-CRT)*. International journal of radiation oncology, biology, physics 78(3):554 (2010).

CA21. D. Antoni, P. Meyer, S. Ame, C. Niederst, K. Bourahla, D. Karamanoukian, G. Noël: *Apport de la radiothérapie conformationnelle tridimensionnelle avec modulation d'intensité (RCMI) dans la maladie de Hodgkin: étude dosimétrique comparant une tomothérapie et une radiothérapie conformationnelle tridimensionnelle*. Cancer Radiotherapie - CANCER RADIOTHER. 14(6):604-604 (2010).

CA22. V. Beneyton, G. Billaud, C. Niederst, P. Meyer, K. Bourahla, C. Schumacher, D. Karamanoukian, G. Noel: *Analyse des contraintes dosimétriques obtenues par trois techniques d'irradiation de tumeurs pulmonaires*. Cancer/Radiothérapie 13(6):687-687 (2009).

CA23. G. Noël, P. Meyer, C. Niederst, D. Antoni, S. Froelich, P. Boyer, B. George, D. Karamanoukian: *Irradiation conformationnelle tridimensionnelle avec modulation d'intensité par tomothérapie de la base du crâne chez 3 patients atteints d'un chordome et un patient atteint d'un chondrosarcome*. Cancer/Radiothérapie; 13(6):663-663 (2009).

CA24. V. Beneyton, P. Quetin, P. Meyer, C. Niederst, P. Lutz, G. Noël: *Place de la tomothérapie dans l'irradiation des tumeurs du tronc de l'enfant*. Cancer/Radiothérapie 13(6):656-656 (2009).

CA25. V. Beneyton, P. Quetin, P. Meyer, C. Niederst, P. Lutz, G. Noël: *Radiothérapie dans la prise en charge des neuroblastomes rétropéritonéaux de l'enfant : une place pour la tomothérapie ?* Cancer/Radiothérapie 13:656–657 (2009).

CA26. Y.-M. Metayer, D.-P. Peiffer, C. Malet, P. Meyer, J. Bellec, and A. Chemin. *Enquête et Recommandations Sur Les Pratiques D'optimisation En Curiethérapie Gynécologique En Débit Pulsé*. Cancer/Radiotherapie 10 :520 (2006)

CA27. Y. Metayer, D. Peiffert, A Chemin, C. Malet, P. Meyer, A. Lisbona: *Consensus en curiethérapie de débit pulse gynécologique*. Cancer/Radiothérapie 9:546 (2005).

CONFERENCES SANS ACTES

CS1. P Meyer. *MV2D topographic imaging for tomodirect treatments*. Journée utilisateur tomothérapie Grand'Est, Metz (2017)

CS2. P. Meyer. *Les besoins actuels en radiothérapie, Focus sur la radiochirurgie.* Converging Day IRCAD, Strasbourg (2017)

CS3. P Meyer, D Antoni. *Irradiations médullaires totals en tomothérapie : le protocole TOMMY*. Journée utilisateur tomothérapie Grand'Est, Strasbourg (2016)

CS4. P Meyer, C Vigneron. *Technique d'irradiation cranio-spinale par tomothérapie.* Journée utilisateur tomothérapie Grand'Est, Nancy (2015)

CS5. P Meyer, M Chea, C Llagostera. *TOMMY group protocol – Physics study*. TMI Accuray Workshop, Paris (2014)

CS6. M Gantier, D Jarnet, D Karamanoukian, R Guerra, P Meyer, C Niederst, G Noel. *Evaluation de l'imagerie multi-modalités du Clinac Novalis TX. Comparaison des systèmes de repositionnement dans le cadre de traitement de cancer de la prostate.* Congrès annuel de la SFPM, Nantes (2011)

CS7. P Meyer, C Niederst, D Jarnet, D Karamanoukian, R Guerra, G Noel. *The impact of MVCT imaging frequency reduction and manual registration suppression on PTV margins: a retrospective analysis on 259 patients treated on Helical Tomotherapy,* International Conference on Tomotherapy, Heidelberg (2011)

CS8. E. Enderlin, C Niederst, P Meyer, D Karamanoukian, G Noel. *Evaluation de l'imagerie de repositionnement MVCT pour les patients traités en tomothérapie*. Congrès annuel de la SFPM, Bordeaux (2010)

CS9. N Dehaynin, F Kuntz, P Meyer, D Karamanoukian, P Pernot, G Noel. *Utilisation des dosimètres à l'alanine pour la mesure de FOC sur un appareil de traitement stéréotaxique*. Congrès annuel de la SFPM, Bordeaux (2010)

CS10. A Nourredine, P Meyer, C Niederst, D Karamanoukian, P Pernot, G Noel. *Acceptance d'un système de dosimétrie par film gafchromique pour le contrôle des plans de traitement IMRT en Tomothérapie*. Congrès annuel de la SFPM, Montauban (2009)

CS11. C Niederst, P Meyer, D Karamanoukian, G Noel. *Planification de traitement en tomothérapie chez des patients présentant des prothèses métalliques*. Congrès annuel de la SFPM, Marseille (2008)

CS12. M Perdrieux, P Meyer, C Niederst, D Karamanoukian, P Pernot, G Noel. *Quantification des facteurs d'influence sur la mesure de dose lors d'un contrôle qualité patient pour les traitements par tomothérapie*. Congrès annuel de la SFPM, Marseille (2008)

CS13. P Meyer, C Niederst, D Karamanoukian, P Pernot, G Noel, SC Losa. *Calibration du système Hi-ART Tomotherapy*. Congrès annuel de la SFPM, Marseille (2008)

CS14. R. Guerra, P. Quetin, P. Meyer, C. Benoit, C.Niederst, S.Heymann, D. Karamanoukian, G. Noel. *La radiothérapie 3D dans le traitement du cancer du sein*. Conférence/débat : l'Alsace contre le cancer du sein, Strasbourg (2008)

CS15. P Quetin, P Meyer, JF Rodier, C Schumacher, C Benoit, GM Jung, G Noel. *Comparaison dosimétrique de 15 patientes traitées en pré-opératoire et 15 patientes traitées en post-opératoire pour un cancer de l'endomètre*. Société Française d'Oncologie Gynécologique, Strasbourg (2006)

CS16. P Meyer, P Quetin, C Roy, B Perrin, D Karamanoukian, GM Jung. *Impact de la modalité d'imagerie sur la mesure du volume de la prostate avant et après curiethérapie par implants permanents d'iode 125*. Congrès annuel de la SFPM, Lyon (2006)

CS17. P Meyer, P Quetin, B Perrin, D Karamanoukian, GM Jung *Evaluation de l'œdème de la prostate après curiethérapie par implants permanents d'iode 125*. Congrès annuel de la SFPM, Lyon (2006)

CS18. M Bonfanti, D Karamanoukian, L Mertz, AC Metivier, P Meyer, C Niederst, G Noel, C Schumacher, GM Jung. *Evaluation des mouvements respiratoires de tumeurs broncho-pulmonaires. Implications sur la délimitation des volumes en radiothérapie*. Congrès annuel de la SFPM, Lyon (2006)

CS19. P Meyer. *Prostate brachytherapy with 125I permanent seeds*. CMS Lunch Symposium at ESTRO25, Leipzig (2006)

CS20. P Meyer, W Dusi, P Chirco, A Constantinesco, P Siffert. *Contrôle en routine des performances des détecteurs numériques plans en radiologie - le projet européen Med-X-Test*, Congrès annuel de la SFPM Reims (2003)

CS21. P Meyer, L Mertz, A Constantinesco, P Siffert *Dosimétrie du patient en temps réel lors de procédures endovasculaires radioguidées*, Congrès annuel de la SFPM, Reims (2003)

CS22. P.Meyer, L.Mertz , S.Castaldo, A.Dieudonne , A.Constantinesco. *Dosimétrie en radiologie interventionnelle*, Congrès annuel de la SFPM, Nantes (2001)

CS23. P. Meyer, L. Mertz, J.M. Blanche, R. Regal, M. Jung, N. Muller, A. Constantinesco, P. Siffert. *Contrôle temps réel de la dose à la peau en radiologie interventionelle*, Congrès annuel de la SFPM, Lille (2000)

SELECTION DE 5 PUBLICATIONS JUGEES SIGNIFICATIVES

Philippe Meyer, Vincent Noblet, Christophe Mazzara, Alex Lallement, *Survey on deep learning for radiotherapy,* Computers in Biology and Medicine 98:126-46 (2018)

Philippe Meyer, Fabien Le Pennec, Susanta K. Hui, Nicolas Dehaynin, Delphine Jarnet, Matthieu Gantier, Claudine Niederst, Christophe Mazzara, Etienne Baudrier, Vincent Noblet. *MV2D topographic imaging: an attractive alternative to MVCT for the localization of breast patients treated with TomoDirect*. Physica Medica 39:33-38 (2017)

Philippe Meyer, Claudine Niederst, Maximilien Scius, Delphine Jarnet, Nicolas Dehaynin, Matthieu Gantier, Waisse Waissi, Nicolas Poulin, Diran Karamanoukian: *Is the lack of respiratory gating prejudicial for left breast TomoDirect treatments?* Physica Medica 32: 644-650 (2016)

Philippe Meyer, Hugo Bouhours, Nicolas Dehaynin, Delphine Jarnet, Matthieu Gantier, Diran Karamanoukian, Claudine Niederst. *The optimal tomotherapy treatment planning parameters for extremity soft tissue sarcomas.* Physica Medica 31: 542-552 (2015)

Philippe Meyer, R Regal, M Jung, P Siffert, L Mertz, A Constantinesco: *Feasibility of a semiconductor dosimeter to monitor skin dose in interventional radiology.* Medical Physics 28(10):2002-6 (2001).